Electron Spin Decoherence in Glassy Matrices

Samuel Meier Jahn

A dissertation
submitted in partial fulfillment of the
requirements for the degree of

Doctor of Philosophy

University of Washington
2023

Reading Committee:
Stefan Stoll, Chair
Gary Drobny
Bruce Robinson

Program Authorized to Offer Degree:
Chemistry

University of Washington

Abstract

Electron Spin Decoherence in Glassy Matrices

Samuel Meier Jahn

Chair of the Supervisory Committee:
Stefan Stoll
Department of Chemistry

Electron spin coherence is the ensemble property of multiple electrons, where their spin states maintain a constant phase relationship. In pulse electron paramagnetic resonance experiments, the electron spin coherence is proportional to the detected signal. In this thesis, we discuss our investigations into the role of the environmental nuclear spins, when the electron is on an organic radical solvated in a frozen glassy matrix. Chapters 0–3 introduce the required background and context. In particular, chapter 2 introduces Yang and Liu's Cluster Correlation Expansion (CCE) [1, 2]. Chapters 4–7 contain the main body where the data is analyzed and discussed; finally, chapter 8 discusses CluE, the home-built software used for the CCE electron spin decoherence simulations of this work. CluE uses structures generated via molecular dynamics to predict electron spin decoherence behavior. We validated CluE simulations against experimental data, and then used in silico structures to determine how different structural features affect electron spin decoherence. Chapter 4 assigns a decoherence contribution to individual nuclei, and identifies the 4–12 Å from the electron as the range where nuclei contribute the most. Chapter 5 looks at the interplay between decoherence pathways that do and do not refocus under different conditions. This could allow some pulsed electron paramagnetic resonance experiments to improve their signal-to-noise ratio. Chapter 6 looks at the effects of isotopic substitution of the water/glycerol matrix protons for deuterons. We find that even when only 1% of the hydrons are protons, the protons still contribute more to decoherence than the 99% deuterons. Additionally, proton clusters contribute more than randomly distributed protons. And Chapter 7 looks at protons within methyl groups. Methyl groups are quantum rotors that are both common, and can have a large influence on electron spin coherence. We investigate the spatial and energetic parameter space: we find that methyl groups drives decoherence most when the methyl groups are 2.5–6 Å away from the electron.

Contents

List of Symbols

Symbol	Description
$\mathbb{1}$	identity matrix
$\|\uparrow\rangle$	eigenvector of $\hat{S}_z$ or $\hat{I}_z$ with eigenvalue $+1/2$
$\|\downarrow\rangle$	eigenvector of $\hat{S}_z$ or $\hat{I}_z$ with eigenvalue $-1/2$
$\|\rightarrow\rangle$	eigenvector of $\hat{S}_x$ with eigenvalue $+1/2$
$\|\leftarrow\rangle$	eigenvector of $\hat{S}_x$ with eigenvalue $-1/2$
α	generic symbol, such as $\alpha \in \{z, +, -\}$ or $\alpha \in \{A_1, A_2, E\}$
A	an irreducible representation of Alt(3) or C_3
A_1	an irreducible representation of S_3 or C_{3v}
A_2	an irreducible representation of S_3 or C_{3v}
$\boldsymbol{A}_n$	hyperfine tensor for nucleus n
A_n	hyperfine zz coupling for nucleus n
Alt(N)	alternating group over N elements
$\boldsymbol{b}_{mn}$	dipole-dipole coupling tensor between nucleus m and n
b_{mn}	dipole-dipole zz coupling between nucleus m and n
β	inverse temperature $\frac{1}{k_\mathrm{B}T}$
$\boldsymbol{B}_0$	applied static magnetic field vector
B_0	applied static magnetic field magnitude
$\mathbb{C}$	set of all complex numbers
C_3	rotational symmetry group of an equilateral triangle in 2D
C_{3v}	symmetry group of an equilateral triangle in 2D
δ_{mn}, δ^n_m	Kronecker delta symbol
$\delta()$	Dirac delta function
e	elementary charge
e	Euler's number
E	energy variable an irreducible representation of S_3 or C_{3v}
$\hat{E}$	identity operator
$\boldsymbol{E}$	electric field vector

Symbol	Description
$\mathrm{E_a}$	an irreducible representation of Alt(3) or C_3
E_a	activation energy
$\mathrm{E_b}$	an irreducible representation of Alt(3) or C_3
ϵ	$\exp(2\mathrm{i}\pi/3)$
$\boldsymbol{g}$	electron g-matrix
g_e	free electron g-factor
g_n	g-factor for nucleus n
g_{zz}	zz component of the electron g-matrix
γ	gyromagnetic ratio
h	Planck constant
$\hbar$	reduced Planck constant
$\hat{H}$	Hamiltonian
$\hat{H}(m_\mathrm{S})$	Hamiltonian in the m_S electron spin manifold
$\hat{H}^{(\pm)}$	Hamiltonian in the $m_\mathrm{S} = \pm\frac{1}{2}$ electron spin manifold
$\mathbb{H}$	Hilbert space
i	number in $\mathbb{C}$, such that $\mathrm{i}^2 = -1$
$\hat{\boldsymbol{I}}$	nuclear spin vector operator in units of $\hbar$
$\hat{I}_x$	nuclear spin x operator in units of $\hbar$
$\hat{I}_y$	nuclear spin y operator in units of $\hbar$
$\hat{I}_z$	nuclear spin z operator in units of $\hbar$
$\hat{I}_+$	nuclear spin raising operator
$\hat{I}_-$	nuclear spin lowering operator
k_B	Boltzmann constant
μ_0	vacuum permeability
μ_B	Bohr magneton
μ_N	nuclear magneton
$\boldsymbol{M}$	magnetic dipole moment
M_x	x-component of $\boldsymbol{M}$
M_y	y-component of $\boldsymbol{M}$
M_z	z-component of $\boldsymbol{M}$
M_0	z-component of $\boldsymbol{M}$ at thermal equilibrium
ν	frequency
ν_t	methyl tunnel splitting frequency
$\mathscr{N}$	normal ordering symbol
ω	angular frequency
ω_t	methyl tunnel splitting angular frequency

Symbol	Description
$\hat{O}$	generic operator
$\mathscr{O}()$	big O notation symbol for "order of" approximation
π	ratio of the circumference to the diameter of a circle
ϕ	azimuthal angle
$\|\psi\rangle$	factor state of a full quantum state
$\|\Psi\rangle$	full quantum state
q	eigenvalue of $\frac{-1}{e}\boldsymbol{\nabla}\boldsymbol{E}^{\mathrm{T}}$ with largest magnitude
Q	quadrupole moment in units of area
$\hat{\rho}$	density matrix
ρ_ψ	density matrix element $\langle\psi\|\hat{\rho}\|\psi\rangle$
s	symmetry index
S_N	symmetric group over N elements
$\hat{\boldsymbol{S}}$	electron spin vector operators in units of $\hbar$
$\hat{S}_x$	electron spin x operator in units of $\hbar$
$\hat{S}_y$	electron spin y operator in units of $\hbar$
$\hat{S}_z$	electron spin z operator in units of $\hbar$
$\hat{\sigma}_x$	Pauli x operator
$\hat{\sigma}_y$	Pauli y operator
$\hat{\sigma}_z$	Pauli z operator
$\|\sigma\rangle$	generic Zeeman state
t	time variable
τ	delay time
θ	longitudinal angle
$\mathsf{\theta}()$	Heaviside step function
$\mathrm{tr}()$	trace
$\mathrm{tr}_{\mathbb{H}}()$	partial trace over $\|\psi\rangle \in \mathbb{H}$
$\mathscr{T}$	Dyson time-ordering symbol
$\mathscr{T}_{\mathrm{P}}$	path-ordering symbol
T	time parameter temperature
$\hat{T}$	kinetic energy operator
T_1	longitudinal relaxation time
T_2	transverse magnetization time
T_2^*	transverse magnetization time with inhomogeneous broadening
T_{M}	(de)coherence time, phase memory time
U	potential energy

Symbol	Description
$\hat{U}$	propagator, or time evolution operator
$\hat{U}(m_{\mathrm{S}})$	propagator in the m_{S} electron spin manifold
$\hat{U}^{(\pm)}$	propagator in the $m_{\mathrm{S}} = \pm\frac{1}{2}$ electron spin manifold
$v(t)$	normalized time-domain signal
$v_C(t)$	normalized time-domain signal for cluster C
$\tilde{v}_C(t)$	CCE auxiliary time-domain signal for cluster C
$v'_C(t)$	CE auxiliary time-domain signal for cluster C
$V(t)$	time-domain signal
V_d	LCE time-domain signal from diagram d
V_n	amplitude of nth time-domain signal
$V_{\mathrm{SE}}(2\tau)$	stretched exponential fit
$V_{\mathrm{SSE}}(2\tau)$	sum of stretched exponentials fit
$V_{\mathrm{PSE}}(2\tau)$	product of stretched exponentials fit
V_3	methyl rotational barrier
V	potential energy
ξ	stretch parameter for a stretched exponential
$\hat{\boldsymbol{x}}$	x unit vector
$\hat{\boldsymbol{y}}$	y unit vector
$\hat{\boldsymbol{z}}$	z unit vector
Z	normalization constant
$\mathbb{Z}$	set of all integers

List of Abbreviations

Abbreviated	**Unabbriviated**
B3LYP	Becke 3-parameter Lee–Yang–Par
CE	Cluster Expansion
CCE	Cluster Correlation Expansion
CHARMM	Chemistry at Harvard Macromolecular Mechanics
CHELPG	CHarges from ELectrostatic Potentials using a Grid-based method
CP	Carr–Purcell
DEER	Double Electron–Electron Resonance
def2-SVP	Split valence Polarization
DFT	Density Functional Theory
EPR	Electron Paramagnetic Resonance
INS	Inelastic Neutron Scattering
LCE	Linked Cluster Expansion
LCL	Low-order Correlations in Liouville space
MD	Molecular Dynamics
MTSSL	(1-oxyl-2,2,5,5-tetramethyl-3-pyrroline-3-methyl)MethaneThioSulfonate Spin Label
NMR	constant Nuclear Magnetic Resonance
NPT	constant Number, Pressure, and Temperature
NVT	constant Number, Volume, and Temperature
PDB	Protein Data Bank file
PELDOR	Pulsed ELectron DOuble Resonance
SV(P)	Split Valence (Polarization)
TEMPO	2,2,6,6-TEtraMethylPiperidine 1-Oxyl
WKB	Wentzel–Kramers–Brillouin

Chapter 0

Introduction

In physics two properties are temporally coherent if they maintain a fixed phase relationship to each other. Here, the coherence we are interested in is between the spin states of electrons precessing in an applied magnetic field. Such coherent systems have relevance in areas from Electron Paramagnetic Resonance (EPR) to quantum computing, where the timescale for which coherence can be maintained, the coherence time, puts a limit on experiments that rely on the coherence. In the world of quantum computing, the coherence lifetime of a qubit limits how many operations can be performed. There are many candidates for spin-qubits, such as nitrogen–vacancy (NV) centers [3–5], GaAs quantum dots[6, 7], and more. Molecular spin-qubits are also of interest [8–10].

While environmental spins can cause decoherence, they can also be useful. By including them as part of the qubit, nuclear spins act as a form of quantum memory[11]. Environmental spins can also provide information on the system under study, especially when their contribution to the observed signal can be separated from the rest of the system; this is the idea behind many EPR experiments [12–14]. In biological EPR, an experiment popular enough to have two common names is Double Electron–Electron Resonance (DEER), a.k.a Pulsed ELectron DOuble Resonance (PELDOR). DEER uses two radical electrons and measures the distance between them.[15–17] This is useful for investigating bio-macromolecule, since the separation between well selected sites can change during, for example, protein-ligand interactions [18]. Additionally, since unpaired electrons are typically unstable, most proteins do not natively contain them, allowing DEER to work on proteins of various sizes and flexibilities.

One of the goals of this work is to develop an in silico method for predicting the coherence timescale in a biologically relevant setting: a nitroxide spin label on a protein surrounded by water. The advantage of such a method, would be to aid in experiment design: a DEER experiment involves selecting amino acid sites to mutate, and then performing the mutagenesis, expressing the protein, and purifying the protein, before reaching a point where the coherence time can be measured, meaning that choosing a site with insufficient coherence time for the desired measurement is costly.

Due to the role of decoherence in quantum computing and EPR investigations, understanding and predicting decoherence is an important problem. There are many decoherence pathways [19], but when most motional degrees of freedom have frozen out (at low temperatures), nuclear spin flip-flops are believed to be the dominant source of decoherence[20–23]. This means that all save spin degrees of freedom can often be neglected, but even in this case, the Hilbert space for N spin-1/2 particles is 2^N-dimensional: for even a few hundred spins, the number of dimensions greatly exceeds the number of atoms in the visible universe. Semi-classical approximations require inputting a flip-flop rate manually, making them descriptive rather than predictive[20, 24–27]. There are many quantum approximations: reduced Liouville space methods [28–33] as well as Hilbert space methods: Cluster Expansion (CE) [34], Linked Cluster Expansion (LCE) [35], Cluster Correlation Expansions (CCE) [1], and ensemble CCE [2]. The reduced Liouville space methods follow the time evolution of a density matrix, while the cluster expansions follow the expectation value for the detection operator, $\hat{S}_+$ here. Instead of trying to deal with the impossibly large Hilbert spaces for systems with many spins, the CE of Witzel and Das Samra breaks systems into many calculable sized clusters and approximates the decoherence behavior from contributions from each cluster[34]. CE has been used successfully to model copper based radicals doped into a crystalline lattice[36]. LCE is a resummed Taylor series[35]. LCE can

provide some analytic insight to more numerical methods like CE or CCE [37]. CCE builds upon the original cluster expansion with insight from the LCE[1, 38]. CCE will be the primary method used for in silico prediction in this work.

Chapter 1–3 will introduce the background theory. Original work will be covered afterward. The common theme throughout the original work is that it all explores the decoherence of an organic radical in a frozen glassy matrix. We look at where to avoid placing nuclear spins to maximize electron spin coherence times, how multi-spin effects cause optimal DEER timings to differ in different conditions, why coherence times scale differently with spin concentrations in different situations and which methyl groups drive decoherence.

Chapter 1

Background: Decoherence and Quantum Spin Dynamics

1.1 An Introduction to Decoherence

An orchestra is an example of a coherent system. All the musicians playing individually is not enough to create beautiful melodies. Additionally, the musicians need to be synchronized or be coherent with each other, so that their individual songs add together to create the symphony that the audience hears. While the musicians are certainly aware of each other, it is the conductor's job to provide an additional prompts to maintain coherence, even in the presence of distractions, such as a restless audience. In this imagined case, there are only enough seats for half the audience, so people must take turns sitting, and the seats are squeaky, so every time a pair of people switch states, the musicians closest to that place in the audience are in more danger of getting disturbed than the other musicians.

The orchestra can be used as an analogy for the spin dynamics during a pulse Electron Paramagnetic Resonance (EPR) experiment. The musicians are the stable radical electron spins, magnetic dipoles playing their songs by precessing about the axis of the applied magnetic field, singing not with sound but with microwaves. The audience is made up of all the nuclear magnetic dipoles, spins that generate magnetic noise as the undergo flip-flops interactions. The conductor in EPR experiments is the spectrometer, who applies microwave pulses to both initialize the electrons into a state with a macroscopic magnetic dipole and to refocus the electron coherence to restore the bulk magnetic moment at the time of detection.

The systems we will be looking at typically have a diluted stable radical surrounded by water and organic molecules, often containing protons from the hydrogen atoms. The systems are frozen and a strong (0.1–10 T) static magnetic field, $\boldsymbol{B}_0$, is applied to the system. Unperturbed, the vector sum of all the electron magnetic moments points along the applied magnetic field; however, pulse EPR experiments typically start with a $\pi/2$ microwave pulse, which, as the name suggests, rotates the magnetic moments of the electrons resonant with the microwave field by $\pi/2$ radians to be perpendicular to the applied magnetic field. This isochromat produces a macroscopic magnetic dipole, $\boldsymbol{M}$, with a measurable component perpendicular to the applied magnetic field that precesses around the applied magnetic field according to the Bloch equation[39]:

$$\frac{\mathrm{d}}{\mathrm{d}t}\boldsymbol{M} = \boldsymbol{M} \times \left(\gamma \boldsymbol{B}_0\right) - \frac{M_x \hat{\boldsymbol{x}} + M_y \hat{\boldsymbol{y}}}{T_2} - \frac{M_z - M_0}{T_1}\hat{\boldsymbol{z}}. \tag{1.1}$$

The three terms on the right hand side are worth discussing. The first is the classical precession terms of a magnetic dipole with gyromagnetic ratio, γ, in an external magnetic field, $\boldsymbol{B}_0$. The second and third are dissipative terms: T_1 is the timescale over which the magnetization realigns with the applied magnetic field, and T_2 is the timescale for the magnetization perpendicular to the applied magnetic field to vanish. From these definitions, and the knowledge that $|\boldsymbol{M}|$ does not grow, it is clear that $T_2 \leq T_1$, but the case where $T_2 < T_1$, and sometimes $T_2 \ll T_1$, needs more explanation. Sticking to a classical picture for now, within the isochromat (set of spins with approximately same resonance frequency), each electron precesses around the local magnetic field, which while at high applied magnetic field strengths is often dominated

by the applied magnetic field, also has components from every other magnetic dipole within the system. These magnetic dipoles are typically magnetic nuclei, which even at cryogenic temperatures, are still in the high-temperature regime, and so thermal fluctuations introduce a time dependent contribution to the magnetic field each electron feels that is different for each electron. This means the precession frequency of each electron also has some stochastic variation. After a time on the order of T_2, the phase angles for all the electrons will uniformly span $[0, 2\pi)$, at which point there will be no net magnetization perpendicular to the applied magnetic field, even if the net magnetic moment has not yet returned to its equilibrium value $M_0\hat{\boldsymbol{z}}$. By convention the applied magnetic field defines the z-axis:

$$\hat{\boldsymbol{z}} := \frac{\boldsymbol{B}_0}{|\boldsymbol{B}_0|}. \tag{1.2}$$

The Bloch equation is phenomenlogical, and should be replaced with a quantum mechanical description for better accuracy. Since the applied magnetic field dominates over inter-spin couplings, it is useful to work in the Zeeman basis: $\hat{S}_z |\uparrow\rangle = +\frac{1}{2} |\uparrow\rangle$ and $\hat{S}_z |\downarrow\rangle = -\frac{1}{2} |\downarrow\rangle$. Under this description, the $\pi/2$ microwave pulse takes the Zeeman states to $|\leftarrow\rangle$ and $|\rightarrow\rangle$, defined by $\hat{S}_x |\rightarrow\rangle = +\frac{1}{2} |\rightarrow\rangle$ and $\hat{S}_x |\leftarrow\rangle = -\frac{1}{2} |\leftarrow\rangle$. Both $|\leftarrow\rangle$ and $|\rightarrow\rangle$ have representations in the Zeeman basis as superposition states.

$$\begin{aligned} |\rightarrow\rangle &= \frac{1}{\sqrt{2}}\Big(|\uparrow\rangle + |\downarrow\rangle \Big). \\ |\leftarrow\rangle &= \frac{1}{\sqrt{2}}\Big(|\uparrow\rangle - |\downarrow\rangle \Big). \end{aligned} \tag{1.3}$$

These are not stationary states and $\langle \hat{S}_x \rangle$ will oscillate with time as long as the two state are unevenly populated. If an excess of electrons are initialized in one state, say $|\rightarrow\rangle$, then left to evolve under only a homgeneous Zeeman Hamiltonian, then $\langle \hat{S}_x(t) \rangle \propto \frac{1}{2}\cos(\omega_0 t)$, where ω_0 is the Larmor frequency. More precisely, given N_e electrons each following

$$\hat{H} = \hbar\omega_0 \hat{S}_z \tag{1.4}$$

with eigenenergies, $\pm\frac{\hbar\omega_0}{2}$, and state

$$|\rightarrow\rangle (t) = \frac{1}{\sqrt{2}}\Big(|\uparrow\rangle \, \mathrm{e}^{-\mathrm{i}\frac{\omega_0}{2}t} + |\downarrow\rangle \, \mathrm{e}^{+\mathrm{i}\frac{\omega_0}{2}t} \Big), \tag{1.5}$$

then

$$\langle \rightarrow | \hat{S}_x(t) | \rightarrow \rangle = \frac{N_\mathrm{e}}{2} \frac{\mathrm{e}^{-\mathrm{i}\omega_0 t} + \mathrm{e}^{+\mathrm{i}\omega_0 t}}{2} = \frac{N_\mathrm{e}}{2}\cos(\omega_0 t). \tag{1.6}$$

The reason that the N_e electrons give a multiplicative factor is because of the assumption that each electron is in an identical system. If instead, there is some distribution of Larmor frequencies, such as from inhomogeneities in the applied magnetic field or from orientation-dependent spin–orbit coupling, then $\hat{H} = \hbar(\omega_0 + \Delta\omega)\hat{S}_z$, and if $\phi := \mod_{2\pi}(\Delta\omega t)$ uniformly spans $[0, 2\pi)$, then

$$\langle \hat{S}_x(t) \rangle = \frac{N_\mathrm{e}}{2} \int_0^{2\pi} \mathrm{d}\phi \; \cos(\omega_0 t + \phi) = 0. \tag{1.7}$$

This does not require $\Delta\omega$ itself to be uniformly distributed, since at long time values, $\mod_{2\pi}(\Delta\omega t)$ will span $[0, 2\pi)$ over $\Delta\omega$ ranges small enough to be equally probable. This is called inhomogeneous broadening, and when included as a contribution to T_2, gives it the name T_2^*.[40] Inhomogeneous broadening can be filtered out by various echo experiments, such as the Hahn echo experiment[41] (shown in figure 1.1).

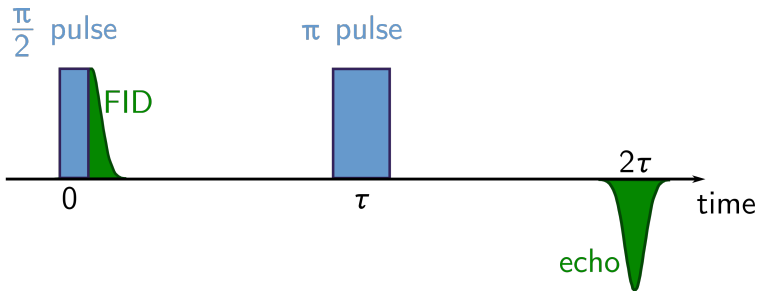

Figure 1.1: This diagram is a typical pulse sequence diagram representing a Hahn echo experiment. Time increases from left to right with $t = 0$ coincident with the $\pi/2$-pulse. The blue rectangles represent the applied microwave pulses; they are labeled by the number of radians they rotate the magnetic dipole moment of the resonant electrons around the y-axis. This magnetic moment's projection onto the x-axis is indicated in green. Immediately after the $\pi/2$-pulse, $\langle \hat{S}_x \rangle > 0$, but (due mostly to inhomogeneous broadening) the $\langle \hat{S}_x \rangle$ decays to zero in what is know as a free-induction decay (FID). At time τ, a π pulse is applied rotating the isochromat's magnetic moment π radians (here, also around the y-axis), so an echo forms at $t = 2\tau$, where $\langle \hat{S}_x(t = 2\tau) \rangle = -\langle \hat{S}_x(t = 0) \rangle$.

The way these echo experiments work is to apply π pulses to the central electron flipping the Zeeman states: $|\uparrow\rangle \rightarrow -|\downarrow\rangle$, and $|\downarrow\rangle \rightarrow |\uparrow\rangle$. This can be applied to $|\rightarrow\rangle$ to determine how the π-pulse affects it. Let the pulse length be t_π, and δt be some duration that satisfies $t_\pi < \delta t \ll \tau$.

$$\begin{aligned} |\rightarrow\rangle\,(t = \tau - \delta t) &= \frac{1}{\sqrt{2}}\Big(|\uparrow\rangle\, \mathrm{e}^{-\mathrm{i}\frac{\omega_0+\Delta\omega}{2}\tau} + |\downarrow\rangle\, \mathrm{e}^{+\mathrm{i}\frac{\omega_0+\Delta\omega}{2}\tau} \Big). \\ |\rightarrow\rangle\,(t = \tau + \delta t) &= \frac{1}{\sqrt{2}}\Big(-|\downarrow\rangle\, \mathrm{e}^{-\mathrm{i}\frac{\omega_0+\Delta\omega}{2}\tau} + |\uparrow\rangle\, \mathrm{e}^{+\mathrm{i}\frac{\omega_0+\Delta\omega}{2}\tau} \Big). \end{aligned} \tag{1.8}$$

If it were not for the phase factors, $|\rightarrow\rangle$ would go to $|\leftarrow\rangle$, and $|\leftarrow\rangle$ to $-|\rightarrow\rangle$; with the phase factors $|\rightarrow\rangle$ and $|\leftarrow\rangle$ are taken to linear combinations of themselves. With this in mind the time evolution of $|\rightarrow\rangle$ after the π-pulse follows

$$|\rightarrow\rangle\,(t > \tau) = \frac{1}{\sqrt{2}}\Big(-|\downarrow\rangle\, \mathrm{e}^{+\mathrm{i}\frac{\omega_0+\Delta\omega}{2}(t-2\tau)} + |\uparrow\rangle\, \mathrm{e}^{-\mathrm{i}\frac{\omega_0+\Delta\omega}{2}(t-2\tau)} \Big), \tag{1.9}$$

so that once equal time has passed pre and post π-pulse ($t = 2\tau$),

$$|\rightarrow\rangle\,(t = 2\tau) = \frac{1}{\sqrt{2}}\Big(-|\downarrow\rangle + |\uparrow\rangle \Big) = |\leftarrow\rangle \tag{1.10}$$

independent of either ω_0 or $\Delta\omega$. And so $\langle \hat{S}_x(t = 2\tau) \rangle = -\langle \hat{S}_x(t = 0) \rangle$, at least when only temporally constant Zeeman couplings are considered.

In reality there are other interactions and so $|\langle \hat{S}_x(t = 2\tau) \rangle| < |\langle \hat{S}_x(t = 0) \rangle|$, and so as $2\tau \rightarrow \infty$, $|\langle \hat{S}_x(t = 2\tau) \rangle| \rightarrow 0$. By repeating the Hahn echo experiment for many values of 2τ and recording the echo amplitude at each 2τ value, the Hahn echo decay can be measured, which can be used to gain information about these other interactions and, by extension, the system under study. Note that unlike with an FID, in the Hahn echo and other echo experiments, the full decay is not observed in a single application of the pulse sequence; each instance of the pulse sequence requires choosing a particular set of delay parameters, so in order measure the echo decay as function of a delay parameter, many instances of the pulse sequence must be used, varying the delay time(s), over the desired range. The primary pulse sequence studied in this work is the Hahn echo[41]. Empirically, the Hahn echo decay takes the form of a stretched exponential[42, 43]:

$$V(2\tau) = V_0 \exp\Big(-\big(\frac{2\tau}{T_\mathrm{M}}\big)^\xi \Big). \tag{1.11}$$

The use of V as the detected signal refers to a measured voltage in the spectrometer; T_M is the phase memory time, the (de)coherence time, or the coherence lifetime, and ξ is the stretching parameter. Together, T_M and

ξ, provide a useful descriptor of echo decays, although higher parameter descriptions also exist and can be useful [44, 45]. The decoherence timescale is not a property of just the system, but of the system and applied pulse sequence[22, 44, 46]. Figure 1.2 illustrates a few mock Hahn echo decays with $\xi \in \{1, 1.5, 2, 2.5, 3\}$. $\xi = 1$ is an exponential decay. And a Gaussian occurs at $\xi = 2$. On top of the stretched exponential decay, often, additional higher-frequency modulations of the echo decay envelope are present that are due to pseudosecular hyperfine couplings to closeby nuclei.

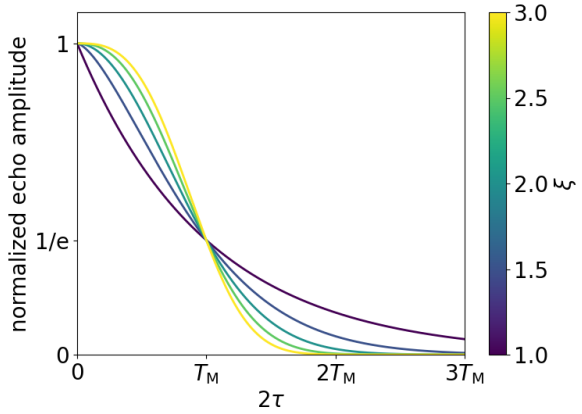

Figure 1.2: The Hahn echo decay often has a stretched exponential form. The above mock Hahn echo decays are shown as stretched exponentials with the same T_M, but several values of ξ (indicated by the color–axis).

1.2 The Propagator

The time–evolution of a non-relativistic quantum state follows the Schrödinger equation:

$$\frac{\mathrm{d}}{\mathrm{d}t}|\Psi\rangle = -\frac{\mathrm{i}}{\hbar}\hat{H}|\Psi\rangle\,. \tag{1.12}$$

Assuming for now that the Hamiltonian is time-independent, the Schrödinger equation can be formally integrated to give the state at time, t.

$$|\Psi(t)\rangle = \exp\left(-\frac{\mathrm{i}}{\hbar}t\hat{H}\right)|\Psi(0)\rangle =: \hat{U}(t)\,|\Psi(0)\rangle\,. \tag{1.13}$$

The propagator, $\hat{U}(t)$, also obeys the Schrödinger equation.

$$\frac{\mathrm{d}}{\mathrm{d}t}\hat{U}(t) = -\frac{\mathrm{i}}{\hbar}\hat{H}\,\hat{U}(t). \tag{1.14}$$

While $|\Psi(0)\rangle$ depends on the specifics of the system, the propagator for zero duration is the identity. Since the choice of temporal origin is arbitrary,

$$\hat{U}(t_1 + t_0) = \hat{U}(t_1)\hat{U}(t_0). \tag{1.15}$$

This also follows from the properties of the exponential function for commuting arguments. But with a time-dependent Hamiltonian, the Hamiltonian at one time may not commute with its past or future self. One way to address this is to break the time-evolution into N time steps, $\tau = t/N$, small enough that the Hamiltonian is approximately constant over each step.

$$\begin{aligned}\hat{U}(t) = &\exp\left(-\frac{\mathrm{i}}{\hbar}\tau\hat{H}_N\right)\exp\left(-\frac{\mathrm{i}}{\hbar}\tau\hat{H}_{N-1}\right)\cdots\exp\left(-\frac{\mathrm{i}}{\hbar}\tau\hat{H}_2\right)\exp\left(-\frac{\mathrm{i}}{\hbar}\tau\hat{H}_1\right)\\ &= 1 - \frac{\mathrm{i}}{\hbar}\tau\sum_n \hat{H}_n + \left(-\frac{\mathrm{i}}{\hbar}\tau\right)^2\sum_{m<n}\hat{H}_n\hat{H}_m + \frac{1}{2}\left(-\frac{\mathrm{i}}{\hbar}\tau\right)^2\sum_n \hat{H}_n^2 + \mathscr{O}(\tau^3).\end{aligned} \tag{1.16}$$

Notice that there are two sources for the quadratic terms in the Taylor expansion: the normal quadratic terms from expanding the exponential functions, and there is also the products of two linear terms from separate exponentials. In both cases, the products are time-ordered from right to left. This is a consequence of multiplying the propagators together in time order. The sums can be simplified by introducing the Dyson time-ordering symbol, $\mathscr{T}$. The $\mathscr{T}$ is notation that indicates that products are to be taken in time order, regardless of the order they are written in. For example,

$$\mathscr{T}\hat{H}(t_0)\hat{H}(t_1) = \theta(t_0 - t_1)\hat{H}(t_0)\hat{H}(t_1) + \theta(t_1 - t_0)\hat{H}(t_1)\hat{H}(t_0), \tag{1.17}$$

where $\theta(t)$ is the Heaviside step function. With $\mathscr{T}$,

$$\sum_{m<n} \hat{H}_n\hat{H}_m + \frac{1}{2}\sum_n \hat{H}_n^2 = \mathscr{T}\frac{1}{2}\sum_{m,n} \hat{H}_n\hat{H}_m. \tag{1.18}$$

Equation (1.16) simplifies to

$$\hat{U}(t) = \mathscr{T}\Big(1 - \frac{\mathrm{i}}{\hbar}\tau\sum_n \hat{H}_n + \frac{1}{2}\Big(-\frac{\mathrm{i}}{\hbar}\tau\Big)^2 \sum_{m,n} \hat{H}_n\hat{H}_m + \mathscr{O}(t^3)\Big). \tag{1.19}$$

At this point the $\tau \to 0$ limit can be taken, turning the sums into integrals:

$$\hat{U}(t) = \mathscr{T}\Big(1 - \frac{\mathrm{i}}{\hbar}\int_0^t \mathrm{d}t'\hat{H}(t') + \frac{1}{2}\Big(-\frac{\mathrm{i}}{\hbar}\Big)^2 \int \mathrm{d}t'\mathrm{d}t''\hat{H}(t')\hat{H}(t'') + \mathscr{O}(t^3)\Big), \tag{1.20}$$

and the Taylor series collected back into a exponential function:

$$\hat{U}(t) = \mathscr{T}\exp\Big(-\frac{\mathrm{i}}{\hbar}\int_0^t \mathrm{d}t'\hat{H}(t')\Big). \tag{1.21}$$

This propagator still follows the Schrödinger equation.

$$\frac{\mathrm{d}}{\mathrm{d}t}\hat{U}(t) = -\frac{\mathrm{i}}{\hbar}\hat{H}(t)\,\hat{U}(t). \tag{1.22}$$

1.3 Statistical Ensembles

Let $|\Psi_1\rangle$, be the state of a single instance of an isolated system, but not necessarily an eigenstate. For a system with state $|\Psi_1\rangle$, the expectation value of some operator, $\hat{O}$, is

$$\langle\hat{O}\rangle = \langle\Psi_1|\hat{O}|\Psi_1\rangle\,. \tag{1.23}$$

If instead, there are many instances of the system, that are not completely identical, there will be a distribution of states; for example, in pulse EPR experiments, even if a collection of electrons are put into a known state with microwave pulses, the state of the surrounding bath of nuclei will likely be unknown. This means the systems as a whole will neither be fully known nor identical over the 10^{12} different detectable electrons in a typical sample. Assuming the systems can exist in one of K different states, and state $|\Psi_k\rangle$ occurs with probability, p_k, the expectation value $\hat{O}$ becomes

$$\big\langle\,\langle\hat{O}\rangle\,\big\rangle = \sum_{k=1}^{K} p_k\,\langle\Psi_k|\hat{O}|\Psi_k\rangle\,. \tag{1.24}$$

The expectation value must be evaluated not only from the quantum state, but also over the various states the system could be in. The instances are assumed to be independent, but they could be separated either spatially, and/or temporally (The same experiment is run multiple times). A convenient way deal with spin ensembles is to use the density operator:

$$\hat{\rho} := \sum_k p_k\,|\Psi_k\rangle\,\langle\Psi_k|\,. \tag{1.25}$$

Often $\hat{\sigma}$ is used for the spin density operator to distinguish it from the full density operator, $\hat{\rho}$. Here this distinction is left to context, as σ is used here for Pauli matrices. The expectation value of $\hat{O}$ in terms of $\hat{\rho}$ can reformulated by introducing an orthonormal basis: $|\Psi_k\rangle = \sum_n c_{nk} |n\rangle$ to insert the identity $\mathbb{1} = \sum_n |n\rangle \langle n|$.

$$\begin{aligned}
\langle \hat{O} \rangle &= \sum_k p_k \langle \Psi_k | \hat{O} | \Psi_k \rangle \\
&= \sum_k p_k \sum_n \langle \Psi_k | \hat{O} | n \rangle \langle n | \Psi_k \rangle \\
&= \sum_k p_k \sum_n \langle n | \Psi_k \rangle \langle \Psi_k | \hat{O} | n \rangle \\
&= \sum_n \langle n | \sum_k p_k |\Psi_k\rangle \langle \Psi_k | \hat{O} | n \rangle \\
&= \sum_n \langle n | \hat{\rho} \hat{O} | n \rangle \\
&= \mathrm{tr}(\hat{\rho}\hat{O}).
\end{aligned} \tag{1.26}$$

Density operators can describe both pure states and mixed states. A pure state is any state whose density operator satisfies

$$\hat{\rho}^2 = \hat{\rho}. \tag{1.27}$$

This occurs when $p_k = \delta_{k,k'}$, so that there is only one term in the sum. All other states are mixed states. Mixed states can occur when there are differences between the states of different instances of the system, or if the system is not isolated from an environment that is not included in $\hat{\rho}$.

A particularly important mixed state is that from a thermal ensemble. At thermal equilibrium, each energy eigenstate, $|n\rangle$, should be occupied according to the Boltzmann distribution at inverse temperature $\beta := \frac{1}{k_\mathrm{B} T}$:

$$\hat{\rho} = \frac{1}{Z} \sum_n \exp\left(-\beta \langle n | \hat{H} | n \rangle \right) |n\rangle \langle n| . \tag{1.28}$$

The normalization constant Z ensures $\mathrm{tr}(\hat{\rho}) = 1$. The thermal density operator is diagonal in an eigenbasis of $\hat{H}$ because the off-diagonal terms will in general have a complex phase, which when averaged over many instance of the system will take the off-diagonal elements to zero. Note that since the $|n\rangle$s are an eigenbasis, the Hamiltonian is diagonal, and since exponentiating every diagonal element of a diagonal matrix is the same as exponentiating the matrix itself,

$$\hat{\rho} = \frac{1}{Z} \exp\left(-\beta \hat{H} \right). \tag{1.29}$$

This no longer references any particular basis, and so should be true in general, although the density operator will not be diagonal in an arbitrary basis. Since $k_\mathrm{B} T$ is often large compared to the energy splittings, so the $\beta \to 0$ limit is applicable:

$$\hat{\rho} \approx \frac{\mathbb{1} - \beta \hat{H}}{\mathrm{tr}\big(\mathbb{1} - \beta \hat{H}\big)}, \tag{1.30}$$

or for nuclear spins, even as

$$\hat{\rho} \approx \frac{\mathbb{1}}{\dim \hat{H}}. \tag{1.31}$$

For a system with only spin degrees of freedom, the dimensionality of the Hilbert space is the product of the spin multiplicities.

1.4 Interaction Picture

The time-dependent expectation value for a Hermitian operator, $\hat{O}$, given an initial state $|\Psi_0\rangle = |\Psi(t=0)\rangle$ and a time-independent Hamiltonian $\hat{H} = \hat{H}_0 + \hat{H}_1$, is

$$\begin{aligned}\langle\hat{O}(t)\rangle &= \langle\Psi_0|\,\mathrm{e}^{+\frac{\mathrm{i}}{\hbar}(\hat{H}_0+\hat{H}_1)t}\hat{O}\,\mathrm{e}^{-\frac{\mathrm{i}}{\hbar}(\hat{H}_0+\hat{H}_1)t}|\Psi_0\rangle \\ &= \mathrm{tr}\Big(\,\mathrm{e}^{-\frac{\mathrm{i}}{\hbar}(\hat{H}_0+\hat{H}_1)t}\hat{\rho}_0\,\mathrm{e}^{+\frac{\mathrm{i}}{\hbar}(\hat{H}_0+\hat{H}_1)t}\hat{O}\Big) \\ &= \mathrm{tr}\Big(\hat{\rho}_0\,\mathrm{e}^{+\frac{\mathrm{i}}{\hbar}(\hat{H}_0+\hat{H}_1)t}\hat{O}\,\mathrm{e}^{-\frac{\mathrm{i}}{\hbar}(\hat{H}_0+\hat{H}_1)t}\Big).\end{aligned} \tag{1.32}$$

The last line follows from the invariance of the trace to cyclic permutations of the product factors in the argument. The Schrödinger picture groups the propagators with the state.

$$\begin{aligned}\langle\hat{O}(t)\rangle &= \Big(\,\langle\Psi_0|\,\mathrm{e}^{+\frac{\mathrm{i}}{\hbar}(\hat{H}_0+\hat{H}_1)t}\Big)\hat{O}\Big(\,\mathrm{e}^{-\frac{\mathrm{i}}{\hbar}(\hat{H}_0+\hat{H}_1)t}\,|\Psi_0\rangle\,\Big) \\ &= \langle\Psi_{\mathrm{S}}(t)|\hat{O}|\Psi_{\mathrm{S}}(t)\rangle \\ &= \mathrm{tr}\Big(\Big(\,\mathrm{e}^{-\frac{\mathrm{i}}{\hbar}(\hat{H}_0+\hat{H}_1)t}\hat{\rho}_0\,\mathrm{e}^{+\frac{\mathrm{i}}{\hbar}(\hat{H}_0+\hat{H}_1)t}\Big)\hat{O}\Big) \\ &= \mathrm{tr}\Big(\hat{\rho}_{\mathrm{S}}(t)\hat{O}\Big).\end{aligned} \tag{1.33}$$

Whereas the time dependence is incorporated into the operator for the Heisenberg picture

$$\begin{aligned}\langle\hat{O}(t)\rangle &= \langle\Psi_0|\Big(\,\mathrm{e}^{+\frac{\mathrm{i}}{\hbar}(\hat{H}_0+\hat{H}_1)t}\hat{O}\,\mathrm{e}^{-\frac{\mathrm{i}}{\hbar}(\hat{H}_0+\hat{H}_1)t}\Big)|\Psi_0\rangle \\ &= \langle\Psi_0|\hat{O}_{\mathrm{H}}(t)|\Psi_0\rangle \\ &= \mathrm{tr}\Big(\hat{\rho}\Big(\,\mathrm{e}^{+\frac{\mathrm{i}}{\hbar}(\hat{H}_0+\hat{H}_1)t}\hat{O}\,\mathrm{e}^{-\frac{\mathrm{i}}{\hbar}(\hat{H}_0+\hat{H}_1)t}\Big)\Big) \\ &= \mathrm{tr}\Big(\hat{\rho}\,\hat{O}_{\mathrm{H}}(t)\Big).\end{aligned} \tag{1.34}$$

The interaction picture is in between the two.[47] Using $\mathbb{1} = \mathrm{e}^{-\frac{\mathrm{i}}{\hbar}\hat{H}_0 t}\,\mathrm{e}^{\frac{\mathrm{i}}{\hbar}\hat{H}_0 t}$,

$$\begin{aligned}\langle\hat{O}(t)\rangle &= \Big(\,\langle\Psi_0|\,\mathrm{e}^{+\frac{\mathrm{i}}{\hbar}(\hat{H}_0+\hat{H}_1)t}\,\mathrm{e}^{-\frac{\mathrm{i}}{\hbar}\hat{H}_0 t}\Big)\Big(\,\mathrm{e}^{\frac{\mathrm{i}}{\hbar}\hat{H}_0 t}\hat{O}\,\mathrm{e}^{-\frac{\mathrm{i}}{\hbar}\hat{H}_0 t}\Big)\Big(\,\mathrm{e}^{\frac{\mathrm{i}}{\hbar}\hat{H}_0 t}\,\mathrm{e}^{-\frac{\mathrm{i}}{\hbar}(\hat{H}_0+\hat{H}_1)t}\,|\Psi_0\rangle\,\Big) \\ &= \langle\Psi_{\mathrm{I}}(t)|\hat{O}_{\mathrm{I}}(t)|\Psi_{\mathrm{I}}(t)\rangle \\ &= \mathrm{tr}\Big(\Big(\,\mathrm{e}^{\frac{\mathrm{i}}{\hbar}\hat{H}_0 t}\,\mathrm{e}^{-\frac{\mathrm{i}}{\hbar}(\hat{H}_0+\hat{H}_1)t}\hat{\rho}_0\,\mathrm{e}^{+\frac{\mathrm{i}}{\hbar}(\hat{H}_0+\hat{H}_1)t}\,\mathrm{e}^{-\frac{\mathrm{i}}{\hbar}\hat{H}_0 t}\Big)\Big(\,\mathrm{e}^{\frac{\mathrm{i}}{\hbar}\hat{H}_0 t}\hat{O}\,\mathrm{e}^{-\frac{\mathrm{i}}{\hbar}\hat{H}_0 t}\Big)\Big) \\ &= \mathrm{tr}\Big(\hat{\rho}_{\mathrm{I}}(t)\,\hat{O}_{\mathrm{I}}(t)\Big).\end{aligned} \tag{1.35}$$

The advantage to doing this can be seen by looking at the time dependence of $|\Psi_{\mathrm{I}}\rangle$.

$$\begin{aligned}\frac{\mathrm{d}}{\mathrm{d}t}|\Psi_{\mathrm{I}}(t)\rangle &= \frac{\mathrm{d}}{\mathrm{d}t}\Big(\,\mathrm{e}^{\frac{\mathrm{i}}{\hbar}\hat{H}_0 t}\,|\Psi_{\mathrm{S}}(t)\rangle\,\Big) \\ &= \frac{\mathrm{i}}{\hbar}\hat{H}_0\,\mathrm{e}^{\frac{\mathrm{i}}{\hbar}\hat{H}_0 t}\,|\Psi_{\mathrm{S}}(t)\rangle - \frac{\mathrm{i}}{\hbar}\,\mathrm{e}^{\frac{\mathrm{i}}{\hbar}\hat{H}_0 t}\big(\hat{H}_0+\hat{H}_1\big)\,|\Psi_{\mathrm{S}}(t)\rangle \\ &= \frac{\mathrm{i}}{\hbar}\hat{H}_0\,\mathrm{e}^{\frac{\mathrm{i}}{\hbar}\hat{H}_0 t}\,|\Psi_{\mathrm{S}}(t)\rangle - \frac{\mathrm{i}}{\hbar}\,\mathrm{e}^{\frac{\mathrm{i}}{\hbar}\hat{H}_0 t}\big(\hat{H}_0+\hat{H}_1\big)\,\mathrm{e}^{-\frac{\mathrm{i}}{\hbar}\hat{H}_0 t}\,\mathrm{e}^{\frac{\mathrm{i}}{\hbar}\hat{H}_0 t}\,|\Psi_{\mathrm{S}}(t)\rangle \\ &= \frac{\mathrm{i}}{\hbar}\hat{H}_0\,|\Psi_{\mathrm{I}}(t)\rangle - \frac{\mathrm{i}}{\hbar}\big(\hat{H}_0 + \,\mathrm{e}^{\frac{\mathrm{i}}{\hbar}\hat{H}_0 t}\hat{H}_1\,\mathrm{e}^{-\frac{\mathrm{i}}{\hbar}\hat{H}_0 t}\big)\,|\Psi_{\mathrm{I}}(t)\rangle \\ &= -\frac{\mathrm{i}}{\hbar}\big(\,\mathrm{e}^{\frac{\mathrm{i}}{\hbar}\hat{H}_0 t}\hat{H}_1\,\mathrm{e}^{-\frac{\mathrm{i}}{\hbar}\hat{H}_0 t}\big)\,|\Psi_{\mathrm{I}}(t)\rangle \\ &= -\frac{\mathrm{i}}{\hbar}\hat{H}_{1\mathrm{I}}(t)\,|\Psi_{\mathrm{I}}(t)\rangle\,.\end{aligned} \tag{1.36}$$

This is the Schrödinger equation again, just with the interaction picture state, and $\hat{H}_{1\mathrm{I}}(t)$ instead of $\hat{H}_0+\hat{H}_1$. And so the Schrödinger equation for the propagator in the interaction representation is

$$\frac{\mathrm{d}}{\mathrm{d}t}\hat{U}_{\mathrm{I}}(t) = -\frac{\mathrm{i}}{\hbar}\hat{H}_{1\,\mathrm{I}}(t)\hat{U}_{\mathrm{I}}(t), \tag{1.37}$$

so

$$\hat{U}_{\mathrm{I}}(t) = \mathscr{T}\Big(\mathrm{e}^{-\frac{\mathrm{i}}{\hbar}\int_0^t \mathrm{d}t'\ \hat{H}_{1\,\mathrm{I}}(t')}\Big). \tag{1.38}$$

1.5 Spin Hamiltonian

Rather than working with the full standard model, quantum electrodynamics, or even the full Schrödinger equation with relativistic corrections, we will focuses on the even narrower spin Hamiltonian.

The spin Hamiltonian is an effective Hamiltonian that only includes spin degrees of freedom—deriving it from the full relativistic Hamiltonian involves taking the partial trace over the spatial degrees of freedom and dropping terms beyond a desired order. An important consequence of this is that the spin degrees of freedom are effective spins and not exactly the true spins of the deeper theory. [48]

The systems we will be looking at have other properties in common that will allow us to ignore some effects and use simplified forms for others.

- The systems are frozen to tens of kelvin, where most motional degrees of freedom can neglected, and assumed static.
- The radicals we will be modeling all have effective spin-1/2.
- We will be working in the limit of a high applied magnetic field.

With these restrictions in mind, we next go over the term of the spin Hamiltonian that are relevant to systems we want to study.

1.5.1 Electron Zeeman

The Zeeman coupling describes the interaction of a spin with the externally applied magnetic field. However, since the spin Hamiltonian is an effective Hamiltonian, the Zeeman coupling is more complicated than simply $g_{\mathrm{e}}\mu_{\mathrm{B}}\boldsymbol{B}_0^{\mathrm{T}}\hat{\boldsymbol{S}}$. Instead, the Zeeman Hamiltonian is

$$\hat{H}_{\mathrm{eZ}} = -\mu_{\mathrm{B}}\boldsymbol{B}_0^{\mathrm{T}}(-\boldsymbol{g})\hat{\boldsymbol{S}}. \tag{1.39}$$

The g-matrix combines the free electron Zeeman coupling with relativistic mass corrections, gauge correction, orbital Zeeman coupling, and spin–orbit coupling to create an effective g-matrix.[48] The sign of the electron's charge is conventionally factored out so that $g_{\mathrm{e}} = 2.00231930436256$ [49, 50]. $\mu_{\mathrm{B}} = 9.2740100783\times10^{-24}$ J/T is the Bohr magneton[51].

For the cases discussed here, the applied magnetic field is large enough that the Zeeman coupling dominates the Hamiltonian. As such it is helpful to define the z-axis as the direction of the applied magnetic field:

$$\hat{\boldsymbol{z}} := \frac{\boldsymbol{B}_0}{B_0}. \tag{1.40}$$

Additionally, in the high magnetic field limit, the off-diagonal elements can usually be neglected, giving a simplified Zeeman Hamiltonian:

$$\hat{H}_{\mathrm{eZ}} \approx -\mu_{\mathrm{B}}B_0(-g_{zz})\hat{S}_z. \tag{1.41}$$

1.5.2 Nuclear Zeeman

In the high magnetic field limit, the nuclear Zeeman coupling is

$$\hat{H}_{\mathrm{nZ}} = -\mu_{\mathrm{N}}B_0(+g_{\mathrm{n}})\hat{I}_z. \tag{1.42}$$

Traditionally, electrons spin operators are represented with $\hat{S}$ and nuclear spin operator with $\hat{I}$. Here g_{n} is the dimensionless g-factor for the nucleus. $\mu_{\mathrm{N}} = 5.0507837461\times10^{-27}$ J/T is the nuclear magneton [52].

1.5.3 Hyperfine

The hyperfine coupling is the magnetic spin–spin interaction between an electron and a nucleus.

$$\hat{H}_{\mathrm{hf}} = \hat{\boldsymbol{S}}^{\mathrm{T}} \boldsymbol{A} \hat{\boldsymbol{I}}. \tag{1.43}$$

For nuclei that are far enough from the electron that the their wavefunctions do not overlap and for their widths' to be negligible, the hyperfine coupling can be approximated as between point dipoles. The magnetic field from a classical magnetic point-dipole $\boldsymbol{\mu}$ as a function of position, $\boldsymbol{r}$, is

$$\boldsymbol{B}(\boldsymbol{r}) = \frac{\mu_0}{4\pi} \frac{1}{r^3} (3\hat{\boldsymbol{r}}\hat{\boldsymbol{r}}^{\mathrm{T}} - \mathbb{1})\boldsymbol{\mu}. \tag{1.44}$$

Here $\hat{\boldsymbol{r}} = \boldsymbol{r}/|\boldsymbol{r}|$ is the unit vector $\boldsymbol{r}$-direction. The vacuum magnetic permeability is $\mu_0 = 1.25663706212 \times 10^{-6}\ \mathrm{T^2 m^3 J^{-1}}$ [53]. Replacing the magnetic moment generating the magnetic field, $\boldsymbol{\mu}$, with either $(-g_{\mathrm{e}}\mu_{\mathrm{B}})\hat{\boldsymbol{S}}$ for the electron or $(g_{\mathrm{n}}\mu_{\mathrm{N}})\hat{\boldsymbol{I}}$ for the nucleus, and then multiplying by the other to couple the electron and nucleus gives the point-dipole hyperfine coupling.

$$\boldsymbol{T} = -\frac{\mu_0}{4\pi} \frac{(-g_{\mathrm{e}}\mu_{\mathrm{B}})(g_{\mathrm{n}}\mu_{\mathrm{N}})}{r^3} \big(3\hat{\boldsymbol{r}}\hat{\boldsymbol{r}}^{\mathrm{T}} - \mathbb{1}\big). \tag{1.45}$$

The point-dipole hyperfine coupling factors as a prefactor of $-\frac{\mu_0}{4\pi}\frac{(-g_{\mathrm{e}}\mu_{\mathrm{B}})(g_{\mathrm{n}}\mu_{\mathrm{N}})}{r^3}$ that sets the scale and units of the coupling, and orientationi-dependent operator:

$$\hat{\boldsymbol{S}}^{\mathrm{T}} \big(3\hat{\boldsymbol{r}}\hat{\boldsymbol{r}}^{\mathrm{T}} - \mathbb{1}\big) \hat{\boldsymbol{I}} \tag{1.46}$$

which can be expanded in terms of spin operators, the angle between $\boldsymbol{r}$ and $\boldsymbol{B}_0 = B_0\hat{z}$, θ, and the angle $\boldsymbol{r}$'s projection onto the xy-plane and the x-axis, ϕ. The result is often referred to as the dipolar alphabet, listed below without the prefactor of $-\frac{\mu_0}{4\pi}\frac{(-g_{\mathrm{e}}\mu_{\mathrm{B}})g_{\mathrm{n}}\mu_{\mathrm{N}}}{r^3}$ [39].

A $(3\cos^2\theta - 1)\hat{S}_z\hat{I}_z$ (secular term)

B $-\frac{1}{4}(3\cos^2\theta - 1)\Big(\hat{S}_+\hat{I}_- + \hat{S}_-\hat{I}_+\Big) = +\frac{1}{2}(1 - 3\cos^2\theta)\Big(\hat{\boldsymbol{S}}^{\mathrm{T}}\hat{\boldsymbol{I}} - \hat{S}_z\hat{I}_z\Big)$ (flip-flop term)

C $\frac{3}{2}\sin\theta\cos\theta\,\mathrm{e}^{-\mathrm{i}\phi}\Big(\hat{S}_z\hat{I}_+ + \hat{S}_+\hat{I}_z\Big)$ (+1–single quantum term)

D $\frac{3}{2}\sin\theta\cos\theta\,\mathrm{e}^{+\mathrm{i}\phi}\Big(\hat{S}_z\hat{I}_- + \hat{S}_-\hat{I}_z\Big)$ (−1–single quantum term)

E $\frac{3}{4}\sin^2\theta\,\mathrm{e}^{-2\mathrm{i}\phi}\hat{S}_+\hat{I}_+$ (+2–quantum term)

F $\frac{3}{4}\sin^2\theta\,\mathrm{e}^{+2\mathrm{i}\phi}\hat{S}_-\hat{I}_-$ (−2–quantum term)

When the electron–nucleus vector is perpendicular to the applied magnetic field at $\theta = \pi/2$, $(3\cos^2\theta - 1) = -1$, so it makes sense to call the prefactor $A_\perp := -\frac{\mu_0}{4\pi}\frac{(-g_{\mathrm{e}}\mu_{\mathrm{B}})g_{\mathrm{N}}\mu_{\mathrm{N}}}{r^3}$.

When the point dipole approximation does not work, system-specific couplings are needed; the coupling can be determined experimentally. $\boldsymbol{A}$ is parameterized by an orientation, and two energy terms, T_{zz} and a Fermi contact coupling, a_0. [54]

$$\boldsymbol{A} = a_0\mathbb{1} + T_{zz}\boldsymbol{R}\begin{bmatrix} -\frac{1}{2} & 0 & 0 \\ 0 & -\frac{1}{2} & 0 \\ 0 & 0 & 1 \end{bmatrix}\boldsymbol{R}^{\mathrm{T}}. \tag{1.47}$$

The orientation information is carried by the orthogonal matrix $\boldsymbol{R}$ that rotates the axes from the eigenframe of $\boldsymbol{A}$ to the frame of interest (usually the lab frame as defined by the applied magnetic field).

Since the magnetic moment of an electrons is larger than the magnetic moment of a nucleus, so too is the electronic Zeeman splitting greater than the nuclear Zeeman splitting. In the high magnetic field regime, electron Zeeman energy is approximately conserved and only the $\hat{S}_z$ hyperfine terms are relevant:

$$\hat{H}_{\mathrm{hf}} \approx \hat{S}_z(\hat{\boldsymbol{z}}^{\mathrm{T}}\boldsymbol{A})\hat{\boldsymbol{I}}. \tag{1.48}$$

This approximation is useful, because with it $\hat{S}_z$ commutes with the total static spin Hamiltonian, and the electron eigenstates are the Zeeman states. This means that free evolution only needs to focus on one electronic manifold at a time, effectively removing a degree of freedom and halving the number of dimensions in the Hilbert space.

1.5.4 Nucleus–Nucleus Dipole–Dipole

Physically, nuclear dipole–dipole coupling is identical to hyperfine coupling: magnetic spin–spin interactions, yet they manifest differently. On the chemical scale nuclei (with radii on the order of fm) are point particles, so the point dipole approximation equation (1.45) is very good.

$$\hat{H}_{\mathrm{dd}} = -\frac{\mu_0}{4\pi}\frac{g_m g_n \mu_{\mathrm{N}}^2}{r^3}\hat{\boldsymbol{I}}_m^{\mathrm{T}}\Big(\frac{3\boldsymbol{r}\boldsymbol{r}^{\mathrm{T}}}{r^2} - \mathbb{1}\Big)\hat{\boldsymbol{I}}_n. \tag{1.49}$$

Here m and n are nuclear indices, so $g_m = g_{\mathrm{n}}$ for nucleus m, and $g_n = g_{\mathrm{n}}$ for nucleus n. Note, for the same distance vector, the nucleus–nucleus dipole–dipole coupling is smaller than the electron–nucleus dipole–dipole coupling by about $\mu_{\mathrm{B}}/\mu_{\mathrm{N}} \approx 1836$, times the ratio of the g-factors, which varies with the identity of the nucleus. Figure 1.3 plots $A_\perp$ for both protons and deuteron against r, as well as $b_\perp = \frac{\mu_0}{4\pi}\frac{g_m g_n \mu_{\mathrm{N}}^2}{r^3}$ for both proton–proton and deuteron–deuteron dipole–dipole coupling. The electron Zeeman and both the proton and deuteron Zeeman splittings for the applied magnetic field of 1.2 T (Q-band) are also shown.

For numerical calculations, working with the full tensor is not harder than just the terms that conserve Zeeman energy, but for analytical models in the high magnetic field limit, it is often useful to keep only the terms that conserve Zeeman energy:

$$\hat{H}_{\mathrm{dd}} \approx -\frac{\mu_0}{4\pi} g_m g_n \mu_{\mathrm{N}}^2 \frac{3\cos^2\theta - 1}{r_{mn}^3}\Big(\hat{I}_{zm}\hat{I}_{zn} - \frac{1}{4}(\hat{I}_{+m}\hat{I}_{-n} + \hat{I}_{-m}\hat{I}_{+n})\Big). \tag{1.50}$$

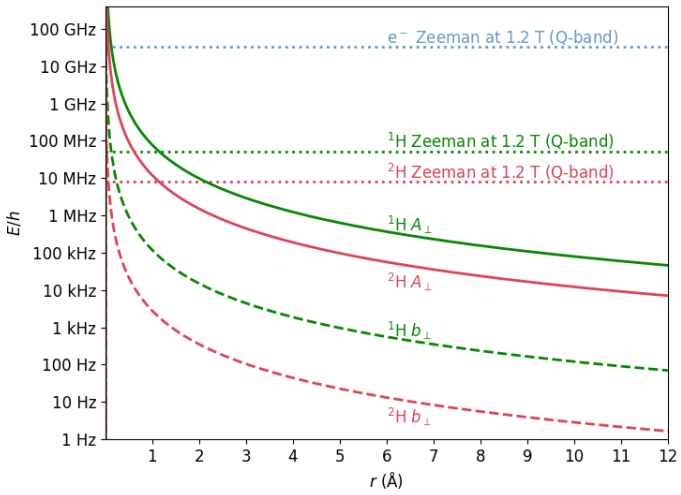

Figure 1.3: This plot compares the different spin Hamiltonian terms, showing the point-dipole $A_\perp$ vs. the electron–nucleus separation for both protons (green solid) and deuterons (red solid), and $b_\perp$ vs. the nucleus–nucleus separation for both protons (green dashed) and deuterons (red dashed). The abscissa is labeled as r, the definition of which depends on whether $A_\perp$ or $b_\perp$ is being referred to. Also, the electron Zeeman splitting (blue dotted), proton Zeeman (green dotted), and deuteron Zeeman (red dotted) at 1.2 T (Q-band) are shown as horizontal lines.

1.5.5 Nuclear Electric Quadrupole

Nuclei with a spin greater that 1/2 do not posses spherically symmetric electric charge distributions, and so their multipole expansion contains more than just a monopole terms. Specifically, the next most significant contribution is the quadrupole term. The nuclear quadrupole coupling is electric, and provides an angular energetic landscape that is governed by the electric field gradient at the site of the nucleus. This makes it sensitive the local bonding environments. Using the Wigner–Eckhart theorem, the nuclear quadrupole coupling can be recast in terms of spin operators.

The nuclear quadrupole coupling has two parameters, K, which determines the overall coupling strength and η, which sets the rhombicity. [55]

$$\boldsymbol{P} = hK\boldsymbol{R}\begin{bmatrix}-1+\eta & 0 & 0\\ 0 & -1-\eta & 0\\ 0 & 0 & 2\end{bmatrix}\boldsymbol{R}^{\mathrm{T}}, \tag{1.51}$$

where the Planck constant is $h = 6.62607015 \times 10^{-34}$ J/Hz [56], and $K = \frac{(eq)(eQ)/h}{4I(2I-1)}$, which itself is made up of multiple parameters, including the elementary charge $e = 1.602176634 \times 10^{-19}$ C [57]. The nuclear quadrupole moment is given by Q, and has units of area, usually given in barns ($1\ \mathrm{b} = 10^{-28}\ \mathrm{m}^2$). The nuclear spin is I. Letting $\boldsymbol{E}$ denote the electric field at the position of the nucleus, for the 3×3 tensor $-\boldsymbol{\nabla}\boldsymbol{E}^{\mathrm{T}}$ (not to be confused with the scalar $-\boldsymbol{\nabla}^{\mathrm{T}}\boldsymbol{E}$), with eigenvalues λ_x, λ_y and λ_z. $q = \lambda_z/e$, and $\eta = (\lambda_x - \lambda_y)/\lambda_z$. As before $\boldsymbol{R}$ is a rotation matrix that rotates the quadrupole coupling into the lab frame. The electric quadrupole coupling's contribution to the Hamiltonian for a nuclear spin is

$$\hat{H}_{\mathrm{quad}} = \hat{\boldsymbol{I}}^{\mathrm{T}}\boldsymbol{P}\hat{\boldsymbol{I}}. \tag{1.52}$$

For a fuller discussion please see [55, 58].

1.5.6 Electron–Electron Coupling

Electrons couple to each other the same way they couple to spin-1/2 nuclei; however, most electrons in the surrounding environment tend to come in antiparallel spin pairs, and so their coupling are mostly canceled out, and can be ignored though-out this text. For the remaining unpaired electrons, we will be looking at systems where the radical concentration is low and so the coupling is weak. The primary way these electrons influence the experiments we will be looking at is through instantaneous diffusion, a process where the applied pulses flip multiple electrons, and so change the magnetic environment around the detected electrons. A model for instantaneous diffusion will be discussed in the next chapter, *Other Method: Semiclassical Methods*, page 31.

1.5.7 Tunnel Splitting

The Hamiltonian is symmetric upon permuting identical particles, and so the potential energy function has number of degenerate minima equal to the number of possible permutations. The spin-statistics theorem requires that the total wave function be antisymmetric upon swapping two identical fermion and symmetric upon swapping identical bosons. Accounting for this by taking appropriate linear combinations of wavefunctions describing the different versions, excludes the states that do not transform with the correct symmetry and shifts the energy levels, introducing tunnel splittings. The magnitude of the tunnel splitting increases as the wavefunctions describing the different versions overlap more. Conversely, when the tunnel splitting are small compared to the experimental resolution, the energetic barrier separating the different permutation versions of the systems can usually be considered insurmountable. [59]

The only tunnel splitting we will need to look at is for methyl groups. Methyl groups contain three protons. Since protons have a low mass, and rotational permutations of the methyl group can proceed by a path that keeps the intra-methyl proton separation constant, the tunnel splitting between the spin-rotational states can be significant [60, 61]. Methyl tunneling is discussed in chapters 3 and 7.

1.5.8 Ideal Pulses

The Pauli matrices all square to the identity: $\hat{\sigma}_\alpha^2 = 1,\ \forall\ \alpha \in \{x, y, x\}$. A useful identity of the Pauli matrices is

$$\begin{aligned} \exp\Big(\mathrm{i}\theta\hat{\sigma}_\alpha\Big) &= \sum_{n=0}^{\infty} \frac{(\mathrm{i}\theta)^n}{n!}\hat{\sigma}_\alpha^n \\ &= \sum_{n,\ \text{even}}^{\infty} \frac{(\mathrm{i}\theta)^n}{n!} + \hat{\sigma}_\alpha \sum_{n,\ \text{odd}}^{\infty} \frac{(\mathrm{i}\theta)^n}{n!} \\ &= \cos(\theta) + \mathrm{i}\hat{\sigma}_\alpha \sin(\theta). \end{aligned} \tag{1.53}$$

For spin-1/2 particles, the spin operators are the identity and $\hat{S}_\alpha = \frac{1}{2}\hat{\sigma}_\alpha$, so equation (1.53) could equally well be put in terms of $\hat{S}_\alpha$, but note that equation (1.53) only holds for spin-1/2 particles. For the experiments we will be looking, the characteristic frequencies are are the order of MHz rather than GHz, while the microwave pulses are on the order of 10–40 ns. This allows the pulses to be modeled as instantaneous. Ideal pulses are represented using the Dirac delta function, and parameterized by an angle, θ, and pulse time t_p. The ideal-pulse Hamiltonian is

$$\hat{H}_{\mathrm{p}\alpha}(t, t_\mathrm{p}, \theta) = \theta\hbar\delta(t - t_\mathrm{p})\hat{S}_\alpha = \frac{-\theta\hbar}{2}\delta(t - t_\mathrm{p})\hat{\sigma}_\alpha. \tag{1.54}$$

The infinite amplitude is a consequence of assuming zero width. The propagator for an ideal pulse is

$$\begin{aligned} \hat{U}_{\mathrm{p}\alpha}(t, t_\mathrm{p}, \theta) = &\ \exp\Big(-\mathrm{i}\frac{\theta}{2}\hat{\sigma}_\alpha \int_{-\infty}^{t} \mathrm{d}t'\ \delta(t' - t_\mathrm{p})\Big) \\ = &\ \begin{cases} 1,\ t < t_p \\ \cos(\theta/2) - \mathrm{i}\hat{\sigma}_i \sin(\theta/2),\ t > t_\mathrm{p} \end{cases} . \end{aligned} \tag{1.55}$$

Combining a series of pulses with a static Hamiltonian, $\hat{H}_\mathrm{sys}$, gives

$$\hat{H}(t) = \hat{H}_\mathrm{sys} + \sum_p \hat{H}_p(t, t_p, \theta_p), \tag{1.56}$$

where p indexes the pulses. Assuming there is a $\pi/2$-pulse at $t = 0$, let τ_p be the time between the pth pulse and the $(p+1)$th pulse if there is a $(p+1)$th pulse, or the time of detection if there is not a $(p+1)$th pulse. The propagator at time $T = \sum_p \tau_p$ is then

$$\hat{U}(T) = \mathscr{T} \prod_p \mathrm{e}^{-\frac{\mathrm{i}}{\hbar}\hat{H}_\mathrm{sys}(t)\tau_p}\Big(\cos(\theta/2)\mathbb{1}(t) - \mathrm{i}\hat{\sigma}(t)\sin(\theta/2)\Big). \tag{1.57}$$

Assuming $\hat{H}_\mathrm{sys}$ itself is time independent, the time parameter $t \in [0, T]$ is present only as a label for the time ordering to be done correctly.

π-Pulses and $\pi/2$-Pulses
Two important cases are $\theta = \pi$ and $\theta = \pi/2$. Assuming $\alpha = y$,

$$\hat{U}_{\mathrm{p}y}(t > t_p, \pi) = -\mathrm{i}\hat{\sigma}_y = \begin{bmatrix} 0 & -1 \\ 1 & 0 \end{bmatrix}. \tag{1.58}$$

$$\hat{U}_{\mathrm{p}y}(t > t_p, \pi/2) = \frac{1}{\sqrt{2}}(1 - \mathrm{i}\hat{\sigma}_y) = \frac{1}{\sqrt{2}}\begin{bmatrix} 1 & -1 \\ 1 & 1 \end{bmatrix}. \tag{1.59}$$

1.6 Pulse Experiments

Pulse EPR experiments work by using a static applied magnetic field to establish a magnetic dipole moment, $\boldsymbol{M}$ in the sample under investigation. Microwave pulses are used to tilt the sample's magnetic moment with respect to the applied magnetic field. Using quadrature detection, both M_x and M_y can be measured simultaneously. $\boldsymbol{M}$ can contain about 10^{12} electron spins, and can be well described classically. On a microscopic scale,

$$M_x \propto \langle \hat{S}_x \rangle \, ; M_y \propto \langle \hat{S}_y \rangle \, . \tag{1.60}$$

Note that measuring M_x and M_y is not the same as measuring $\hat{S}_x$ and $\hat{S}_y$, since the wavefunction for $\boldsymbol{M}$ contains around 10^{12} spins and measuring M_x and M_y minimally perturbs any individual spin [62]. This means that to detection operator we will use can be the non-Hermitian $\hat{S}_+ = \hat{S}_x + \mathrm{i}\hat{S}_y$. Using the Hamiltonian of equation (1.56), and assuming the system has had an infinite amount time to equilibrate before the first pulse at $t = 0$, the initial density matrix is

$$\hat{\rho}_{0^-} = \frac{\exp\Big(- \beta \hat{H}_{\mathrm{sys}} \Big)}{\mathrm{tr}\Big(\exp\Big(- \beta \hat{H}_{\mathrm{sys}} \Big) \Big)}, \tag{1.61}$$

the expected signal is given by

$$V(T) \propto \frac{1}{\mathrm{tr}(\hat{\rho}_{0^-})} \mathrm{tr}\Big(\hat{\rho}_0 \hat{U}(T) \hat{S}_+ \hat{U}(T)^\dagger \Big). \tag{1.62}$$

The $\hat{H}_{\mathrm{sys}}$ we will be using is approximately block diagonal: $\langle m_{\mathrm{S}} | \hat{H}_{\mathrm{sys}} | m'_{\mathrm{S}} \rangle = 0$ for $m_{\mathrm{S}} \neq m'_{\mathrm{S}}$. This allows the spin Hamiltonian in the electron spin m_{S} manifold to be defined as

$$\begin{aligned} \hat{H}_{\mathrm{sys}}(m_{\mathrm{S}}) &:= \langle m_{\mathrm{S}} | \hat{H}_{\mathrm{sys}} | m_{\mathrm{S}} \rangle \, ; \\ \hat{H}^{(\pm)} &:= \hat{H}_{\mathrm{sys}}(m_{\mathrm{S}} = \pm \frac{1}{2}); \end{aligned} \tag{1.63}$$

however, $\hat{H}_p(t, t_p, \theta_p)$, by design, mixes the m_{S} levels. There are two types of pulses we will need to account for, the $\pi/2$-pulse at $t = 0$, and the one or more π-pulses. The $\pi/2$-pulse will be incorporated into the initial density matrix:

$$\begin{aligned} \hat{\rho}(t = 0^+) &= \hat{U}_{\mathrm{p}y}(t = 0^+, t_{\mathrm{p}} = 0, \frac{\pi}{2}) \hat{\rho}_{0^-} \hat{U}_{\mathrm{p}y}(t = 0^+, t_{\mathrm{p}} = 0, \frac{\pi}{2})^\dagger \\ &= \frac{1}{\sqrt{2}} \Big(1 - \mathrm{i}\hat{\sigma}_y \Big) \frac{1}{Z} \begin{bmatrix} \exp(-\beta \hat{H}^{(+)}) & 0 \\ 0 & \exp(-\beta \hat{H}^{(-)}) \end{bmatrix} \frac{1}{\sqrt{2}} \Big(1 + \mathrm{i}\hat{\sigma}_y \Big) \\ &= \frac{1}{2Z} \begin{bmatrix} \exp(-\beta \hat{H}^{(+)}) + \exp(-\beta \hat{H}^{(-)}) & \exp(-\beta \hat{H}^{(+)}) - \exp(-\beta \hat{H}^{(-)}) \\ \exp(-\beta \hat{H}^{(+)}) - \exp(-\beta \hat{H}^{(-)}) & \exp(-\beta \hat{H}^{(+)}) + \exp(-\beta \hat{H}^{(-)}) \end{bmatrix} \\ &=: \begin{bmatrix} \hat{\rho}^{(++)} & \hat{\rho}^{(+-)} \\ \hat{\rho}^{(-+)} & \hat{\rho}^{(--)} \end{bmatrix}. \end{aligned} \tag{1.64}$$

Taking $\hat{\rho}(0^+)$ as the initial state, the pulse sequences we will be looking at only require including π-pulses into the propagator. The timescale over which the density matrix returns to thermal equilibrium is called T_1, and will here be assumed to be much longer than the experimental timescale. This assumption is valid for spin-1/2 species at low concentrations in solid matrices at low temperature.

Going into the interaction picture with $\hat{H}_0 = \sum_p \hat{H}(t, t_p, \pi)$,

$$\hat{H}_1(t) = \left(\mathscr{T} \exp\Big(- \frac{\mathrm{i}}{\hbar} \int_{t_1}^{t} \mathrm{d}t' \sum_p \hat{H}(t', t_p, \pi) \Big) \right)^\dagger \hat{H}_{\mathrm{sys}} \mathscr{T} \exp\Big(- \frac{\mathrm{i}}{\hbar} \int_{t_1}^{t} \mathrm{d}t' \sum_p \hat{H}(t', t_p, \pi) \Big) \tag{1.65}$$

Let $n_\pi(t)$ be the number of π-pulse that have occurred by time t. The interaction Hamiltonian becomes

$$\hat{H}_1(t) = (-\mathrm{i}\hat{\sigma}_y)^{n(t)}\hat{H}_{\mathrm{sys}}(\mathrm{i}\hat{\sigma}_y)^{n(t)} \tag{1.66}$$

Here are the $\hat{H}_1(t)$s for $n(t) \leq 1$.

$$\hat{H}_1\Big(n(t)=0\Big) = \begin{bmatrix}\hat{H}^{(+)} & 0\\ 0 & \hat{H}^{(-)}\end{bmatrix}; \tag{1.67}$$

$$\hat{H}_1\Big(n(t)=1\Big) = \begin{bmatrix}\hat{H}^{(-)} & 0\\ 0 & \hat{H}^{(+)}\end{bmatrix}. \tag{1.68}$$

The Hamiltonian remains block diagonal, but the $\hat{H}^{(+)}$ and $\hat{H}^{(-)}$ switch every π-pulse, so the interaction system Hamiltonian is $\hat{H}\Big(m_{\mathrm{S}}(t)\Big)$, and the propagator is

$$\begin{aligned}\hat{U}(t) &= \mathscr{T}\exp\Big(-\frac{\mathrm{i}}{\hbar}\int_{t_1}^{t}\mathrm{d}t'\hat{H}\Big(m_{\mathrm{S}}(t')\Big)\Big)\\ &= \mathscr{T}\prod_p \exp\Big(-\frac{\mathrm{i}}{\hbar}(t_{p+1}-t_p)\hat{H}\Big(m_{\mathrm{S}}(t_p^+)\Big)\Big)\\ &= \mathscr{T}\prod_p \exp\Big(-\frac{\mathrm{i}}{\hbar}\tau_p\hat{H}\Big(m_{\mathrm{S}}(t_p^+)\Big)\Big).\end{aligned} \tag{1.69}$$

The duration from pulse p to the next pulse (or detection if p is the final pulse) is here given the symbol τ_p. Since m_{S} is non-constant, once π-pulses are introduced, the definition of $\hat{U}^{(\pm)}(t)$ needs to be updated:

$$\hat{U}^{(\pm)}(t) := \hat{U}\big(t, m_{\mathrm{S}}(t=0) = \pm\frac{1}{2}\big). \tag{1.70}$$

This definition is consistent whether for the propagator of the whole pulse sequence after initialization, $\hat{U}^{(\pm)}(t)$, or the free evolution between pulses $\hat{U}^{(\pm)}(\tau)$.

$$\hat{U}^{(\pm)}(t) = \mathscr{T}\prod_p \hat{U}^{(\pm)_p}(\tau_p). \tag{1.71}$$

With the time evolution operator known, the Heisenberg picture detection operator is

$$\begin{aligned}\hat{S}_{+\mathrm{H}}(t) &= \begin{bmatrix}\hat{U}^{(+)}(t)^\dagger & 0\\ 0 & \hat{U}^{(-)}(t)^\dagger\end{bmatrix}\begin{bmatrix}0 & \mathbb{1}\\ 0 & 0\end{bmatrix}\begin{bmatrix}\hat{U}^{(+)}(t) & 0\\ 0 & \hat{U}^{(-)}(t)\end{bmatrix}\\ &= \begin{bmatrix}0 & \hat{U}^{(+)}(t)^\dagger\hat{U}^{(-)}(t)\\ 0 & 0\end{bmatrix}.\end{aligned} \tag{1.72}$$

The signal is then

$$\begin{aligned}V(T) &\propto \frac{1}{\mathrm{tr}(\hat{\rho}_{0^-})}\mathrm{tr}\Bigg(\begin{bmatrix}\hat{\rho}^{(++)} & \hat{\rho}^{(+-)}\\ \hat{\rho}^{(-+)} & \hat{\rho}^{(--)}\end{bmatrix}\begin{bmatrix}0 & \hat{U}^{(+)}(T)^\dagger\hat{U}^{(-)}(T)\\ 0 & 0\end{bmatrix}\Bigg)\\ &= \frac{1}{\mathrm{tr}(\hat{\rho}_0)}\mathrm{tr}\Big(\hat{\rho}^{(-+)}\hat{U}^{(+)}(T)^\dagger\hat{U}^{(-)}(T)\Big).\end{aligned} \tag{1.73}$$

To focus on the physics of interest is is helpful to define a normalized signal.

$$\begin{aligned}v(T) &:= \frac{V(T)}{V(0^+)}\\ &= \frac{1}{\mathrm{tr}(\rho(0^+)\hat{S}_+)}\mathrm{tr}\Big(\rho(0^+)\hat{U}(T)^\dagger\hat{S}_+\hat{U}(T)\Big)\\ &= \frac{1}{\mathrm{tr}(\rho^{(-+)})}\mathrm{tr}\Big(\rho^{(-+)}\hat{U}^{(+)}(T)^\dagger\hat{U}^{(-)}(T)\Big).\end{aligned} \tag{1.74}$$

In the nuclear high temperature limit, all the Zeeman state are equally populated, meaning the density matrix is proportional to the identity: $\hat{\rho}^{(-+)} = \frac{1}{Z}\mathbb{1} = \prod_n(2I_n+1)^{-1}\mathbb{1}$. This simplifies equation (1.74) to

$$v(t) = \frac{1}{Z}\mathrm{tr}\Big(\hat{U}^{(+)}(t)\hat{U}^{(-)}(t)^\dagger\Big). \tag{1.75}$$

1.6.1 FID

The Free Induction Decay (FID) is the one of the simplest pulse EPR experiments. While instrumental limitations impose a dead-time of 80–150 ns where the signal cannot be measured, the FID itself is recorded in real time, meaning $T = t$. The signal is

$$v_{\mathrm{FID}}(t) = \frac{1}{Z}\mathrm{tr}\Big(\hat{U}^{(+)}(t)^{\dagger}\hat{U}^{(-)}(t)\Big). \tag{1.76}$$

The signal lifetime is dominated by inhomogeneous broadening.

1.6.2 Hahn Echo

The Hahn echo adds a π-pulse, and is the primary pulse sequence of interest for this work. From (1.55), a π pulse at $t = \tau$ has the propagator $\hat{U}_y(t, \tau, \pi/2) = \theta(\tau - t) + \mathrm{i}\hat{\sigma}_y\theta(t - \tau)$, where $\theta()$ is the Heaviside step function. In terms of the free evolution nuclear sub-propagator turns $\hat{U}^{(\pm)}$ into $\hat{U}^{(\mp)}$. The time of signal detection, T, from the start of the pulse sequence is 2τ, and so the signal is written as $v(2\tau)$ rather than $v(\tau)$.

$$v_{\mathrm{Hahn}}(2\tau) = \frac{1}{Z}\mathrm{tr}\Big(\hat{U}^{(+)}(\tau)^{\dagger}\hat{U}^{(-)}(\tau)^{\dagger}\hat{U}^{(+)}(\tau)\hat{U}^{(-)}(\tau)\Big). \tag{1.77}$$

The Hahn echo as a function of 2τ cannot be measure in real time, as each value of 2τ requires running the experiment with a different delay time, τ. The Hahn echo is the primary experiment throughout this text, and this is the form of the signal that will be used in the upcoming many body expansions.

1.6.3 Refocused Echo

The 2D refocused echo will also be of interest in chapter 4. Similar to the progression from the FID to the Hahn echo, the refocused echo introduces another pulse, and a second delay time. For $\hat{U}_i^{(\pm)} := \exp(-\mathrm{i}\hbar\hat{H}^{(\pm)}\tau_i)$, the signal is

$$v_{\mathrm{re}}(2\tau_1, 2\tau_2) = \frac{1}{Z}\mathrm{tr}\Big(\hat{U}_1^{(+)\dagger}\hat{U}_1^{(-)\dagger}\hat{U}_2^{(-)\dagger}\hat{U}_2^{(+)\dagger}\hat{U}_2^{(-)}\hat{U}_2^{(+)}\hat{U}_1^{(+)}\hat{U}_1^{(-)}\Big). \tag{1.78}$$

Here detection occurs at $T = 2\tau_1 + 2\tau_2$, but both $2\tau_1$ and $2\tau_2$ are needed to parameterize, meaning that the refocused echo is $v_{\mathrm{re}}(2\tau_1, 2\tau_2)$ and not $v_{\mathrm{re}}(2\tau_1 + 2\tau_2)$. The refocused echo will be the focus of chapter 5.

1e12 electrons all around.
They exist both down and up, up and down.
With their moments ringing out like a gong,
they're coherent at first, but not for long.
With the many nuclear spins to be found,
the Hahn echo decays to the ground.

Chapter 2

Background: Cluster Expansions

The previous chapter introduced the types of systems and experiments that we will be looking. It also introduced the formal method of simulating coherent electron spins in a environment containing nuclear spins; however, as presented, the method is practically impossible since the Hilbert space dimensionality scales exponentially with the number of spins. For example, 100 spin-1/2 nuclei require a $2^{100} = 1{,}267{,}650{,}600{,}228{,}229{,}401{,}496{,}703{,}205{,}376 \approx 10^{30}$ dimensions. This may be small compared to the approximately 10^{80} protons in the visible universe, but at 266 spin-1/2 nuclei, the Hilbert space dimensionality reaches $2^{266} \approx 10^{80}$. 500 spin-1/2 nuclei require $2^{500} \approx 10^{150}$ Hilbert space dimensions and 1000 spin-1/2 nuclei need $2^{1000} \approx 10^{301}$ Hilbert space dimensions, a number far higher than the count of protons in the visible universe. Cluster expansions are a mathematical tool that allows reasonable accurate approximate solutions to be found.

Cluster expansions are a class of methods where the system is broken up into subsets, referred to as clusters, and for each cluster, a contribution to the total signal calculated. These contributions are then combined together to approximate the total signal. There are several distinct methods that qualify as cluster expansions, such as Witzel and Das Sarma's Cluster Expansion (CE)[34], Saikin, Yao and Sham's Linked Cluster Expansion (LCE)[35], and Yang and Liu's Cluster Correlation Expansion (CCE)[1, 2]. The primary method we will be using is CCE; however, LCE will be used as well. Additionally, since the theory of LCE leads directly into the justification for the assumptions of CCE, this chapter will start with a description of LCE.

2.1 Linked Cluster Expansion

Saikin, Yao and Sham's Linked Cluster Expansion (LCE)[35] is based from the Taylor series of the signal with respect to the part of the spin Hamiltonian that does not commute with the Zeeman term. Each term of the series can be assigned a Feynman diagram as a mnemonic. By reordering the Taylor series, LCE partially re-sums the series, so that the signal takes the form of $\exp(\sum V_d)$, rather than $\sum V_d$.

2.1.1 Setup

The spin Hamiltonian we will be looking at is

$$\begin{aligned}\hat{H}(m_{\mathrm{S}}(t)) = & -(-g_{zz}\mu_{\mathrm{B}})B_0 m_{\mathrm{S}}(t) - \sum_{n=1}^{N} g_n \mu_{\mathrm{N}} B_0 \hat{I}_{z,n} \\ & + m_{\mathrm{S}}(t) \sum_{n=1}^{N} A_n \hat{I}_{z,n} \\ & + \sum_{m=1}^{N-1} \sum_{n=m+1}^{N} b_{mn}\Big(\hat{I}_{z,m}\hat{I}_{z,n} - \frac{1}{4}\hat{I}_{+,m}\hat{I}_{-,n} - \frac{1}{4}\hat{I}_{-,m}\hat{I}_{+,n}\Big).\end{aligned} \tag{2.1}$$

The time dependence of m_{S} comes from the pulse sequence, which will be assumed to use ideal π-pulses that instantaneously changes m_{S} when the pulses are applied. Returning to the interaction picture, it will be useful to choose the base Hamiltonian as

$$\hat{H}_0(m_{\mathrm{S}}) = m_{\mathrm{S}} \sum_n A_n \hat{I}_{z,n}. \tag{2.2}$$

The interaction Hamiltonians are

$$\hat{H}_{1\mathrm{I}}(m_{\mathrm{S}}, t) = \exp\Big(+\frac{\mathrm{i}}{\hbar}\sum_n A_n \hat{I}_{z,n} \int_0^t \mathrm{d}t' m_{\mathrm{S}}(t')\Big)\, \hat{H}_{1\mathrm{S}}(m_{\mathrm{S}})\, \exp\Big(-\frac{\mathrm{i}}{\hbar}\sum_n A_n \hat{I}_{z,n} \int_0^t \mathrm{d}t' m_{\mathrm{S}}(t')\Big). \tag{2.3}$$

Here $\hbar = 1.054571817 \times 10^{-34}$ J $(\mathrm{rad/s})^{-1}$ [63]. Since the base Hamiltonian only contains $\hat{I}z$s, it commutes with itself at different times and so the time ordering symbol has been elided. Since the spin Hamiltonian in the Schrödinger picture, $\hat{H}_{1\ \mathrm{S}}$ is composed of spin operators, finding the interaction Hamiltonian requires determining how the spin operators transform. The interaction picture spin operators are

$$\begin{aligned} \hat{I}_z(m_{\mathrm{S}}, t) &= \hat{I}_z; \\ \hat{I}_\pm(m_{\mathrm{S}}, t) &= \mathrm{e}^{\pm\frac{\mathrm{i}A}{\hbar}\int_0^t \mathrm{d}t' m_{\mathrm{S}}(t')}\hat{I}_\pm. \end{aligned} \tag{2.4}$$

So all that needs to be done to get the interaction spin Hamiltonian is to replace every $\hat{I}_{\pm,n}$ in the spin Hamiltonian with $\mathrm{e}^{\pm\frac{\mathrm{i}A_n}{\hbar}\int_0^t \mathrm{d}t' m_{\mathrm{S}}(t')}\hat{I}_{\pm,n}$. Both the Hahn echo and refocused echo signals can be written as

$$v(T) = \frac{1}{Z}\mathrm{tr}\Big(\rho^{(-+)}\mathscr{T}\big(\mathrm{e}^{-\frac{\mathrm{i}}{\hbar}\int_0^T \mathrm{d}t \hat{H}_{1\,\mathrm{I}}(m_{\mathrm{S}}{}', t)}\big)^\dagger \mathscr{T}\big(\mathrm{e}^{-\frac{\mathrm{i}}{\hbar}\int_0^T \mathrm{d}t \hat{H}_{1\,\mathrm{I}}(m_{\mathrm{S}}, t)}\big)\Big), \tag{2.5}$$

where T is the time from the start of the pulse sequence to the signal detection. For the Hahn echo, $T_{\mathrm{hahn}} = 2\tau$ is a function of a single delay parameter, while for the refocused echo, $T_{\mathrm{re}} = 2\tau_1 + 2\tau_2$ has two delay parameters. Currently, the expression is written with two propagators, one for the ket, and one for the bra. But matrix multiplication is associative, so the expression is unchanged by multiplying the two propagators together ahead of time.[1] To accommodate the adjoint symbol on the bra's propagator, a couple changes are needed. First, the time coordinate will be replaced by a path coordinate: $t \to p$. If t runs from 0 to T, the path variable p runs from 0 to $2T$.

$$t(p) = \theta(T - p)p + \theta(p - T)(2T - p). \tag{2.6}$$

To convert from p to t, it helpful to think of time as running forward from 0 to T and then backward down to 0. This implies

$$\mathrm{d}t(p) = \Big(\theta(T - p) - \theta(p - T)\Big)\mathrm{d}p. \tag{2.7}$$

This change accounts for the $\mathrm{i} \to -\mathrm{i}$ part of taking the Hermitian transpose. The change from t to p also allows the correct multiplication order to be specified by replacing the time ordering symbol with a path ordering symbol: $\mathscr{T} \to \mathscr{T}_{\mathrm{P}}$. The result of these notational changes is

$$v(t) = \frac{1}{Z}\mathrm{tr}\Big(\rho^{(-+)}\mathscr{T}_{\mathrm{P}}\big(\mathrm{e}^{-\frac{\mathrm{i}}{\hbar}\int_P \mathrm{d}t' \hat{H}(m_{\mathrm{S}}, t')}\big)\Big), \tag{2.8}$$

where both t' and m_{S} are functions of p.

2.1.2 Pairwise Contractions

The first few terms of the Taylor series for the path propagator are

$$\mathscr{T}_P\big(\mathrm{e}^{-\frac{\mathrm{i}}{\hbar}\int_P \mathrm{d}t' \hat{H}(m_{\mathrm{S}}, t')}\big) = 1 - \frac{\mathrm{i}}{\hbar}\int_P \mathrm{d}t' \hat{H}(m_{\mathrm{S}}, p') + \frac{(-\mathrm{i}/\hbar)^2}{2!}\int_{P_2}\int_{P_1} \mathrm{d}t_2\, \mathrm{d}t_1\, \mathscr{T}_P\big(\hat{H}(m_{\mathrm{S}2}, p_2)\hat{H}(m_{\mathrm{S}1}, p_1)\big) + \cdots. \tag{2.9}$$

Each term can be further expanded into the sum of products of spin operators: $\hat{I}_{z\,m}(p)$, $\hat{I}_{+\,m}(p_2)\hat{I}_{-\,n}(p_1)$, $\hat{I}_{+\,n}(p_2)\hat{I}_{+\,n}(p_1)$, etc. Since spin operators referring to different spins commute, each product can be factored into terms of the form

$$\langle n'|\,\hat{I}_{\alpha_k,n}(p_k)\cdots\hat{I}_{\alpha_2,n}(p_2)\hat{I}_{\alpha_1,n}(p_1)\,|n\rangle\,. \tag{2.10}$$

The path ordering will rearrange the operators, so it is convenient to look at these matrix elements after the ordering and to choose a path ordered indexing, i.e. $p_k \geq p_{k-1} \geq \cdots \geq p_1$. Here α denotes the spin operator: $\alpha \in \{z,+,-\}$, and n, the spin. The states, $|n\rangle$ and $|n'\rangle$ depend on the density matrix, but if the density matrix is diagonal, then only the $|n'\rangle = |n\rangle$ terms contribute. Some matrix elements can immediately be evaluated to zero: the difference in the number of raising and lowering operators must match the difference in spin quantum numbers between the bra and ket. When the bra and ket are the same state, only matrix elements with the same number of raising and lowering operator will be non-zero. Additionally, the raising and lowering operators act on some extremal states to yield zero.

$$\begin{aligned}\hat{I}_+\,|\uparrow\rangle &= \langle\uparrow|\,\hat{I}_- = 0.\\ \hat{I}_-\,|\downarrow\rangle &= \langle\downarrow|\,\hat{I}_+ = 0.\end{aligned} \tag{2.11}$$

This goes farther than simply the left-most or right-most operator: using the commutation identity $AB = BA + [A,B]$, the operators can be rearranged if their commutators are known.

$$\begin{aligned}\big[\hat{I}_+(p_1),\hat{I}_-(p_2)\big] = \big[\,&\mathrm{e}^{+\frac{\mathrm{i}m_{\mathrm{S}}(p_1)At(p_1)}{2\hbar}}\hat{I}_+,\,\mathrm{e}^{-\frac{\mathrm{i}m_{\mathrm{S}}(p_2)At(p_2)}{2\hbar}}\hat{I}_-\big]\\ &\mathrm{e}^{+\frac{\mathrm{i}A(m_{\mathrm{S}}(p_1)t(p_1)-m_{\mathrm{S}}(p_2)t(p_2))}{2\hbar}}\big[\hat{I}_+,\hat{I}_-\big]\\ &\mathrm{e}^{+\frac{\mathrm{i}A(m_{\mathrm{S}}(p_1)t(p_1)-m_{\mathrm{S}}(p_2)t(p_2))}{2\hbar}}\,2\hat{I}_z.\end{aligned} \tag{2.12}$$

And

$$\begin{aligned}\big[\hat{I}_z(p_1),\hat{I}_\pm(p_2)\big] &= \big[\hat{I}_z,\,\mathrm{e}^{\pm\frac{\mathrm{i}m_{\mathrm{S}}(p_2)At(p_2)}{2\hbar}}\hat{I}_+\big]\\ &= \pm\,\mathrm{e}^{\pm\frac{\mathrm{i}m_{\mathrm{S}}(p_2)At(p_2)}{2\hbar}}\,\hat{I}_\pm.\end{aligned} \tag{2.13}$$

Something else that is important to notice is that the commutators have one fewer spin operator after evaluation than the original product. This means that although rearranging operators this way creates additional terms, the terms that are created are simpler to evaluate. Two more pieces of vocabulary are needed. First is the normal ordering symbol, $\mathscr{N}$; whereas the time ordering symbol says to arrange operators according to chronology, the normal ordering symbol says to arrange operators to give a null matrix element: raising operators should be placed to the far right if the state is $|\uparrow\rangle$ (since $\hat{I}_+\,|\uparrow\rangle = 0$) and lowering operators should be placed on the far right when the ket is $|\downarrow\rangle$ (since $\hat{I}_-\,|\downarrow\rangle = 0$). The second introduction is spin operator contractions, defined as the difference between the path-ordered and normal-ordered products.

$$\overbrace{\hat{I}_{\alpha_1}(p_1)\hat{I}_{\alpha_2}(p_2}^{} := \mathscr{T}_P\big(\hat{I}_{\alpha_1}(p_1)\hat{I}_{\alpha_2}(p_2)\big) - \mathscr{N}\big(\hat{I}_{\alpha_1}(t_1)\hat{I}_{\alpha_2}(p_2)\big). \tag{2.14}$$

There are three options for operators, $\alpha \in \{z,+,-\}$, and only operators that do not commute need to be explicitly examined. The contraction reorders the operators, so the written order does not matter. This leaves 3 possible pairwise contractions: $(+,-)$, $(+,z)$, and $(-,z)$. The contraction between $\hat{I}_-(p_1)$, and $\hat{I}_-(p_2)]$ in a spin-up state is

$$\begin{aligned}\langle\uparrow|\,\overbrace{\hat{I}_+(p_1)\hat{I}_-(p_2)}\,|\uparrow\rangle &= \begin{cases}\langle\uparrow|\,\hat{I}_+(p_1)\hat{I}_-(p_2) - \hat{I}_-(p_2)\hat{I}_+(p_1)\,|\uparrow\rangle\,,\ p_1 > p_2\\ \langle\uparrow|\,\hat{I}_-(p_2)\hat{I}_+(p_1) - \hat{I}_-(p_2)\hat{I}_+(p_1)\,|\uparrow\rangle\,,\ p_2 > p_1\end{cases}\\ &= \langle\uparrow|\,\theta(p_1-p_2)\big[\hat{I}_+(p_1),\hat{I}_-(p_2)\big]\,|\uparrow\rangle\\ &= \langle\uparrow|\,\theta(p_1-p_2)\,\mathrm{e}^{+\frac{\mathrm{i}A}{\hbar}\int_{p_2}^{p_1}\mathrm{d}t'\ m_{\mathrm{S}}(p')}\,2\hat{I}_z\,|\uparrow\rangle\,.\end{aligned} \tag{2.15}$$

And for a spin-down state,

$$\begin{aligned}\langle\downarrow|\,\overbrace{\hat{I}_+(p_1)\hat{I}_-(p_2)}\,|\downarrow\rangle &= \begin{cases}\langle\downarrow|\,\hat{I}_+(p_1)\hat{I}_-(p_2)-\hat{I}_+(p_1)\hat{I}_-(p_2)\,|\downarrow\rangle\,,\ p_2<p_1\\ \langle\downarrow|\,\hat{I}_-(t_2)\hat{I}_+(p_1)-\hat{I}_+(p_1)\hat{I}_-(p_2)\,|\downarrow\rangle\,,\ p_1<p_2\end{cases}\\ &= \langle\downarrow|-\theta(p_2-p_1)\big[\hat{I}_+(p_1),\hat{I}_-(p_2)\big]\,|\downarrow\rangle\\ &= \langle\downarrow|-\theta(p_2-p_1)\,\mathrm{e}^{-\frac{\mathrm{i}A}{\hbar}\int_{p_1}^{p_2}\mathrm{d}t'\ m_{\mathrm{S}}(p')}\,2\hat{I}_z\,|\downarrow\rangle\,.\end{aligned} \tag{2.16}$$

These results can be summarized as

$$\begin{aligned}\overbrace{\hat{I}_+(p_1)\hat{I}_-(p_2)} &= -2\,\mathrm{e}^{+\frac{\mathrm{i}A}{\hbar}\int\mathrm{d}t' m_{\mathrm{S}}(p')}\big(\theta(p_2-p_1)\delta_{n,\downarrow}-\theta(p_1-p_2)\delta_{n,\uparrow}\big)\hat{I}_z\\ &=: -2\,\mathrm{e}^{+\frac{\mathrm{i}A}{\hbar}\int\mathrm{d}t' m_{\mathrm{S}}(p')}G(p_2-p_1)\hat{I}_z,\end{aligned} \tag{2.17}$$

where the Green's function, $G(p_2-p_1)$, is defined as

$$G(p_2-p_1) := \theta(p_2-p_1)\delta_{\psi,\downarrow}-\theta(p_1-p_2)\delta_{\psi,\uparrow}. \tag{2.18}$$

The same process can be gone through with $\hat{I}_\pm(p_1)$ and $\hat{I}_z(p_2)$

$$\begin{aligned}\langle\uparrow|\,\overbrace{\hat{I}_+(p_1)\hat{I}_z(p_2)}\,|\uparrow\rangle &= \begin{cases}\langle\uparrow|\,\hat{I}_+(p_1)\hat{I}_z(p_2)-\hat{I}_z(p_2)\hat{I}_+(p_1)\,|\uparrow\rangle\,,\ p_1>p_2\\ \langle\uparrow|\,\hat{I}_z(p_2)\hat{I}_+(p_1)-\hat{I}_z(p_2)\hat{I}_+(p_1)\,|\uparrow\rangle\,,\ p_2>p_1\end{cases}\\ &= \langle\uparrow|\,\theta(p_1-p_2)\big[\hat{I}_+(p_1),\hat{I}_z(p_2)\big]\,|\uparrow\rangle\\ &= +\langle\uparrow|-\theta(p_1-p_2)\hat{I}_+(p_1)\,|\uparrow\rangle\,.\end{aligned} \tag{2.19}$$

And

$$\begin{aligned}\langle\downarrow|\,\overbrace{\hat{I}_+(p_1)\hat{I}_z(p_2)}\,|\downarrow\rangle &= \begin{cases}\langle\downarrow|\,\hat{I}_+(p_1)\hat{I}_z(p_2)-\hat{I}_+(p_1)\hat{I}_z(p_2)\,|\downarrow\rangle\,,\ p_1>p_2\\ \langle\downarrow|\,\hat{I}_z(p_2)\hat{I}_+(p_1)-\hat{I}_+(p_1)\hat{I}_z(p_2)\,|\downarrow\rangle\,,\ p_2>p_1\end{cases}\\ &= \langle\downarrow|-\theta(p_2-p_1)\big[\hat{I}_+(p_1),\hat{I}_z(p_2)\big]\,|\downarrow\rangle\\ &= +\langle\downarrow|\,\theta(p_2-p_1)\hat{I}_+(p_1)\,|\downarrow\rangle\,.\end{aligned} \tag{2.20}$$

This summarizes to

$$\begin{aligned}\overbrace{\hat{I}_+(p_1)\hat{I}_z(p_2)} &= \big(\theta(p_2-p_1)\delta_{\psi,\downarrow}-\theta(p_1-p_2)\delta_{\psi,\uparrow}\big)\hat{I}_+(p_1)\\ &= \hat{I}_+(p_1)G(p_2-p_1).\end{aligned} \tag{2.21}$$

Similarly for $\hat{I}_-(p_1)$ and $\hat{I}_z(p_2)$

$$\begin{aligned}\langle\uparrow|\,\overbrace{\hat{I}_-(p_1)\hat{I}_z(p_2)}\,|\uparrow\rangle &= \begin{cases}\langle\uparrow|\,\hat{I}_-(p_1)\hat{I}_z(p_2)-\hat{I}_-(p_1)\hat{I}_z(p_2)\,|\uparrow\rangle\,,\ p_1>p_2\\ \langle\uparrow|\,\hat{I}_z(p_2)\hat{I}_-(p_1)-\hat{I}_-(p_1)\hat{I}_z(p_2)\,|\uparrow\rangle\,,\ p_2>p_1\end{cases}\\ &= \langle\uparrow|-\theta(p_2-p_1)\big[\hat{I}_-(p_1),\hat{I}_z(p_2)\big]\,|\uparrow\rangle\\ &= \langle\uparrow|-\theta(p_2-p_1)\hat{I}_-(p_1)\,|\downarrow\rangle\,.\end{aligned} \tag{2.22}$$

And

$$\begin{aligned}\langle\downarrow|\,\overbrace{\hat{I}_-(p_1)\hat{I}_z(p_2)}\,|\downarrow\rangle &= \begin{cases}\langle\downarrow|\,\hat{I}_-(p_1)\hat{I}_z(p_2)-\hat{I}_z(p_2)\hat{I}_-(p_1)\,|\downarrow\rangle\,,\ p_1>p_2\\ \langle\downarrow|\,\hat{I}_z(p_2)\hat{I}_-(p_1)-\hat{I}_z(p_2)\hat{I}_-(p_1)\,|\downarrow\rangle\,,\ p_2>p_1\end{cases}\\ &= \langle\downarrow|\,\theta(p_1-p_2)\big[\hat{I}_-(p_1),\hat{I}_z(p_2)\big]\,|\downarrow\rangle\\ &= \langle\downarrow|\,\theta(p_1-p_2)\hat{I}_-(p_1)\,|\downarrow\rangle\,.\end{aligned} \tag{2.23}$$

Together

$$\begin{aligned}\overbrace{\hat{I}_-(p_1)\hat{I}_z}(p_2) &= -\big(\theta(p_2-p_1)\delta_{\psi,\uparrow}-\theta(p_1-p_2)\delta_{\psi,\downarrow}\big)\hat{I}_-(p_1)\\ &= -G(p_2-p_1)\hat{I}_-(p_1).\end{aligned} \tag{2.24}$$

Combining these gives the following box of key equations.

Key Equation

$$G(p_2-p_1) := \theta(p_2-p_1)\delta_{\psi,\downarrow}-\theta(p_1-p_2)\delta_{\psi,\uparrow}. \tag{2.25}$$

$$\begin{aligned}\overbrace{\hat{I}_+(p_1)\hat{I}_-}(p_2) &= -2\,\mathrm{e}^{+\frac{\mathrm{i}A_n}{\hbar}\int_{p_1}^{p_2}\mathrm{d}t' m_{\mathrm{S}}(p')}\hat{I}_z(p_2)G(p_2-p_1).\\ \overbrace{\hat{I}_+(p_1)\hat{I}_z}(p_2) &= \hat{I}_+(p_1)G(p_2-p_1).\\ \overbrace{\hat{I}_z(p_1)\hat{I}_-}(p_2) &= -\hat{I}_-(p_2)G(p_2-p_1).\end{aligned} \tag{2.26}$$

2.1.3 Stacked Contractions

Since contractions yield one fewer spin operators rather than a c-number, contractions can stack

$$\overbrace{\hat{I}_{\alpha_1,m}(t_1)\hat{I}_{\alpha_2,m}(t_2)\hat{I}_{\alpha_3,m}}(t_3) \tag{2.27}$$

The shortest contraction is meant to be evaluated first and so on. Operators nested three-deep are called locked terms.

$$\overbrace{\hat{I}_{\alpha_1,m}(t_1)\hat{I}_{\alpha_2,m}(t_2)\hat{I}_{\alpha_3,m}(t_3)\hat{I}_{\alpha_4,m}}(t_4) \tag{2.28}$$

Locked Term Example

To evaluate

$$\overbrace{\hat{I}_+(p_1)\hat{I}_-(p_2)\hat{I}_+(p_3)\hat{I}_-}(p_4) \tag{2.29}$$

we start with the innermost contraction and work up

$$\overbrace{\hat{I}_z(p)\hat{I}_+(p_3)\hat{I}_-}(p_4)\big(-2\,\mathrm{e}^{+\frac{\mathrm{i}A}{\hbar}\int_{p_1}^{p_2}\mathrm{d}t' m_{\mathrm{S}}(p')}G(p_2-p_1)\big) \tag{2.30}$$

The next contraction evaluates to

$$\hat{I}_+\overbrace{(p_3)\hat{I}_-}(p_4)\big(-2\,\mathrm{e}^{+\frac{\mathrm{i}A}{\hbar}\int_{p_1}^{p_2}\mathrm{d}t' m_{\mathrm{S}}(p')}G(p_2-p_1)\big)G(p_3-p_2) \tag{2.31}$$

The final contraction yields

$$\big(-2\,\mathrm{e}^{+\frac{\mathrm{i}A}{\hbar}\int_{p_1}^{p_2}\mathrm{d}t' m_{\mathrm{S}}(p')}G(p_2-p_1)\big)G(p_3-p_2)\big(-2\,\mathrm{e}^{+\frac{\mathrm{i}A}{\hbar}\int_{p3}^{p4}\mathrm{d}t' m_{\mathrm{S}}(p')}G(p_4-p_3)\big), \tag{2.32}$$

and so

$$\overbrace{\hat{I}_+(p_1)\hat{I}_-(p_2)\hat{I}_+(p_3)\hat{I}_-}(p_4) = 4\,\mathrm{e}^{+\frac{\mathrm{i}A}{\hbar}\int_{p_1}^{p_2}\mathrm{d}t' m_{\mathrm{S}}(p')}\,\mathrm{e}^{+\frac{\mathrm{i}A}{\hbar}\int_{p3}^{p4}\mathrm{d}t' m_{\mathrm{S}}(p')}G(p_2-p_1)G(p_3-p_2)G(p_4-p_3). \tag{2.33}$$

2.1.4 Feynman Diagrams

The procedure thus far is to expand the propagator to the desired order, and for each term in the series, use equation (2.14) along with the contraction rules to evaluate each term. This gives a collection of partial time-domain signals, $\{V_d(T)\}$. The Taylor series can be a lot to write down, and so to help keep track of all the contractions, Feynman diagrams are introduced. Each unique valid diagram evaluates to a $V_d(T)$, and each $V_d(T)$ can be assigned a diagram. The following Feynman rules are from [1, 35, 37], and assume that contractions are done starting at $\hat{I}_+$ and ending at $\hat{I}_-$.

Feynman Rules: Expressions to Diagrams

1. Only terms with an equal number of $\hat{I}_{+,m}$ and $\hat{I}_{-,m}$ $\forall$ m can be non-zero.

2. For each spin operator place a vertex, a $\bullet$ for $\hat{I}_+$, a $\bigcirc$ for $\hat{I}_-$, and a $\square$ for $\hat{I}_z$.

3. For each factor of $b_{mn}\hat{I}_{\alpha m}(t)\hat{I}_{\alpha' n}(t)$, connect the vertices representing the operators by a coupling coupling line, dashed for $\alpha = \alpha' = z$ and a squiggly line for $\alpha = \pm$, $\alpha' = \mp$.

4. For each $\hat{I}_\alpha(t_1)\hat{I}_{\alpha'}(t_2)$ draw a solid arrow from the $\hat{I}_\alpha$ vertex to the $\hat{I}'_\alpha$ or vice-versa depending on the identities of α and α': each $\hat{I}_+$ should have one outgoing arrow, while each $\hat{I}_-$ must have a net of one incoming arrow either via a single incoming arrow, or two incoming arrow and one outgoing arrow. Each $\hat{I}_z$ should have no net arrows: either no arrows or one in and one out. For nested contractions, start a $\hat{I}_+$ and chain together arrows until the final $\hat{I}_-$ is reached. All arrow chains should start at a $\hat{I}_+$ and end with an $\hat{I}_-$.

Feynman Rules: Diagrams to Expressions

1. Label each $\square$ with $\hat{I}_z$, each $\bullet$ with $\hat{I}_-$, and each $\bigcirc$ with $\hat{I}_-$.

2. Coupling lines connect different spins at a single time—label each dashed coupling line with a time p. Write a coupling factor into the expression: for each squiggly coupling write a $-b_{mn}/4$, and for each dashed line, a b_{mn}. The spin operators that the coupling lines connect should be labeled with the same time (an infinite speed of light assumption), and spin indices m and n corresponding to the subscript of b_{mn}.

3. Arrows connect a single spin across different times—starting from each $\hat{I}_+$, follow the arrow to the $\hat{I}_\alpha$; write down a $\hat{I}_{\alpha,m}(t_1)\hat{I}_{\alpha',n}(p_2)\delta_{mn}$, where the times p_1, and p_2 come from the labels given in the previous step. If $\hat{I}_\alpha = \hat{I}_-$ and $\hat{I}_-$ has two incoming arrows, contract the expressions of each chain up to this point. If there is an outgoing arrow, contract the expression with the next spin operator.

4. Evaluate the contractions.

5. For a diagram with k interaction lines include an overall factor of $\frac{(-\mathrm{i}/\hbar)^k}{k!}$ from the Taylor expansion.

6. Integrate each time parameter over the pulse contour.

7. Sum over all spin indices.

8. Do a weighted average over spin states.

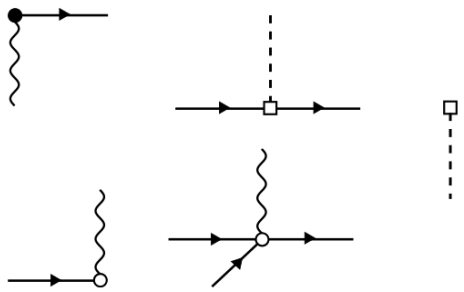

Figure 2.1: The possible vertices are an $\hat{I}_+$ with one outgoing arrow and a coupling line, an $\hat{I}_-$ with one coupling line and either one incoming arrow or two incoming and one outgoing, an $\hat{I}_z$ with a coupling line and either zero arrows or one incoming and one outgoing arrow.

Diagrams that do not form connected graphs separate into the products of the individual diagrams, except for the Taylor series prefactor

$$\frac{(-\mathrm{i}/\hbar)^{k_1+k_2}}{(k_1+k_2)!} = \frac{(-\mathrm{i}/\hbar)^{k_1}}{k_1!}\frac{(-\mathrm{i}/\hbar)^{k_2}}{k_2!}\frac{k_1!k_2!}{(k_1+k_2)!}. \tag{2.34}$$

This last factor divides out the number of ways of forming that particular pair of diagrams, meaning that while a particular product of diagrams is generated by the Taylor series multiple times, they are weighted to only count as one. Any two diagrams shows up multiplied together in the series. This means it is possible to factor all the contributions from each connected diagram apart and sum them individually. For example, let $V_d = V_d(T)$ and $V_{d'} = V_{d'}(T)$, for two distinct connected diagrams, the Taylor series factors as

$$1 + V_d + V_{d'} + \frac{1}{2}(V_dV_{d'} + V_{d'}V_d) + \frac{1}{2}V_d^2 + \frac{1}{2}V_{d'}^2 + \cdots = \Big(1 + V_d + \frac{1}{2}V_d^2\cdots\Big)\Big(1 + V_{d'} + \frac{1}{2}V_{d'}^2\cdots\Big). \tag{2.35}$$

The end result is that each $V_d(T)$ factors out as the Taylor series for an exponential. So rather than summing all possible diagrams, only connected diagrams need to be summed and put into the exp() function:

$$\begin{aligned} v(T) &= \sum_{d\in \substack{\text{all}\\ \text{diagrams}}} V_d(T) \\ &= \prod_{d\in \substack{\text{connected}\\ \text{diagrams}}} \exp(V_d(T)) \\ &= \exp\Big(\sum_{d\in \substack{\text{connected}\\ \text{diagrams}}} V_d(T)\Big). \end{aligned} \tag{2.36}$$

For a Hahn echo $T = 2\tau$. For a refocused echo $T = 2\tau_1 + 2\tau_2$. Equation (2.36) is what we need to lead into CCE. For an example of LCE, please see chapter 5.

2.2 Cluster Correlation Expansion

Cluster Correlation Expansion (CCE) is being increasingly used to model electron decoherence in a variety of systems: irradiated malonic acid [46, 64], boron nitride [65, 66], carbon nanotubes [67], erbium doped crystals [68, 69], diamond [70–75], silicon carbide [76, 77], and various two-dimensional materials [78, 79]. CCE has also been used to screen the phase memory times of radicals in various crystals [80]. CCE will be the primary simulation method we use in the upcoming chapters.

The Cluster Correlation Expansion (CCE) can be built up with or without LCE, but the convergence of CCE follows from the LCE, so LCE will be used as the starting point here. The simplest flip–flop Feynman diagram is

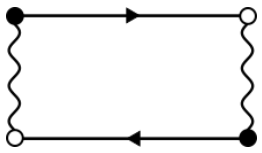

which involves exactly two bath spins. The third-order diagram

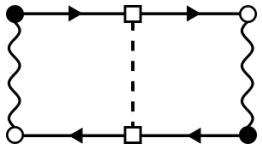

also involves two bath spins. In contrast, the two flip–flop diagram perturbed by a third spin,

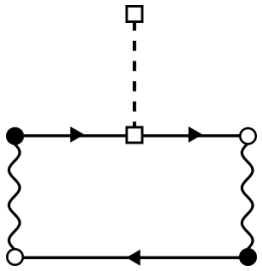

and the ring diagram where all three bath spin are involved in the flip–flop,

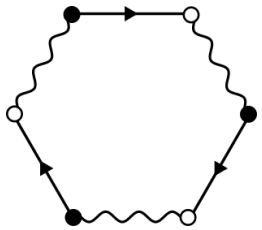

are also third-order diagrams, but involve three spins. From a graph theory perspective this make sense; for N vertices (bath spins), it takes at minimum $N-1$ edges (couplings) to form a connected graph. To contribute to an echo decay, every $\hat{I}_{+n}$ in a diagram must be paired with a $\hat{I}_{-n}$, so two vertices require at least two edges, which requires at least one additional edge beyond the $N-1$ edges. This means that for a N bath spin cluster, its lowest-order contributing diagram is $\mathscr{O}\big((bT)^N\big)$.

The cluster correlation expansion re-partitions the diagrams based not on order, but on the number of bath spins involved. Specifically, the contribution of all diagrams containing exactly n spins is

$$\tilde{v}^{(n)}(T) = \exp\Big(\sum_{d \,\in\, n\text{-spin diagrams}} V_d(T)\Big). \tag{2.37}$$

Since the $\tilde{v}^{(n)}(T)$ contains only n-spin diagrams, the full signal factors as

$$\begin{aligned} v(T) &= \exp\Big(\sum_{d \in \text{ diagrams}} V_d(T)\Big) \\ &= \exp\Big(\sum_{n=0}^{N} \sum_{d \in n\text{-spin diagrams}} V_d(T)\Big) \\ &= \prod_{n=0}^{N} \exp\Big(\sum_{d \in n\text{-spin diagrams}} V_d(T)\Big) \\ &= \prod_{n=0}^{N} \tilde{v}^{(n)}(T). \end{aligned} \tag{2.38}$$

Each $\tilde{v}^{(n)}(T)$ only contains n-spin diagrams, but $\tilde{v}^{(n)}(T)$ can be further factored by which n spins are in each diagram. Specifically, it makes sense to define a cluster auxiliary signal $\tilde{v}_C(T)$; for each set of bath spins, C, the auxiliary cluster signal, $\tilde{v}_C(T)$, is the contribution from all diagrams that contain every spin in the cluster and no other spins:

$$\tilde{v}_C(T) = \exp\Big(\sum_{\substack{d \in |C|\text{-spin diagrams} \\ \text{spins} \in C}} V_d(T)\Big). \tag{2.39}$$

For $\tilde{v}_C(T)$ to be a factor of $\tilde{v}^{(n)}(T)$, $|C| = n$, so n does not need to be explicit in the notation for cluster auxiliary signals. This definition ensures that for clusters C and C', where $C \neq C'$, the diagrams that go into $\tilde{v}_C(T)$ are different than those that go into $\tilde{v}_{C'}(T)$ even if $C \cap C' \neq \emptyset$. It also ensures that every diagram occurs in some $\tilde{v}_C(T)$, so that

$$v(T) = \prod_{C} \tilde{v}_C(T). \tag{2.40}$$

The cluster auxiliary signals can be computed numerically without explicitly evaluating any Feynman diagrams. Let the cluster, C, be a proper subset of the system, S. The auxiliary signal for S can be found first calculating the system signal $v_S(T)$, and the auxiliary signals for all possible clusters and then dividing the cluster auxiliary signals out.

$$\tilde{v}_S(T) = v_S(T) \prod_{C \subset S} \frac{1}{\tilde{v}_C(T)}. \tag{2.41}$$

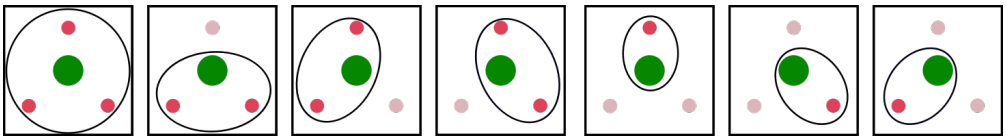

Figure 2.2: Shown above are all the valid clusters for a system with an electron and three nuclei: they all include the electron (green), and a least one magnetic nucleus (red). The cluster of the electron alone evaluates to the identity as well as any subset that does not include the electron, which is why the electron must be in each cluster. The above system has one 3-cluster, three 2-clusters and three 1-clusters.

This works because the division leads to subtraction of the diagrams in the implicit exponentials. This provides a recursive recipe for determining the auxiliary signals of any size, since each cluster can be used as its own smaller system, until their are no proper subclusters, at which point the auxiliary signal and the cluster signal the same. Figure 2.2 illustrate the clusterization for a small system with only three nuclei. As described so far, auxiliary signals require more steps to calculate than the full signal for that cluster, so the full CCE, while formally exact, is at least as difficult (or impossible for large systems), as diagonalizing the system Hamiltonian to begin with. As with LCE, the advantage comes when it is possible to neglect

higher-order terms; the n-CCE (equivalently, CCE-n) approximation is

$$v(T) \approx v^{(n)}(T) = \prod_{|C|\leq n} \tilde{v}_C(T). \tag{2.42}$$

In practice the number of clusters scales combinatorially with cluster size, so cutoffs are chosen and all auxiliary signals for clusters that are beyond the cutoffs are assumed to be unity. What this means is that rather than the product running over all clusters, it only runs over the clusters that meet the cutoff criteria. In the following chapters, we use several different cutoff schemes, so the details of each cutoff methodology will be discussed where it is used.

Note that there are cases where the CCE can become unstable, and special care needs to taken, such as when the hyperfine coupling is on a comparable scale as the nucleus–nucleus dipole–dipole coupling [38], or around clock–transitions [81]. The danger is that cluster auxiliary signals show up in the denominator for auxiliary signals for super-clusters. One of the fundamental assumptions of CCE is that the products of auxiliary signals for subsets of a system capture most of the physics. If this assumption is violated, unbalanced deep modulations can build up in the denominator, leading to the erroneous prediction that $v(T) > v(0)$.

CCE comes in several flavors. The original CCE [1] uses a specific Zeeman bath state. This allows the influence of the spins outside a cluster to be partially included by computing their mean fields contribution. The disadvantages are that multiple bath states must be averaged over and mixed states cannot be directly used. Ensemble CCE [2] uses a density matrix from a mixed state, but sacrifices the ability to use the mean fields from spins outside a cluster. Since the systems we will be looking at are in the temperature regime, where spins nuclear spins are nearly unpolarized, the mean field from other spins can be neglected and the ensemble CCE is the version used throughout this work. Additionally, there is generalized CCE [70]. In order to work in a single electron spin manifold at time, the hyperfine coupling was approximated from $\hat{\boldsymbol{S}}^{\mathrm{T}} \sum_n \boldsymbol{A}_n \hat{\boldsymbol{I}}_n$ to $m_{\mathrm{S}} \hat{\boldsymbol{z}}^{\mathrm{T}} \sum_n \boldsymbol{A}_n \hat{\boldsymbol{I}}_n$. In some cases, this assumption must be relaxed: this means working with $\hat{H}$ rather than $\hat{H}(m_{\mathrm{S}}) = \langle m_{\mathrm{S}}|\hat{H}|m_{\mathrm{S}}\rangle$, because $\langle m_{\mathrm{S}}|\hat{H}|m'_{\mathrm{S}}\rangle \neq 0$ for $m_{\mathrm{S}} \neq m'_{\mathrm{S}}$, but otherwise the methodology is the same.

CCE Procedure:

1. Find all 1-clusters (2-spin systems including the detected electron spin and one bath spin) not excluded by a cutoff, either ignoring the $N-1$ other bath spins or using their mean field.
2. Calculate auxiliary signals for all the 1-clusters found. Since there are no proper subclusters, these iauxiliary signals are the full 1-cluster signals.
3. Find all the 2-clusters not excluded by a cutoff.
4. Calculate the 2-cluster auxiliary signals. Since each 2-cluster has two proper subclusters, each full signal must be divided by the appropriate 1-cluster auxiliary signals to get the corresponding 2-cluster auxiliary signal.
5. Continue finding higher-order clusters and building auxiliary signals until the target maximum cluster size is reached.
6. Multiply all the auxiliary signals together to get an approximation of the full system signal.
7. Repeat the process, varying the parameters to be averaged over, such as the initial bath state, the direction of the applied magnetic field, the isotope composition, or the exact solvent placement.

2.2.1 Three-Spin Systems

The Hahn echo signal for a system consisting of an electron and two spin-1/2 nuclei with the same Larmor frequency, ω_{N}, can be analytically solved[34] by assuming a spin Hamiltonian of the form

$$\hat{H}(m_{\mathrm{S}} = \pm\frac{1}{2}) = \pm\frac{\hbar\omega_0}{2} + \Big(\hbar\omega_{\mathrm{N}} \pm \frac{A_m}{2}\Big)\hat{I}_{zm} + \Big(\hbar\omega_{\mathrm{N}} \pm \frac{A_n}{2}\Big)\hat{I}_{zn} + b\Big(\hat{I}^z_m\hat{I}_{zn} - \frac{1}{4}\hat{I}_{+m}\hat{I}_{-n} - \frac{1}{4}\hat{I}_{-m}\hat{I}_{+n}\Big). \tag{2.43}$$

Writing the Hamiltonian as a 4×4 in the Zeeman basis,

$$\hat{H}(m_{\mathrm{S}} = \pm\frac{1}{2}) = \pm\frac{\hbar\omega_0}{2}\mathbb{1} + \begin{bmatrix} \hbar\omega_{\mathrm{N}} \pm \frac{A_m+A_n}{4} + \frac{b}{4} & 0 & 0 & 0 \\ 0 & \pm\frac{A_m-A_n}{4} - \frac{b}{4} & -\frac{b}{4} & 0 \\ 0 & -\frac{b}{4} & \mp\frac{A_m-A_n}{4} - \frac{b}{4} & 0 \\ 0 & 0 & 0 & -\hbar\omega_{\mathrm{N}} \mp \frac{A_m+A_n}{4} + \frac{b}{4} \end{bmatrix} \begin{matrix} \uparrow\uparrow \\ \uparrow\downarrow \\ \downarrow\uparrow \\ \downarrow\downarrow \end{matrix}. \tag{2.44}$$

The row labels are indicated to the right of the matrix. The $|\uparrow\uparrow\rangle$ and $|\downarrow\downarrow\rangle$ nuclear spin states are eigenstates, leaving only a 2×2 matrix to be diagonalized:

$$\begin{aligned} \hat{H}_{2\times2}(m_{\mathrm{S}} = \pm\frac{1}{2}) = & \pm\frac{\hbar\omega_0}{2}\mathbb{1} + \frac{1}{4}\begin{bmatrix} \pm\Delta A - b & -b \\ -b & \mp\Delta A - b \end{bmatrix} \\ & = (\pm\frac{\hbar\omega_0}{2} - b)\mathbb{1} + \hat{h}_{\pm}. \end{aligned} \tag{2.45}$$

Here $\Delta A := A_m - A_n$. Since the identity commutes with everything, we can focus on $\hat{h}^{\pm}$, everything not proportional to the identity. Defining $\epsilon := b/\Delta A$, $\hat{h}_+$ takes the form

$$\hat{h}_+ = \frac{\Delta A}{4}\begin{bmatrix} 1 & -\epsilon \\ -\epsilon & 1 \end{bmatrix}, \tag{2.46}$$

and $\hat{h}_-$ is related by the similarity transform $\hat{h}_- = \hat{\sigma}_x\hat{h}_+\hat{\sigma}_x^{-1}$, where $\hat{\sigma}_x = \hat{\sigma}_x^{-1}$ is the Pauli x-matrix. The matrix of eigenvalues for $\hat{h}_+$ is

$$\hat{\Lambda}_+ = \frac{\Delta A}{4}\begin{bmatrix} \sqrt{1+\epsilon^2} & 0 \\ 0 & -\sqrt{1+\epsilon^2} \end{bmatrix}. \tag{2.47}$$

Similarly $\hat{\Lambda}_- = \hat{\sigma}_x\hat{\Lambda}_+\hat{\sigma}_x$. Defining $x := \sqrt{\frac{1+\sqrt{1+\epsilon^2}}{\epsilon}}$, the eigenvectors are

$$\hat{X}_+ = \frac{1}{2\sqrt{1+\frac{1}{\epsilon^2}}}\begin{bmatrix} x & 1/x \\ -1/x & x \end{bmatrix}. \tag{2.48}$$

Let

$$\omega_{\mathrm{mod}} := \frac{1}{8\hbar}\sqrt{\Delta A^2 + b^2}, \tag{2.49}$$

and

$$\hat{u}_{\pm} = \hat{X}_{\pm}\begin{bmatrix} \exp\big(\mp 2\mathrm{i}\omega_{\mathrm{mod}}\tau\big) & 0 \\ 0 & \exp\big(\pm 2\mathrm{i}\omega_{\mathrm{mod}}\tau\big) \end{bmatrix}\hat{X}_{\pm}^{\dagger}, \tag{2.50}$$

so that

$$\hat{u}_+ = \frac{1}{2\sqrt{1+\frac{1}{\epsilon^2}}}\begin{bmatrix} x^4\,\mathrm{e}^{-2\mathrm{i}\omega_{\mathrm{mod}}\tau} + x^{-4}\,\mathrm{e}^{+2\mathrm{i}\omega_{\mathrm{mod}}\tau} & 2\mathrm{i}\sin(2\omega_{\mathrm{mod}}\tau) \\ 2\mathrm{i}\sin(2\omega_{\mathrm{mod}}\tau) & x^4\,\mathrm{e}^{+2\mathrm{i}\omega_{\mathrm{mod}}\tau} + x^{-4}\,\mathrm{e}^{-2\mathrm{i}\omega_{\mathrm{mod}}\tau} \end{bmatrix}. \tag{2.51}$$

And $\hat{u}_-$ is the same but with the rows and columns reversed: $\hat{u}_- = \hat{\sigma}_x\hat{u}_+\hat{\sigma}_x$. The full propagator for $\hat{H}_{2\times2}(m_{\mathrm{S}} = \pm\frac{1}{2})$ over duration τ is

$$\hat{U}_{2\times2}(m_{\mathrm{S}} = \pm\frac{1}{2}) = \hat{u}_{\pm}\,\mathrm{e}^{\frac{-\mathrm{i}\tau}{\hbar}(\pm\frac{\hbar\omega_0}{2} - b)} \tag{2.52}$$

which can be used in the Hahn echo signal:

$$v(2\tau) = \frac{1}{4}\mathrm{tr}\Big(\hat{U}(m_{\mathrm{S}} = \frac{1}{2})^{\dagger}\hat{U}(m_{\mathrm{S}} = -\frac{1}{2})^{\dagger}\hat{U}(m_{\mathrm{S}} = \frac{1}{2})\hat{U}(m_{\mathrm{S}} = -\frac{1}{2})\Big). \tag{2.53}$$

There are several simplifications available. The first is to note that constant terms in the Hamiltonian do not contribute, and neither do terms that are a constant times m_{S} since equal time is spent in each electronic

manifold. This means that the nuclear $|\uparrow\uparrow\rangle$ and $|\downarrow\downarrow\rangle$ states refocus fully: only the $\hat{u}_\pm$ factor of $\hat{U}_{2\times2}(m_S = \pm\frac{1}{2})$ varies with 2τ. This leaves the Hahn echo signal as

$$v(2\tau) = \frac{1}{2} + \frac{1}{4}\mathrm{tr}\Big(\hat{u}_+^\dagger \hat{u}_-^\dagger \hat{u}_+ \hat{u}_-\Big). \tag{2.54}$$

Defining $z := x^4\,\mathrm{e}^{-2\mathrm{i}\omega_{\mathrm{mod}}\tau} + x^{-4}\,\mathrm{e}^{+2\mathrm{i}\omega_{\mathrm{mod}}\tau}$, $s := 2\mathrm{i}\sin(2\omega_{\mathrm{mod}}\tau)$, and $N^2 := 2\sqrt{1+\frac{1}{\epsilon^2}}$, the propagators simplify:

$$\hat{u}_+ = \frac{1}{N^2}\begin{bmatrix} z & s \\ s & z^* \end{bmatrix}. \tag{2.55}$$

$$\hat{u}_+\hat{u}_- = \frac{1}{N^4}\begin{bmatrix} |z|^2 + s^{*2} & 2zs \\ 2z^*s & |z|^2 + s^2 \end{bmatrix}. \tag{2.56}$$

$$\hat{u}_+^\dagger \hat{u}_-^\dagger \hat{u}_+\hat{u}_- = \frac{1}{N^8}\begin{bmatrix} \big||z|^2 + s^{*2}\big|^2 + 4z^{*2}|s|^2 & 2(zs + z^*s^*)(|z|^2 + s^2 + s^{*2}) \\ 2(zs^* + z^*s)(|z|^2 + s^2 + s^{*2}) & \big||z|^2 + s^2\big|^2 + 4z^2|s|^2 \end{bmatrix}. \tag{2.57}$$

So that

$$\begin{aligned} v(2\tau) &= \frac{1}{2} + \frac{1}{2N^8}\Big||z|^2 + s^{*2}\Big|^2 + \frac{1}{N^8}(z^2 + z^{*2})|s|^2 \\ &= \frac{1}{2} + \frac{1}{2(1+\frac{1}{\epsilon^2})^2}\Big|\frac{1}{\epsilon^2} + \cos(2\omega_{\mathrm{mod}}2\tau)\Big|^2 + \frac{1}{2(1+\frac{1}{\epsilon^2})^2}\Big(1 + (1+\frac{2}{\epsilon^2})\cos(2\omega_{\mathrm{mod}}2\tau)\Big)\Big(1 - \cos(2\omega_{\mathrm{mod}}2\tau)\Big). \end{aligned} \tag{2.58}$$

This simplifies to

$$v(2\tau) = 1 - \Big(\frac{2\epsilon}{1+\epsilon^2}\Big)^2 \sin^4(\omega_{\mathrm{mod}}2\tau). \tag{2.59}$$

Remembering that $\epsilon = b/\Delta A$,

$$v(2\tau) = 1 - \Big(\frac{2b\Delta A}{b^2 + \Delta A^2}\Big)^2 \sin^4\big(\frac{\sqrt{b^2+\Delta A^2}}{8\hbar}2\tau\big). \tag{2.60}$$

In energy-space, drawing a right triangle with edges b and ΔA, and hypotenuse $\sqrt{b^2+\Delta A^2}$, reveals that the modulation depth can be written in terms of an angle α: $\Big(\frac{2b\Delta A}{b^2+\Delta A^2}\Big)^2 = \sin^2(2\alpha) \in [0,1]$. Equation (2.60) allows for a restricted form of 2-CCE to be written analytically:

$$v^{(2)}(2\tau) = \prod_{m<n}\Big(1 - \Big(\frac{2b_{mn}\Delta A_{mn}}{b_{mn}^2 + \Delta A_{mn}^2}\Big)^2 \sin^4\big(\frac{\sqrt{b_{mn}^2+\Delta A_{mn}^2}}{8\hbar}2\tau\big)\Big). \tag{2.61}$$

2.3 Other Methods

There are several other methods to model the spin dynamics of large spin systems under pulse sequence excitation that are worth mentioning.

2.3.1 Semiclassical Methods

Romanelli and Kevan have an excellent review of semiclassical methods for calculating electron spin echo decays[82, 83].

Mims modeled the nuclear magnetic moments semiclassically, viewing flip-flops as a stochastic sudden-jump process, or as a continuous variable with Gaussian distribution and Markovian time dependence [84]. Stochastic flip-flops require as an input, the flip-flop rate, while the Markovian process requires inputting correlation time. Instantaneous diffusion provides an example case with a result that can be multiplicatively combined with CCE.

Instantaneous Diffusion

This section derives the analytic form for the instantaneous diffusion envelope seen in [85]. The following derivation is based on [82]. Instantaneous diffusion arises from the change in local magnetic field caused by the microwave pulse. Since the electron spins are not infinitely dilute, when a population of electron spins is flipped by a microwave pulse, the magnetic fields generated by those electrons will also reverse directions, and change the sign of any associated interaction terms. Note that because the flip-flops described by instantaneous diffusion are a result of the microwave pulses, the rate is known a priori. This can be described semi-classically by ignoring any perturbation a particular electron has on its environment, and only looking at how the electron spins respond to changes in their environments. The electron spin coherence can be described with a functional integral.

$$v(T) = \int \mathscr{D}\omega(t) P[\omega(t)] \, \mathrm{e}^{\mathrm{i} \int_0^T \mathrm{d}t \ \omega(t)}. \tag{2.62}$$

In other words, the detected electron precesses with a time dependent rate, $\omega(t)$, which changes its phase by $\mathrm{e}^{\mathrm{i} \int_0^T \mathrm{d}t \ \omega(t)}$. Since many electrons contribute to the observed signal, any particular $\omega(t)$ occurs with probability $P[\omega(t)]$. In order to account for all the electrons, all $\omega(t)$ functions must be integrated over, $\int \mathscr{D}\omega(t)$. This notation represents an extreme multidimensional integral, where ω at every time point is a separate degree of freedom. Let $\omega_n = \omega(n\Delta t)$ for $n \in [0, N_t]$ and $N_t \Delta t = T$.

$$\int \mathscr{D}\omega(t) := \lim_{N_\mathrm{t} \to \infty} \prod_{n=0}^{N_\mathrm{t}} \int \mathrm{d}\omega_n. \tag{2.63}$$

Discrete probabilities require $\sum_i P_i = 1$; probability densities require $\int \mathrm{d}x P(x) = 1$. And so too do the functional probability densities require

$$\int \mathscr{D}\omega(t) P[\omega(t)] = 1. \tag{2.64}$$

Assuming the sample is homogeneous with N electrons distributed throughout a volume, V, the probability for a given spin state should be independent of the position of the spin, the probability of a particular $\omega(t)$ factors into the probability for a particular spin configuration $P(\{\mathbf{r}_n\})$, and a particular set of spin states $P[\{m_n(t)\}]$.

$$\begin{aligned} P[\omega(t)] =& P(\{\mathbf{r}_n\}) P[\{m_n(t)\}] \\ =& \prod_n^N P(\mathbf{r}_n) P[m_n(t)] \\ =& \prod_n^N \frac{\mathrm{d}V_n}{V} P[m_n(t)]. \end{aligned} \tag{2.65}$$

The last step assumes the probability of electron n being at position $\boldsymbol{r}_n$ is the equal to the fraction of the total volume it occupies as a point-particle, $P(\boldsymbol{r}_n) = \frac{\mathrm{d}V_n}{V}$; since the electron is assumed to be in volume V, the probability is normalized: $\int \frac{\mathrm{d}V_n}{V} = 1$. In order to make use of this, $\int_0^T \mathrm{d}t \ \omega(t)$ needs to be separated into a spatial part and a spin part:

$$\int_0^T \mathrm{d}t \ \omega(t) = \frac{\mu_0}{4\pi} \gamma_\mathrm{e}^2 \hbar (3\cos^2(\theta) - 1) r^{-3} \int_0^T \mathrm{d}t \ m_\mathrm{S}(t) m_n(t). \tag{2.66}$$

Here $\mu_0 = 1.25663706212 \times 10^{-6} \ \mathrm{T^2 \, m^3 \, J^{-1}}$ is the vacuum magnetic permeability [53], and $\gamma_\mathrm{e} = 1.76085963023 \times 10^{11} \ \mathrm{rad \, s^{-1} \, T^{-1}}$ is the electron gyromagnetic ratio [86]. The spin quantum number of the detected electron is denoted $m_\mathrm{S}(t)$, while the spin quantum number of bath electron n is $m_n(t)$. This can be used to separate the functional integral as

$$\begin{aligned} v(T) =& \int \prod_n^N \mathscr{D}m_n(t) P[m_n(t)] \left(\int \frac{r_n^2 \mathrm{d}r_n \ \mathrm{d}\cos\theta_n \ \mathrm{d}\phi_n}{V} \, \mathrm{e}^{\mathrm{i} \frac{\mu_0}{4\pi} \gamma_\mathrm{e}^2 \hbar (3\cos^2(\theta)-1) r_n^{-3} \int_0^T \mathrm{d}t \ m_\mathrm{S}(t) m_n(t)} \right) \\ =& \left(\int \mathscr{D}m(t) P[m(t)] \int \frac{r^2 \mathrm{d}r \ \mathrm{d}\cos\theta \ \mathrm{d}\phi}{V} \, \mathrm{e}^{\mathrm{i} \frac{\mu_0}{4\pi} \gamma_\mathrm{e}^2 \hbar (3\cos^2(\theta)-1) r^{-3} \int_0^T \mathrm{d}t \ m_s(t) m(t)} \right)^N. \end{aligned} \tag{2.67}$$

Let $V = \frac{4}{3}\pi R^3$. The radial integral simplifies by assuming no spin polarization, so that $P[m(t)] = P[-m(t)]$. Then the new variable $r' := \text{sign}(m(t))r$ gives $\mathrm{d}r' = \text{sign}(m(t))\mathrm{d}r$ and the range of integration goes from $-R$ to R: $\int_{-R}^{R} \frac{\mathrm{d}r'}{2V}$. This is not completely correct as any finite temperature will have some degree of spin polarization, leading to a non-zero imaginary component; however, the imaginary part is small and requires special care to observe [87], so only the real-valued portion will be kept here. Defining, $C := \gamma_e^2(3\cos^2(\theta) - 1)\int_0^{2\tau} \mathrm{d}t\ m_s(t)m(t)$, and $x := r'^{-3}$, the measure for x is $\mathrm{d}x = 3r'^{-4}\mathrm{d}r'$, and the radial integral is $\frac{1}{3}\int \frac{\mathrm{d}x}{V} x^{-2}\,\mathrm{e}^{\mathrm{i}Cx}$. The real part is even in x, while the imaginary part is odd and cancels out over the extended range.

$$\begin{aligned}\frac{1}{3}\int_{\substack{-\infty\\|x|>R^{-3}}}^{\infty} \frac{\mathrm{d}x}{2V} x^{-2}\,\mathrm{e}^{\mathrm{i}Cx} =& \frac{1}{3}\int_{R^{-3}}^{\infty} \frac{\mathrm{d}x}{\frac{4}{3}\pi R^3} x^{-2}\cos(Cx)\\ =& -\frac{1}{3}\frac{1}{\frac{4}{3}\pi R^3} x^{-1}\cos(Cx)\Big|_{R^{-3}}^{\infty} + \frac{1}{3}|C|\int_{R^{-3}}^{\infty} \frac{\mathrm{d}x}{\frac{4}{3}\pi R^3} x^{-1}\sin(|C|x)\\ =& \frac{1}{4\pi}\cos(|C|R^{-3}) + \frac{1}{3}|C|\int_{R^{-3}}^{\infty} \frac{\mathrm{d}x}{\frac{4}{3}\pi R^3} x^{-1}\sin(|C|x)\end{aligned} \tag{2.68}$$

The cosine function is even, and so any information on the sign of C is lost in the integration. It then makes sense to replace C with $|C|$. The remaining integral may be evaluated by going to the complex plane and taking the Cauchy principal value.

$$\frac{1}{3}\int_{\substack{-\infty\\|x|>R^{-3}}}^{\infty} \frac{\mathrm{d}x}{V} x^{-2}\,\mathrm{e}^{\mathrm{i}Cx} = \frac{1}{4\pi}\cos(|C|R^{-3}) - \frac{\pi|C|}{3V}. \tag{2.69}$$

For the first term, the angular integrals will give a factor of 2π to cancel the $\frac{1}{4\pi}$. For the second term, the azimuthal integral gives a 2π. The $(3\cos^2(\theta) - 1)$ inside the $|C|$ needs to evaluated piecewise. Noting $3\cos^2(\theta) = 1$ at $\cos(\theta) = \frac{1}{\sqrt{3}}$, so with $u := \cos(\theta)$,

$$\begin{aligned}\int_{-1}^{1} \mathrm{d}u\ \big|(3u^2-1)\big| =& +\int_{-1}^{-\frac{1}{\sqrt{3}}} \mathrm{d}u\ (3u^2-1) - \int_{-\frac{1}{\sqrt{3}}}^{\frac{1}{\sqrt{3}}} \mathrm{d}u\ (3u^2-1) + \int_{\frac{1}{\sqrt{3}}}^{1} \mathrm{d}u\ (3u^2-1)\\ =& +(u^3-u)\big|_{-1}^{-\frac{1}{\sqrt{3}}} - (u^3-u)\big|_{-\frac{1}{\sqrt{3}}}^{\frac{1}{\sqrt{3}}} + (u^3-u)\big|_{\frac{1}{\sqrt{3}}}^{1}\\ =& -4(\frac{1}{3\sqrt{3}} - \frac{1}{\sqrt{3}})\\ =& \frac{8}{3\sqrt{3}}.\end{aligned} \tag{2.70}$$

Putting everything together,

$$v(T) = \Big(\int \mathscr{D}m(t)P[m(t)]\big(\cos(|C|R^{-3}) - \frac{8}{3\sqrt{3}}\frac{\pi}{3V}\gamma_e^2\int_0^{2\tau} \mathrm{d}t\ m_s(t)m(t)\big)\Big)^N. \tag{2.71}$$

The $V \to \infty$ limit for $\cos(|C|R^{-3})$ and the integral it is in is 1. The $\frac{1}{V}$ term is simpler to write as $\frac{c}{N}$, in terms of the concentration c and the number of spins N.

$$\begin{aligned}v(T) =& \lim_{N\to\infty}\left(1 - \frac{16\pi}{3\sqrt{3}}\frac{\pi c}{3N}\gamma_e^2\int \mathscr{D}m(t)P[m(t)]\int_0^T \mathrm{d}t\ m_s(t)m(t)\right)^N\\ =& \exp\left(-\frac{16\pi^2}{9\sqrt{3}}\frac{\mu_0\gamma_e^2 c}{4\pi}\int \mathscr{D}m(t)P[m(t)]\int_0^{2\tau} \mathrm{d}t\ m_s(t)m(t)\right)\end{aligned} \tag{2.72}$$

So far the only assumption made about $P[m(t)]$ is that $P[m(t)] = P[-m(t)]$, meaning this expression should be valid for any unpolarized homogeneous spin-$\frac{1}{2}$ distribution. For the Hahn echo, $T = 2\tau$, and

$$m_S(t) = -\frac{1}{2}\Big(\theta(\tau - t) - \theta(t - \tau)\Big). \tag{2.73}$$

For instantaneous diffusion, it is reasonable to use

$$P[m(t)] = \eta\delta[m(t) - m(0)\theta(\tau - t) + m(0)\theta(t - \tau)] + (1 - \eta)\delta[m(t) - m(0)] : \tag{2.74}$$

the surrounding spins either flip with probability η or remain in their original state for the entire experiment. Here the delta functional can be defined in terms of Kronecker delta functions:

$$\delta[m(t) - m(0)] := \lim_{N_t \to \infty} \prod_{n=0}^{N_t} \delta(m(t_n) - m(0)) : \tag{2.75}$$

By assumption $m(0) = \pm\frac{1}{2}$. Evaluating the functional integral,

$$\begin{aligned}\int \mathscr{D}m(t)P[m(t)]\Big|\int_0^{2\tau} \mathrm{d}t\ m_s(t)m(t)\Big| &= \int \mathscr{D}m(t)\big((1-\eta)\delta[m(t)-m(0)] + \eta\delta[m(t)-m_s(t)]\big)\Big|\int_0^{2\tau} \mathrm{d}t\ m_s(t)m(t)\Big| \\ &= \frac{2\tau\eta}{4}.\end{aligned} \tag{2.76}$$

Putting this into the coherence function,

$$\begin{aligned}v(2\tau) &= \exp\Big(-\frac{4\pi^2}{9\sqrt{3}}\frac{\mu_0}{4\pi}\gamma_e^2\hbar\, c\eta\, 2\tau\Big) \\ &= \mathrm{e}^{-\frac{2\tau}{\tau_{\mathrm{ID}}}},\end{aligned} \tag{2.77}$$

where

$$\tau_{\mathrm{ID}} := \frac{9\sqrt{3}}{4\pi^2}\frac{4\pi}{\mu_0\gamma_e^2\hbar\, c\eta}. \tag{2.78}$$

For a refocused echo, each spin has two chances to flip. In the refocused echo there are two π-pulses, one at $t_1 = \tau_1$, and one at $t_2 = 2\tau_1 + \tau_2$. Assuming both π-pulses are identical,

$$\begin{aligned}P[m(t)] = \quad & (1-\eta)^2\delta\big[m(t) - m(0)\big] \\ & + (1-\eta)\eta\delta\big[m(t) - m(0)\theta(t_1 - t) + m(0)\theta(t - t_1)\big] \\ & + \eta(1-\eta)\delta\big[m(t) - m(0)\theta(t_2 - t) + m(0)\theta(t - t_2)\big] \\ & + \eta^2\delta\big[m(t) - m(0)\theta(t_1 - t) + m(0)\theta(t - t_1)\theta(t_2 - t) - m(0)\theta(t_2 - t)\big],\end{aligned} \tag{2.79}$$

where within each $\delta[]$ exactly one Heaviside step function is nonzero $\forall\ t$ save over sets with zero Lebesgue measure. The functional integral evaluates to

$$\begin{aligned}&\int \mathscr{D}m(t)P[m(t)]\Big|\int_0^{2\tau_1+2\tau_2} \mathrm{d}t\ m_s(t)m(t)\Big| \\ &= (1-\eta)^2 \times 0 + (1-\eta)\eta\frac{2\tau_2}{4} + \eta(1-\eta)\frac{2\tau_1}{4} + \eta^2\frac{2\tau_1 + 2\tau_2}{4} \\ &= \eta\frac{2\tau_1 + 2\tau_2}{4}.\end{aligned} \tag{2.80}$$

Under this model, instantaneous diffusion depends only on the total evolution time $(2\tau_1 + 2\tau_2)$, and not on $2\tau_1$ or $2\tau_2$ individually.

$$v(2\tau_1 + 2\tau_2) = \mathrm{e}^{-\frac{2\tau_1+2\tau_2}{\tau_{\mathrm{ID}}}}. \tag{2.81}$$

2.3.2 Cluster Expansion

Witzel and Das Sarma's cluster expansion (CE)[34] is based on the concept of dividing the total normalized signal into smaller tractable auxiliary signals, v'_C, which depend upon only a non-empty subset (a cluster) of

the full system. CE is a precursor to CCE; CCE converges better on smaller systems and for most applications CCE is recommended[1, 38]. Nonetheless, CE has been used successfully [36].

Witzel and Das Sarma define their cluster expansion over all possible disjoint non-empty sets of clusters. For a system with N bath particles, there are $2^N - 1$ non-empty subsets. And for each subset with k elements, there are B_k possible partitions, where B_k in the kth Bell number.

$$N_{\text{sets}} = \sum_{k=1}^{N} \binom{n}{k} B_k. \tag{2.82}$$

Let D_p be the pth disjoint non-empty set of clusters. Witzel and Das Sarma build their cluster expansion in the form

$$v(2\tau) = \sum_{p=1}^{N_{\text{sets}}} \prod_{C \in D_p} v'_C. \tag{2.83}$$

The $p = 1$ set is the one which takes the entire system as the only cluster. The definition of v'_C is such so as to give the full $v(2\tau)$ when the sum is taken over all possibilities. Equation (2.83) serves as an implicit definition of the v'_Cs, which can be found recursively as

$$v'_C = v_C - \sum_{p=2}^{N_{\text{sets}}} \prod_{C \in D_p} v'_C. \tag{2.84}$$

The distinction between v_C and v'_C is that v_C is the signal that would arise from only the cluster C in isolation of the environment, while v'_C is an auxiliary signal derived form v_C: for every subcluster $C_i \subset C$, v'_C is v_C with their auxiliary signals subtracted out. When all the cluster contributions in a given set partition are multiplied together and then added to the products from every other partition of the system, the full $v(\tau)$ must be restored.

For the system S, the first term in the sum of equation (2.83) is v'_S, and the rest of the terms are the sum of product of all the possible $v'_C v'_{S-C}$ partition. But by definition v'_S is the full v_S minus these very same $v'_C v'_{S-C}$ partitions. So by construction equation (2.83) converges to the full solution.

It is useful to look at the signals from the smallest clusters. For a single-element cluster, the auxiliary signal v' is equal to the cluster signal v.

$$v'_{\{n\}} = v_{\{n\}}. \tag{2.85}$$

For a cluster of two nuclei, m and n, equation 2.84 gives

$$v'_{\{m,n\}} = v_{\{m,n\}} - v'_{\{m\}} v'_{\{n\}} - v'_{\{m\}} - v'_{\{n\}}. \tag{2.86}$$

In this expression, $v_{\{m,n\}}$ needs to be calculated quantum-theoretically. For a cluster of three nuclei, we get

$$\begin{aligned} v'_{\{l,m,n\}} = v_{\{l,m,n\}} &- v'_{\{l,m\}} v'_{\{n\}} - v'_{\{l,n\}} v'_{\{m\}} - v'_{\{m,n\}} v'_{\{k\}} - v'_{\{l\}} v'_{\{m\}} v'_{\{n\}} \\ &- v'_{\{l,m\}} - v'_{\{l,n\}} - v'_{\{m,n\}} - v'_{\{l\}} - v'_{\{m\}} - v'_{\{n\}}. \end{aligned} \tag{2.87}$$

The value of equation (2.83) is that restricting the sum to only include clusters such that $|C| \leq k$ for some k where v_C is calculable, can provide a reasonable approximation for v_S

2.3.3 Liouville Space Method

The above cluster expansion methods all operate in Hilbert space. The concept of splitting simulations up by nuclei also exists in Liouville space [29, 30]. The LCL (Low-order Correlations in Liouville space) method is superficially similar to a cluster expansion, although it works by reducing the state space using sets of nuclei to define how far to reduce. This is the reverse of the cluster expansions, which use the clusters to decide how far to build. The LCL has been implemented in the NMR community and in the Spinach software package

[33, 88]. In LCL the density vector is broken into basis vectors.

$$\begin{aligned} |\rho(t)\rangle &= |\bigotimes_{n=0}^{N} \boldsymbol{a}_n(t)\cdot\boldsymbol{\sigma}\rangle \\ &= \sum_{i}^{2^{2(N+1)}} 2^{k_i}\, b_i(t)\, |B_i\rangle\,, \end{aligned} \tag{2.88}$$

where $\boldsymbol{\sigma} = [\mathbb{1}, \sigma_z, \frac{1}{\sqrt{2}}\sigma_+, \frac{1}{\sqrt{2}}\sigma_-]$, $\boldsymbol{a} = [a_1, a_z, a_+, a_-]$, and $k_i + 1$ is the spin order, the number of non-identity spin operators used to construct $|B_i\rangle$. The second line expands the four choices for each n into a sum over 4^{N+1} terms. Each $b_i(t)$ is computed from an initial $b_i(0)$ via the Liouville–von Neumann equation, which reads in Liouville space

$$\frac{\mathrm{d}}{\mathrm{d}t}\,|\rho\rangle = \hat{\hat{L}}\,|\rho\rangle\,, \tag{2.89}$$

where $\hat{\hat{L}}$ is the Liouvillian. In Hilbert space

$$\frac{\mathrm{d}}{\mathrm{d}t}\hat{\rho} = -\mathrm{i}\,[\hat{H}, \hat{\rho}]. \tag{2.90}$$

Substituting in equation (2.88),

$$\frac{\mathrm{d}}{\mathrm{d}t}\hat{\rho} = -\mathrm{i}\sum_{i}^{2^{2(N+1)}} b_i(t)[\hat{H}, \hat{B}_i]. \tag{2.91}$$

The expectation value of $\hat{S}_+$ is

$$\begin{aligned} \langle \hat{S}_+ \rangle &= \mathrm{tr}(\hat{S}_+ \hat{\rho}(t)) \\ &= \mathrm{tr}(\hat{S}_+ \bigotimes_{n} \boldsymbol{a}_n(t)\cdot\boldsymbol{\sigma}). \end{aligned} \tag{2.92}$$

Here it is important to note that $\hat{S}_+$ is shorthand for $\bigotimes \hat{S}_i$, where $\hat{S}_i$ is the raising operator for the electron, but the identity for all nuclei. Since there are N nuclei, it is convenient to define $n = 0$ to refer to the electron.

$$\begin{aligned} \langle \hat{S}_+ \rangle &= \mathrm{tr}(\bigotimes_{m} \hat{S}_m \bigotimes_{n} \boldsymbol{a}_n(t)\cdot\boldsymbol{\sigma}) \\ &= \mathrm{tr}\Big(\bigotimes_{n} \big(\hat{S}_n \boldsymbol{a}_n(t)\cdot\boldsymbol{\sigma}\big)\Big) \\ &= \prod_{n} \mathrm{tr}(\hat{S}_n\, \boldsymbol{a}_n(t)\cdot\boldsymbol{\sigma}). \end{aligned} \tag{2.93}$$

If $\hat{S}_n$ were always the identity everything would work out to unity, but when $n = 0$, $\hat{S}_n = \hat{S}_+$. Since $\hat{S}_+\boldsymbol{\sigma} = [\hat{S}_+, -\hat{S}_+, 0, 0]$, and all are traceless matrices, equation (2.93) may be written as

$$\langle \hat{S}_+ \rangle = 1 - \mathrm{tr}(\boldsymbol{a}_0(t)\cdot\boldsymbol{\sigma}). \tag{2.94}$$

The difficulty in equation (2.99) is that $\boldsymbol{a}_0(t)$ requires the full 4^{N+1} dimensional Liouvillian to compute.

Cluster expansion philosophy would suggest to define a density matrix for an isolated cluster as

$$\hat{\rho}'_C = \bigotimes_{n\in C} \boldsymbol{a}'^{C}_n \cdot \boldsymbol{\sigma}. \tag{2.95}$$

Incorporating the larger system gives

$$\hat{\rho}_C = \bigotimes_{n} \boldsymbol{a}^{C}_n \cdot \boldsymbol{\sigma} \tag{2.96}$$

where

$$\boldsymbol{a}_n^C = \begin{cases} \boldsymbol{a}_n'^C, \ n \in C \\ [1,0,0,0], \ n \notin C \end{cases} . \tag{2.97}$$

The density matrix up to spin order $k+1$ could then be written in terms of either the original basis or the same basis in cluster notation

$$\begin{aligned} |\rho\rangle_C^{(k)} &= \sum_{\substack{i \\ k_i \leq k}} 2^{k_i} \, b_i(t) \, |B_i\rangle \\ &= \sum_{\substack{C \\ |C| \leq k+1}} |\bigotimes_n \boldsymbol{a}_n^C \cdot \boldsymbol{\sigma}\rangle \end{aligned} \tag{2.98}$$

But the LCL propagates each $|B_i\rangle$ with a reduced Liouvillian $\hat{\hat{L}}_X$, not an $\hat{\hat{L}}_C$ for each cluster. The Liouvillian $\hat{\hat{L}}_X$, operates in the space spanned by the set of $|B_i\rangle$s with $k_i < k$: this is distinguished from propagating each cluster density matrix on its own. The basis vectors can get mixed by the Liouvillian, $\hat{\hat{L}}_X$, clusters are not isolated entities. This means that while it is true that

$$\begin{aligned} \langle \hat{S}_+ \rangle &= 1 - \sum_C \mathrm{tr}(\boldsymbol{a}_0^C(t) \cdot \boldsymbol{\sigma}) \\ &= 1 - \sum_C v_C^{\mathrm{LCL}}(t), \end{aligned} \tag{2.99}$$

it is also misleading because unlike cluster expansions, LCL imposes no form of cluster isolation, and so it is not meaningful to talk about the contribution from a particular cluster.

The principle used to simplify the exponentially scaling computation to a polynomial scaling problem is similar in CE, CCE, and LCL. There are some differences both in implementation and in philosophy. They both impose a cutoff to the order of the correlations that the method is allowed to generate, but the LCL still allows full communication between all nuclei in the system, albeit through restricted pathways, while the cluster expansions treat their clusters as isolated systems.

Other differences include that LCL is a Liouville space method; while there are time-saving techniques exclusive to Liouville space evolution, it is important to note that the dimension of Liouville space is the square of the Hilbert space for the same system.

Additionally, CE and CCE both give time-dependent expectation values $\langle \hat{O}(t) \rangle$, while LCL ends with the density vector $|\rho(t)\rangle$, which can then be used to find $\langle \hat{O}(T) \rangle$, but could also give $\langle \hat{O}'(T) \rangle$ for $\hat{O} \neq \hat{O}'$ without any additional time evolutions. In contrast, CE and CCE would need to be run separately for each $\hat{O}$. This means that LCL and CCE likely have different use cases.

With a nearly infinite Hilbert space,
to solve, impossible in any case,
thus approximations are required.
Here cluster approximations don't get tired.
They break the problem into many parts,
evaluation with computer arts.

Chapter 3

Background: Methyl Rotors

Methyl groups (CH_3) are an important source of electron spin decoherence in many systems[22]. Even when temperatures are cold enough for most motional degrees of freedom to be frozen out, the low mass of the methyl hydrogens allows the otherwise spatially fixed atoms to undergo coordinated quantum tunneling, resulting is a net rotation of the methyl group. Since hydrons have magnetic dipole moments, methyl rotations can redistribute the magnetic moments if they are not all the same.

Methyl groups are also heralded as an excellent system for studying the quantum-to-classical transition: at high temperatures they act as classical hindered rotors, yet at low temperatures, quantum phenomena become pronounced. [61, 89]. There is a large body of literature around modeling and understanding methyl groups in Inelastic Neutron Scattering (INS)[90–92], Nuclear Magnetic Resonance (NMR)[93, 94], and Electron Paramagnetic Resonance (EPR) [22, 46, 60, 95–100] .

Systems with multiple methyl rotors, such as TEMPO or MTSSL which have two pairs of geminal methyl groups, have the potential for rotor–rotor coupling; however, current EPR techniques do not seem able to resolve methyl–methyl coupling [98, 101], and so this chapter will not discuss it. Instead, this chapter will introduce the physics of single methyl groups as will be relevant for studying electron spin decoherence.

3.1 Permutation Symmetry

For any system with N particles of which N_n are identical particles, the Hamiltonian is invariant to permutations of the identical particles. For a chemical system, this means that the potential energy function, $V(\boldsymbol{r}_1, \cdots \boldsymbol{r}_{N_1}, \cdots)$, has at least $N_{\text{perm}} = \prod_n N_n!$ degenerate minima, where n runs over every unique type of particle. For nuclei in molecules where these minima are often well separated, solutions to the Schrödinger equation, local to different minima, are referred to as different versions of the molecule [59]. The spin-statistics theorem requires that the wavefunction contain equal probability density in each of these minima with amplitudes such that the total wavefunction is antisymmetric between different versions of the system separated by odd permutations of identical fermions, and symmetric for all other permutations of identical particles (fermions and bosons).

Let $|\Psi_i\rangle$ be a wavefunction describing the ith nuclear permutation, such that the the full wavefunction

$$|\Psi\rangle \approx \frac{1}{\sqrt{N_{\text{perm}}}} \sum_{i=1}^{N_{\text{perm}}} s_i \, |\Psi_i\rangle \, . \tag{3.1}$$

Here the s_is, are coefficients that ensure the wavefuntion has the correct symmetry. The total permutation symmetry group is

$$G_{\text{perm}} = \bigotimes_n S_{N_n}, \tag{3.2}$$

where S_N is the symmetric group over N elements. Specifically, if the N_n nuclei of type n are fermions, $|\Psi\rangle$ must transform as the totally antisymmetric one-dimensional irreducible representation of S_{N_n}, which we will call A_2. And if the N_n nuclei of type n are bosons, $|\Psi\rangle$ must transform as the totally symmetric

one-dimensional irreducible representation of S_{N_n}, which we will call A_1. This must hold for all nuclei. These assumptions are reasonable for nuclei in a frozen matrix, where the wavefunction quickly goes to nearly zero at nuclear coordinates away from these different versions. The $|\Psi_i\rangle$s are not physically valid, since they do not have the correct symmetry with respect to permutations of identical nuclei; however, in non-relativistic quantum mechanics, the Pauli principle is an additional requirement for valid states on top of the Schödinger equation. As such, the Hamiltonian may act on $|\Psi_i\rangle$s as an operator. Let δe be the desired error tolerance, for the propagator over duration T, $\hat{U}(T)$. If

$$\langle\Psi_i|\hat{U}(T)|\Psi_j\rangle < \delta e,\ \forall\ i \neq j, \tag{3.3}$$

using any of the $|\Psi_i\rangle$s instead of the full $|\Psi\rangle$ will give the same predictions. When $\langle\Psi_i|\hat{U}(T)|\Psi_j\rangle$ is small $\forall\, t \leq T$, a Taylor expansion gives an equivalent condition for energy tolerance δE: assuming a time-independent Hamiltonian,

$$|\,\langle\Psi_i|\hat{H}|\Psi_j\rangle\,| = |\,\langle\Psi_i|\hat{T}+V|\Psi_j\rangle\,| < \delta E,\ \forall\ i \neq j. \tag{3.4}$$

If the different versions of the system are separated by large potential barriers, the $|\Psi_i\rangle$s will not significantly overlap (small potential contribution $|\,\langle\Psi_i|V|\Psi_j\rangle\,|$), and the $|\Psi_i\rangle$s will be flat where the other $|\Psi_i\rangle$s are significant (small kinetic contribution $|\,\langle\Psi_i|\hat{T}|\Psi_j\rangle\,|$).

This assumption is often implicit in magnetic resonance models, where in the construction of spin–states, the product space over the spin–states of each nuclei is used without regard for the Pauli principle. Frequently, this is justified since for nuclei to swap places they must pass through regions with high potential barriers. [59] However, methyl groups contain three hydrogens, and a $2\pi/3$ rotation of the methyl group achieves an even permutation of the hydrogens while maintaining the separations of the methyl hydrogens. These three minima are frequently not well separated, and the $|\Psi_i\rangle$s corresponding to the three even permutations of each methyl group should be included when modelling methyls. Notably though, this does not require that the odd permutations be included, as the barrier separating the three odd permutations from the three even permutations is much higher as it requires the hydrogen to pass by each other, either getting close to each other or by significantly distorting the methyl from its ground state configuration. [102]

Going from the single-version spin Hamiltonian to a spin Hamiltonian that accounts for even permutations (or all permutations) does not change the Hilbert space dimensionality. While conceptually accounting for the extra permutations requires tensoring together the eight-dimensional spin Hamiltonian with a three dimensional rotational Hamiltonian (one for each unique even permutation), the Pauli principle excludes the extra dimensions. With N identical particles and N occupied states, there is only one linear combination of of permutations that is consistent with the spin statistics theorem.

It important to distinguish between two types of symmetry. The three methyl protons have S_3 permutation symmetry, and the potential landscape allows all but even permutations to be neglected. This makes the methyl protons' effective symmetry group the alternating group over three elements, Alt(3). These groups are

$$\begin{aligned} S_3 &= \{(), (123), (321), (12), (23), (13)\}; \\ \mathrm{Alt}(3) &= \{(), (123), (321)\}. \end{aligned} \tag{3.5}$$

The parentheses represent the permutations: () is the identity; (123) swaps element 1 with element 2, 2 with 3, and 3 with 1; (321) swaps 3 with 2, 2 with 1, and 1 with 3; (12) swaps 1 and 2; (23) swaps 2 and 3, and (13) swaps 1 and 3. There is also the C_{3v} point group symmetry of the methyl rotor. This is a spatial symmetry of the configuration. If only rotations are relevant, the point group symmetry can be simplified to C_3. Somewhat by coincidence the permutation symmetry groups are isomorphic to the point group symmetries.

$$\begin{aligned} S_3 &\equiv C_{3v}. \\ \mathrm{Alt}(3) &\equiv C_3. \end{aligned} \tag{3.6}$$

Here "$\equiv$" is used to indicate the two groups are isomorphic to each other. This can lead to confusion, since the point group symmetry can be broken, while the permutation symmetry holds regardless of the point group symmetry. The only place we will use the point group symmetry is to approximate the form of the rotational potential, but the results in regard to tunnel splitting and Hilbert space dimensionality are a consequence of the permutation symmetry, not the point group symmetry.

3.2 Symmetry-Adapted Bases

This section briefly introduces how to develop a basis that has a target symmetry from a generic basis. Special attention is given to the Zeeman basis of three spin-1/2 particles, and the symmetric group over three elements, S_3.

Let $\hat{P}^{(\alpha)}$ be the character projection operator for the αth irreducible representation of group G. When applied to a basis state, $\hat{P}^{(\alpha)}$ separates out the component of the basis state that transforms as αth irreducible representation. The formula for $\hat{P}^{(\alpha)}$ is [103]

$$\hat{P}^{(\alpha)} = \frac{d_\alpha}{|G|} \sum_{g \in G} c^{(\alpha)}(g)^* \hat{O}_g. \tag{3.7}$$

The size of the group is denoted $|G|$, and d_α is the dimensionality of the αth irreducible representation. The sum runs over all elements of the group; $c^{(\alpha)}(g)$ is the character of g, under the αth irreducible representation, and $\hat{O}_g$ is the operator that performs g. For example, the character table of S_3 is shown below, where the irreducible representations borrow their names from the isomorphic C_{3v} group[103].

S_3	()	(123)	(321)	(12)	(23)	(13)
A_1	1	1	1	1	1	1
A_2	1	1	1	-1	-1	-1
E	2	-1	-1	0	0	0

The corresponding projection operators are

$$\begin{aligned}
\hat{P}^{(A_1)} &= \frac{1}{6}\Big(() + (123) + (321) + (12) + (23) + (13)\Big);\\
\hat{P}^{(A_2)} &= \frac{1}{6}\Big(() + (123) + (321) - (12) - (23) - (13)\Big);\\
\hat{P}^{(E)} &= \frac{2}{6}\Big(() - (123) - (321)\Big).
\end{aligned} \tag{3.8}$$

For three protons there are $2^3 = 8$ Zeeman states in the basis: $|\uparrow\uparrow\uparrow\rangle$, $|\downarrow\uparrow\uparrow\rangle$, $|\uparrow\downarrow\uparrow\rangle$, $|\uparrow\uparrow\downarrow\rangle$, $|\uparrow\downarrow\downarrow\rangle$, $|\downarrow\uparrow\downarrow\rangle$, $|\downarrow\downarrow\uparrow\rangle$, and $|\downarrow\downarrow\downarrow\rangle$. The elements of S_3 swap nuclear spin states, but do not change the relative number of $\uparrow$s and $\downarrow$s. This means that there is one symmetry-adapted basis state made of $|\uparrow\uparrow\uparrow\rangle$, another of $|\downarrow\downarrow\downarrow\rangle$, three made from linear combinations of $|\downarrow\uparrow\uparrow\rangle$, $|\uparrow\downarrow\uparrow\rangle$, and $|\uparrow\uparrow\downarrow\rangle$, and three more from combinations of $|\uparrow\downarrow\downarrow\rangle$, $|\downarrow\uparrow\downarrow\rangle$, and $|\downarrow\downarrow\uparrow\rangle$. The symmetry-adapted states can be found by applying the projection operator to the various Zeeman states.

$$\begin{aligned}
\hat{P}^{(\mathrm{A}_1)}\,|\downarrow\uparrow\uparrow\rangle &= \frac{1}{3}\Big(\,|\downarrow\uparrow\uparrow\rangle + |\uparrow\downarrow\uparrow\rangle + |\uparrow\uparrow\downarrow\rangle\,\Big);\\
\hat{P}^{(\mathrm{A}_2)}\,|\downarrow\uparrow\uparrow\rangle &= 0.
\end{aligned} \tag{3.9}$$

Note that $\hat{P}^{(\mathrm{A}_2)}\,|\downarrow\uparrow\uparrow\rangle = 0$ means that there is no way within this basis to construct a state that satisfies the Pauli principle for fermions. An important subgroup of S_3 is the alternating group over three elements, Alt(3). So before looking for the E states, the character table of Alt(3), is shown below, where $\epsilon = \mathrm{e}^{2\pi \mathrm{i}/3}$ and where the irreducible representations borrow their names from the isomorphic C_3 group[103].

Alt(3)	()	(123)	(321)
A	1	1	1
$\mathrm{E_a}$	1	ϵ	ϵ^*
$\mathrm{E_b}$	1	ϵ^*	ϵ

The projection operator are

$$\begin{aligned}
\hat{P}^{(\mathrm{A})} &= \frac{1}{6}\Big(() + (123) + (321)\Big);\\
\hat{P}^{(\mathrm{E_a})} &= \frac{1}{6}\Big(() + \epsilon^*(123) + \epsilon(321)\Big);\\
\hat{P}^{(\mathrm{E_b})} &= \frac{1}{6}\Big(() + \epsilon(123) + \epsilon^*(321)\Big).
\end{aligned} \tag{3.10}$$

The reason to introduce the Alt(3) projection operators here is because the two groups allow for spin states that are simultaneous adapted for both symmetry groups.

$$\begin{aligned}
\hat{P}^{(\mathrm{A}_1)}\hat{P}^{(\mathrm{A})}\left|\downarrow\uparrow\uparrow\right\rangle &= \hat{P}^{(\mathrm{A})}\left|\downarrow\uparrow\uparrow\right\rangle = \frac{1}{3}\Big(\left|\downarrow\uparrow\uparrow\right\rangle + \left|\uparrow\downarrow\uparrow\right\rangle + \left|\uparrow\uparrow\downarrow\right\rangle\Big);\\
\hat{P}^{(\mathrm{E})}\hat{P}^{(\mathrm{E_a})}\left|\downarrow\uparrow\uparrow\right\rangle &= \hat{P}^{(\mathrm{E_a})}\left|\downarrow\uparrow\uparrow\right\rangle = \frac{1}{3}\Big(\left|\downarrow\uparrow\uparrow\right\rangle + \epsilon^*\left|\uparrow\downarrow\uparrow\right\rangle + \epsilon\left|\uparrow\uparrow\downarrow\right\rangle\Big);\\
\hat{P}^{(\mathrm{E})}\hat{P}^{(\mathrm{E_b})}\left|\downarrow\uparrow\uparrow\right\rangle &= \hat{P}^{(\mathrm{E_b})}\left|\downarrow\uparrow\uparrow\right\rangle = \frac{1}{3}\Big(\left|\downarrow\uparrow\uparrow\right\rangle + \epsilon\left|\uparrow\downarrow\uparrow\right\rangle + \epsilon^*\left|\uparrow\uparrow\downarrow\right\rangle\Big).
\end{aligned} \tag{3.11}$$

The A state of Alt(3) is also the A_1 state of S_3, and the E_a and E_b states of Alt(3) are also two orthogonal E states of S_3. Let $s \in \{-1, 0, 1\}$ denote the irreducible representation: $s = 0$ corresponds to A and $|s| = 1$ to E. Noting $\epsilon^{-1} = \epsilon^*$, the symmetry-adapted spin basis is

$$\begin{aligned}
\left|\mathrm{spin}_{s=0}(m_I = 3/2)\right\rangle &= \left|\uparrow\uparrow\uparrow\right\rangle;\\
\left|\mathrm{spin}_{s}(m_I = 1/2)\right\rangle &= \frac{1}{\sqrt{3}}\Big(\left|\downarrow\uparrow\uparrow\right\rangle + (\epsilon^*)^s\left|\uparrow\downarrow\uparrow\right\rangle + \epsilon^s\left|\uparrow\uparrow\downarrow\right\rangle\Big);\\
\left|\mathrm{spin}_{s}(m_I = -1/2)\right\rangle &= \frac{1}{\sqrt{3}}\Big(\left|\uparrow\downarrow\downarrow\right\rangle + (\epsilon^*)^s\left|\downarrow\uparrow\downarrow\right\rangle + \epsilon^s\left|\downarrow\downarrow\uparrow\right\rangle\Big);\\
\left|\mathrm{spin}_{s=0}(m_I = -3/2)\right\rangle &= \left|\downarrow\downarrow\downarrow\right\rangle.
\end{aligned} \tag{3.12}$$

The $s = 0$ states have $I = 3/2$, and the $s = \pm 1$ states have $I = 1/2$. Equation (3.12) gives a spin-only basis that satisfies the Pauli principle with regard to even permutations.

3.3 The Methyl Hamiltonian

Methyl dynamics varies with temperature, and so too does it contribution to electron spin decoherence; in a frozen glassy matrix below ≈ 50 K, methyl-driven electron spin decoherence flattens out as a function of temperature[22]. Yet even at low temperatures where the rotational barrier is significantly greater than the thermal energy, methyl groups can still drive electron spin decoherence. This section focuses on this low-temperature regime and follows [104–106] to derive the methyl Hamiltonian and discusses how the Pauli principle is satisfied by the rotor states.

Treating the carbons as fixed, the CH_3 rotor has 3 protons with 9 spatial degrees of freedom. The dimensionality of the problem can be reduced in the low-energy regime by assuming that the CH bond length is constant and that the non-hydrogen atom that the methyl group is bonded to fix the protons positions on the direction of the rotor axis, leaving three degrees of freedom, the angles of each proton with respect to some arbitrary zero direction. The effective Hamiltonian is

$$\hat{H} = \hat{H}_{\mathrm{spin}} + \sum_{i=1}^{3}\Big(\frac{-\hbar^2}{2mr_0^2}\big(\frac{\partial}{\partial\phi_i}\big)^2 + V(\phi_i)\Big) + \sum_{i=1}^{2}\sum_{j=i+1}^{3} U(|\phi_i - \phi_j|). \tag{3.13}$$

The $U(|\phi_i - \phi_j|)$s are the proton–proton interaction terms and are repulsive. The $V(\phi)$ is the potential from interactions with the environment. Back interactions from the methyl's influence on the environment will be ignored. Swapping any proton pair leaves $\hat{H}$ unchanged, so $\hat{H}$ has S_3 permutation symmetry; however it does not have C_{3v} point group symmetry, since the $V(\phi_i)$s are not constrained to have any particular rotational symmetry. Take for example, $\hat{C}_3$, that takes $\phi_i \to \phi_i + 2\pi/3\ \forall\ i \in \{1, 2, 3\}$. Applying $\hat{C}_3$ to the rotational $V(\phi_i)$s gives

$$\hat{C}_3\Big(V(\phi_1) + V(\phi_2) + V(\phi_3)\Big) = V(\phi_1 + \frac{2\pi}{3}) + V(\phi_2 + \frac{2\pi}{3}) + V(\phi_3 + \frac{2\pi}{3}). \tag{3.14}$$

To see that the $V(\phi_i)$s are not C_3 symmetric, it is sufficient to find a counter example. When $\phi_1 \approx \phi_2 \approx \phi_3$, $\sum_i V(\phi_i) \approx 3V(\phi_1)$, but $\hat{C}_3\sum_i V(\phi_i) \approx 3V(\phi_1 + 2\pi/3)$. Although the $V(\phi_i)$s are not C_3 symmetric, $\phi_1 \approx \phi_2 \approx \phi_3$ is a high-energy configuration, and the ground state configuration where the three protons form

an equilateral triangle does have C_{3v} point group symmetry. The important point is that the point group symmetry comes from the ground state configuration, and not the Hamiltonian for an arbitrary configuration.

It will be helpful to choose the new variables that separate the overall rotation of the methyl rotor from the relative positions of the protons within the methyl group:

$$\begin{bmatrix} X \\ Y \\ \chi \end{bmatrix} = \begin{bmatrix} \frac{1}{\sqrt{2}} & -\frac{1}{\sqrt{2}} & 0 \\ \frac{1}{\sqrt{6}} & \frac{1}{\sqrt{6}} & -\frac{2}{\sqrt{6}} \\ \frac{1}{3} & \frac{1}{3} & \frac{1}{3} \end{bmatrix} \begin{bmatrix} \phi_1 \\ \phi_2 \\ \phi_3 \end{bmatrix} - \begin{bmatrix} 0 \\ 0 \\ \pi \end{bmatrix}. \tag{3.15}$$

Taking J to be the Jacobian for this transformation,

$$\begin{bmatrix} \frac{\partial}{\partial \phi_1} \\ \frac{\partial}{\partial \phi_2} \\ \frac{\partial}{\partial \phi_3} \end{bmatrix} = \begin{bmatrix} \frac{1}{\sqrt{2}} & \frac{1}{\sqrt{6}} & \frac{1}{3} \\ -\frac{1}{\sqrt{2}} & \frac{1}{\sqrt{6}} & \frac{1}{3} \\ 0 & -\frac{2}{\sqrt{6}} & \frac{1}{3} \end{bmatrix} \begin{bmatrix} \frac{\partial}{\partial X} \\ \frac{\partial}{\partial Y} \\ \frac{\partial}{\partial \chi} \end{bmatrix} = J \begin{bmatrix} \frac{\partial}{\partial X} \\ \frac{\partial}{\partial Y} \\ \frac{\partial}{\partial \chi} \end{bmatrix}. \tag{3.16}$$

Noting that

$$J^{\mathrm{T}} J = \begin{bmatrix} 1 & 0 & 0 \\ 0 & 1 & 0 \\ 0 & 0 & \frac{1}{3} \end{bmatrix}, \tag{3.17}$$

the Hamiltonian becomes

$$\begin{aligned} \hat{H} = \hat{H}_{\mathrm{spin}} &- \frac{3}{3}\frac{\hbar^2}{2(3mr_0^2)}\big(\frac{\partial}{\partial \chi}\big)^2 + V(\chi, X, Y) \\ &- 3\frac{\hbar^2}{2mr_0^2}\big(\frac{\partial}{\partial X}\big)^2 - 3\frac{\hbar^2}{2mr_0^2}\big(\frac{\partial}{\partial Y}\big)^2 + U(|\sqrt{2}X|) + U(|\sqrt{\frac{3}{2}}Y - \frac{1}{\sqrt{2}}X|) + U(|-\sqrt{\frac{3}{2}}Y - \frac{1}{\sqrt{2}}X|), \end{aligned} \tag{3.18}$$

for $\phi \in [0, 2\pi)$, $\chi \in (-\pi, \pi]$, $X \in (-\frac{2\pi}{\sqrt{2}}, \frac{2\pi}{\sqrt{2}})$, and $Y \in (-\frac{4\pi}{\sqrt{6}}, \frac{4\pi}{\sqrt{6}})$. The variable X and Y describe how the proton are arranged on the circle drawn by the protons when rotating the methyl group, while χ is a global rotation of the methyl rotor.

Given that V describes intermolecular couplings, but the Us describe the intramolecular coupling, at least to a first approximation it makes sense to assume that X and Y are controlled almost exclusively by the intramolecular potential and only minimally perturbed by the intermolecular potential. Additionally, we will assume that the wavefunction is localized around the values that minimize the intramolecular potential U: $X = X_0$, and $Y = Y_0$. Under these assumptions, $V(\chi, X, Y) \approx V(\chi, X_0, Y_0) =: V(\chi)$, and separates the Hamiltonian as

$$\hat{H} \approx \hat{H}_{\mathrm{spin}} + \hat{H}_{\mathrm{rot}}(\chi) + \hat{H}_{\mathrm{vib}}(X, Y). \tag{3.19}$$

The advantage of this approximation is the separation of variables. Writing the rotational potential as a Fourier series gives

$$V(\chi) = \sum_{n=0}^{\infty} \Big(a_n \cos(3n\chi) + b_n \sin(3n\chi) \Big). \tag{3.20}$$

The coefficients a_n and b_n are the Fourier coefficients for the potential. Restricting the sum to contain only $3n\chi$, rather than the $n\chi$, comes from the C_{3v} point group symmetry assumption.

The general form is rarely available, and the rotational potential is usually simplified by only including up to the $n = 1$ term, occasionally the $n = 2$ term[107]. Truncating at $n = 1$, defining $\chi = 0$ at a one of the minima, and using the $n = 0$ term to set the minimum of $V(\chi)$ to zero, the resulting potential is parameterized by the single number V_3, which correspond to the difference from the minimum potential to the maximum potential.

$$V(\chi) = V_3 \frac{1 - \cos(3\chi)}{2}. \tag{3.21}$$

In the limit as $V_3 \to \infty$,

$$V(\chi) = \frac{V_3}{2}\Big(1 - \cos(3\chi)\Big) \approx \frac{9V_3}{4} \begin{cases} \chi^2 \\ (\chi - \frac{2\pi}{3})^2 \\ (\chi + \frac{2\pi}{3})^2 \end{cases}, \tag{3.22}$$

depending upon which of the three potential wells is expanded around. Ignoring the existence of the other two wells and solving the Schrödinger equation in a particular well will give localized solutions, $\psi^{(l)}(\chi - j2\pi/3),\ j \in \{-1, 0, 1\}$ and quantum number $l \in \mathbb{N}$. Near the center of the well and low l, $\psi^{(l)}(\chi - j2\pi/3)$ will approximate that of a harmonic oscillator with anharmonicity growing with l and $|\chi - j2\pi/3|$. These states represent the rotational state of the methyl rotor: for example, $\psi^{(l)}(\chi)$ can be interpreted as proton 1 being in the well at $\chi = 0$, and protons 2 and 3 being in the wells at $\chi = 2\pi/3$, and $\chi = -2\pi/3$ respectively. The three $\psi^{(l)}(\chi - j2\pi/3)$s are degenerate, and do not satisfy the Pauli principle; however, a linear combination of these states allows the correct permutation symmetry to be enforced, and a unique ground state to be established. [61]

Deriving the symmetry-adapted rotational states is nearly identical to how the symmetry-adapted spin states were found earlier. The symmetry-adapted rotational states are

$$|\mathrm{rot}_s^{(l)}\rangle = \frac{1}{\sqrt{3}} \sum_{j=-1}^{1} \epsilon^{-sj} \psi^{(l)}(\chi - j2\pi/2) : \tag{3.23}$$

Again, $s \in \{-1, 0, 1\}$ denotes the irreducible representation with 0 corresponding to A and ± 1 to the two E states, and $\epsilon = \mathrm{e}^{2\pi \mathrm{i}/3}$. In S_3, for even l the states transform as either the A_1 or E irreducible representation, while for odd l, they transform as A_2 or E. In Alt(3), the states transform as A, E_a, or $E_\mathrm{a}\ \forall\ l$.

Figure 3.1 shows a schematic of what these states look like. Given a methyl rotor where χ specifies a particular orientation, the states projected onto χ: $\psi_s(\chi) = \langle\chi|\mathrm{rot}_s\rangle$ have equal likelihood of being found in all three equivalent orientations. The phase relationship between minima for $\psi_s(\chi)$ differs among the states rather than the likelihood of rotor orientation.

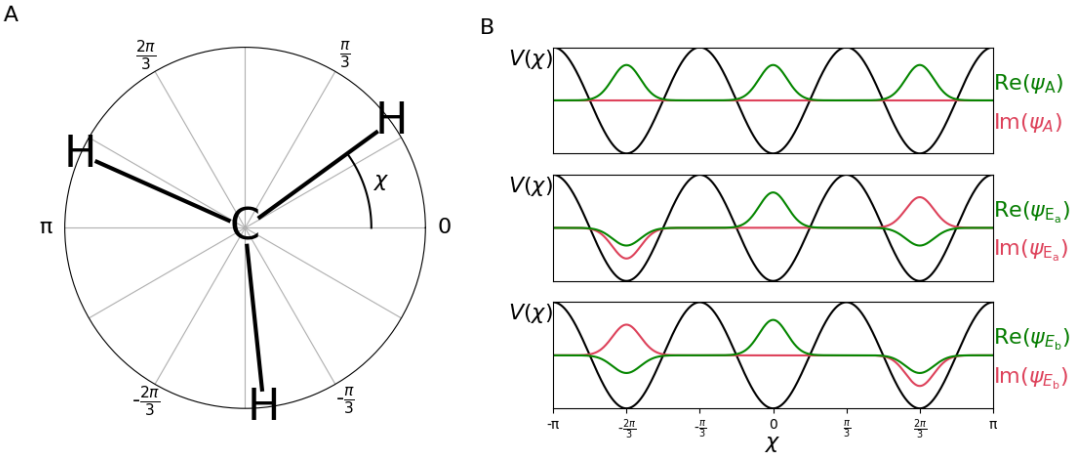

Figure 3.1: **A**: A methyl group shown as a Newman projection is rotated to an angle χ. **B** from top to bottom shows the real (green) and imaginary (red) part of the ground state wave function, and the two degenerate first excited state wave functions. The rotational potential, $V(\chi)$, is shown in black. Here $\psi_s(\chi) := \langle\chi|\mathrm{rot}_s^{(0)}\rangle$. State labels are provided to the right of the plots.

Since we are interested in low temperatures, we assume that the methyl group is in the vibrational ground state. We will use a basis of definite parity, $|\mathrm{vib_a}\rangle$ and $|\mathrm{vib_b}\rangle$. Let $|\mathrm{vib}_a\rangle$ be the basis state with the ordering $0 \leq \langle\phi_1\rangle < \langle\phi_2\rangle < \langle\phi_3\rangle < 2\pi$ and $|\mathrm{vib}_b\rangle$ the same, but with protons 2 and 3 swapped: $0 \leq \langle\phi_1\rangle < \langle\phi_3\rangle < \langle\phi_2\rangle < 2\pi$. The symmetry-adapted vibrational states are

$$\begin{aligned} |\mathrm{vib}_{\mathrm{A}_1}\rangle &= \frac{1}{\sqrt{2}}\Big(|\mathrm{vib_a}\rangle + |\mathrm{vib_b}\rangle\Big); \\ |\mathrm{vib}_{\mathrm{A}_2}\rangle &= \frac{1}{\sqrt{2}}\Big(|\mathrm{vib_a}\rangle - |\mathrm{vib_b}\rangle\Big). \end{aligned} \tag{3.24}$$

For a protiated methyl group, the Pauli principle requires that the wavefunction have A_2 symmetry under S_3.[91] Neither the spin states nor the $l = 0$ rotational states have A_2 in their bases, but they can be combined

to get an A_2 state since E⊗E = A_1⊕A_2⊕E. There are several options for how to label $|\text{spin}\rangle$, $|\text{rot}(\chi)\rangle$, and $|\text{vib}(X,Y)\rangle$ for $|\Psi\rangle$ to have A_2 symmetry: [106]

$$|\Psi_{A_2}\rangle = \begin{cases} |\text{spin}_A\rangle \otimes |\text{rot}_A^{(l)}\rangle \otimes |\text{vib}_{A_2}\rangle \\ \frac{1}{\sqrt{2}}\Big(|\text{spin}_{E_a}\rangle \otimes |\text{rot}_{E_b}^{(l)}\rangle - (-1)^l |\text{spin}_{E_b}\rangle \otimes |\text{rot}_{E_a}^{(l)}\rangle \Big) \otimes |\text{vib}_{A_1}\rangle \\ \frac{1}{\sqrt{2}}\Big(|\text{spin}_{E_a}\rangle \otimes |\text{rot}_{E_b}^{(l)}\rangle + (-1)^l |\text{spin}_{E_b}\rangle \otimes |\text{rot}_{E_a}^{(l)}\rangle \Big) \otimes |\text{vib}_{A_2}\rangle \end{cases} . \tag{3.25}$$

The $(-1)^l$ accounts for the parity of the rotational state. It is worth looking at how many unique $|\Psi_{A_2}\rangle$s there are. The $|\text{spin}_A\rangle$ has $I = 3/2$, and has four states. There is one $|\text{rot}_A^{(l)}\rangle$ per l, and one $|\text{vib}_{A_2}\rangle$, so $|\text{spin}_A\rangle \otimes |\text{rot}_A^{(l)}\rangle \otimes |\text{vib}_{A_2}\rangle$ has four states. Next $|\text{spin}_{E_a}\rangle$ and $|\text{spin}_{E_b}\rangle$ each contain two states, while $|\text{rot}_{E_a}^{(l)}\rangle$ and $|\text{rot}_{E_b}^{(l)}\rangle$ only contain one state per l. There is also one $|\text{vib}_{A_1}\rangle$ in the basis, and so $\Big(|\text{spin}_{E_a}\rangle \otimes |\text{rot}_{E_b}^{(l)}\rangle - (-1)^l |\text{spin}_{E_b}\rangle \otimes |\text{rot}_{E_a}^{(l)}\rangle \Big) \otimes |\text{vib}_{A_2}\rangle$ contains two states, and $\Big(|\text{spin}_{E_a}\rangle \otimes |\text{rot}_{E_b}^{(l)}\rangle + (-1)^l |\text{spin}_{E_b}\rangle \otimes |\text{rot}_{E_a}^{(l)}\rangle \Big) \otimes |\text{vib}_{A_1}\rangle$ contains two states. This means that there are eight possible $|\Psi_{A_2}\rangle$s per l. Since we will be working exclusively with $l = 0$, this is the same number as Zeeman states. The reason adding rotational and vibrational states did not change the dimensionality of the Hilbert space is because we added the minimum number of basis states for each extra degree of freedom, so that the requirement for A_2 symmetry forced there to be only one symmetry-adapted basis state for each Zeeman state. The extra degrees of freedom allow for more states to be represented, but these extra states are excluded because they do not satisfy the Pauli principle. From now on we will assume $l = 0$, and not explicitly write l.

3.4 Effective Spin Hamiltonian

There are several ways of modeling the methyl dynamics within the context of a spin system. One way is to include the rotor degrees of freedom directly into the Hamiltonian [96]. This direct method can make good predictions, but it does not account for the Pauli principle and so will not be used here. Another is to note that only spin degrees of freedom are being experimentally probed so the rotational degrees of freedom can be projected out [108]. This section follows [108] and projects the rotational states onto the spin–space, leaving an effective Hamiltonian over only spin degrees of freedom. We will deviate from [108] and wait until the last step to approximate the full S_3 permutation group as an effective Alt(3) group.

The symmetry-adapted states can be uniquely specified as $|I, m_I, s_{\text{vib}}\rangle$, where I is the total spin; m_I is the z projected spin, and $s_{\text{vib}} \in \{A_1, A_2\}$ is the symmetry label of the vibrational state.

$$\begin{aligned} |I = \frac{3}{2}, m_I, A_2\rangle &= |\text{spin}_0, m_I\rangle \otimes |\text{rot}_0\rangle \otimes |\text{vib}_{A_2}\rangle . \\ |I = \frac{1}{2}, m_I, A_1\rangle &= \frac{1}{\sqrt{2}}\Big(|\text{spin}_1, m_I\rangle \otimes |\text{rot}_{-1}\rangle - |\text{spin}_{-1}, m_I\rangle \otimes |\text{rot}_1\rangle \Big) \otimes |\text{vib}_{A_1}\rangle . \\ |I = \frac{1}{2}, m_I, A_2\rangle &= \frac{1}{\sqrt{2}}\Big(|\text{spin}_1, m_I\rangle \otimes |\text{rot}_{-1}\rangle + |\text{spin}_{-1}, m_I\rangle \otimes |\text{rot}_1\rangle \Big) \otimes |\text{vib}_{A_2}\rangle . \end{aligned} \tag{3.26}$$

The matrix elements of the vibrational Hamiltonian are

$$\begin{aligned} \langle \text{vib}_{A_2} | \hat{H}_{\text{vib}} | \text{vib}_{A_2} \rangle &= E_{\text{vib},2}; \\ \langle \text{vib}_{A_1} | \hat{H}_{\text{vib}} | \text{vib}_{A_1} \rangle &= E_{\text{vib},1}; \\ \langle \text{vib}_{A_1} | \hat{H}_{\text{vib}} | \text{vib}_{A_2} \rangle &= 0. \end{aligned} \tag{3.27}$$

The matrix elements of the rotational Hamiltonian are

$$\langle \text{rot}_s | \hat{H}_{\text{rot}} | \text{rot}_{s'} \rangle = \begin{cases} \frac{1}{2}\hbar\omega_0, \ s = s' = 0 \\ \frac{1}{2}\hbar\omega_0 + \hbar\omega_t, \ s = s' = \pm 1 \\ 0, \ \text{otherwise} \end{cases} . \tag{3.28}$$

Here, $\hbar\omega_t$ is the tunnel splitting—the energy gap between the ground state and the first excited state. It is also helpful to use ω_t as the tunneling (angular) frequency, the tunnel splitting in rad/s, as well as $\nu_t = \omega_t/2\pi$,

the tunnel splitting or tunneling frequency in Hz. The zero-point energy is denoted as $\frac{1}{2}\hbar\omega_0$. The non-zero matrix elements of $\hat{H}_{\text{rot-vib}} := \hat{H}_{\text{rot}} + \hat{H}_{\text{vib}}$ are

$$\begin{aligned}
\langle I = \frac{3}{2}, m_{\text{I}}, A_2 | \hat{H}_{\text{rot-vib}} | I = \frac{3}{2}, m_{\text{I}}, A_2 \rangle &= \frac{1}{2}\hbar\omega_0 + E_{\text{vib},2}; \\
\langle I = \frac{1}{2}, m_{\text{I}}, A_1 | \hat{H}_{\text{rot-vib}} | I = \frac{1}{2}, m_{\text{I}}, A_1 \rangle &= \frac{1}{2}\hbar\omega_0 + \hbar\omega_{\text{t}} + E_{\text{vib},1}; \\
\langle I = \frac{1}{2}, m_{\text{I}}, A_2 | \hat{H}_{\text{rot-vib}} | I = \frac{1}{2}, m_{\text{I}}, A_2 \rangle &= \frac{1}{2}\hbar\omega_0 + \hbar\omega_{\text{t}} + E_{\text{vib},2}.
\end{aligned} \tag{3.29}$$

In the symmetry-adapted basis

$$\hat{H}_{\text{rot-vib}} = \frac{\hbar\omega_0 \mathbb{1}}{2} + \begin{bmatrix}
E_{\text{vib},2} & 0 & 0 & 0 & 0 & 0 & 0 & 0 \\
0 & E_{\text{vib},2} & 0 & 0 & 0 & 0 & 0 & 0 \\
0 & 0 & \hbar\omega_{\text{t}} + E_{\text{vib},1} & 0 & 0 & 0 & 0 & 0 \\
0 & 0 & 0 & \hbar\omega_{\text{t}} + E_{\text{vib},2} & 0 & 0 & 0 & 0 \\
0 & 0 & 0 & 0 & \sqrt{2}\hbar\omega_{\text{t}} + E_{\text{vib},2} & 0 & 0 & 0 \\
0 & 0 & 0 & 0 & 0 & \sqrt{2}\hbar\omega_{\text{t}} + E_{\text{vib},1} & 0 & 0 \\
0 & 0 & 0 & 0 & 0 & 0 & E_{\text{vib},2} & 0 \\
0 & 0 & 0 & 0 & 0 & 0 & 0 & E_{\text{vib},2}
\end{bmatrix} \begin{matrix}
I, m_{\text{I}}, s_{\text{vib}} \\
\frac{3}{2}, \frac{3}{2}, A_2 \\
\frac{3}{2}, \frac{1}{2}, A_2 \\
\frac{1}{2}, \frac{1}{2}, A_1 \\
\frac{1}{2}, \frac{1}{2}, A_2 \\
\frac{1}{2}, -\frac{1}{2}, A_2 \\
\frac{1}{2}, -\frac{1}{2}, A_1 \\
\frac{3}{2}, -\frac{1}{2}, A_2 \\
\frac{3}{2}, -\frac{3}{2}, A_2
\end{matrix} \tag{3.30}$$

with the labels on the far right indicating the state labels. The tool to get an effective spin Hamiltonian is the partial trace:

$$\hat{H}^{(\text{spin-rot})}_{\text{rot-vib}} = \text{tr}_{\text{vib}}(\hat{H}_{\text{rot-vib}}). \tag{3.31}$$

Defining

$$\begin{aligned}
\hat{O}_{iji'j'} &:= |\text{spin-rot}_i\rangle \langle \text{spin-rot}_{i'}| \otimes |\text{vib}_j\rangle \langle \text{vib}_{j'}| ; \\
h_{iji'j'} &:= \text{tr}(\hat{H}^{\dagger}_{\text{rot-vib}} \hat{O}_{iji'j'}) / \text{tr}(\hat{O}^{\dagger}_{iji'j'} \hat{O}_{iji'j'});),
\end{aligned} \tag{3.32}$$

allows the rotational-vibrational Hamiltonian to be written as

$$\hat{H}_{\text{rot-vib}} = \sum_{i,i' \in \text{spin-rot}} \sum_{j,j' \in \text{vib}} h_{iji'j'} |\text{spin-rot}_i\rangle \langle \text{spin-rot}_{i'}| \otimes |\text{vib}_j\rangle \langle \text{vib}_{j'}| , \tag{3.33}$$

the partial trace is defiened as [109]

$$\begin{aligned}
\text{tr}_{\text{vib}}(\hat{H}_{\text{rot-vib}}) &:= \sum_{i,i' \in \text{spin-rot}} \sum_{j,j' \in \text{vib}} h_{iji'j'} |\text{spin-rot}_i\rangle \langle \text{spin-rot}_{i'}| \, \text{tr}(|\text{vib}_j\rangle \langle \text{vib}_{j'}|) \\
&= \sum_{i,i' \in \text{spin-rot}} \sum_{j,j' \in \text{vib}} h_{iji'j'} \langle \text{vib}_{j'} | \text{vib}_j \rangle |\text{spin-rot}_i\rangle \langle \text{spin-rot}_{i'}| .
\end{aligned} \tag{3.34}$$

In the basis of $|\text{spin}_0(I = 3/2, m_{\text{I}})\rangle \otimes |\text{rot}_0\rangle$, $|\text{spin}_1(I = 1/2, m_{\text{I}})\rangle \otimes |\text{rot}_{-1}\rangle$, and $|\text{spin}_{-1}(I = 1/2, m_{\text{I}})\rangle \otimes |\text{rot}_1\rangle$, the $\hat{H}^{(\text{spin-rot})}_{\text{rot-vib}}$ matrix is

$$\hat{H}^{(\text{spin-rot})}_{\text{rot-vib}} = (\frac{\hbar\omega_0}{2} + \bar{E}_{\text{vib}})\mathbb{1} + \begin{bmatrix}
\frac{\Delta E_{\text{vib}}}{2} & 0 & 0 & 0 & 0 & 0 & 0 & 0 \\
0 & \frac{\Delta E_{\text{vib}}}{2} & 0 & 0 & 0 & 0 & 0 & 0 \\
0 & 0 & \hbar\omega_{\text{t}} & \frac{\Delta E_{\text{vib}}}{2} & 0 & 0 & 0 & 0 \\
0 & 0 & \frac{\Delta E_{\text{vib}}}{2} & \hbar\omega_{\text{t}} & 0 & 0 & 0 & 0 \\
0 & 0 & 0 & 0 & \hbar\omega_{\text{t}} & \frac{\Delta E_{\text{vib}}}{2} & 0 & 0 \\
0 & 0 & 0 & 0 & \frac{\Delta E_{\text{vib}}}{2} & \hbar\omega_{\text{t}} & 0 & 0 \\
0 & 0 & 0 & 0 & 0 & 0 & \frac{\Delta E_{\text{vib}}}{2} & 0 \\
0 & 0 & 0 & 0 & 0 & 0 & 0 & \frac{\Delta E_{\text{vib}}}{2}
\end{bmatrix} \begin{matrix}
I, m_{\text{I}}, s_{\text{spin}}, s_{\text{rot}} \\
\frac{3}{2}, \frac{3}{2}, 0, 0 \\
\frac{3}{2}, \frac{1}{2}, 0, 0 \\
\frac{1}{2}, \frac{1}{2}, 1, -1 \\
\frac{1}{2}, \frac{1}{2}, -1, 1 \\
\frac{1}{2}, -\frac{1}{2}, -1, 1 \\
\frac{1}{2}, -\frac{1}{2}, 1, -1 \\
\frac{3}{2}, -\frac{1}{2}, 0, 0 \\
\frac{3}{2}, -\frac{3}{2}, 0, 0
\end{matrix} \tag{3.35}$$

with $\Delta E_{\text{vib}} := E_{\text{vib},2} - E_{\text{vib},2}$, and $\bar{E}_{\text{vib}} := (E_{\text{vib},2} + E_{\text{vib},2})/2$.

Taking the partial trace over rotational states as well as vibrational states, gives a matrix in the $|\text{spin}_s(I, m_{\text{I}})\rangle$ basis with identical matrix elements as $\hat{H}^{(\text{spin-rot})}_{\text{rot-vib}}$:

$$\hat{H}^{(\text{spin})}_{\text{rot-vib}} = \text{tr}_{\text{rot-vib}}(\hat{H}_{\text{rot-vib}}) = (\frac{\hbar\omega_0}{2} + \bar{E}_{\text{vib}})\mathbb{1} + \begin{bmatrix} \frac{\Delta E_{\text{vib}}}{2} & 0 & 0 & 0 & 0 & 0 & 0 & 0 \\ 0 & \frac{\Delta E_{\text{vib}}}{2} & 0 & 0 & 0 & 0 & 0 & 0 \\ 0 & 0 & \hbar\omega_{\text{t}} & \frac{\Delta E_{\text{vib}}}{2} & 0 & 0 & 0 & 0 \\ 0 & 0 & \frac{\Delta E_{\text{vib}}}{2} & \hbar\omega_{\text{t}} & 0 & 0 & 0 & 0 \\ 0 & 0 & 0 & 0 & \hbar\omega_{\text{t}} & \frac{\Delta E_{\text{vib}}}{2} & 0 & 0 \\ 0 & 0 & 0 & 0 & \frac{\Delta E_{\text{vib}}}{2} & \hbar\omega_{\text{t}} & 0 & 0 \\ 0 & 0 & 0 & 0 & 0 & 0 & \frac{\Delta E_{\text{vib}}}{2} & 0 \\ 0 & 0 & 0 & 0 & 0 & 0 & 0 & \frac{\Delta E_{\text{vib}}}{2} \end{bmatrix} \begin{matrix} I, m_{\text{I}} \\ \frac{3}{2}, \frac{3}{2} \\ \frac{3}{2}, \frac{1}{2} \\ \frac{1}{2}, \frac{1}{2} \\ \frac{1}{2}, \frac{1}{2} \\ \frac{1}{2}, -\frac{1}{2} \\ \frac{1}{2}, -\frac{1}{2} \\ \frac{3}{2}, -\frac{1}{2} \\ \frac{3}{2}, -\frac{3}{2} \end{matrix} \tag{3.36}$$

While $\hat{H}^{(\text{spin})}_{\text{rot-vib}}$, is the desired effective Hamiltonian, to use it in conjunction with other spin couplings, it will be helpful to cast $\hat{H}^{(\text{spin})}_{\text{rot-vib}}$ into the Zeeman basis. Let $|\sigma\rangle$ be a spin state in the Zeeman basis, and $\hat{\Lambda}$ be a unitary operator that transforms $|\sigma\rangle$ to the $|\text{spin}_s(I, m_{\text{I}})\rangle$ basis.

$$\begin{aligned} \langle \text{spin}_s | \hat{H}^{(\text{spin-rot})}_{\text{rot-vib}} | \text{spin}_{s'} \rangle &= \langle \sigma_s | \hat{\Lambda}^\dagger \hat{H}^{(\text{spin-rot})}_{\text{rot-vib}} \hat{\Lambda} | \sigma_{s'} \rangle \\ &=: \langle \sigma_s | \hat{H}_{\text{eff}} | \sigma_{s'} \rangle \,. \end{aligned} \tag{3.37}$$

So $\hat{H}_{\text{eff}} = \hat{\Lambda}^\dagger \hat{H}^{(\text{spin-rot})}_{\text{rot-vib}} \hat{\Lambda}$. In matrix form $\hat{\Lambda}$ is an 8×8 matrix.

$$\hat{\Lambda} = \frac{1}{\sqrt{3}} \begin{bmatrix} \sqrt{3} & 0 & 0 & 0 & 0 & 0 & 0 & 0 \\ 0 & 1 & 1 & 0 & 1 & 0 & 0 & 0 \\ 0 & \epsilon & \epsilon^* & 0 & 1 & 0 & 0 & 0 \\ 0 & \epsilon^* & \epsilon & 0 & 1 & 0 & 0 & 0 \\ 0 & 0 & 0 & 1 & 0 & \epsilon^* & \epsilon & 0 \\ 0 & 0 & 0 & 1 & 0 & \epsilon & \epsilon^* & 0 \\ 0 & 0 & 0 & 1 & 0 & 1 & 1 & 0 \\ 0 & 0 & 0 & 0 & 0 & 0 & 0 & \sqrt{3} \end{bmatrix}. \tag{3.38}$$

The Zeeman basis effective Hamiltonian is

$$\begin{aligned} \hat{H}_{\text{eff}} = {} & (\frac{1}{2}\hbar\omega_0 + \bar{E}_{\text{vib}})\mathbb{1} \\ & + \begin{bmatrix} \frac{\Delta E_{\text{vib}}}{2} & 0 & 0 & 0 & 0 & 0 & 0 & 0 \\ 0 & \frac{2\hbar\omega_{\text{t}}}{3} & \frac{-\hbar\omega_{\text{t}}}{3} + \frac{\Delta E_{\text{vib}}}{2} & 0 & \frac{-\hbar\omega_{\text{t}}}{3} & 0 & 0 & 0 \\ 0 & \frac{-\hbar\omega_{\text{t}}}{3} + \frac{\Delta E_{\text{vib}}}{2} & \frac{2\hbar\omega_{\text{t}}}{3} & 0 & 0 & 0 & 0 & 0 \\ 0 & 0 & 0 & \frac{2\hbar\omega_{\text{t}}}{3} + \frac{\Delta E_{\text{vib}}}{2} & 0 & \frac{-\hbar\omega_{\text{t}}}{3} & \frac{-\hbar\omega_{\text{t}}}{3} & 0 \\ 0 & \frac{-\hbar\omega_{\text{t}}}{3} & \frac{-\hbar\omega_{\text{t}}}{3} & 0 & \frac{2\hbar\omega_{\text{t}}}{3} + \frac{\Delta E_{\text{vib}}}{2} & 0 & 0 & 0 \\ 0 & 0 & 0 & \frac{-\hbar\omega_{\text{t}}}{3} & 0 & \frac{2\hbar\omega_{\text{t}}}{3} & \frac{-\hbar\omega_{\text{t}}}{3} + \frac{\Delta E_{\text{vib}}}{2} & 0 \\ 0 & 0 & 0 & \frac{-\hbar\omega_{\text{t}}}{3} & 0 & \frac{-\hbar\omega_{\text{t}}}{3} + \frac{\Delta E_{\text{vib}}}{2} & \frac{2\hbar\omega_{\text{t}}}{3} & 0 \\ 0 & 0 & 0 & 0 & 0 & 0 & 0 & \frac{\Delta E_{\text{vib}}}{2} \end{bmatrix} \begin{matrix} \uparrow\uparrow\uparrow \\ \uparrow\uparrow\downarrow \\ \uparrow\downarrow\uparrow \\ \uparrow\downarrow\downarrow \\ \downarrow\uparrow\uparrow \\ \downarrow\uparrow\downarrow \\ \downarrow\downarrow\uparrow \\ \downarrow\downarrow\downarrow \end{matrix} \end{aligned} \tag{3.39}$$

with the Zeeman state labels on the right. To put this in terms of spin operators, the Hilbert–Schmidt inner product can be used to determine the coefficient i.e. $c_{\hat{S}} = \text{tr}(\hat{H}^\dagger_{\text{eff}} \hat{S})/\text{tr}(\hat{S}^\dagger \hat{S})$. Noting that only the zero-quantum matrix elements are non-zero, many of the potential spin operators can be ruled out a priori.

$$\begin{aligned} \hat{H}_{\text{eff}} = {} & \frac{1}{2}\hbar\omega_0 + \frac{\hbar\omega_{\text{t}}}{2} - \frac{2\hbar\omega_{\text{t}}}{3} \sum_{m=1}^{2} \sum_{n=m+1}^{3} \Big(\hat{I}_{z\,m} \hat{I}_{z\,n} + \frac{1}{2}\big(\hat{I}_{+\,m} \hat{I}_{-\,n} + \hat{I}_{-\,m} \hat{I}_{+\,n} \big) \Big) \\ & + E_{\text{vib},2} + \Delta E_{\text{vib}} \Big(\hat{I}_{z2} \hat{I}_{z3} + \frac{1}{2}\big(\hat{I}_{+2} \hat{I}_{-3} + \hat{I}_{-2} \hat{I}_{+3} \big) \Big). \end{aligned} \tag{3.40}$$

The terms proportional to the identity can be dropped without affecting the physics, and after simplification, the effective Hamiltonian is

$$\hat{H}_{\text{eff}} = -\frac{2\hbar\omega_{\text{t}}}{3}\sum_{m=1}^{2}\sum_{n=m+1}^{3}\hat{\boldsymbol{I}}_m^{\text{T}}\hat{\boldsymbol{I}}_n + \Delta E_{\text{vib}}\hat{\boldsymbol{I}}_2^{\text{T}}\hat{\boldsymbol{I}}_3. \tag{3.41}$$

The terms within $\hat{H}_{\text{eff}}$ are two-spin effective exchange interactions. The energy separation ΔE_{vib} is the tunnel splitting between different parities. Since the potential barrier to odd permutations is significantly greater than for even permutations, it is safe to assume

$$\Delta E_{\text{vib}} \approx 2\left|\langle \text{vib}_{\text{a}}|\hat{H}|\text{vib}_{\text{b}}\rangle\right| \approx 0. \tag{3.42}$$

This approximation is equivalent to ignoring the odd permutations of S_3, and only dealing with Alt(3). Once the rotational tunnel splitting, $\hbar\omega_{\text{t}}$, is known, either by experiment or calculation, methyl tunneling effects can be included in the spin Hamiltonian. Since most proton pairs lie on different methyl groups, and since different methyl rotors likely have different tunnel splittings, let

$$J_{mn} := \begin{cases} -\frac{2}{3}\hbar\omega_{\text{t}}, \ m \text{ and } n \text{ on the same methyl, which has tunnel splitting } \hbar\omega_{\text{t}} \\ 0, \ \text{otherwise} \end{cases}. \tag{3.43}$$

The resulting system Hamiltonian is

$$\begin{aligned} \hat{H} = & -g\mu_{\text{B}}\boldsymbol{B}_0^{\text{T}}\hat{\boldsymbol{S}} + \sum_n g_n\mu_{\text{N}}\boldsymbol{B}_0^{\text{T}}\hat{\boldsymbol{I}}_n \\ & + \sum_n \frac{\mu_0}{4\pi}\frac{g_{\text{e}}\mu_{\text{B}}g_n\mu_{\text{N}}}{r_n^3}\hat{\boldsymbol{I}}_n^{\text{T}}(\mathbb{1} - 3\boldsymbol{r}_n\boldsymbol{r}_n^{\text{T}}/r_n^2)\hat{\boldsymbol{S}} \\ & + \sum_m\sum_{n>m}\frac{\mu_0}{4\pi}\frac{g_m g_n\mu_{\text{N}}^2}{r_{mn}^3}\hat{\boldsymbol{I}}_m^{\text{T}}(\mathbb{1} - 3\boldsymbol{r}_{mn}\boldsymbol{r}_{mn}^{\text{T}}/r_{mn}^2)\hat{\boldsymbol{I}}_n \\ & + \sum_m\sum_{n>m} J_{mn}\hat{\boldsymbol{I}}_m^{\text{T}}\hat{\boldsymbol{I}}_n. \end{aligned} \tag{3.44}$$

This is the Hamiltonian we will use for decoherence simulations, following You et al.[64] who were the first to combine the effective methyl Hamiltonian with Cluster Correlation Expansion (CCE [1, 2]) for electron spin decoherence simulations.

The extra terms in equation (3.44) will almost certainly break the C_{3v} point group symmetry of the methyl rotor. This does not affect the conclusion, because the derivation is based on the S_3 permutation symmetry of the methyl protons, which is still present in equation (3.44). The only place the point group symmetry of the methyl group was used, was in the Fourier series expansion of the rotational potential, equation (3.20), in using $3n\chi$ rather than χ. The additional terms that break the C_{3v} symmetry of the rotor do not invalidate equation (3.20) either, because those terms are in the spin Hamiltonian, and trying to incorporate them into equation (3.20) would then be double counting them.

3.5 Tunnel Splitting

Since the tunnel splitting, ω_t, is the parameter governing the scale of the methyl spin Hamiltonian, and since the tunnel splitting is quite sensitive to the environmental potential, V_3, which itself can vary by a couple orders of magnitude depending upon the system [61], it is worth taking some time to discuss the available methods to measure or calculate the tunnel splitting.

Depending on the nature of the experiment or calculation, the tunnel splitting may be directly or indirectly found: either V_3 or the activation energy, E_a may also be what is directly measured. The tunnel splitting can be determined experimentally via INS [90, 91], NMR (usually E_a) [110–112] or EPR (E_a or ω_t) [96, 113, 114], and computationally (V_3) by quantum calculations [96, 115] or even classical molecular dynamics [115]. See [107] for an excellent review on measuring tunnel splittings.

Figure 3.2 shows a collection of tunnel splittings from literature [96, 110–115], with an emphasis on amino acids. While the V_3 values spans about an order of magnitude, the tunnel splitting has an enormous range: just the median tunnel splittings for the various species lie in the interval (20 kHz, 8 MHz).

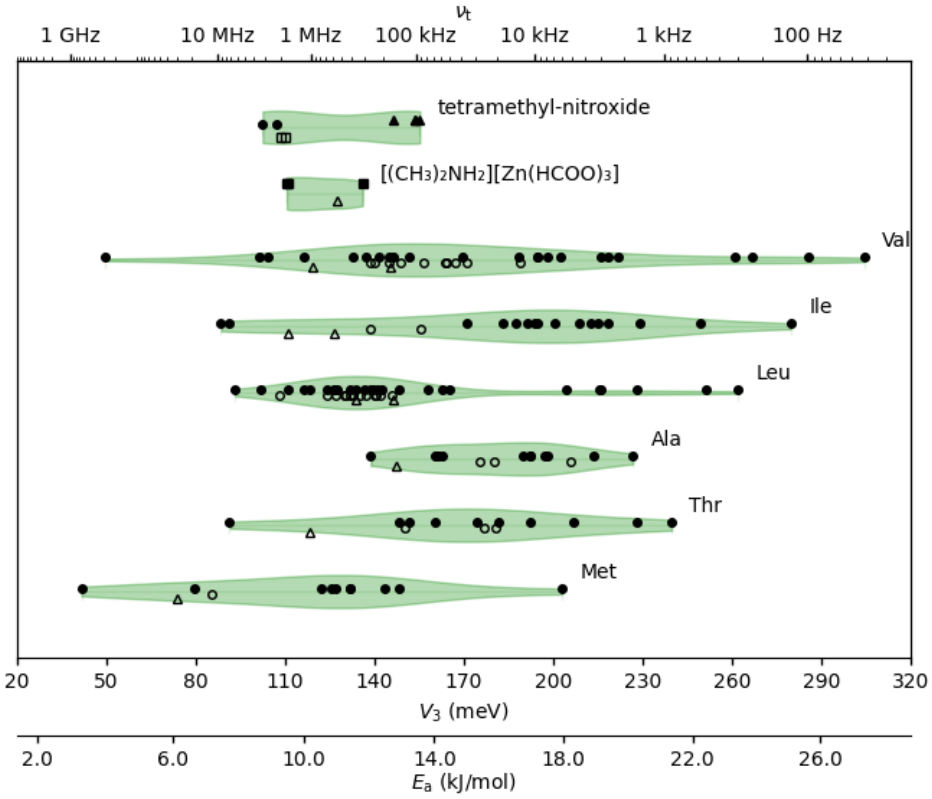

Figure 3.2: The above values for the methyl tunnel splitting come from the publications [96, 99, 100, 110–115]. The solid symbols are from fits to experimental measurements and the open symbols come from calculations. The different shapes communicate the source value: □ for tunnel splitting, △ for V_3, and ◯ for activation energy. Axes are provided for ν_t, V_3, and E_a.

In order to compare tunnel splitting values from different sources, we need a way to convert among $\hbar\omega_t$, V_3, and E_a. This requires solving the Schrödinger equation:

$$\Big(-\frac{\hbar^2}{2I_{CH_3}}\big(\frac{\partial}{\partial\chi}\big)^2 + V_3\frac{1-\cos(3\chi)}{2} - E\Big)\,|\psi\rangle = 0. \tag{3.45}$$

Here I_{CH_3} is the moment of inertia for a methyl rotor. This gives as a function of V_3, the zero-point energy,

$\frac{1}{2}\hbar\omega_0$, and the tunnel splitting. The activation energy is

$$E_\mathrm{a} = V_3 - \frac{1}{2}\hbar\omega_0(V_3), \tag{3.46}$$

This is a Mathieu equation. Mathieu equations have solutions in terms of infinite series [116–118], but as for a closed-form expression, approaches based on Feynman's path integral formalism [119] or the WKB approximation are useful [120, 121]. The ground A state and excited E states can be approximately derived via the dilute-instanton-gas method [122, 123] as

$$\begin{aligned} E_\mathrm{A} &= \frac{1}{2}\hbar\omega_0' - 2\hbar K\,\mathrm{e}^{-\frac{S_0}{\hbar}}; \\ E_\mathrm{E} &= \frac{1}{2}\hbar\omega_0' + \hbar K\,\mathrm{e}^{-\frac{S_0}{\hbar}}. \end{aligned} \tag{3.47}$$

The energies contain S_0, the action of a rotational instanton [124], the minimal action of a methyl rotor starting in one classical minimum at $t = 0$ and one of the other minima at $t = \infty$. The path itself has the methyl sitting in one minimum from $t = 0$ to $t = t_\mathrm{jump}$ at which point it quickly transitions (hence the name instanton), to the other minimum, where it stays, similar to the more classical rotational jump model [91]. The single-instanton action is

$$S_0 = \frac{8\sqrt{I_{\mathrm{CH_3}}V_3/2}}{3}. \tag{3.48}$$

There is also the normalization constant:

$$K = \sqrt{\frac{48}{\pi\hbar}}\Big(\frac{V_3^3/8}{I_{\mathrm{CH_3}}}\Big)^{\frac{1}{4}} \tag{3.49}$$

The tunnel splitting is simply the difference, $E_\mathrm{E} - E_\mathrm{A}$:

$$\begin{aligned} \omega_\mathrm{t} &= 3K\,\mathrm{e}^{-\frac{S_0}{\hbar}} \\ &= 3\sqrt{\frac{48}{\pi\hbar}}\Big(\frac{V_3^3/8}{I_{\mathrm{CH_3}}}\Big)^{\frac{1}{4}}\exp\Big(-\frac{8\sqrt{I_{\mathrm{CH_3}}V_3/2}}{3\hbar}\Big). \end{aligned} \tag{3.50}$$

As expected for tunneling phenomena, the tunnel splitting is highly dependent upon the barrier, V_3, and moment of inertia, $I_{\mathrm{CH_3}}$.

While the analytic expression may be useful for understanding trends, numeric methods are cheap and accurate enough to be better suited when precise values are desired [123]. Using a free-rotor basis, it is reasonably easy to solve the Schrödinger equation numerically [125]:

$$|n\rangle = \frac{1}{\sqrt{2\pi}}\exp\Big(\mathrm{i}n\chi\Big). \tag{3.51}$$

The kinetic energy has matrix elements

$$\langle m|\frac{-\hbar^2}{2I_{\mathrm{CH_3}}}\frac{\mathrm{d}^2}{\mathrm{d}\chi^2}|n\rangle = \frac{1}{2\pi}\int_0^{2\pi}\mathrm{d}\chi\frac{\hbar^2}{2I_{\mathrm{CH_3}}}n^2\exp\Big(\mathrm{i}(n-m)\chi\Big) = \frac{\hbar^2}{2I_{\mathrm{CH_3}}}n^2\delta_m^n \tag{3.52}$$

Here δ_m^n is the Kronecker delta symbol. And the potential energy has matrix elements

$$\begin{aligned} \langle m|V(\chi)|n\rangle &= \frac{1}{2\pi}\int_0^{2\pi}\mathrm{d}\chi\frac{V_3}{2}\Big(1-\cos(3\chi)\Big)\exp\Big(\mathrm{i}(n-m)\chi\Big) \\ &= \frac{1}{2\pi}\frac{V_3}{4}\int_0^{2\pi}\mathrm{d}\chi\Big(2\exp\Big(\mathrm{i}(n-m)\chi\Big) - \exp\Big(\mathrm{i}(n-m+3)\chi\Big) - \exp\Big(\mathrm{i}(n-m-3)\chi\Big)\Big) \\ &= \frac{V_3}{4}\Big(2\delta_m^n - \delta_{m-n}^{+3} - \delta_{m-n}^{-3}\Big). \end{aligned} \tag{3.53}$$

Diagonalizing the Hamiltonian and evaluating the difference between the lowest two eigen-energies at various V_3s creates a map between V_3 and the tunnel splitting. This and $E_a = V_3 - \frac{1}{2}\hbar\omega_0$, provide the method figure 3.2 uses to shows the published values in all three parameters ν_t, V_3, and E_a.

Figure 3.3(A) show the low-energy spectrum calculated using $I_{C^1H_3} = 5.3 \times 10^{-47}$ kg m^2 = 3.2 u Å^2, and $I_{C^2H_3} = 10.6 \times 10^{-47}$ kg m^2 = 6.4 u Å^2[125], from the 1.088 Å C–H bond length [126] and consequent H–H separation of 1.78 Å. The calculations used 77 basis vectors ($-38 \leq n \leq 38$). For the most part, only the primary energy levels are visible. The splitting between the A and E levels are barely visible near $V_3 = 0$ for the low-energy states. Figure 3.3(B) shows the tunnel splitting for both a protiated methyl group and a deuterated methyl group, calculated both numerically [125] and with the dilute-instanton-gas approximation [123]. The numeric method becomes unstable as the numeric method requires subtracting two nearly identical numbers, but where it converges the two methods are very close. Note the instanton method assumes large V_3 and so breaks down near $V_3 = 0$. Figure 3.3(C) divides the numeric tunnel splitting by the instanton approximation. The instanton approximation systematically overestimates the tunnel splitting, but even for the protiated methyl the ratio hits 0.9 around $V_3 \approx 30$ meV, and 0.95 $V_3 \approx 120$ meV.

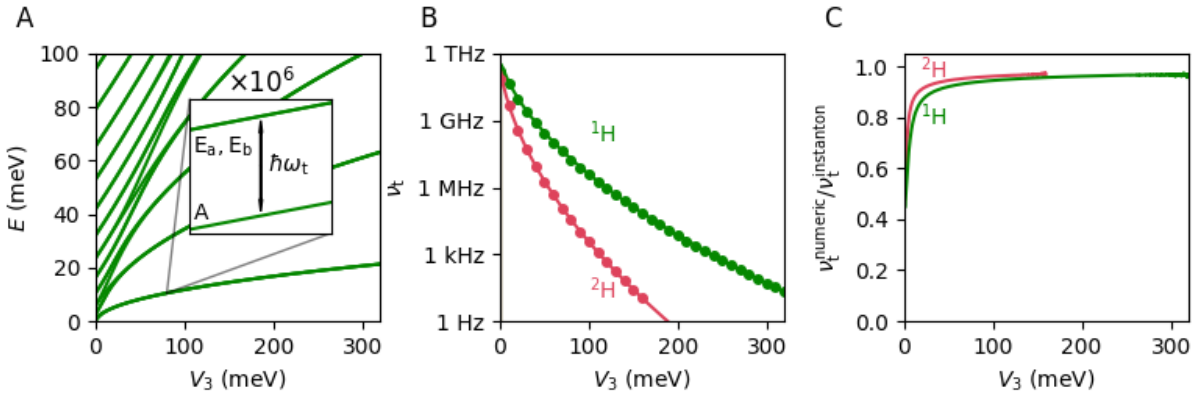

Figure 3.3: **A** shows the ^{1}H-methyl rotational spectrum vs. the barrier potential, V_3, calculated as in [125] using 77 basis states. Note that at this scale the A and E states appear nearly degenerate. **B** shows the tunnel splitting vs. V_3 for a ^{1}H-methyl rotor (green), and a ^{2}H-methyl rotor (red). The dots are the numeric difference from **A**, while the curves use the dilute-instanton-gas approximation [123]. The tunnel splitting is a small difference between large numbers, and so the numeric difference begins to become unstable at large V_3s, so the numeric calculations for the ^{2}H-methyl do not extend to as high V_3 values. **C** shows the ratio of the numeric tunnel splitting over the dilute-instanton-gas tunnel splitting.

Methyls rotors with their symmetry,
the ground's not degenerate into three.
Since quantum dynamics allow for hops,
the tunnel splitting adds extra flip-flops.
Once matrix elements are inspected,
gives a Hamiltonian projected.

Chapter 4

Glassy Matrices

Acknowledgements
This chapter details work published in [127]. All the experimental work was done by Elizabeth Canarie of the Stoll Lab, University of Washington, Seattle. The principal investigator for this work was Stefan Stoll, University of Washington, Seattle. The p_1TAM [128] was a gift from Valery V. Khramtsov and Benoit Driesschaert of the In Vivo Multifunctional Magnetic Resonance Imaging Center, West Virginia University, Morgantown. I performed the computational work for this project: the molecular dynamics, the spin dynamics simulations, and the spin contribution analysis. I also wrote CluE (see chapter 8) to implement Yang and Liu's Cluster Correlation Expansion (CCE)[1, 2].

Pulsed Electron Paramagnetic Resonance (EPR) studies on biomolecules, such as proteins, often involve attaching a stable radical, a spin label, to the biomolecule and then rapidly freezing the solution to try and immobilize the system while preserving a room temperature configuration. This means that the resulting sample is a glass, amorphous rather than crystalline. To further prevent crystal growth, glycerol ($C_3H_8O_3$) is often added. To extend coherence times, the solvents are often replaced with deuterated versions.

Due to its success in the world of qubits, Yang and Liu's Cluster Correlation Expansion (CCE)[1, 2] appeared to be a good candidate for predicting coherence times for bio-relevant systems as well; however, there are some questions that are important to address:

- Does CCE work for molecular qubits?
- Does CCE work with glassy matrices?
- How does isotope composition affect the calculations?
- Are in silico protein models accurate and diverse enough to get an accurate coherence time prediction?

Around the time of this project CCE was demonstrated to work in crystalline environments for organic radicals [46], so the first point was answered in the affirmative. This chapter will focus on the second point, by working with radicals that provide analogies to common spin labels, but lack proteins and their associated complications, to provide a good preliminary system for testing CCE in glassy environments.

The systems we will be investigating in this chapter are shown in figure 4.1. The molecule named 2,2,6,6,-tetramethylpiperidine-1-oxyl (TEMPO) is a six membered ring with a nitroxide radical; the unpaired electron resides predominately in the region between the nitrogen and oxygen atoms. The four methyl groups provide steric barriers to slow down chemical reduction of the radical. We used both h_{18}-TEMPO and d_{18}-TEMPO. We also investigated the perdeuterated trityl radical p_1TAM [128], a carbon-centered radical, again with steric protection from reduction.

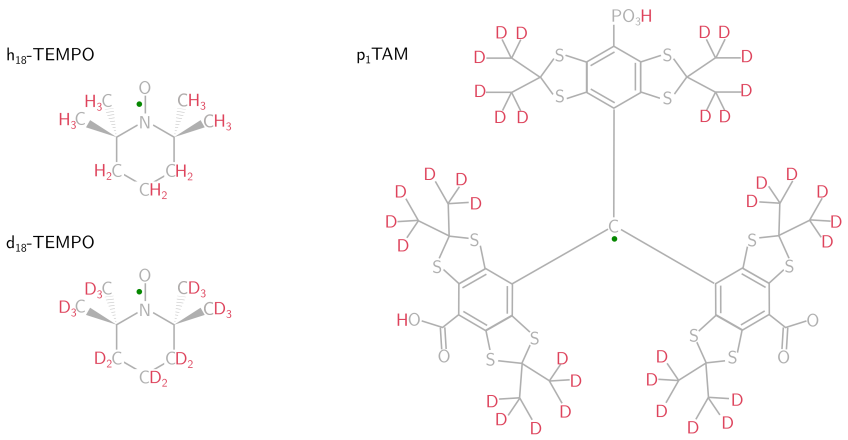

Figure 4.1: The three radicals under study are 2,2,6,6,-tetramethylpiperidine-1-oxyl (TEMPO) in both natural abundance isotopologues and deuterated isotopologues, h_{18}-TEMPO and d_{18}-TEMPO, as well as the perdeuterated trityl radical p_1TAM [128].

Experimentally, protons drive decoherence significantly faster than deuterons, so understanding spin-1/2 dominated systems is important. From a theoretical and computational perspective, the proton bath is simpler than the deuteron bath: protons do not have an electric quadrupole moment, and their spin operators have faithful 2-dimensional matrix representations rather than the minimal 3-dimensions for deuterons. For this chapter, we will stick with a protiated matrix, but we will come back to matrix deuteration in chapter 6.

We chose to use a Hahn echo experiment to measure the electron spin coherence:

$$\hat{U}_{\text{Hahn}}(2\tau) = \exp(-\frac{i\tau}{\hbar}\hat{H}_0)\hat{U}_\pi \exp(-\frac{i\tau}{\hbar}\hat{H}_0)\hat{U}_{\pi/2}, \tag{4.1}$$

where $\hat{H}_0$ is the static Hamiltonian and $\hat{U}_\theta$ is the propagator describing a θ pulse. Figure 4.2 provides a schematic diagram of the Hahn echo experiment.

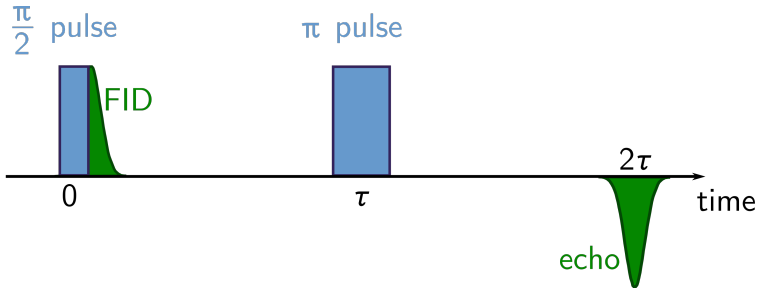

Figure 4.2: The Hahn echo experiment starts with a $\pi/2$ pulse to initialize the electrons into a non-stationary state, with expected magnetization in the x-direction, perpendicular to the applied magnetic field that defines the z-axis. The time dependencies of the electrons varies slightly within the initialized isochromat, so the ensemble expectation value $\langle \hat{S}_x \rangle \to 0$ with time, a free-induction decay (FID). At time τ, a π pulse is applied, taking the spin-up Zeeman state to the spin-down Zeeman state and vice versa while leaving the accumulated phase the same. At time 2τ, the electron, has accumulated matching positive and negative phase so $\langle \hat{S}_x \rangle$ once again increases in magnitude, but the sign is reversed because the π pulse causes a π rotation about the y-axis taking $x \to -x$.

4.1 Experimental Methods

The experiments on h_{18}-TEMPO, d_{18}-TEMPO, and p_1TAM were performed by Elizabeth Canarie. Save for some temperature scans, all the experiments were done at 20 K. The majority of the experiments used a magnetic field of about 1.2 T, and microwave irradiation at 33.8 GHz (Q-band), from a Bruker Elexsys E580 spectrometer, amplified by a 300 W TWT amplifier (Applied Systems Engineering). Samples were placed in a Bruker D2 dielectric resonator. Additionally a Hahn echo decay of d_{18}-TEMPO was also performed at an applied magnetic field of about 0.34 T, and a microwave irradiation at 9.6 GHz (X-band), amplified by a 1 kW TWT amplifier (Applied Systems Engineering) and directed into a Bruker MD4 dielectric resonator. Echo-detected field sweeps were used to determine the magnetic field that would maximize the signal to noise ratio, while keeping dispersion low. Spin flip angles were set by varying the pulse lengths (table 4.1), and calibrated by Rabi oscillation experiments. Table 4.1 lists the Hahn echo parameters: duration of the $\pi/2$-pulse ($t_{\frac{\pi}{2}}$), duration of the π-pulse (t_π), and minimum value of τ used.

	$t_{\frac{\pi}{2}}$ (ns)	t_π (ns)	min(τ) (ns)
h_{18}-TEMPO	26	52	200
d_{18}-TEMPO	10	20	250
p_1TAM	14	28	250
d_{18}-TEMPO (X-band)	14	28	400

Table 4.1: Experimental time parameters: $\pi/2$ pulse length, π pulse length, minimum τ used.

The T_1 time was estimated to be on the order of a second by varying the shot repetition time until there were no observable changes to the echo amplitude; this occurred roughly in the range of $[0.7, 1]$s for typical samples and $[0.12, 5]$ s for the 5 µM d_{18}-TEMPO samples.

4.2 Molecular Dynamics

To model the systems we used an approach similar to [129], a TEMPO molecule and a p_1TAM molecule were built in Avogadro [130], and then geometry optimized with ORCA 4.01 [131, 132] using the SV(P) basis and B3LYP functional. CHARMM-GUI [133] was used to build Gromacs [134] topology files for paramagnetic version of the molecules. To account for the radical species, charge distributions, generated with CHELPG (CHarges from ELectrostatic Potentials using a Grid-based method), were substituted in for the ones generated for the paramagnetic analog. Next, Gromacs was used to solvate the molecules with 5183 and 2717 waters, for TEMPO and p_1TAM respectively. Glycerols were not included in the Molecular Dynamics (MD). Since the hydron concentration of water–glycerol solutions differs very little from that of pure water[135], the error introduced is expected to be small. Figure 4.3 shows [H] against the water:glycerol ratio expressed as a mass percent glycerol.

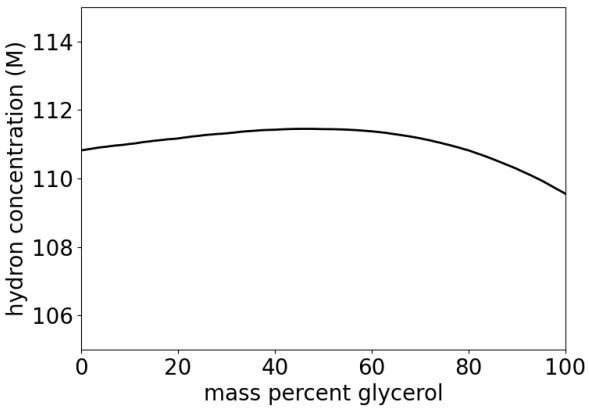

Figure 4.3: The data for this plot comes from [135], and shows the hydron concentration vs. the mass percent of the water–glycerol solution that glycerol comprises. Note the narrow molarity range on the ordinate, and that [H] is fairly constant throughout.

The molecular dynamics simulations used the CHARMM36 force field [136]. For long-range electrostatic couplings, we used the particle mesh Ewald method. To pre-equlibrate the system, after an energy minimization step, the systems were evolved at NVT and then NPT conditions for 100 ps each in 2 fs steps. For the production runs, following Lerbret and Affouard [137], the systems were propagated at 300 K for 100 ns in 1 fs steps and then the temperature was instantly dropped to 100 K for 5 ns. The final MD frame was used as the structure for the spin dynamics simulation.

4.3 Quantum Spin Dynamics

To model the spin physics, the following theory was used:

$$\begin{aligned}\hat{H}(m_{\mathrm{S}}) = \; & -(-g\mu_{\mathrm{B}})B_0 m_{\mathrm{S}}(t) \\ & + \sum_{n}^{N}\left(-\mu_{\mathrm{N}} g_n B_0 \hat{I}_{z\,n} + m_{\mathrm{S}}(t)(\hat{\boldsymbol{z}}^{\mathrm{T}}\boldsymbol{A}_n)\hat{\boldsymbol{I}}_n + \hat{\boldsymbol{I}}_n^{\mathrm{T}}\boldsymbol{P}_n\hat{\boldsymbol{I}}_n\right) \\ & + \sum_{\substack{m,n \\ m<n}}^{N} \delta_{g_n,g_m}\hat{\boldsymbol{I}}_m^{\mathrm{T}}\boldsymbol{b}_{mn}\hat{\boldsymbol{I}}_n.\end{aligned} \tag{4.2}$$

The right-hand side of the first line contains the electron Zeeman coupling in the $m_{\mathrm{S}}(t)$ spin manifold. The time dependence of m_{S} is assumed to come entirely from the microwave pulses. The second line contains all the single nuclear spin terms: the nuclear Zeeman interaction, the hyperfine coupling, and the nuclear electric quadrupole interactions. The quadrupole couplings apply only to spin-1 and up particle, deuterons and the nitrogen. In addition to the secular $\hat{S}_z\hat{I}_z$ hyperfine terms, the $\hat{S}_z\hat{I}_\pm$ pseudosecular hyperfine terms are also kept, but the terms involving $\hat{S}_\pm$ are dropped because they do not conserves Zeeman energy and so do not contribute much at high applied magnetic fields. The advantage from dropping them is that the time-independent part of the Hamiltonian commutes with $\hat{S}_z$. This means that each electron spin Zeeman state can be evolved separately, and the simpler Hamiltonian, $\hat{H}(m_{\mathrm{S}}) := \langle m_{\mathrm{S}}|\hat{H}|m_{\mathrm{S}}\rangle$, can be used instead of including the electron spin degree of freedom as in $\hat{H}$. The third line describes the nucleus–nucleus coupling; the δ_{g_n,g_m} reflects the approximation that Zeeman energy is conserved and helps with computational efficiency by removing interactions that are not likely to be significant. Save for the ^{14}N on TEMPO, coupling tensors between spin pairs are treated as point-dipoles. The ^{14}N hyperfine coupling is taken as [-13.9, -13.9, 122.3] MHz. The ^{14}N also has an electric quadrupole moment of $\frac{e^2qQ}{h} = 3.5$ MHz and $\eta = 0.68$ [138]. The other particles with an electric quadrupole moment are the deuterons. To get the quadrupole coupling parameters

for d_8-TEMPO, the geometry optimized structure for h_8-TEMPO was used a starting point, and from ORCA, $\frac{e^2qQ}{h} = 194.5$ kHz and $\eta = 0.02$. Additionally, these values were assumed for all CD deuterons.

Several cutoffs were imposed on the CCE simulations: a system radius, a neighbor cutoff, and an orientation averaging grid cutoff. The system radius describes the maximum distance from the central spin that a spin can be without being dropped from consideration. The neighbor cutoff is used for clusterization: clusters must be connected graphs where vertices are bath spins and edges are decided by the neighbor cutoff. Here, the neighbor cutoff is a threshold on the magnitude of the perpendicular dipole–dipole coupling. Note that this is equivalent to distance-based neighbor cutoff. The advantage of an orientation independent neighbor cutoff rather than the full dipole–dipole coupling directly is that the clusters from different orientations will be the same. The orientation averaging is necessary because the system is amorphous and so the orientation of each radical, with respect to the applied magnetic field, is uncorrelated with the other radicals. The orientation grid cutoff is the number of distinct orientations used to approximate the system. For this, a Lebedev grid was used [139]. To ensure an appropriate cutoff, the system radius was incremented in steps of 1 Å or the neighbor coupling cutoff was lowered by a factor of $10^{0.2}$ until the T_{M} from any further steps satisfied $\frac{|T_{\mathrm{M}i+1} - T_{\mathrm{M}i}|}{T_{\mathrm{M}i+1}} < 10^{-3}$. Next the converged single-orientation parameters were used for sequential Lebedev grid sizes {6, 14, 26, 38, ...}, until the same criterion was met. Table 4.2 shows the converged parameters.

system	system radius (Å)	neighbor cutoff (Hz)	orientations	spins	2-clusters
h_{18}-TEMPO	17	100	170	1,442	165,750
d_{18}-TEMPO	15	630	170	996	20,607
p_1TAM	19	100	14	1,934	213,068
d_{18}-TEMPO (X-band)	17	63	74	1442	231,754

Table 4.2: Simulation Parameters

4.4 Results and Discussion

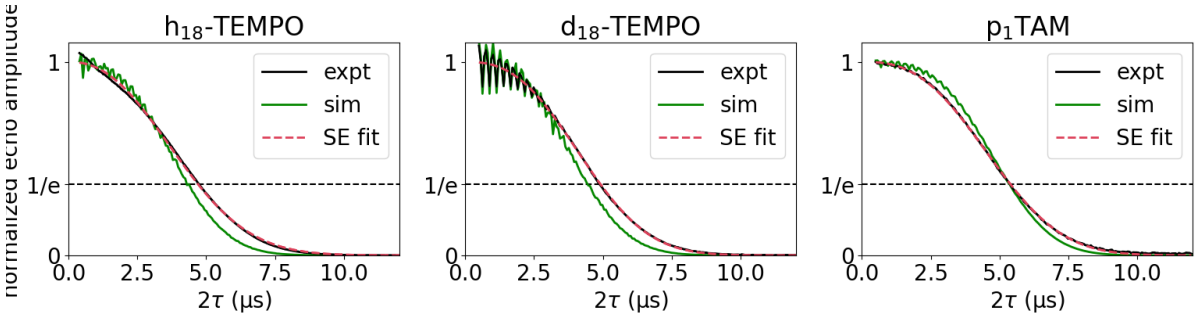

Figure 4.4: The Q-band experimental data are shown in black, the simulations in green, and the stretched exponential fits to the experiments are shown in red. From left to right the data (with experiment fit parameters) are for 200 μM h_{18}-TEMPO (T_M = 4.7 μs, ξ = 2.3), 100 μM d_{18}-TEMPO (T_M = 4.9 μs, ξ = 2.6), and 10 μM p_1TAM (T_M = 5.4 μs, ξ = 2.7).

The converged orientation-averaged CCE simulations along with the experimental data are shown in figure 4.4. The CCE simulations well predict the decoherence behaviors both in timescale and shape. Note that due to spectrometer limitations the earliest 2τ exceeds zero by several hundred nanoseconds (see table 4.1), and as a consequence the relative scaling of the experimental data is unclear. For this reason, the simulations were scaled to match at the earliest experimental time point. The simulations even capture the ESEEM modulations from d_{18}-TEMPO's deuterons [13, 140, 141].

A parametric way to compare the experiments to the simulations is to fit them to stretched exponentials:

$$V_{\mathrm{SE}}(2\tau) = V_0 \exp\Big(-(2\tau/T_{\mathrm{M}})^{\xi}\Big), \tag{4.3}$$

and to compare the fitted T_M and ξ. While the stretched-exponential description is generally good, h_{18}-TEMPO in particular deviates from the SE form at early times. There is precedence in the literature to account for this deviations from a single stretched exponential by using a sum of stretched exponentials (SSE)[44]:

$$V_{\mathrm{SSE}}(2\tau) = \sum_n V_n \exp\Big(-(2\tau/T_{\mathrm{M}n})^{\xi_n}\Big). \tag{4.4}$$

On one hand, the multiple stretched exponentials can be viewed as a fitting basis, and while the fit parameters may be informative toward the system, each stretched exponential does not directly mimic a physical process. On the other hand, if trying to assign a physical process to each stretched exponential, this description suggests multiple populations of central spins, each with a different primary decoherence pathway. Another possible assumption is to assume multiple independent pathways all operating on one population. This would give a product of stretched exponentials (PSE).

$$V_{\mathrm{PSE}}(2\tau) = V_0 \prod_n \exp\Big(-(2\tau/T_{\mathrm{M}n})^{\xi_n}\Big). \tag{4.5}$$

The PSE description can equally be thought of as just a fitting basis: $\ln(V_{\mathrm{PSE}}(2\tau)/V_0) = -\sum_n (2\tau/T_{\mathrm{M}n})^{\xi_n}$.

Figure 4.5 shows the fitted T_Ms and ξs for a stretched exponential (SE). For the experimental h_{18}-TEMPO Hahn echo decays, where there is a clear deviation from the stretched exponential, both SSE and PSE fit parameters are included as well. The general trend is that the simulations predict a slightly faster and more stretched decay than what the experiments see. In the case of h_{18}-TEMPO, the SE experimental fit matches the timescale the best, while the SSE and PSE fits match the stretch parameter the best, and are more similar to each other than either is to the SE fit.

Both the SSE and PSE fits also find a faster decay with stretching parameter under one. This is a notable failure of the CCE simulations for h_{18}-TEMPO. This is likely due to methyl tunneling: the three protons of

the methyl group have low masses, so even at temperatures low enough for the methyl group to be classically frozen, the protons can undergo coordinated tunneling, rotating the methyl group and redistributing the magnetic spins [60, 61]. This theory behind this phenomenon was discussed in chapter 3, and simulations including it will be shown in chapter 7.

Figure 4.6 shows the experimental h_{18}-TEMPO Hahn echo decay along with each of the three fits: a single stretched exponential, the sum of two stretched exponentials, and the product of two stretched exponentials. While the SE fit fails to follow the early-time behavior that both SSE and PSE capture, they all agree that there is a sub-Gaussian stretched exponential with a timescale of about 5 µs. This is the component that the CCE simulations predict and can be attributed to nucleus–nucleus flip-flops with unequal hyperfine coupling.

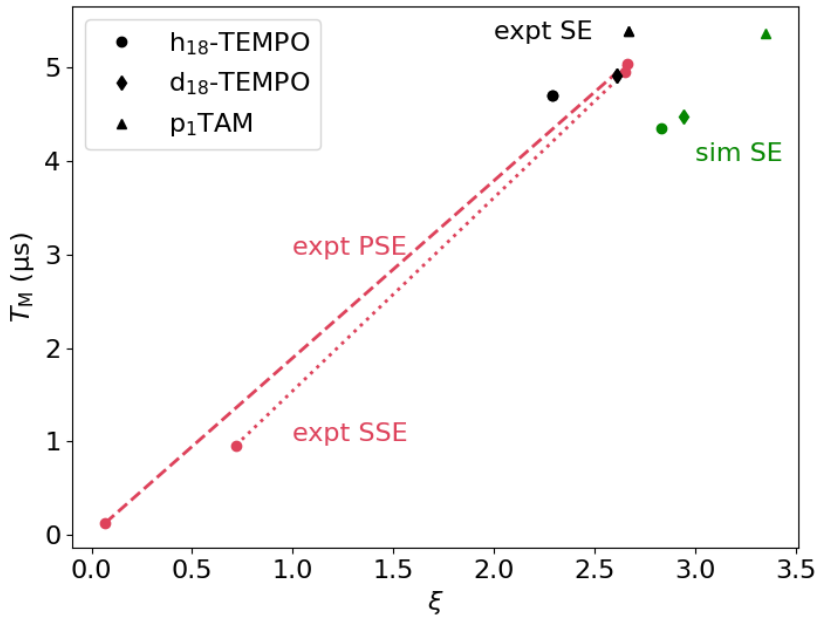

Figure 4.5: This figure shows the T_M and ξ parameters for stretched exponential (SE) fit to the experimental data (black) and the simulations (green), for h_{18}-TEMPO (circles), d_{18}-TEMPO (diamonds), and p_1TAM (triangles). The h_{18}-TEMPO experiments also have been fit with sum of two stretched exponentials (SSE), and a product of two stretched exponentials (PSE); these are shown in red connected with a dotted and dashed line respectfully to indicate they are part of the same fit.

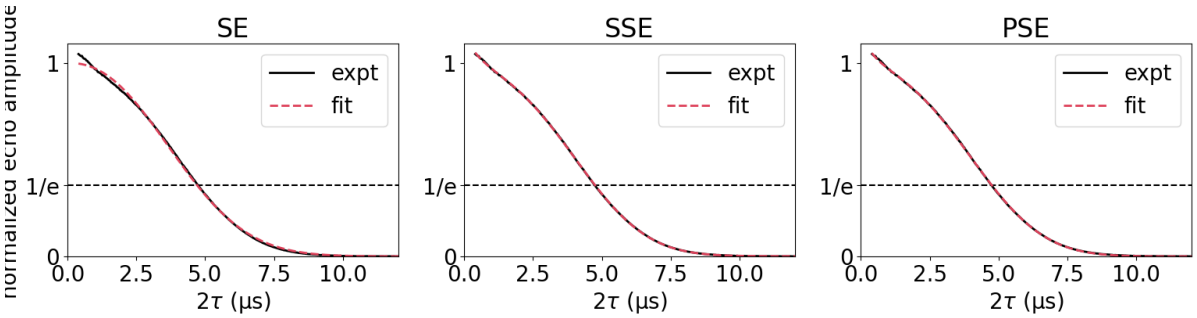

Figure 4.6: This figure shows the experimental h_{18}-TEMPO Hahn echo decay (black) with different fits (red): a stretched exponential (SE) fit (left), a sum of two stretched exponentials (SSE) fit (middle), and a product of two stretched exponentials (PSE) fit (right). Both the SSE and PSE fits are able to reproduce the early time deviations from a stretched exponential.

X-Band

All these experiments were performed at Q-band ($\approx$ 1.2 T), so to test other magnetic fields, one of the samples, d_{18}-TEMPO, was also used in an X-band experiment (0.34 T). Figure 4.7 shows the X-band data for both the experiment and simulation. Again, the simulation predicts the coherence decay reasonably well, including the deuterium ESEEM.

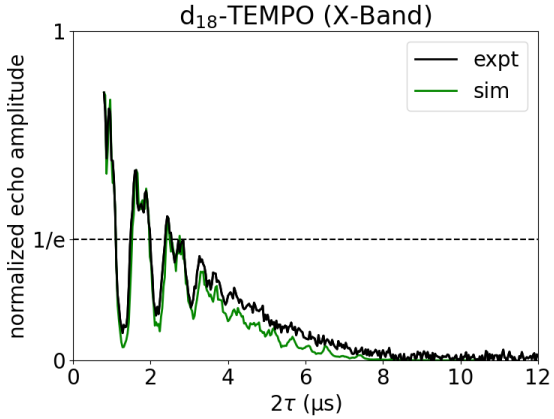

Figure 4.7: The experimental Hahn echo decay for 10 μM d_{18}-TEMPO in a 1:1 mass:mass water:glycerol solution is show in black and the simulated Hahn echo decay (without glycerol) is shown in green.

Now that confidence in the CCE simulations has been established by the experiment, the in silico nature of the simulations can be used to further investigate the mechanisms involved in the central spin decoherence. Since every orientation has the same set of clusters, each cluster, or spin can be assigned a contribution to the central spin decoherence. Given that the system contains N-spins, by removing from the CCE product, every cluster that contains spin n, the overall coherence time for this $(N-1)$-spin system is extended a small amount, as compared to the original N-spin system. Figure 4.8 illustrates the ΔT_{M} definition. Since each nuclear spin can be assigned a ΔT_{M}, this can be used to quantify how much each spin contributes to the overall decoherence rate. It is important to note that these contributions are not additive.

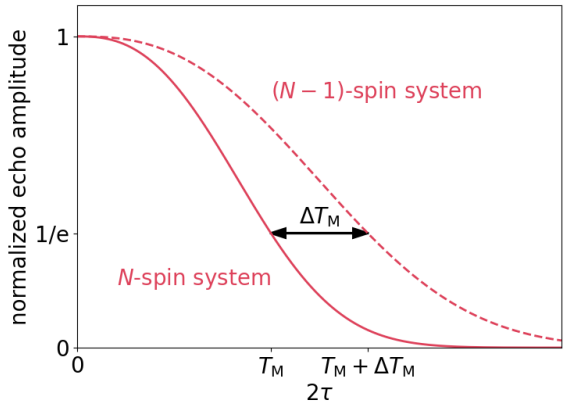

Figure 4.8: This not-to-scale schematic illustrates the ΔT_{M} definition: using the full simulation as a reference, the system is resimulated without a particular nuclear spin. All the clusters that spin was part of can no longer be formed and the echo decay is slightly lengthened. Since a typical ΔT_{M} is on the order of nanoseconds and T_{M} is on the µs scale, the above is greatly exaggerated for visual clarity.

Figure 4.9(top) shows these contributions, as colored atoms in a Pymol rendering of the PDB files. The approximate location of the radical electron is indicated in green. Qualitatively, most protons only contribute a small amount to the total decoherence; however, there is a shell around the central spin where the hydrons contribute more. This observation is made more quantitative in figure 4.9(bottom), where the same coloring is used with the corresponding values indicated on the left ordinate. The abscissa is the distance from the central electron. The hydrons that contribute the most have ΔT_{M}s on the order of tens of nanoseconds and are in the in distance range of 4–8 Å away from the unpaired electron. The nuclei closer than this are in the "spin diffusion barrier", which is attributed to the strong hyperfine coupling here. The literature values for the spin diffusion barrier vary: 7–10 Å[22, 26], 4–6.6 Å[142], and <6 Å[143], but are all greater than the 4 Å found here. [144, 145] The discrepancy likely comes from measuring polarization transfer vs. electron spin decoherence. Additionally, the spins beyond about 8 Å are more weakly coupled to the central electron spin, which make sense in light of the inverse cubic relationship between hyperfine coupling strength and separation. These qualities are displayed by all three radicals, but there are also differences in their ΔT_{M} profiles, notably in the 2–4 Å region. The d_{18}-TEMPO sample has spins that contribute more than the h_{18}-TEMPO in this region, whereas p_1TAM has none. Referring to the structures (figure 4.1), p_1TAM, has no hydrons in 2–4 Å region, while d_{18}-TEMPO has deuterons instead of the protons of h_{18}-TEMPO, suggesting it is the ESEEM modulations (seen in figure 4.4) that are responsible for the larger ΔT_{M}. Although the oscillations are damped significantly by $2\tau = T_{\mathrm{M}}$, the fact that these oscillation are visible in the trace at all suggests that they are individually stronger than any of nucleus–nucleus flip-flop driven oscillations.

Figure 4.9 also shows in red, the T_{M} resulting from only including the spins within the distance indicated on the abscissa; the T_{M} flattens out by about 12 Å. Even through the number of protons at a distance r from the electron roughly scales as r^2, the average contribution falls off fast enough for the T_{M} to primarily set by the protons within 12 Å of the lone electron.

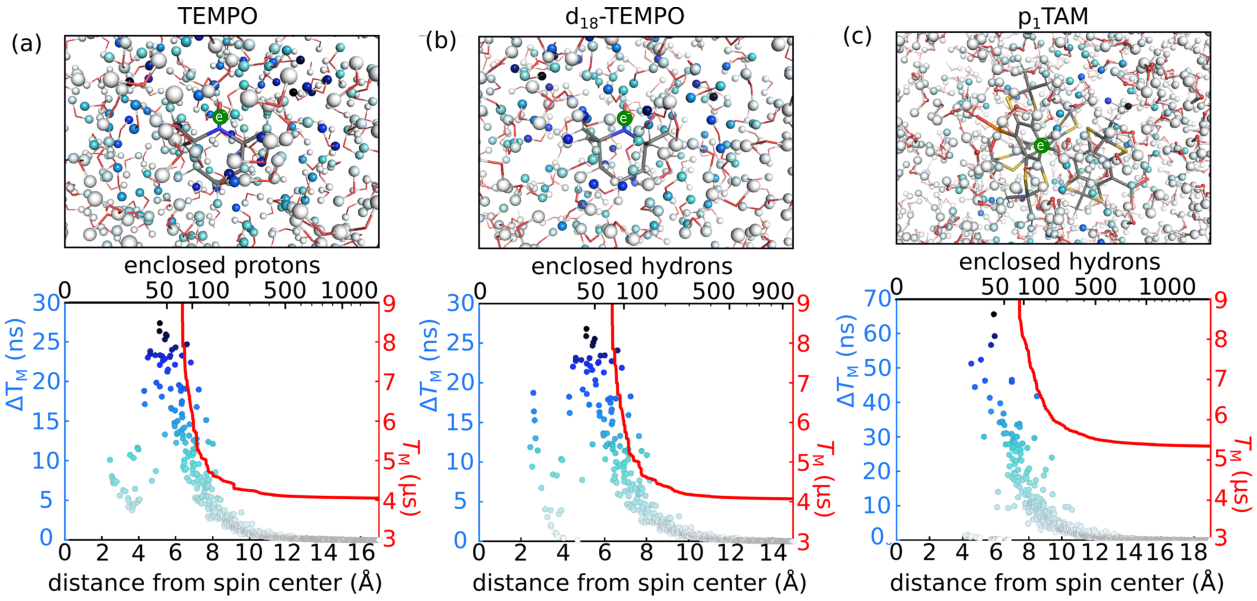

Figure 4.9: Columns **(a)**, **(b)**, and **(C)**, refer to h_{18}-TEMPO, d_{18}-TEMPO, and p_1TAM respectively. The top row shows rendering of the molecule's PDB colored according to how much each spin affects the T_M. The green dot indicates where the unpaired electron approximately located, The bottom row plots ΔT_M vs the distance to the central spin on the left ordinate, which also serves to translate the colors to values. On the right ordinate, the T_M from including only the spins within the distance on the abscissa. The top abscissa indicate the number of hydrons eclosed with the distance on the bottom abscissa.

4.5 Conclusion

The CCE method works well for glassy matrices when combined with MD to generate a structure. Even for systems like h_{18}-TEMPO where methyl group tunneling effects are visible, the dominant part of the Hahn echo decay envelope can be captured with just pairwise flip-flops. Deuterium ESEEM modulations are also reproduced by the CCE simulations. The spin diffusion barrier is observed in silico up to about 4 Å. Within this distance ESEEM still influences the signal, but the protons primary driving decoherence are in the 4–8 Å, after which the contributions are minimal and level off significantly by about 12 Å. This demonstrates that beyond predicting the coherence decay, CCE on glassy matrices can be used to gain physical insights.

Radicals within glassy matrices,
predicting their behavior is no breeze.
With experimental validation,
trust can be found in calculation.
Which spins have the largest ΔT_M
Ångströms, within four to twelve, it is them.

Chapter 5

Glassy Matrices: Refocused Echo

Acknowledgements
This chapter details work done in [146] in collaboration with Thorsten Bahrenberg, Akiva Feintuch and Daniella Goldfarb of the Department of Chemical and Biological Physics, Weizmann Institute of Science, Rehovot, Israel, who did all the experimental work. I ran the Molecular Dynamics (MD), Cluster Correlation Expansion (CCE)[1, 2], and Linked Cluster Expansion (LCE)[35] on 3-maleimido-proxyl, and evaluated the lowest order flip-flop diagram for the refocused echo.

So far we have been focused on the Hahn echo. This is useful because the Hahn echo is a minimal experiment for exploring nucleus–nucleus flip-flop driven electron spin decoherence; however, the coherence time depends on the pulse sequence used, and not just the system [22, 44, 46]. From the perspective of applications to the pump–probe experiment Double Electron-Electron Resonance (DEER), the Hahn echo is the probe sequence for three-pulse DEER [15, 16], whereas four-pulse DEER is the predominately used version, since it is does not have a dead time [147, 148]. There are even higher pulse count versions of DEER [149, 150], but these are less frequently employed due to the added complexity [151]. The Hahn echo sequence has one delay parameter, τ. This is the delay before the FID coherence loss is reversed with a π-pulse, forming an echo of the FID at time 2τ; however, this echo too can be refocused with another π-pulse. This is the refocused echo experiment. The refocused echo sequence has two delay parameters τ_1 and τ_2. The refocused echo sequence serves as the probe sequence for the pump–probe experiment four-pulse DEER. With the notation that $\hat{H}_0$ is the time-independent part of the spin Hamiltonian, and $\hat{U}_\theta$ is the propagator for a θ pulse, the refocused echo experiment is described by

$$\hat{U}_{\mathrm{RE}}(2\tau_1, 2\tau_2) = \exp(-\frac{\mathrm{i}\tau_2}{\hbar}\hat{H}_0)\hat{U}_\pi \exp(-\frac{\mathrm{i}\tau_2}{\hbar}\hat{H}_0) \exp(-\frac{\mathrm{i}\tau_1}{\hbar}\hat{H}_0)\hat{U}_\pi \exp(-\frac{\mathrm{i}\tau_1}{\hbar}\hat{H}_0)\hat{U}_{\pi/2}. \tag{5.1}$$

Schematically, figure 5.1 depicts the refocused echo.

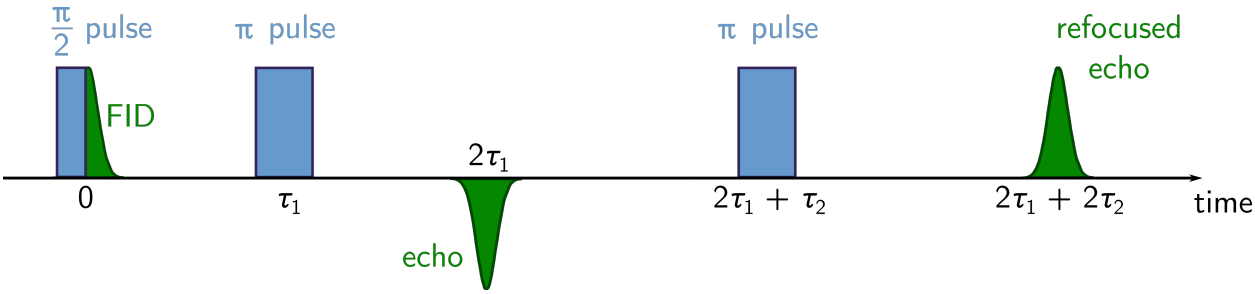

Figure 5.1: The refocused echo starts out with a Hahn echo sequence ($\pi/2$ initialization pulse—τ_1 delay—π pulse—τ_1 delay), but then applies another π pulse τ_2 after the first echo, and as the first π pulse refocuses the FID, the second π pulse, refocuses the echo at time $2\tau_1 + 2\tau_2$.

As before, assuming $\langle m'_{\mathrm{S}}|\hat{H}_0|m_{\mathrm{S}}\rangle \approx 0$, for $m'_{\mathrm{S}} \neq m_{\mathrm{S}}$, allows us to define $\hat{H}(m_{\mathrm{S}}) := \langle m_{\mathrm{S}}|\hat{H}|m_{\mathrm{S}}\rangle$. The time evolution operator for the refocused echo is then

$$\begin{aligned}\hat{U}_{\mathrm{RE}}(m_{\mathrm{S}} = \pm\frac{1}{2}, 2\tau_1, 2\tau_2) = &\ \exp(-\frac{\mathrm{i}\tau_2}{\hbar}\hat{H}(\pm\frac{1}{2}))\exp(-\frac{\mathrm{i}\tau_2}{\hbar}\hat{H}(\mp\frac{1}{2}))\exp(-\frac{\mathrm{i}\tau_1}{\hbar}\hat{H}(\mp\frac{1}{2}))\exp(-\frac{\mathrm{i}\tau_1}{\hbar}\hat{H}(\pm\frac{1}{2})) \\ =: &\ \hat{U}_2^{(\pm)}\hat{U}_2^{(\mp)}\hat{U}_1^{(\mp)}\hat{U}_1^{(\pm)},\end{aligned} \tag{5.2}$$

where $\hat{U}_i^{(\pm)} := \exp(-\frac{\mathrm{i}\tau_i}{\hbar}\hat{H}(\pm\frac{1}{2}))$. In the Heisenberg picture

$$\hat{S}_+(2\tau_1, 2\tau_2) = \hat{U}_{\mathrm{RE}}(+\frac{1}{2}, 2\tau_1, 2\tau_2)^\dagger \hat{U}_{\mathrm{RE}}(-\frac{1}{2}, 2\tau_1, 2\tau_2). \tag{5.3}$$

The normalized signal for the 2D refocused echo is

$$\begin{aligned}v_{\mathrm{RE}}(2\tau_1, 2\tau_2) = &\ \frac{1}{Z}\mathrm{tr}\Big(\hat{\rho}^{(-+)}\hat{S}_+(2\tau_1, 2\tau_2)\Big) \\ = &\ \frac{1}{Z}\mathrm{tr}\Big(\hat{\rho}^{(-+)}\hat{U}_1^{(+)\dagger}\hat{U}_1^{(-)\dagger}\hat{U}_2^{(-)\dagger}\hat{U}_2^{(+)\dagger}\hat{U}_2^{(-)}\hat{U}_2^{(+)}\hat{U}_1^{(+)}\hat{U}_1^{(-)}\Big).\end{aligned} \tag{5.4}$$

In the high-temperature limit where $\hat{\rho}^{(-+)}$ is approximately proportional to the identity, the refocused echo is symmetric upon switching $2\tau_1$ and $2\tau_2$. To show this, it is helpful to first define $\hat{u}_i^{(\pm)} := \hat{U}_i^{(\mp)\dagger}\hat{U}_i^{(\pm)\dagger}\hat{U}_i^{(\mp)}\hat{U}_i^{(\pm)}$.

$$\begin{aligned}v_{\mathrm{RE}}(2\tau_1, 2\tau_2) &= \frac{1}{Z}\mathrm{tr}\Big(\hat{U}_1^{(+)\dagger}\hat{U}_1^{(-)\dagger}\hat{U}_2^{(-)\dagger}\hat{U}_2^{(+)\dagger}\hat{U}_2^{(-)}\hat{U}_2^{(+)}\hat{U}_1^{(+)}\hat{U}_1^{(-)}\Big) \\ &= \frac{1}{Z}\mathrm{tr}\Big(\hat{U}_1^{(+)\dagger}\hat{U}_1^{(-)\dagger}\hat{u}_2^{(+)}\hat{U}_1^{(+)}\hat{U}_1^{(-)}\Big) \\ &= \frac{1}{Z}\mathrm{tr}\Big(\hat{u}_2^{(+)}\hat{U}_1^{(+)}\hat{U}_1^{(-)}\hat{U}_1^{(+)\dagger}\hat{U}_1^{(-)\dagger}\Big) \\ &= \mathrm{tr}\Big(\hat{u}_2^{(+)}\hat{u}_1^{(+)\dagger}\Big).\end{aligned} \tag{5.5}$$

The trace can be expanded and the complex conjugations pushed around to give

$$\begin{aligned}v_{\mathrm{RE}}(2\tau_1, 2\tau_2) &= \frac{1}{Z}\sum_{i,j}\big(\hat{u}_2^{(+)}\big)_{ij}\big(\hat{u}_1^{(+)\dagger}\big)_{ji} \\ &= \frac{1}{Z}\sum_{i,j}\big(\hat{u}_2^{(+)}\big)_{ij}\big(\hat{u}_1^{(+)}\big)^*_{ij} \\ &= \frac{1}{Z}\sum_{i,j}\Big(\big(\hat{u}_2^{(+)}\big)^*_{ij}\big(\hat{u}_1^{(+)}\big)_{ij}\Big)^* \\ &= \frac{1}{Z}\sum_{i,j}\Big(\big(\hat{u}_2^{(+)\dagger}\big)_{ji}\big(\hat{u}_1^{(+)}\big)_{ij}\Big)^* \\ &= v_{\mathrm{RE}}(2\tau_2, 2\tau_1)^*.\end{aligned} \tag{5.6}$$

So the real part of $v_{\mathrm{RE}}(2\tau_1, 2\tau_2)$ is unchanged by switching the values of τ_1 and τ_2, while the imaginary part changes sign.

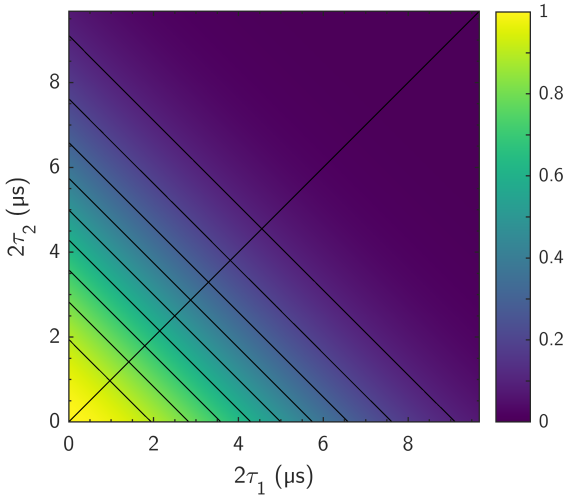

Figure 5.2: The above decay is a mock decay, showing a monotonic decrease in coherence with total time. The two axes are $2\tau_1$ and $2\tau_2$, which corresponds to a total experiment time of $T = 2\tau_1 + 2\tau_2$. The color represents the normalized amplitude of the refocused echo. The contour lines follow constant amplitude paths. Specifically the plot shows $v(T) = \exp\Big(-(T/6\ \mu\text{s})^2\Big)$.

Beyond the symmetry of $v_{\text{RE}}(2\tau_1, 2\tau_2)$ when $2\tau_1$ and $2\tau_2$ are swapped, the behavior of the echo amplitude as a function of $2\tau_1$ and $2\tau_2$ is unclear. A naive initial guess is that the refocused echo amplitude depends only on the total evolution time, $T = 2\tau_1 + 2\tau_2$, and not on $2\tau_1$ or $2\tau_2$ individually. This guess is shown in figure 5.2, and seems reasonable from an entropic perspective; however there is more to the story. Firstly, when $2\tau_1 = 2\tau_2$, the refocused echo sequence is a two-π-pulse Carr–Purcell (CP-2) sequence, which is known to increase the coherence time [152, 153]. The n π-pulse sequences, CP-n, follow a similar scheme: they keep applying π-pulses to recover the echo from the previous pulses, but they tend to be one delay parameter sequences, since the π-pulses are evenly spaced throughout the experiment. Here we will be examining the 2D refocused echo, and exploring how it intersects the 1D CP experiment.

5.1 3-Maleimido-Proxyl

The primary system we will be studying is 3-maleimido-proxyl in 4:1 volume:volume water:glycerol as depected in figure 5.3.

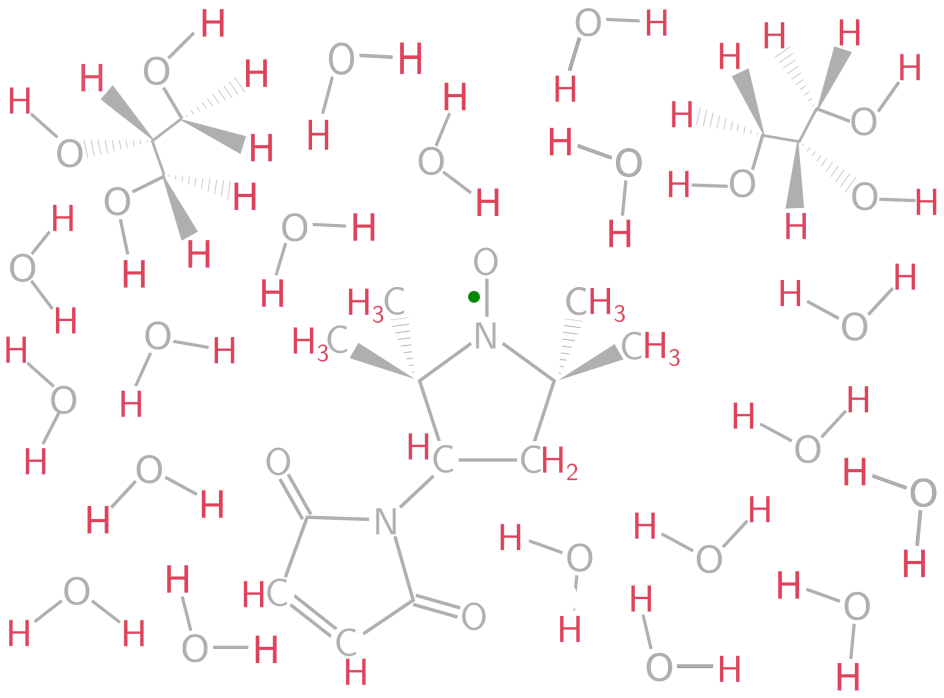

Figure 5.3: The above cartoon shows the Lewis structure of 3-maleimido-proxyl, solvated by water and glycerol. The hydrogens are colored red, and the electron is shown as a green dot.

5.1.1 Experimental Methods

The 25 K 3-maleimido-proxyl experiments were performed by Thorsten Bahrenberg, Akiva Feintuch, and Daniella Goldfarb with their home-built 94.9 GHz (W-band) spectrometer [154, 155]. The $\frac{\pi}{2}$-pulses were 25 ns or 20 ns, and the π-pulses were twice that at 50 ns or 40 ns. The shot repetition time was 20 ms.

Figure 5.4(A) shows the 2D refocused Hahn echo experiments for 3-maleimido-proxyl. Unlike the mock data of figure 5.2, the real data shows Carr–Purcell behavior, where along a line of constant evolution time, $T = 2\tau_1 + 2\tau_2$, the echo amplitude is maximized when $2\tau_1 = 2\tau_2$. While the echo amplitude should be symmetric in $2\tau_1$ and $2\tau_2$, the two parameters are used differently in DEER. The choice of $2\tau_2$ is typically made by looking at the expected distance between the spin labels and ensuring $2\tau_2$ is long enough to measure the echo modulations. Next, $2\tau_1$ is set to maximize the echo amplitude. Figure 5.4(B) shows the 3-maleimido-proxyl refocused echo data again, but normalized slice-wise by $2\tau_2$: for every value of $2\tau_2$, the echo amplitude $v(2\tau_1, 2\tau_2)$ is scaled such that the maximum along that $2\tau_2$–slice is one. This requires that the normalization constant becomes a function of $2\tau_2$:

$$v_{\text{sw}}(2\tau_1, 2\tau_2) = \frac{v(2\tau_1, 2\tau_2)}{N(2\tau_2)}. \tag{5.7}$$

Figure 5.4(A,B) shows the optimal $2\tau_1$ for a given $2\tau_2$ as a red line, and figure 5.4(A) also includes the optimal τ_2 for a given τ_1. Note that the $2\tau_1$ that maximizes electron spin coherence for a given $2\tau_2$ is neither $2\tau_1 = 0$ which would minimize the total evolution time, nor $2\tau_1 = 2\tau_2$ which are Carri–Purcell conditions. To better understand this, we will look at numerical simulations in the next section.

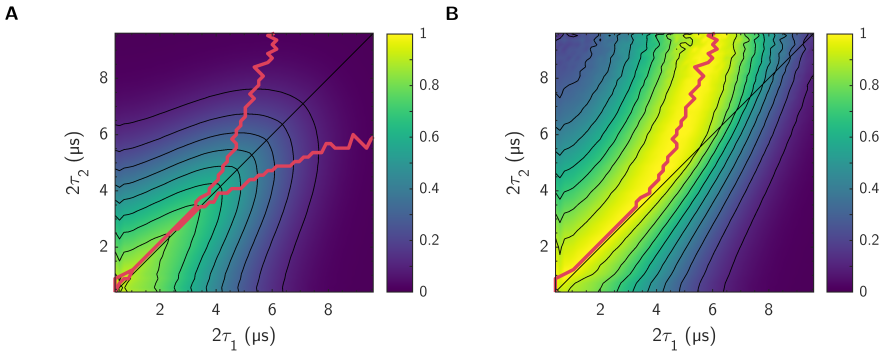

Figure 5.4: **A** plots the 3-maleimido-proxyl in 4:1 volume-volume water:glycerol refocused Hahn echo data vs. $2\tau_1$ and $2\tau_2$; the total evolution time is $T = 2\tau_1 + 2\tau_2$. The color–axis indicates the echo amplitude at time T. **B** slice-wise normalizes the refocused echo data for each $2\tau_2$, such that the maximum value along every $2\tau_2$ slice is unity. The red line follows the maximum. The maximum is also shown in **A**, as well as the maximum for $2\tau_1$ slice-wise normalized data.

5.1.2 Numerical Simulations

The numerical simulations started by using Density Functional Theory (DFT) to get a geometry-optimized 3-maleimido-proxyl structure (DFT, B3LYP, and def2-SVP). Electrostatic information was found via CHELPG (CHarges from ELectrostatic Potentials using a Grid-based method), and used to modify a CHARMM-GUI [133] structure for a diamagnetic analog of 3-maleimido-proxyl to 3-maleimido-proxyl. Next, 3038 waters and 188 glycerols were put into a Molecular Dynamics (MD) box, and energy minimized using steepest descent to get all the inter-molecular forces under 1000.0 kJ/mol/nm. Next, the system was propagated at 300 K under NVT conditions for 100 ps in 2 fs steps, and then for another 100 ps under NPT conditions, again with 2 fs steps. The production run started at 300 K for 25 ns in 1 fs steps before instantly dropping to 100 K for 5 ns in 1 fs steps. The system was evolved in GROMACS with the CHARMM36 force-field, using the particle mesh Ewald method for long-range electrostatics, the V-rescale thermostat and the Parrinello–Rahman barostat. The last MD frame was used for spin dynamics simulations.

The spin dynamics used all spins within 12 Å of the electron which encompasses 512 protons, and two nitrogens. The neighbor cutoff used was 1.58 kHz nucleus–nucleus dipole coupling. The 3.38 T applied magnetic field means that the 3-maleimido-proxyl absorption spectrum is significantly wider than the available excitation bandwidth, and so not all orientations of 3-maleimido-proxyl contribute equally. To address this, EasySpin[156] was used to generate an orientation selectivity map, and these weights were multiplicatively combined with the Lebedev weights for orientation averaging. The resulting orientation grid was then renormalized. Figure 5.5 shows a 3-CCE simulation of 3-maleimido-proxyl using 14 orientations.

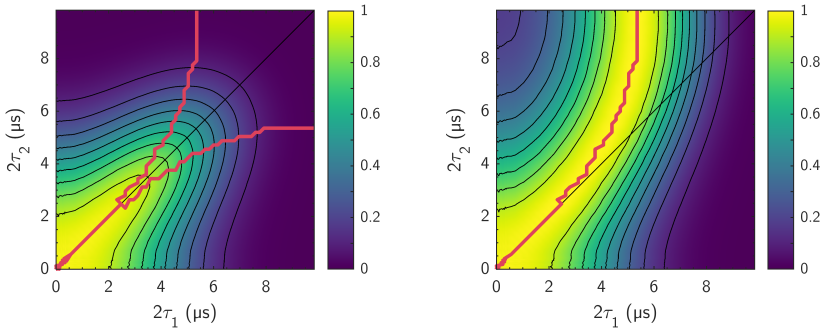

Figure 5.5: **A** shows a 3-CCE simulation of the refocused echo for 3-maleimido-proxyl using 14 orientations. **B** shows the slice-wice normalized version of the simulation.

While there is some orientation dependence, a better match can be achieved by reallocating computational time from 14 orientations at 3-CCE to just the dominant orientation at 4-CCE, as shown in figure 5.6. Specifically, look at the angle of the optimal $2\tau_1$ line with respect to the $2\tau_1 = 2\tau_2$ line compared with the experimental data in figure 5.4.

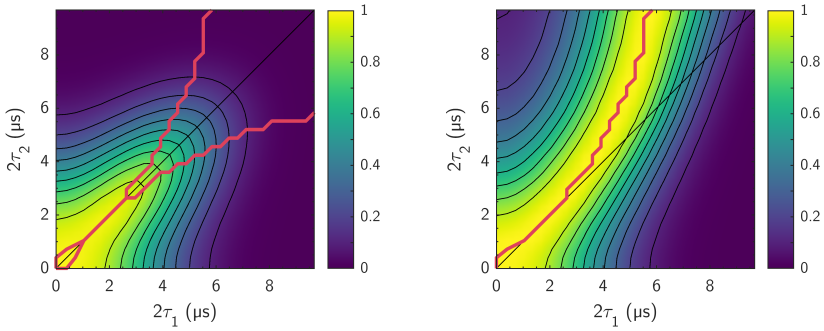

Figure 5.6: **A** shows a 4-CCE simulation of the refocused echo for 3-maleimido-proxyl using a single orientation. **B** shows the slice-wice normalized version of the simulation.

5.1.3 Evaluation of the Second-Order Flip-Flop Diagram

The optimal $2\tau_1$ is balanced between minimizing the total evolution time, $T = 2\tau_1 + 2\tau_2$, and achieving Carr–Purcell conditions, $2\tau_1 = 2\tau_2$. The 2-CCE simulation shows the strongest Carr–Purcell effect; however, even along $2\tau_1 = 2\tau_2$, the 2-CCE simulation loses echo amplitude with total evolution time. In this section we will use Linked Cluster Expansion (LCE[35]) to examine a large source of the Carr–Purcell effect. In the Taylor expansion of the echo amplitude, the lowest-order two-spin flip-flop term that does not evaluate to zero has the Feynman diagram shown below.

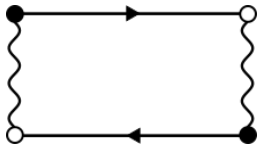

Following the Feynman rules from chapter 2 translates the diagram to

$$V_2 = \sum_{m,n} \sum_{|\psi\rangle = |m\rangle \otimes |n\rangle} \rho_\psi \frac{(-\mathrm{i}/\hbar)^2}{2!} \int_P \mathrm{d}t_1 \int_P \mathrm{d}t_2 \, \langle m| \langle n| \, (-b_{m,n}/4)^2 \overbrace{\hat{I}_{+,m}(p_1)\hat{I}_{-,m}}(p_2) \overbrace{\hat{I}_{+,n}(p_2)\hat{I}_{-,n}}(p_1) \, |n\rangle \, |m\rangle \, . \tag{5.8}$$

The first sum is over all spins that the diagram can represent. The second sum is over all initial states for the spins; each initial state comes with the corresponding weight from the density matrix, $\rho_\psi = \langle\psi|\hat{\rho}|\psi\rangle$. The integrals are over time but follow the path, $t: \ 0 \to T \to 0$, as $p: 0 \to 2T$, defined by the pulse sequence. The first step to evaluating this expression is to simplify all the contractions.

$$\begin{aligned}
V_2 &= \sum_{m,n} \sum_{|\psi\rangle} \rho_\psi \frac{b_{m,n}^2}{16} \frac{(-\mathrm{i}/\hbar)^2}{2!} \, \langle m| \langle n| \, (-2\hat{I}_{z,m})(-2\hat{I}_{z,n}) \int_P \mathrm{d}t_1 \int_P \mathrm{d}t_2 \, G_m(p_2 - p_1) G_n(p_2 - p_1) \, |n\rangle \, |m\rangle \\
&= \sum_{m,n} \sum_{|\psi\rangle} \rho_\psi \frac{b_{m,n}^2}{16} \frac{(-\mathrm{i}/\hbar)^2}{2!} \, \langle m| \langle n| \, (-2\hat{I}_{z,m})(-2\hat{I}_{z,n}) \int_P \mathrm{d}t_1 \int_P \mathrm{d}t_2 \\
&\quad \times \, \mathrm{e}^{+\frac{\mathrm{i}A_m}{\hbar} \int_{p_2}^{p_1} \mathrm{d}t' \ m_\mathrm{S}(p')} \big(\theta(p_2 - p_1)\delta_{m,\downarrow} - \theta(p_1 - p_2)\delta_{m,\uparrow} \big) \\
&\quad \times \, \mathrm{e}^{+\frac{\mathrm{i}A_n}{\hbar} \int_{p_1}^{p_2} \mathrm{d}t' \ m_\mathrm{S}(p')} \big(\theta(p_1 - p_2)\delta_{n,\downarrow} - \theta(p_2 - p_1)\delta_{n,\uparrow} \big) \, |n\rangle \, |m\rangle \\
&= \sum_{m,n} \sum_{|\psi\rangle} \rho_\psi \frac{b_{m,n}^2}{16} \frac{(-\mathrm{i}/\hbar)^2}{2!} \, \langle m| \langle n| \, (+4\hat{I}_{z,m}\hat{I}_{z,n}) \\
&\quad \times - \int_P \mathrm{d}t_1 \int_P \mathrm{d}t_2 \, \mathrm{e}^{-\frac{\mathrm{i}(A_m - A_n)}{\hbar} \int_{p_1}^{p_2} \mathrm{d}t' \ m_\mathrm{S}(p')} \big(\theta(p_2 - p_1)\delta_{m,\downarrow}\delta_{n,\uparrow} + \theta(p_1 - p_2)\delta_{m,\uparrow}\delta_{n,\downarrow} \big) \, |n\rangle \, |m\rangle \, .
\end{aligned} \tag{5.9}$$

The first step substituted the contractions for the appropriate Green's functions. The second equality, expanded the Green's functions in terms of Heaviside step functions, and the last equality collected terms, using the identity $\theta(p)\theta(-p) = 0$. At this point the brackets can be evaluated. The details of the evaluation depend on the state populations, ρ_ψ. In the high-temperature limit, 2 spin-1/2 nuclei give $\rho_\psi = \frac{1}{2^2}$. There are four states in the Hilbert space for the two spins, but the sum over states separates into one sum containing a factor of $\delta_{m,\downarrow}\delta_{n,\uparrow}$ and another containing $\delta_{m,\uparrow}\delta_{n,\downarrow}$. The result after summation is

$$\begin{aligned}
V_2 &= \sum_{m,n} \frac{1}{4} \frac{b_{m,n}^2}{16} \frac{(-\mathrm{i}/\hbar)^2}{2!} \int_P \mathrm{d}t_1 \int_P \mathrm{d}t_2 \, \mathrm{e}^{-\frac{\mathrm{i}(A_m - A_n)}{\hbar} \int_{p_1}^{p_2} \mathrm{d}t' \ m_\mathrm{S}(p')} \big(\theta(p_2 - p_1) + \theta(p_1 - p_2) \big) \\
&= \sum_{m,n} \frac{1}{4} \frac{b_{m,n}^2}{16} \frac{(-\mathrm{i}/\hbar)^2}{2!} \int_P \mathrm{d}t_1 \int_P \mathrm{d}t_2 \, \mathrm{e}^{-\frac{\mathrm{i}(A_m - A_n)}{\hbar} \int_{p_1}^{p_2} \mathrm{d}t' \ m_\mathrm{S}(p')}
\end{aligned} \tag{5.10}$$

The second line identifies $\theta(-p) + \theta(p) = 1$, ignoring the point at $p = 0$ which has zero Lebesgue measure, and so will not contribute to the integrals. For a function $f(x)$, $\int_a^c \mathrm{d}x f(x) = \int_a^b \mathrm{d}x f(x) + \int_b^c \mathrm{d}x f(x)$, so long as $f(x)$ has a continuous antiderivative. This can be used to separate the integration variables.

$$\begin{aligned}
V_2 &= \sum_{m,n} \frac{1}{4} \frac{b_{m,n}^2}{16} \frac{(-\mathrm{i}/\hbar)^2}{2!} \int_P \mathrm{d}t_2 \, \mathrm{e}^{-\frac{\mathrm{i}(A_m - A_n)}{\hbar} \int_0^{p_2} \mathrm{d}t' \ m_\mathrm{S}(p')} \int_P \mathrm{d}t_1 \, \mathrm{e}^{-\frac{\mathrm{i}(A_m - A_n)}{\hbar} \int_{p_1}^{0} \mathrm{d}t' \ m_\mathrm{S}(p')} \\
&= \sum_{m,n} \frac{1}{4} \frac{b_{m,n}^2}{16} \frac{(-\mathrm{i}/\hbar)^2}{2!} \int_P \mathrm{d}t_2 \, \mathrm{e}^{-\frac{\mathrm{i}(A_m - A_n)}{\hbar} \int_0^{p_2} \mathrm{d}t' \ m_\mathrm{S}(p')} \int_P \mathrm{d}t_1 \, \mathrm{e}^{+\frac{\mathrm{i}(A_m - A_n)}{\hbar} \int_0^{p_1} \mathrm{d}t' \ m_\mathrm{S}(p')} \\
&= \sum_{m,n} \frac{1}{4} \frac{b_{m,n}^2}{16} \frac{(-\mathrm{i}/\hbar)^2}{2!} \left| \int_P \mathrm{d}t \, \mathrm{e}^{-\frac{\mathrm{i}(A_m - A_n)}{\hbar} \int_0^{p} \mathrm{d}t' \ m_\mathrm{S}(p')} \right|^2
\end{aligned} \tag{5.11}$$

The second equality swapped the integration bounds of one of the exponential integrals at the cost of a minus sign. The last line identified the two integrals as complex conjugates of each other. So far the pulse sequence has been arbitrary; however, to evaluate the integral over a pulse sequence path P, the pulse sequence will need to be chosen. Here we will choose to look at the refocused Hahn echo. The first step is to evaluate the integral in the exponential, $\int_0^p \mathrm{d}t'\ m_\mathrm{S}(p')$. The path dependence of m_S is determined by the π-pulses at τ_1 and $2\tau_1+\tau_2$, as well as switching electron spin manifolds at the $\hat{S}_+$.

$$m_\mathrm{S}(p) = m_\mathrm{S}(p=0)\begin{cases} +1 & ,\ 0<p<\tau_1 \\ -1 & ,\ \tau_1<p<2\tau_1+\tau_2 \\ +1 & ,\ 2\tau_1+\tau_2<p<2\tau_1+2\tau_2 \\ -1 & ,\ 2\tau_1+2\tau_2<p<2\tau_1+3\tau_2 \\ +1 & ,\ 2\tau_1+3\tau_2<p<3\tau_1+4\tau_2 \\ -1 & ,\ 3\tau_1+4\tau_2<p<4\tau_1+4\tau_2 \end{cases}. \tag{5.12}$$

The integral measure expands as $\mathrm{d}t' = \mathrm{d}p' \frac{\mathrm{d}t'}{\mathrm{d}p'}$;

$$\frac{\mathrm{d}t'}{\mathrm{d}p'} = \begin{cases} +1 & ,\ 0<p<2\tau_1+2\tau_2 \\ -1 & ,\ 2\tau_1+2\tau_2<p<4\tau_1+4\tau_2 \end{cases}. \tag{5.13}$$

Putting these together, the integral in the exponent evaluates to

$$\int_0^p \mathrm{d}t'\ m_\mathrm{S}(p') = \int_0^p \mathrm{d}p'\ \frac{\mathrm{d}t'}{\mathrm{d}p'} m_\mathrm{S}(p') = m_\mathrm{S}(p'=0)\begin{cases} p & ,\ 0<p<\tau_1 \\ 2\tau_1-p & ,\ \tau_1<p<2\tau_1+\tau_2 \\ p-2\tau_1-2\tau_2 & ,\ 2\tau_1+\tau_2<p<2\tau_1+3\tau_2 \\ 2\tau_1+4\tau_2-p & ,\ 2\tau_1+3\tau_2<p<3\tau_1+4\tau_2 \\ p-4\tau_1-4\tau_2 & ,\ 3\tau_1+4\tau_2<p<4\tau_1+4\tau_2 \end{cases}. \tag{5.14}$$

Taking $m_\mathrm{S}(p'=0) = -1/2$, and defining $\omega_{mn} := \frac{(A_m - A_n)}{4\hbar}$, the remaining integral is

$$\begin{aligned} \left| \int_\mathrm{re} \mathrm{d}t\ \mathrm{e}^{\mathrm{i}4\omega_{mn}\int_0^p \mathrm{d}t'\ m_\mathrm{S}(p')} \right|^2 &= \left| \int_0^{4\tau_1+4\tau_2} \mathrm{d}p \left(\frac{\mathrm{d}t(p)}{\mathrm{d}p}\right) \mathrm{e}^{-\mathrm{i}4\omega_{mn}\int_0^p \mathrm{d}t'\ m_\mathrm{S}(p')} \right|^2 \\ &= \Bigg| \int_0^{\tau_1} \mathrm{d}p\ \mathrm{e}^{\mathrm{i}2\omega_{mn}p} + \int_{\tau_1}^{2\tau_1+\tau_2} \mathrm{d}p\ \mathrm{e}^{\mathrm{i}2\omega_{mn}(2\tau_1-p)} + \int_{2\tau_1+\tau_2}^{2\tau_1+2\tau_2} \mathrm{d}p\ \mathrm{e}^{\mathrm{i}2\omega_{mn}(p-2\tau_1-2\tau_2)} \\ &\quad - \int_{2\tau_1+2\tau_2}^{2\tau_1+3\tau_2} \mathrm{d}p\ \mathrm{e}^{\mathrm{i}2\omega_{mn}(p-2\tau_1-2\tau_2)} - \int_{2\tau_1+3\tau_2}^{3\tau_1+4\tau_2} \mathrm{d}p\ \mathrm{e}^{\mathrm{i}2\omega_{mn}(2\tau_1+4\tau_2-p)} - \int_{3\tau_1+4\tau_2}^{4\tau_1+4\tau_2} \mathrm{d}p\ \mathrm{e}^{\mathrm{i}2\omega_{mn}(p-4\tau_1-4\tau_2)} \Bigg|^2 \end{aligned} \tag{5.15}$$

This integral can be simplified by combining the integrals that run over intervals of the same duration,

$$\begin{aligned} &\left| \int_\mathrm{re} \mathrm{d}t\ \mathrm{e}^{\mathrm{i}4\omega_{mn}\int_0^p \mathrm{d}t'\ m_\mathrm{S}(p')} \right|^2 \\ &\quad = \left| (1-\mathrm{e}^{-\mathrm{i}2\omega_{mn}\tau_1}) \int_0^{\tau_1} \mathrm{d}p\ \mathrm{e}^{\mathrm{i}2\omega_{mn}p} + (\mathrm{e}^{\mathrm{i}2\omega_{mn}\tau_1} - \mathrm{e}^{\mathrm{i}2\omega_{mn}\tau_2}) \int_0^{\tau_1+\tau_2} \mathrm{d}p\ \mathrm{e}^{-\mathrm{i}2\omega_{mn}p} + (\mathrm{e}^{-\mathrm{i}2\omega_{mn}\tau_2} - 1) \int_0^{\tau_2} \mathrm{d}p\ \mathrm{e}^{\mathrm{i}2\omega_{mn}p} \right|^2 \\ &\quad = \frac{4}{\omega_{mn}^2} \Big(\cos(\omega_{mn}2\tau_1) - \cos(\omega_{mn}2\tau_2) \Big)^2 \end{aligned} \tag{5.16}$$

Substituting this into the full expression gives

$$\begin{aligned} V_2 &= \sum_{m,n} \frac{1}{4} \frac{b_{m,n}^2}{16} \frac{(-\mathrm{i}/\hbar)^2}{2!} \frac{4}{\omega_{mn}^2} \Big(\cos(\omega_{mn}2\tau_1) - \cos(\omega_{mn}2\tau_2) \Big)^2 \\ &= -\frac{1}{2!} \sum_{m,n} \frac{(b_{m,n}/\hbar)^2}{16\omega_{mn}^2} \Big(\cos(\omega_{mn}2\tau_1) - \cos(\omega_{mn}2\tau_2) \Big)^2 \end{aligned} \tag{5.17}$$

Finally, expanding ω_{mn} back to $\frac{\Delta A_{mn}}{4\hbar}$, and restricting the sum to $m < n$ gives

$$V_2 = -\sum_{m<n} \left(\frac{b_{mn}}{\Delta A_{mn}}\right)^2 \Big(\cos(\omega_{mn} 2\tau_1) - \cos(\omega_{mn} 2\tau_2)\Big)^2. \tag{5.18}$$

Finally, the diagrams contribution to the refocused echo is a factor of $\exp(V_2)$. Note that when $2\tau_1 = 2\tau_2$, this diagram does not contribute to electron spin decoherence, which means that this diagram perfectly follows Carr–Purcell behavior.

Returning to our 3-maleimido-proxyl system, figure 5.7's top row shows $\exp(V_2)$, 2-CCE, 3-CCE and 4-CCE simulations for the orientation at which 3-maleimido-proxyl was probed by the experiment. Note that along the $2\tau_1 = 2\tau_2$ line, $\exp(V_2)$ remains constant as expected from equation (5.18), while along lines of constant evolution time, $2\tau_1 + 2\tau_2 = T$, the decay appear similar across all the simulations. Below each CCE simulation in figure 5.7, is the slice-wise normalized signal, while below the $\exp(V_2)$ is

$$f(2\tau_1, 2\tau_2) := \exp\Big(\sum_{d>2} V_d\Big) \approx \frac{v^{(4)}(2\tau_1, 2\tau_2)}{\exp(V_2)}, \tag{5.19}$$

estimated by taking the 4-CCE simulation and dividing out $\exp(V_2)$. $f(2\tau_1, 2\tau_2)$ represents the contribution of all higher-order diagrams. While $f(2\tau_1, 2\tau_2)$ displays some Carr–Purcell effect at short T, there is a more pronounced decay with T. This suggests the interpretation that the refocused Hahn echo amplitude depends on two competing behaviors, a Carr–Purcell-like behavior that is mostly captured by $\exp(V_2)$, and a decay that only depends on the total evolution time, which is the most part of $f(2\tau_1, 2\tau_2)$.

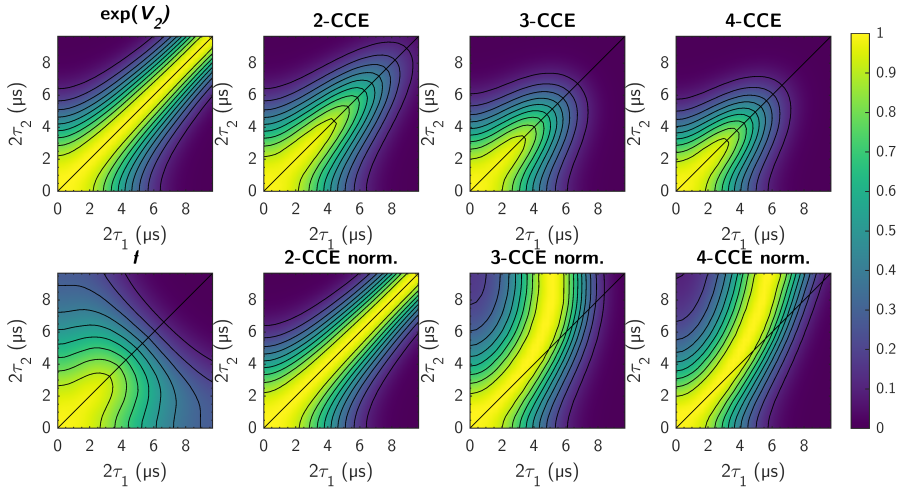

Figure 5.7: The top row contains simulations of increasing comprehensivity: from only the $\exp(V_2)$ terms on the left, to 2-CCE through 4-CCE. Below each CCE simulation is the slice-wise normalized version, while below the LCE simulation, is the quotient $v^{(4)}/\exp(V_2)$, revealing that a lot of what the higher-order clusters contribute is a decay that falls off with the total time and does not follow Carr–Purcell expectations.

This explains why the optimal $2\tau_1$ for a given $2\tau_2$ is neither $2\tau_1 = 0$ nor $2\tau_1 = 2\tau_2$: the partial derivative of the signal with respect to $2\tau_1$ is

$$\frac{\partial}{\partial 2\tau_1} v(2\tau_1, 2\tau_2) = \frac{\partial}{\partial 2\tau_1} \exp(V_2) f(2\tau_1, 2\tau_2) = v(2\tau_1, 2\tau_2) \frac{\partial V_2}{\partial 2\tau_1} + \exp(V_2) \frac{\partial f(2\tau_1, 2\tau_2)}{\partial 2\tau_1}.. \tag{5.20}$$

First, note that $\exp(V_2)$ and $f(2\tau_1, 2\tau_2)$ are always positive. Next, note that $\frac{\partial V_2}{\partial 2\tau_1} = 0$ at $2\tau_1 = 2\tau_2$, and since $2\tau_1 = 2\tau_2$ is a maximum, $\frac{\partial V_2}{\partial 2\tau_1}$ is positive at $2\tau_1$ values slightly less than $2\tau_2$. To the degree that $f(2\tau_1, 2\tau_2)$ is a stricly decreasing function of T, as suggested by figure 5.7, $\frac{\partial f(2\tau_1, 2\tau_2)}{\partial 2\tau_1}$ is negative. This means that

$\frac{\partial v(2\tau_1,2\tau_2)}{\partial 2\tau_1}$ is zero at some $2\tau_1 < 2\tau_2$ and negative at $2\tau_1 = 2\tau_2$. The optimal $2\tau_1$ as a function of $2\tau_2$ solves

$$f(2\tau_1, 2\tau_2)\frac{\partial V_2}{\partial 2\tau_1} = -\frac{\partial f(2\tau_1, 2\tau_2)}{\partial 2\tau_1}, \tag{5.21}$$

and follows the path that balances the two decay sources. When both contributions are on a similar scale, the path will be noticably away from both $2\tau_1 = 2\tau_2$ and $2\tau_1 = 0$.

5.2 Other Systems

Bahrenberg performed the refocused echo experiments on 3-maleimido-proxyl in deuterated and partially deuterated water/glycerol, as well as on two other radicals, trityl OXO63 [157–159], which is used as a spin label, and Gd(III) from $GdCl_3$, which is analogous to the Gd(III) spin label Gd-C2 [160, 161]. Both were measured in both a protiated and a deuterated environment. Although no more simulations were done for these extra systems, we will briefly look at the experimental data and discuss how they fit in with the results from earlier.

5.2.1 3-Maleimido-Proxyl: Deuteration Series

The dependence of the refocused Hahn echo for 3-maleimido-proxyl on the solvent proton concentration was also investigated. Figure 5.8(A) shows the refocused Hahn echo for 3-maleimido-proxyl in a 25% deuterated solvent (4:1 volume:volume water:glycerol). Figure 5.8(B) shows the slice-wise normalized refocused echo data.

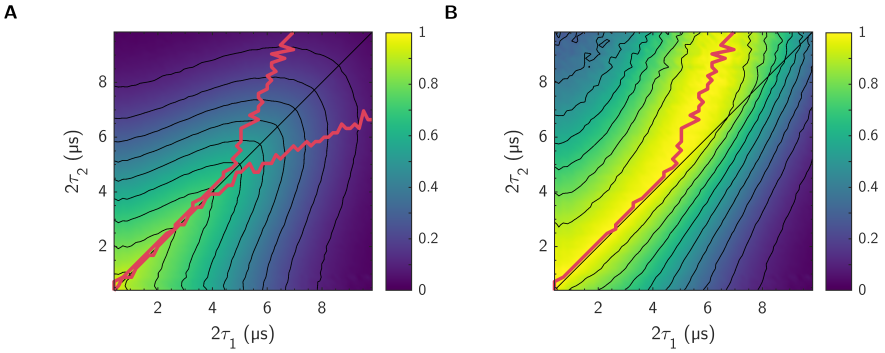

Figure 5.8: 100 μM 3-maleimido-proxyl in 25% deuterated solvent (water/glycerol): **A** shows the refocused echo amplitude on the color–axis vs. $2\tau_1$ and $2\tau_2$. **B** shows the slice-wise normalized amplitude.

The overall shape of the refocused echo decay is basically the same as for the protiated case; the time scale of the decay is slightly longer, and the optimal $2\tau_1$ for a given $2\tau_2$ path is a little noisier, but the same pattern holds. Both of the stated differences are likely due to the 25% deuteration, indirectly and directly. The extended coherence time is explainable by the the 25% reduction in proton concentration (see the next chapter). And the added noise in the $2\tau_1(2\tau_2)$ path is likely due to ESEEM modulations from the deuterium. Figure 5.9 shows the refocused Hahn echo under the same two normalization schemes for 3-maleimido-proxy in a 50% deuterated solvent (4:1 volume:volume water:glycerol). And figure 5.10 is analogous, except the the solvent is 75% deuterated.

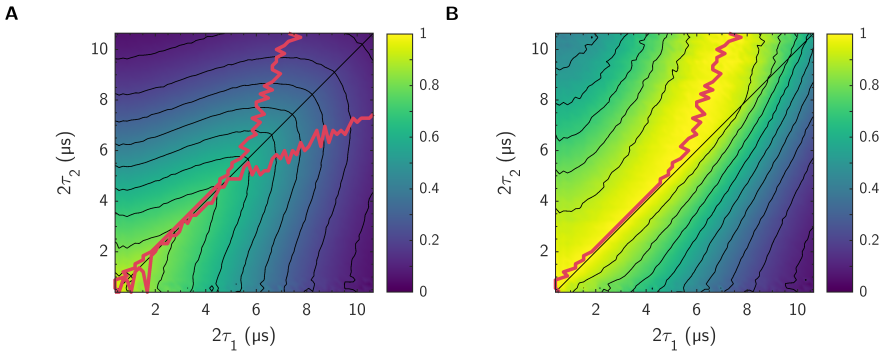

Figure 5.9: 100 µM 3-maleimido-proxyl in 50% deuterated solvent (water/glycerol): **A** shows the refocused echo amplitude on the color–axis vs. $2\tau_1$ and $2\tau_2$. **B** shows the slice-wise normalized amplitude.

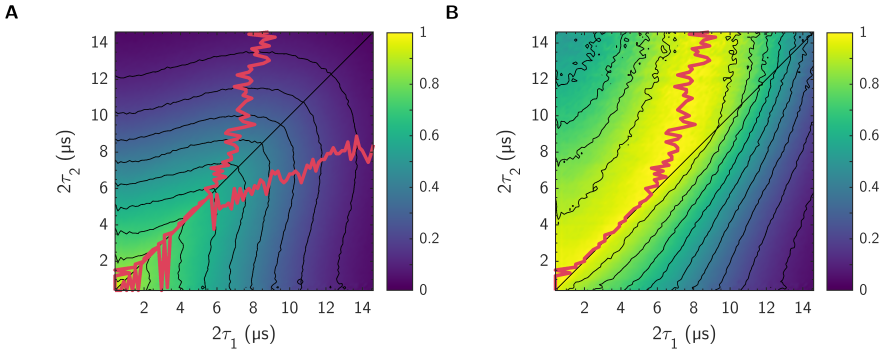

Figure 5.10: 100 µM 3-maleimido-proxyl in 75% deuterated solvent (water/glycerol): **A** shows the refocused echo amplitude on the color–axis vs. $2\tau_1$ and $2\tau_2$. **B** shows the slice-wise normalized amplitude.

So far the trend is unchanged: deuteration extends the coherence time and adds noise to optimal $2\tau_1(2\tau_2)$ path; however, upon reaching nearly fully deuterated solvent, the trend no longer holds. Figure 5.11 shows the refocused Hahn echo amplitude and the slice-wise normalized refocused echo amplitude for 3-maleimido-proxy in a fully deuterated solvent (4:1 volume:volume water:glycerol). Here, the refocused decho amplitude shows almost no sign of the Carr–Purcell effect. Likely, this indicates that the dominant decoherence pathway is different. One possible mechanism that only depends on the total evolution time is instantaneous diffusion [85]. For the 100 µM 3-maleimido-proxyl concentration and an inversion efficiency of η, the time–scale for instantaneous diffusion is

$$T_{\mathrm{ID}} = \frac{20\ \mu\mathrm{s}}{\eta}. \tag{5.22}$$

This suggests that instantaneous diffusion alone does explain the observed decay. For 200 µM TEMPO in water/glycerol, the Hahn echo T_{M} increased with increasing mass percent glycerol up until about 50% glycerol by mass, suggesting that there was some degree of TEMPO aggregation [127]. It is plausible that the effective 3-maleimido-proxyl concentration here was greater than 100 µM due to aggregation during the

freezing process, but whether or not it is enough to make instantaneous diffusion significant in deuterated solvent case is unclear.

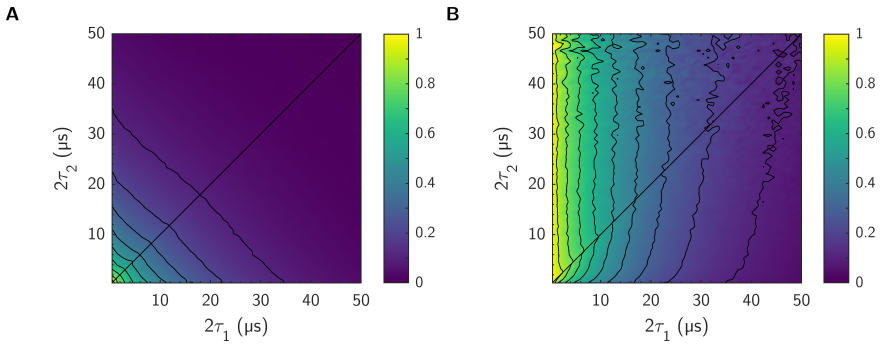

Figure 5.11: 100 µM 3-maleimido-proxyl in ≈ 100% deuterated solvent (water/glycerol): **A** shows the refocused echo amplitude on the color–axis vs. $2\tau_1$ and $2\tau_2$. **B** shows the slice-wise normalized amplitude.

Figure 5.12 shows the Hahn echo T_Ms for these same samples. Additionally, the data are fit to

$$\log_{10}(T_M/\text{s}) = \log_{10}(T_M(1\text{ M})/\text{s}) - p\log_{10}([^1\text{H}]/\text{M}), \tag{5.23}$$

which is the log-log space version of $T_M = T_M(1\text{ M})([^1\text{H}]/\text{M})^{-p}$. The blue curve assumes the fully deuterated sample is 1% protiated; the fit values are

$$\begin{aligned}\log_{10}(T_M(1\text{ M})/\text{s}) = &-5.15 \pm 0.08;\\ p = &\ 0.21 \pm 0.05.\end{aligned} \tag{5.24}$$

The red curve does not include the fully deuterated point in the fit, with fit results of

$$\begin{aligned}\log_{10}(T_M(1\text{ M})/\text{s}) = &-4.7 \pm 0.1;\\ p = &\ 0.48 \pm 0.06.\end{aligned} \tag{5.25}$$

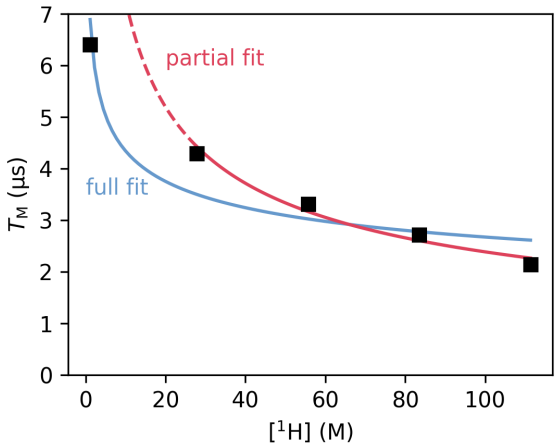

Figure 5.12: This plot shows the experimental T_Ms of 100 µM 3-maleimido-proxyl in variously deuterated solvents as a function of proton concentration. The blue line is a fit to all the data. The red line shows a fit to the non-fully deuterated points. The red line is dashed where it is extrapolating.

When the fully deuterated point is included in the fit, the $T_M([^1H])$ curve is flatter over the region where the non-fully deuterated data are. The RMSD for the full fit is about 0.5 µs, while the RMSD for the partial fit is about 0.1 µs. Although it is expected that fitting less data with the same model should give a better fit, it is consistent with the refocused echo data to hypothesize that the primary electron spin decoherence mechanism is different in the fully deuterated case, and so does not meet the assumptions of the model.

In anticipation of the following chapter, note that $p < 1$.

5.2.2 Trityl OXO63

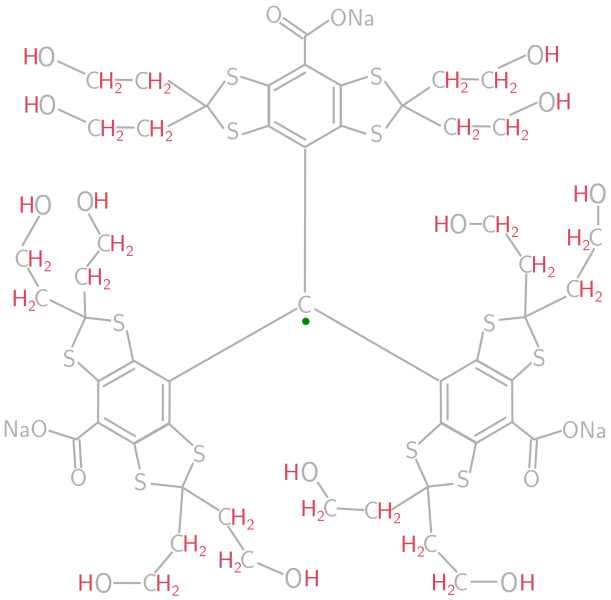

Figure 5.13: The above cartoon shows the Lewis structure of trityl OXO63. The hydrogens are colored red, and the electron is shown as a green dot.

Figure 5.13 shows the structure of trityl OXO63, and figure 5.14 shows the refocused echo data for trityl OXO63 in protiated water/glycerol. Mostly the exhibited decoherence behavior is the same as for 3-maleimido-proxyl. The asymmetry between the optimal $2\tau_1(2\tau_2)$ and $2\tau_2(2\tau_1)$, is attributed to an experimental imperfection since in the high-nuclear-temperature limit that is applicable here, the two paths should be symmetric as shown earlier.

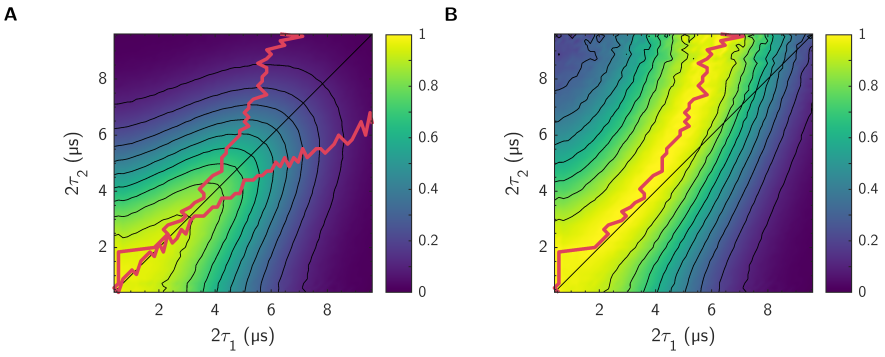

Figure 5.14: 100 µM trityl OXO63 in protiated solvent (water/glycerol): **A** shows the refocused echo amplitude on the color–axis vs. $2\tau_1$ and $2\tau_2$. **B** shows the slice-wise normalized amplitude.

And figure 5.15 shows the refocused echo data for trityl OXO63 deuterated water/glycerol. While not as fully, here too the Carr–Purcell effect is gone, and the optimal $2\tau_1(2\tau_2)$ is a $2\tau_1$ as short as possible.

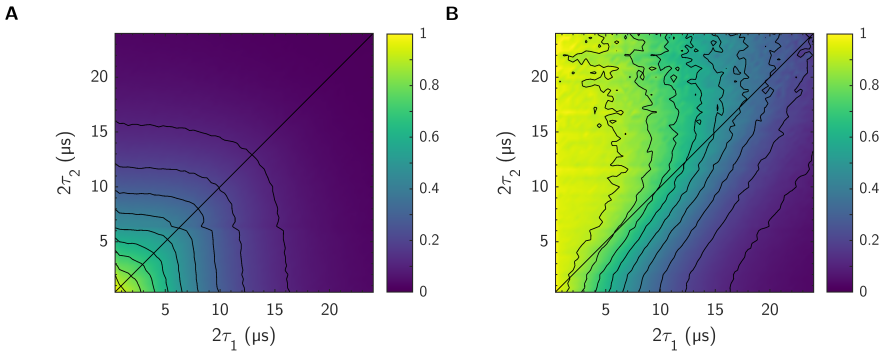

Figure 5.15: 100 µM trityl OXO63 in deuterated solvent (water/glycerol): **A** shows the refocused echo amplitude on the color–axis vs. $2\tau_1$ and $2\tau_2$. **B** shows the slice-wise normalized amplitude.

5.2.3 Gd(III)

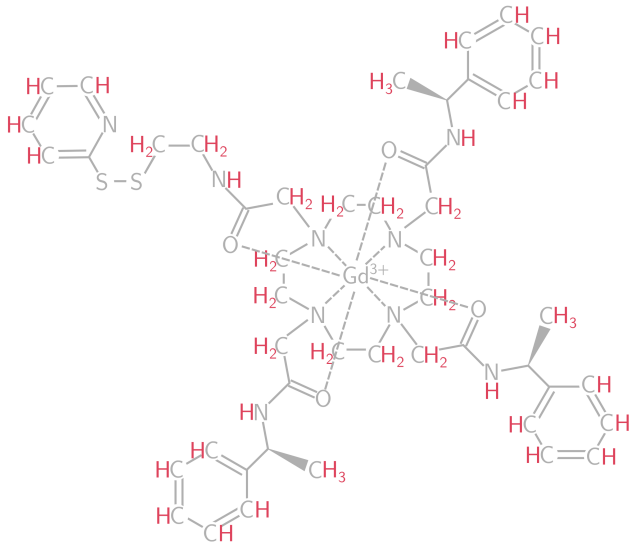

Figure 5.16: The above cartoon shows the Lewis structure of Gd-C2. The hydrogens are colored red.

The last radical that was investigated was Gd(III) from $GdCl_3$. This salt has gadolinium in the same oxidation state as the Gd(III) spin label shown in figure 5.16. Gd(III) contains an effective electron spin of 7/2. The refocused echo data is shown in figure 5.17(A), and the slice-wise normalized data is shown in figure 5.17(B). The Gd(III) system has two distinct behaviors; the long-time behavior appears to be governed by Carr–Purcell mechanism, but the short-time behavior deviates significantly. A transient zero field splitting mechanism is a good candidate explanation [162].

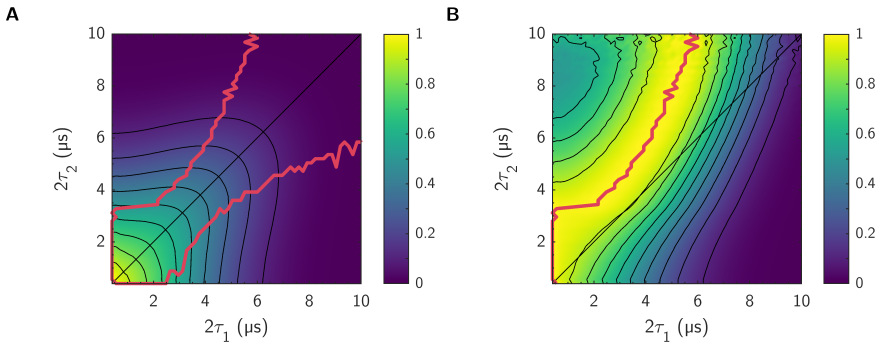

Figure 5.17: 100 µM $GdCl_3$ in protiated solvent (water/glycerol): **A** shows the refocused echo amplitude on the color–axis vs. $2\tau_1$ and $2\tau_2$. **B** shows the slice-wise normalized amplitude.

The deuteration again lengthens the coherence time, and removes Carr–Purcell effects.

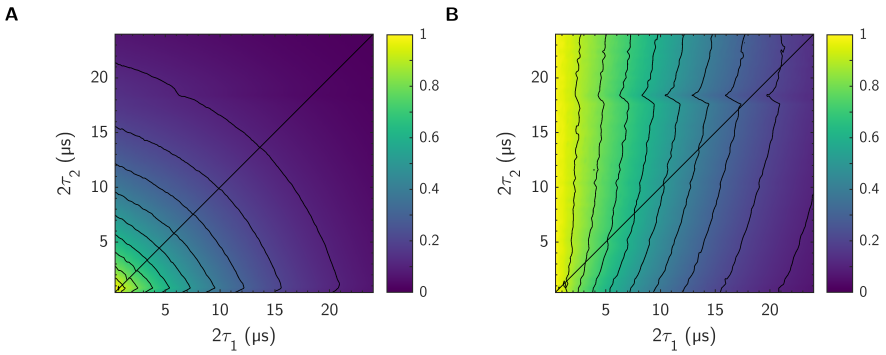

Figure 5.18: 100 µM $GdCl_3$ in deuterated solvent (water/glycerol): **A** shows the refocused echo amplitude on the color–axis vs. $2\tau_1$ and $2\tau_2$. **B** shows the slice-wise normalized amplitude.

5.3 Conclusion

The refocused-echo experiments and simulations for protiated solvents show how much pairwise flip-flops dominates the decoherence mechanism and are responsible for the Carr–Purcell effect, as the contributions from other mechanisms produce a decay that depends primarily upon the total experiment time.

When Carr–Purcell refocusable processes are dominant, following the exact Carr–Purcell conditions may not be optimal for a given $2\tau_2$, especially at longer experiment time, for there are still mechanisms that depend on the total time.

Experiments with various radical and solvent protiations suggest that while this holds for different common spin labels, decays in deuterated solvent tend to be near monotonic in the total evolution time.

The balance between these two distinct decay behaviors has practical consequences. DEER experiments often try to minimize the total experiment time by selecting short a $2\tau_1$. This makes sense for systems

like the examined deuterated systms whose coherence decays are not governed by processes that are not recovered at Carr–Purcell conditions. However, for systems that have a strong Carr–Purcell effects like the examined protiated systems, choosing a $2\tau_1$ slightly under the $2\tau_2$ will likely give more signal. This means that before running a DEER experiment, it is likely worth scanning $2\tau_1$ to find the optimal signal-to-noise ratio. Extending $2\tau_1$ for better coherence times has been used in [163].

The refocused echo is part of DEER,
CP or zero, should the times be near?
At neither shortest time nor Carr–Purcell,
the signal is maximal, so we tell.
At the balance of multiple pathways.
this is the place to set the pulse delays.

Chapter 6

Partially Deuterated Matrices

Acknowledgements
This chapter details work published in [164]. All the experimental work was done by Elizabeth Canarie of the Stoll Lab, University of Washington, Seattle. The principal investigator for this work was Stefan Stoll, University of Washington, Seattle. I ran the simulations, developed the simple analytic model of how proton concentration affects the Hahn echo decay, and performed the correlation analysis.

So far we have only focused on systems in a protiated matrix, yet experiments like DEER are often performed after substituting the solvent protons for deuterons, since deuterons have one, a smaller magnetic dipole moment ($g_{\mathrm{D}} = 0.8574$, as compared to protons with $g_{\mathrm{H}} = 5.5857$), and two, a nuclear quadrupole moment, which provides an orientation and chemical environment dependent torque on the deuterons, detuning them from resonance with each other so that flip-flops no longer conserve nuclear Zeeman energy. These factors combine to extend the electron spin coherence time as compared with the protiated version of the system [18]. For the same reason people deuterate the protein itself when extra long coherence times are needed [165, 166]. While better than a fully protiated system from a coherence time perspective, it should be noted that deuterating biological systems can be difficult and expensive. And sometimes D_2O can even cause proteins to precipitate out of solution. [167, 168]

In chapter 3, we introduced a list of questions regarding the use of the Cluster Correlation Expansion (CCE)[1, 2]:

- Does CCE work for molecular qubits? → **Yes** [46].
- Does CCE work with glassy matrices? → **Yes** [127].
- How does isotope composition affect the calculations?
- Are in silico protein models accurate and diverse enough to get an accurate coherence time prediction?

The first was answered in [46] and the second in [127], which was discussed in chapter 3. In this chapter we will focus on the third question. Specifically, we will use the Hahn echo to investigate d_{18}-TEMPO in a partially deuterated 1:1 mass:mass: water:glycerol solvent as shown in figure 6.1.

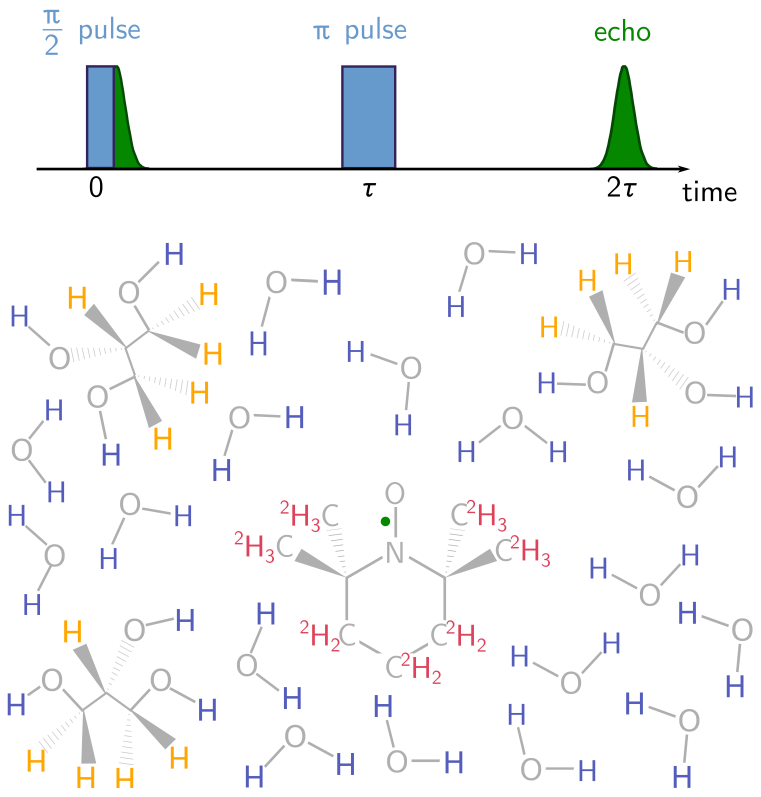

Figure 6.1: The Hahn echo diagram schematically shows the pulse sequence. Note that it is not to scale. Applied microwave pulses are show in blue: a $\pi/2$ pulse to initialized the electron spins and a π pulse is used refocus the coherence. The electrons' signal amplitude is shown in green and is significant at two points: starting at $t \approx 0$ is a Free-Induction Decay (FID), and centered at $t \approx 2\tau$ is the echo. The above cartoon of d_{18}-TEMPO in a 1:1 mass:mass water:glycerol (approximately 5:1 mole:mole) solvent has the hydrons color coded. The d_{18}-TEMPO's deuterons are red. Solvent exchangeable hydrons are blue, and solvent non-exchangeable hydrons are yellow. The radical electron is green.

6.1 Experimental Methods

The experimental work summerized in this section was done by Elizabeth Canarie. Three samples series were prepared, each varying the proton-to-deuteron ratio differently:

1. H_2O:h_8-glycerol with D_2O:d_8-glycerol,
2. D_2O:d_3-glycerol with D_2O:d_8-glycerol,
3. H_2O:d_5-glycerol with D_2O:d_8-glycerol,

all with about 5 μM d_{18}-TEMPO. For a given total proton concentration, the difference between these samples lies in how many protons are in solvent exchangeable O-H bonds vs. solvent non-exchangeable C-H bonds. The following discussion will start out with only the H_2O:h_8-glycerol to D_2O:d_8-glycerol series, introducing the other two near the end.

The EPR experiments were all done at 20 K and at Q-band, approximately 1.2 T, but the exact magnetic field was selected by using an echo-detected field sweep to find the maximum echo amplitude for $\langle \hat{S}_x \rangle$, while keeping $\langle \hat{S}_y \rangle$ small. The spectrometer used was a Bruker Elexsys E580 combined with a Applied Systems Engineering 390 W traveling-waveguide-tube microwave amplifier. The samples sat in a Bruker D2 dielectric resonator and were thermally controlled via a cryogen-free sample cooling system from ColdEdge and Bruker.

The pulse angles were varied by changing the pulse durations, 10 ns for the $\pi/2$ pulses and 20 ns for the π pulse. These values were selected by measuring the Rabi oscillations. The minimum τ used was 250 ns. The shot repetition time was increased until further extensions did not increase the echo amplitude at 120 ms or more.

Due to technical limitations and since high temporal resolution was needed at short 2τs but long 2τs were also needed, the Hahn echo decays were acquired in two parts: a short high resolution part with $\Delta\tau =$ 10 ns and $\tau \leq 11$ µs, and a long low-resolution part with $\Delta\tau = 624$ ns and $\tau \leq 250$ µs, and then stitched together.

6.2 Molecular Dynamics

The same TEMPO molecule as from chapter 3 and [127] was used, the one based on the method described in [129]: starting from a DFT geometry optimized with the SV(P) basis and the B3LYP functional via ORCA 4.0.1, the CHELPG (CHarges from ELectrostatic Potentials using a Grid-based method) routine was used to determine the correct charges to convert a GROMACS topology generated by CHARMM-GUI[133] for a paramagnetic analog of TEMPO into topology file for TEMPO.

This time however, 1500 glycerols were randomly placed around the TEMPO in adition to the 7469 waters. The molecular dynamics simulation was done with GROMACS 2019.2 using the CHARMM36 [136] force field. From the initial structure, an initial energy minimization was performed, and then the system was propagated under NVT conditions for 100 ps followed by NPT conditions for another 100 ps, both at 300 K in 2 fs steps. The production runs, again based on that of Lerbret and Affouard [137], used 1 fs steps and started at 300 K for 25 ns, before instantly being changed to 100 K for the final 2 ns. The temperature was controlled with the V-rescale modified Berendsen thermostat. The pressure was set with Parrinello–Rahman barostat to 1 bar. The final system volume was a cube with 72.57 Å to an edge. This means the total proton concentration was 117.0 M, slightly higher than the experimental system with [H] = 111.5 M [135].

6.3 Quantum Spin Dynamics

The spin dynamics for one central electron and N magnetic nuclei were modeled with

$$\begin{aligned}\hat{H}(m_{\mathrm{S}}) = & -B_0(-\mu_{\mathrm{B}} g_{zz}) m_{\mathrm{S}} - B_0 \mu_{\mathrm{N}} \sum_n^N g_n \hat{I}_z \\ & + m_{\mathrm{S}} \boldsymbol{z}^{\mathrm{T}} \sum_n^N \boldsymbol{A}_n \hat{\boldsymbol{I}}_n + \sum_n^N \hat{\boldsymbol{I}}_n^{\mathrm{T}} \boldsymbol{P}_n \hat{\boldsymbol{I}}_n \\ & + \sum_{\substack{m,n \\ m<n}}^N \delta_{g_{\mathrm{n},n}, g_{\mathrm{n},m}} \hat{\boldsymbol{I}}_m^{\mathrm{T}} \boldsymbol{b}_{mn} \hat{\boldsymbol{I}}_n .\end{aligned} \tag{6.1}$$

The Hahn echo pulses were treated as ideal pulses: m_{S} instantly changes at $t = \tau$. Since the applied magnetic field, $\boldsymbol{B}_0$, is used to define the z-axis, only the z-component of the Zeeman couplings were included. The hyperfine coupling for most atoms was calculated with the point-dipole approximation; however, the electron is not localized to a point in space from the perspective of TEMPO's ^{14}N; the hyperfine tensor eigenvalues for the nitrogen were set to $A_{xx} = A_{yy} = -13.8725$ MHz, and $A_{zz} = 122.329$ MHz, where theses coordinates are in the molecular frame with x parallel to the N-O bond and the y-axis defined as the component orthogonal to x, of the separation vector between the two carbons bonded to the nitrogen [169].

For the nuclear quadrupole coupling of the nitrogen, we used the same axes to define the tensor's eigenframe and $\frac{e^2 q Q}{h} = 3.5$ MHz, and $\eta = 0.68$, giving principal values of $\{-0.28, -1.47, +1.75\}$ MHz [138].

The nucleus–nucleus coupling in the model is the through-space point dipole coupling. Only couplings between like–nuclei were included, because flip-flops between unlike nuclei do not conserve Zeeman energy. Since all examined clusters contain only protons, only deuterons, or only the nitrogen, the CCE product for a single orientation factors as

$$v(2\tau) = v^{\mathrm{N}}(2\tau) v^{\mathrm{H}}(2\tau) v^{\mathrm{D}}(2\tau). \tag{6.2}$$

The nitrogen signal is unique in that there is only one nitrogen in the system, which contributes only a single 1-cluster that is always present. The signal from this nitrogen is fairly orientation dependent but independent of the proton-to-hydron ratio. By assuming the nitrogen signal is uncorrelated with the hydron signal, the nitrogen signal can be replaced with the orientation averaged nitrogen signal and factored out of the orientation averaging sum. This means the nitrogen signal, $\langle v^{\mathrm{N}}(2\tau)\rangle$, only needs to be calculated once (with a large number of orientations), which can be included as a factor to the signal from a mixture of protons and deuterons.

The instantaneous diffusion timescale can be calculated as in [85], and at the samples' 5 μM d_{18}-TEMPO concentrations, and assuming and excitation probability of $\eta = 0.25$, evaluates to

$$\tau_{\mathrm{ID}} = \frac{9\sqrt{3}}{4\pi^2}\frac{4\pi}{\mu_0}\frac{1}{\gamma_{\mathrm{e}}^2\hbar\, C\eta} \approx 1600\ \mu\mathrm{s}, \tag{6.3}$$

which is not completely negligible for the low proton concentration samples with a T_{M} on the order of 100 μs. To account for instantaneous diffusion, we include a factor of

$$v_{\mathrm{ID}}(2\tau) = \exp\left(-\frac{2\tau}{\tau_{\mathrm{ID}}}\right) \tag{6.4}$$

in addition to the CCE simulations. With these assumptions, the Hahn echo decay is simulated with

$$v(2\tau) = \exp\left(-\frac{2\tau}{\tau_{\mathrm{ID}}}\right)\left\langle v^{\mathrm{N}}(2\tau)\right\rangle_{\mathrm{ori}}\left\langle v^{(2),\mathrm{H}}(2\tau)\ v^{(2),\mathrm{D}}(2\tau)\right\rangle_{\mathrm{ori,iso}}. \tag{6.5}$$

We used Monte-Carlo CCE to compute $\langle v^{(2),\mathrm{H}}(2\tau)\ v^{(2),\mathrm{D}}(2\tau)\rangle_{\mathrm{ori,iso}}$: we selected a random orientation and isotopologue, simulated the Hahn echo decay and accumulated it into an average signal. We repeated this procedure until the average signal converged. The convergence test we used started by finding the average signal from a randomly selected half of the configuration signals and calculating the RMSD with the other half. To hedge against non-representative ways of splitting the configuration signals, 1000 random ways of dividing the configuration signals were selected, and the average RMSD was compared against a threshold of 5e-3.

The CCE truncation parameters, system size and the dipole-dipole neighbor cutoff, were found separately for the fully protiated system and the fully deuterated system. Within each 100% system, the system size was incremented by 1 Å and then the neighbor cutoff was lowered by a factor of $10^{0.2}$ until neither changed the RMSD by 0.01 or more. The 100% protiated system converged to a system size of 11 Å in radius and 3.981 kHz neighbor cutoff, while the fully deuterated system converged to 16 Å and 63 Hz. These values were used to inform the choice of truncation parameters for the mixtures. Deuterons were included up to 16 Å from the central electron, while protons at a mole-fraction of x, were included up to

$$R_{^1\mathrm{H}}(x) = x^{-1/3}\ 16\ \text{Å}. \tag{6.6}$$

This keeps the total number of protons roughly constant. Different neighbor cutoffs were also implemented for protons and deuterons.

$$b_I(x) = \begin{cases} x \times 3981\ \text{Hz, for } {}^1\mathrm{H} \\ (1-x) \times 63\ \text{Hz, for } {}^2\mathrm{H} \end{cases}. \tag{6.7}$$

This choice scales the neighbor cutoffs with concentration so as to maintain a roughly constant number of clusters as x varies.

Truncation Parameter Convergence Check
To ensure these choices are reasonable, several isotope ratios were resimulated with $R_{^1\mathrm{H}}(x) = x^{-1/3}17$ Å and $b_I^{\mathrm{test}}(x) = 10^{-0.2}b_I(x)$. These are shown in figure 6.2. The resulting decays are very similar, suggesting that the truncation parameters are reasonable well converged for arbitrary proton fractions.

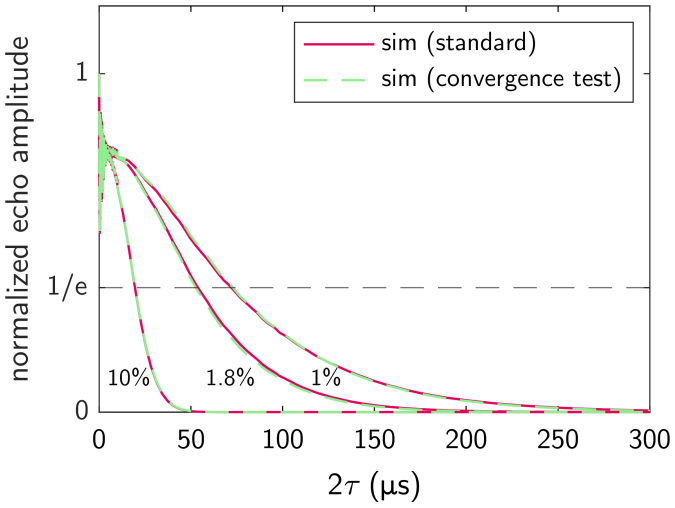

Figure 6.2: The Hahn echo decays with $R_{^1\mathrm{H}}(x) = x^{-1/3}$ 17 Å and $b_I^{\mathrm{test}}(x) = 10^{-0.2} b_I(x)$ for proton fractions in $\{1\%, 1.8\%, 10\%\}$ are shown with light green dashed lines. The red curves are the corresponding decays, simulated as discussed in the main text.

CCE Level Check

Due to the large number of simulations needed, the CCE was restricted to to 2-CCE. To estimate the error this caused, 3-CCE simulations were done for both the fully protiated and fully deuterated systems. Note that while the systems are not converged with respect to cluster level, the error is small compared to the time scale of the decay and so it is reasonable to assume 2-cluster are primarily responsible for the Hahn echo decay, and that higher-order clusters can be neglected for a coarse-grained view.

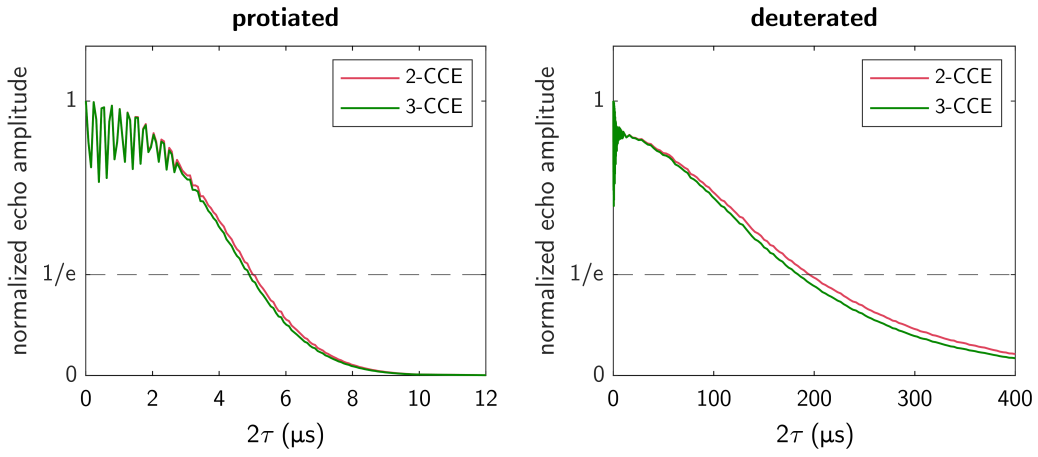

Figure 6.3: The fully protiated system's Hahn echo decay (left) and fully deuterated system's Hahn echo decay (right) are show above, simulated with both 2-CCE (red) and 3-CCE (green).

6.4 Results and Discussion

Figure 6.4 shows the results for the primary series where the proton-to-hydron ratio was varied by mixing fully deuterated water and glycerol with natural abundance water and glycerol; the experimental Hahn echo decays are plotted as normal with the color–axis communicating the proton to hydron fraction. The simulated Hahn echo decays for the same proton fractions are shown reflected below the 2τ-axis. The decays are scaled by fitting them to a stretched exponential decay:

$$V(2\tau) = V_0 \exp\Big(-(\frac{2\tau}{T_{\mathrm{M}}})^{\xi}\Big), \tag{6.8}$$

and dividing out the prefactor, V_0. Overall the agreement is fairly good; however, the simulations tend to over-predict T_{M} by approximately 20%. This is likely due to restricting the simulations to the 2-CCE level.

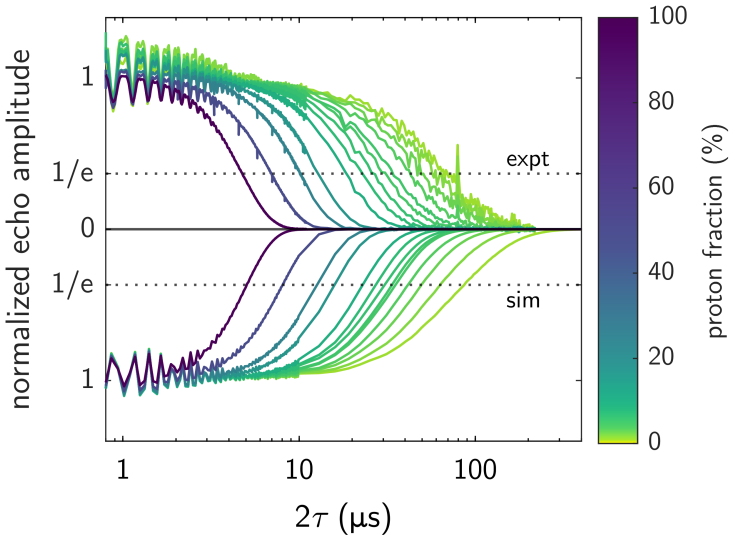

Figure 6.4: The experimental Hahn echo decays are shown above the 2τ-axis, while the simulated decays for the same proton fraction (color–axis), are reflected below the 2τ-axis. The decays were fit to stretched exponentials and then scaled by dividing out the fitted amplitude.

To better parse the data, figure 6.5 shows the fitted T_{M} and ξ vs. proton concentration, $[^1\mathrm{H}]$. Additionally figure 6.5 includes a fit to experimental $T_{\mathrm{M}}([^1\mathrm{H}])$, of the form

$$\log_{10}(T_{\mathrm{M}}/\mathrm{s}) = \log_{10}(T_{\mathrm{M}}(1\ \mathrm{M})/\mathrm{s}) - p\log_{10}([^1\mathrm{H}]/\mathrm{M}); \tag{6.9}$$

revealing

$$\begin{aligned} \log_{10}(T_{\mathrm{M}}(1\ \mathrm{M})/\mathrm{s}) = & -4.04 \pm 0.02; \\ p = & \ 0.64 \pm 0.02. \end{aligned} \tag{6.10}$$

Note that in [164], p was reported as 0.65: the proton concentration for the fully protiated data point was misentered by mistake. The error in [164] does not affect the conclusions. On one hand, one might expect that p equals one since dipole–dipole coupling scales as $1/r^3$, a quantity with units of 1/volume, and indeed this is consistent with [42] where $[^1\mathrm{H}]$ was changed by using different solvents, as well as with experimental [170] and simulated [171] electron spin driven electron spin decoherence, as well with $^{13}\mathrm{C}$ driven electron spin decoherence simulations [80, 172]. On the other hand, $p < 1$ is consistent with chapter 4 which follows [146], as well as the $p \approx 0.85$ from electron spin decoherence experiments on P donors in $^{29}\mathrm{Si}$ exploring the 4.7%–99.2% mole fraction range [173]. This suggests that p depends on the system.

Figure 6.5 also include a simulation series where the deuteron contribution $v^{(2),\mathrm{D}}(2\tau)$ was set to unity, removing any direct influence the deuterons may have. Notably, eliding the deuterons has very little influence

on either T_{M} or ξ, even down to $[^1\mathrm{H}] = 1$ M. This means that the observed $p = 0.64$ should have an explanation that depends only on the protons and not the deuterons.

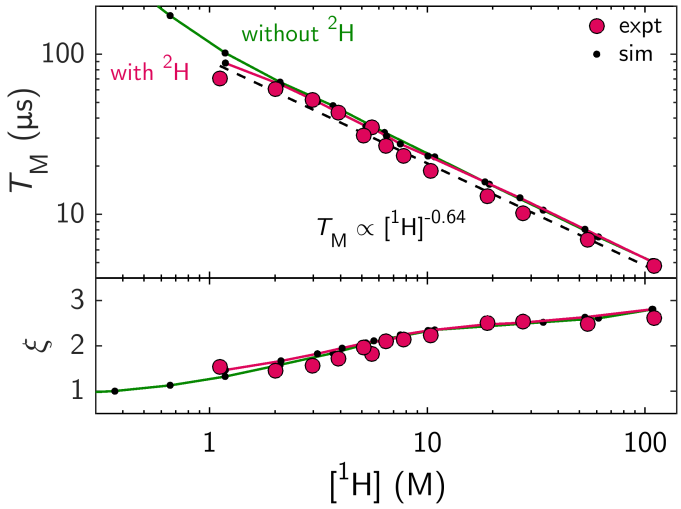

Figure 6.5: The stretched-exponential fit parameters are shown vs. proton concentration, $[^1\mathrm{H}]$. The top panel shows T_{M} and the bottom panel shows ξ. The experimental data is represented with red circles. The full simulations including both protons and deuterons are shown as dots connected with a red curve, while the simulations that elide the deuterons are similarly shown with green. Additionally, a fit to the experimental data is shown with a dashed curve.

6.4.1 Analytical approximation

In this section we will build a simple model of the concentration dependence of the coherence time. Although this model will ultimately fail, observing which assumption causes it to fail will provide some insights.

Instead of the full dipole–dipole Hamiltonian, we will only use the secular (zz) coupling and the flip-flop terms between nuclei.

$$\begin{aligned}\hat{H}_{\mathrm{dd}}(m_{\mathrm{S}}) \approx\ & \frac{\mu_0}{4\pi}\hbar^2\gamma_{\mathrm{e}}\gamma_{\mathrm{H}} m_{\mathrm{S}} \sum_n \frac{1-3\cos^2\theta_{en}}{|\boldsymbol{R}_n|^3}\hat{I}_{zn} \\ & + \frac{\mu_0}{4\pi}\hbar^2\gamma_{\mathrm{H}}^2 \sum_{m,\ n>m} \frac{1-3\cos^2\theta_{mn}}{|\boldsymbol{r}_{mn}|^3}\Big(\hat{I}_{zm}\hat{I}_{zn} - \frac{1}{4}\hat{I}_{+m}\hat{I}_{-n} - \frac{1}{4}\hat{I}_{-m}\hat{I}_{+n}\Big) \\ =:\ & \sum_n A_n m_{\mathrm{S}} \hat{I}_{zn} \\ & + \sum_{m,\ n>m} b_{mn}\Big(\hat{I}_{zm}\hat{I}_{zn} - \frac{1}{4}\hat{I}_{+m}\hat{I}_{-n} - \frac{1}{4}\hat{I}_{-m}\hat{I}_{+n}\Big).\end{aligned} \tag{6.11}$$

This allows the 2-CCE proton signal to be analytically expressed [34] with $\Delta A_{mn} := A_n - A_m$, $k_{mn} := (\frac{2b_{mn}\Delta A_{mn}}{b_{mn}^2+\Delta A_{mn}^2})^2$ and $\omega_{mn} := \frac{1}{8\hbar}\sqrt{b_{mn}^2 + \Delta A_{mn}}$ as

$$\begin{aligned} v(2\tau) &= \prod_{m=1}^{N-1}\prod_{n=m+1}^{N}\Big(1 - k_{mn}\sin^4(\omega_{mn}2\tau)\Big) \\ &=: \prod_{m=1}^{N-1}\prod_{n=m+1}^{N}\Big(1 - 2f_{mn})\Big). \end{aligned} \tag{6.12}$$

Using the approximation $1 - 2f_{mn} \approx \exp(-2f_{mn})$,

$$\begin{aligned} v(2\tau) &= \prod_{m,n>m} \exp\left(-2f_{mn}\right) + \mathscr{O}(f^2) = \exp\left(-2\sum_{m,n>m} f_{mn}\right) + \mathscr{O}(f^2) \\ &= \exp\left(-\sum_{m,n} f_{mn}\right) + \mathscr{O}(f^2). \end{aligned} \tag{6.13}$$

In the last step, the sum was changed to run over all m, n rather than requiring $n > m$. This requires defining $f_{nn} := 0 \;\forall\; n$. Next, in order to incorporate the different configurations, the single-configuration signal needs to averaged over all N_c configurations.

$$\begin{aligned} \langle v(2\tau)\rangle_\mathrm{config} &= \frac{1}{N_\mathrm{c}}\sum_{i=1}^{N_\mathrm{c}} \exp\Big(-\sum_{m,n} f^i_{mn}\Big) + \mathscr{O}(f^2) \\ &= 1 - \frac{1}{N_\mathrm{c}}\sum_{i=1}^{N_\mathrm{c}}\sum_{m,n} f^i_{mn} + \frac{1}{N_\mathrm{c}}\sum_{i=1}^{N_\mathrm{c}}\frac{1}{2!}\Big(\sum_{m,n} f^i_{mn}\Big)^2 + \mathscr{O}(f^2). \end{aligned} \tag{6.14}$$

In the second line, the exponential was Taylor expanded. The reason for doing this is to note that the error introduced by doing the sum inside the exponential rather than correctly outside is $\mathscr{O}(f^2)$, and so will be lumped in with the $\mathscr{O}(f^2)$ we already have.

$$\begin{aligned} \langle v(2\tau)\rangle_\mathrm{config} &= \frac{1}{N_\mathrm{c}}\sum_{i=1}^{N_\mathrm{c}} \exp\Big(-\sum_{m,n} f^i_{mn}\Big) + \frac{1}{2!}\Big(\frac{1}{N_\mathrm{c}}\sum_{i=1}^{N_\mathrm{c}}\sum_{m,n} f^i_{mn}\Big)^2 + \mathscr{O}(f^2) \\ &= \exp\Big(-\sum_{m,n}\frac{1}{N_\mathrm{c}}\sum_{i=1}^{N_\mathrm{c}} f^i_{mn}\Big) + \mathscr{O}(f^2). \end{aligned} \tag{6.15}$$

By defining a probability density function, $P(\boldsymbol{R}, \boldsymbol{r})$, the sum can be converted into an integral over the electron–proton separation $\boldsymbol{R}$, and proton–proton separation, $\boldsymbol{r}$.

$$v(2\tau) = \exp\Big(-\int \mathrm{d}^3\boldsymbol{r}\;\mathrm{d}^3\boldsymbol{R}\; f(\boldsymbol{R}, \boldsymbol{r}, 2\tau)P(\boldsymbol{R}, \boldsymbol{r})\Big). \tag{6.16}$$

The conversion from sum to integral is exact when the sum is included in $P(\boldsymbol{R}, \boldsymbol{r})$.

$$P(\boldsymbol{R}, \boldsymbol{r}) := \frac{1}{N_\mathrm{c}}\sum_i\sum_{m,n}\delta(\boldsymbol{R} - \boldsymbol{R}^i_m)\delta(\boldsymbol{R} - \boldsymbol{r}^i_{mn} - \boldsymbol{R}^i_m), \tag{6.17}$$

But if we assume no correlation between $\boldsymbol{R}$ and $\boldsymbol{r}$, then the probabilities can be factored apart:

$$P(\boldsymbol{R}, \boldsymbol{r}) \approx P(\boldsymbol{R})P(\boldsymbol{r}) \approx [^1\mathrm{H}]^2 g(\boldsymbol{R})g(\boldsymbol{r}). \tag{6.18}$$

The $[^1\mathrm{H}]$ is the proton concentration. Factoring $[^1\mathrm{H}]$ out allows us to put the expression in terms of the pair correlation functions; however, this assumes that the correlation functions $g(\boldsymbol{R})$ and $g(\boldsymbol{r})$, themselves are independent of proton concentration, which as we will soon see is not fully justified. Going back to the predicted signal,

$$v(2\tau) \approx \exp\Big(-[^1\mathrm{H}]^2\int \mathrm{d}^3\boldsymbol{r}\;\mathrm{d}^3\boldsymbol{R}\; g(\boldsymbol{R})g(\boldsymbol{r})f(\boldsymbol{R}, \boldsymbol{r}, 2\tau)\Big), \tag{6.19}$$

the total proton concentration factors out of the integral, which we will define as

$$F(2\tau) := \int \mathrm{d}^3\boldsymbol{r}\;\mathrm{d}^3\boldsymbol{R}\; g(\boldsymbol{R})g(\boldsymbol{r})f(\boldsymbol{R}, \boldsymbol{r}, 2\tau). \tag{6.20}$$

Empirically, the signal is a stretched exponential, so relating the two forms of $v(2\tau)$ gives

$$\exp\Big(-[^1\mathrm{H}]^2 F(2\tau)\Big) = \exp\Big(\big(-2\tau/T_\mathrm{M}\big)^\xi\Big) \tag{6.21}$$

implying

$$T_\mathrm{M}^{-\xi} \propto [^1\mathrm{H}]^2. \tag{6.22}$$

In other words,

$$T_\mathrm{M} \propto [^1\mathrm{H}]^{-2/\xi}. \tag{6.23}$$

And

$$p = -\frac{\mathrm{d}\ln(T_\mathrm{M}/1\ \mathrm{s})}{\mathrm{d}\ln([^1\mathrm{H}]/1\ \mathrm{M})} = \frac{2}{\xi} + \frac{\ln(T_\mathrm{M}/1\ \mathrm{s})}{\xi}\frac{\mathrm{d}\xi}{\mathrm{d}\ln([^1\mathrm{H}]/1\ \mathrm{M})} \approx \frac{2}{\xi}. \tag{6.24}$$

In the dilute limit, it is reasonable to neglect exclusion volumes and assume uniform constant correlation functions: $g(\boldsymbol{R}) = g(\boldsymbol{r}) = 1$. When this assumption is used, $F(2\tau) \to F_{0,0}(2\tau)$, to indicate 0 exclusion volume for either correlation function. The signal now takes the form

$$v(2\tau) = \exp\Big(-[^1\mathrm{H}]^2 F_{0,0}(2\tau)\Big). \tag{6.25}$$

In this limit, diluting $[^1\mathrm{H}] \to a[^1\mathrm{H}]$, the unitless a can be moved into the integral via

$$F_{0,0}(2\tau) \to a^{-2} F_{0,0}(a\cdot 2\tau). \tag{6.26}$$

So that

$$\begin{aligned} v(2\tau, a) &= \exp\Big(-[^1\mathrm{H}]^2 F_{0,0}(a\cdot 2\tau)\Big) \\ &= v(a\cdot 2\tau). \end{aligned} \tag{6.27}$$

This means that as $[^1\mathrm{H}] \to 0$, we expect T_M to scale as a, meaning $\xi \to 2$, and $p \to 1$. Unfortunately, this cannot be directly tested via experiment, since even in the case that sub-molar proton concentrations could be achieved, the coherence time would be limited by deuteron-driven electron spin decoherence, as well as instantaneous diffusion. Luckily these limits can be circumvented in silico by dropping the deuterons and instantaneous diffusion from the simulations. Simulations for two cases are shown in figure 6.6, simply dropping the other sources of decoherence, and additionally treating all protons as solvent exchangeable, regardless of their chemical environment.

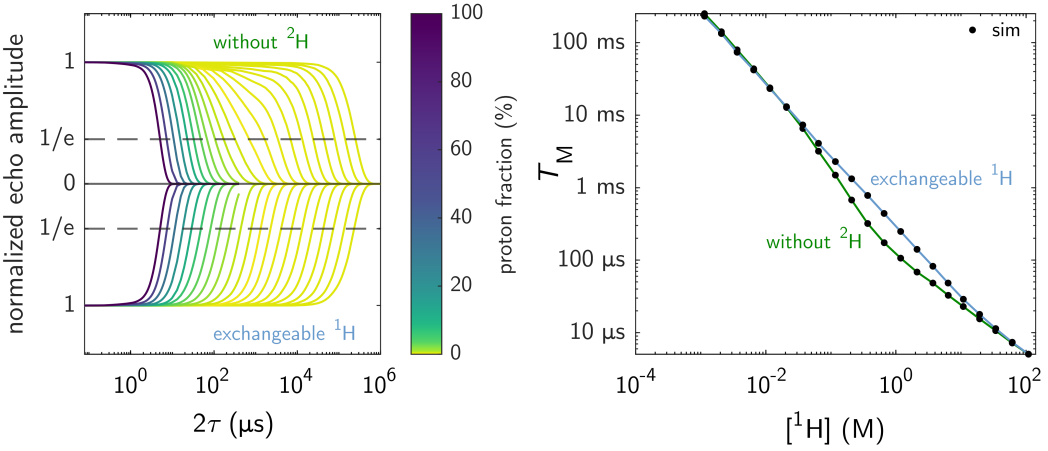

Figure 6.6: The left panel shows the primary Hahn echo simulations vs. 2τ, colored by proton fraction for the proton-only simulation (top), and the all solvent exchangeable proton simulation (inverted). The right plot shows the fitted $T_\mathrm{M}([^1\mathrm{H}])$.

Figure 6.7 shows the fitted ξ for the experimental data, the proton-only simulations, and the simulations where in addition to only including protons, all the protons are also treated as solvent exchangeable regardless of bonding environment. Figure 6.7 also shows p for the same cases; for the experimental data, $p = 0.64$ from the fit, while for the simulations, the p comes from the numerical derivatives. While the proton-only simulations agree reasonably with the experiments, neither displays the predicted relationship between ξ and p; however, the fully exchangeable simulation series does follow the $p = 2/\xi$ trend predicted from the simple model. This suggests the spatial correlations between the protons is non-negligible and worth further investigation.

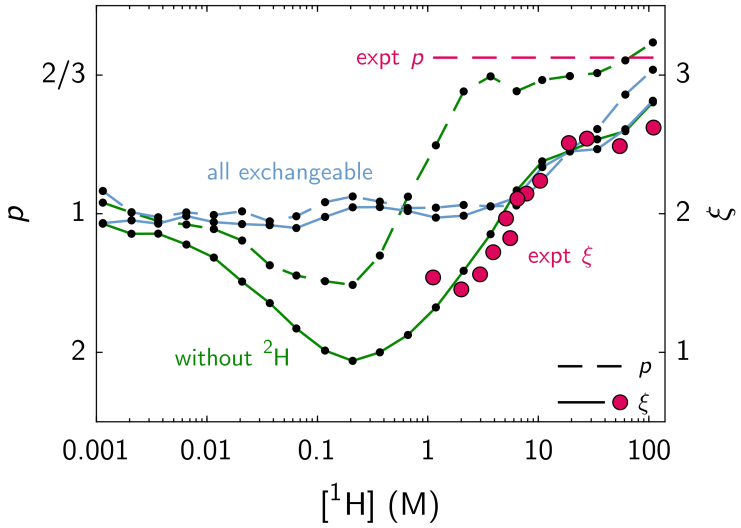

Figure 6.7: The dashed lines show p (left ordinate) vs. concentration, and the solid lines and circles show ξ (right ordinate) vs. [^{1}H]. Red shows experimental data. Green shows the proton-only simulations, and blue shows the proton-only simulations where all protons are assumed to be solvent exchangeable. The two ordinates are set up so that under the simple model's $p = 2/\xi$ prediction, the dashed lines and solid lines should overlap. This only occurs for the all-exchangeable series.

6.4.2 Spatial Correlation Between Protons

The failure of the simple model suggested that spatial correlations from solvent non-exchangeable protons are important in determining a system's electron spin decoherence behavior. To study this we will introduce two other isotopologues of glycerol: d_3-glycerol and d_5-glycerol. Glycerol, $C_3H_5(OH)_3$, has three solvent exchangeable hydrons and five solvent non-exchangeable hydrons. This means that the isotopic identity of the five non-exchangeable hydrons will be correlated. For example in a 99% deuterated solution, a randomly selected hydron will have a 1% chance of of being a proton; however, if that proton is one of glycerol's CH hydrons, the chance the other four CH hydrons are also protons is both very high and independent of the bulk concentration. To investigate what role this has on decoherence, two other data sets were experimentally and computationally examined. Starting from a 99% deuterated solution, protons were introduced either on exchangeable OH bonds (via H_2O:d_5-glycerol) or on non-exchangeable CH bonds (with D_2O:d_3-glycerol). These primary data are shown in figure 6.8, and the fitted T_Ms are shown in figure 6.9(A).

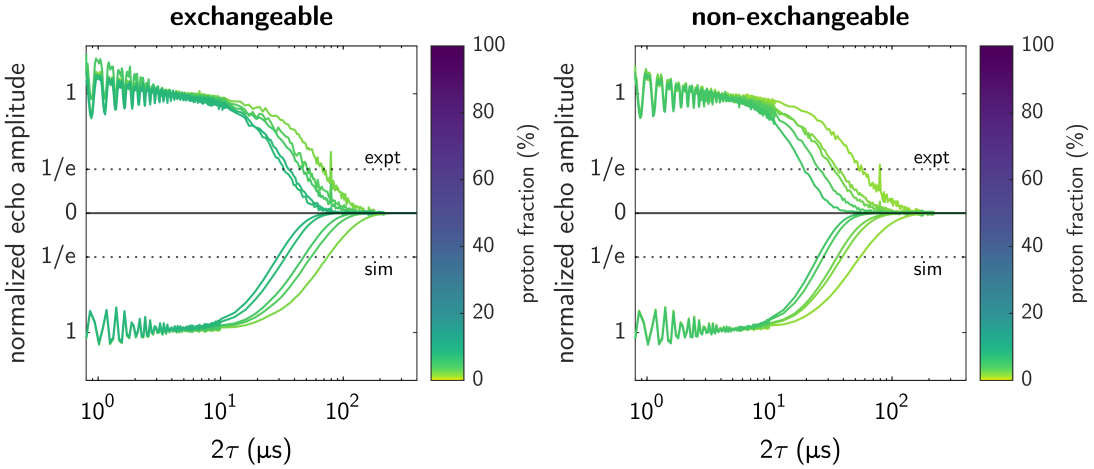

Figure 6.8: The left plot shows the Hahn echo decays for the O^1H substitution series, and the right plot shows the C^1H_5 substitution series' Hahn echo decays. The experimental data are above the 2τ-axis, while the corresponding simulations are reflected below the 2τ-axis. Again, the color–axis indicates the proton fraction.

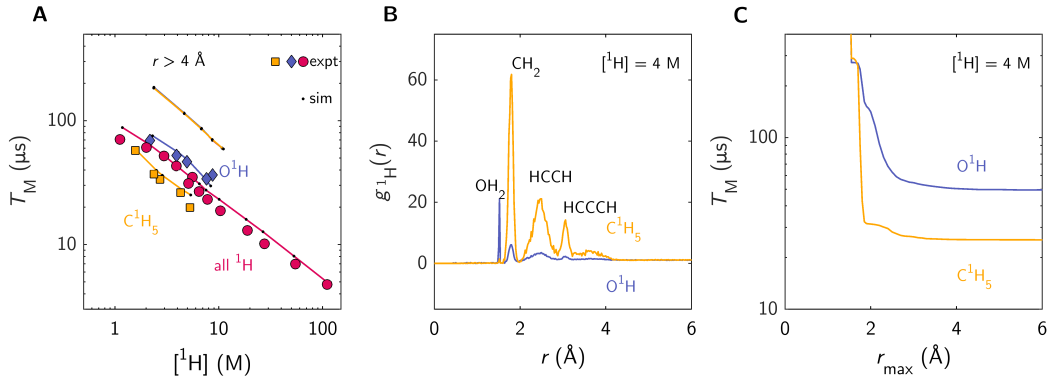

Figure 6.9: Panel A shows the coherence time as proton concentration is varied. The all ^1H series (red, circle for experimental data and a dotted line for the simulations) introduces protons by adding H_2O and glycerol to the fully deuterated solution. The C^1H_5 series (yellow, squares for the experimental data and a dotted line for the simulations) adds protons by mixing in D_2O and d_3-glycerol to the fully deuterated solution. The O^1H series (blue, diamonds for the experimental data and a dotted line for the simulations) uses H_2O and d_5-glycerol to increase the proton concentration. The simulation labeled with "$r > 4$ Å", use only clusters where the protons are separated by at least 4 Å are included. Panel B shows $g(r)$ calculated from the MD structure for the C^1H_5 series and O^1H series, both at a proton concentration of 4 M. The peaks are labeled with their corresponding proton pairs. Panel C show the T_M for each of the systems in panel B, were 2-clusters were only included if the protons were separated by the distance on the abscissa or less. Note that because stretched-exponential fits failed for short r_{max}s, these T_Ms are the time at which the echo amplitude equals 1/e times the initial amplitude, rather than the T_M from fitting to a stretched exponential.

Figure 6.9 A shows T_M vs. proton concentration, filled circles for the experimental data and dots connected by lines for the simulation. Shown in red, is the all ^1H substitution series seen earlier. Blue shows the O^1H substitution series, while yellow shows the C^1H_5 substitution series. Note that for a given bulk $[^1H]$, the O^1H substitution series, where the proton positions are least correlated with each other, has the longest T_M, while the C^1H_5 substitution series, where the protons are more spatially correlated, has the shortest T_M, and the all ^1H series with an intermediate level of spatial correlation between the protons, has an intermediate T_M.

To help make sense of this, figure 6.9(B) shows the Radial Distribution Functions (rdfs) for an O^1H

substituted sample and a C^1H_5 at $[^1H] = 4$ M, calculated from the same PDB file used for the simulations. The peaks indicate distances where the relative probability of finding a proton is higher than the bulk probability. The peaks are labeled to show which proton pairs are primarily responsible for the peaks. Note that the C^1H_5 correlations are strong enough that glycerol's CH_2, HCCH, and HCCCH peaks are visible in the O^1H sample's rdf even with 99% deuterated glycerol. In contrast the O^1H_2 peak is barely visible in the rdf of the C^1H_5 sample for 99% deuterated water.

Figure 6.9(C) shows the T_M from simulation only including clusters separated by distances up to the distance shown on the abscissa. For the C^1H_5 system, the primary distances where the T_M drops correspond to the separation between glycerol's geminal protons with a smaller but still significant drop at the distance of glycerol's vicinal protons. The O^1H_2 sample's T_M only drops slightly further at the OH_2 separation, and a majority of the T_M reduction occurs at the distances corresponding glycerol's geminal and vicinal protons, although the drops are broader than in the C^1H_5 sample and do not drop as far. The broadness likely comes from O^1H pairs at similar separations, but the C^1H_5 clusters from the 1% protiated glycerol still appears to be playing an important role in driving electron spin decoherence.

This provides evidence that it is these correlated C^1H_5 clusters that are primarily responsible for the differences between the three substitution series. As a further test, figure 6.9(A) includes a set of simulations where only protons separated by at least 4 Å are included. Naturally this leads to longer coherence times, but notably all three series lie atop each other.

The analytic 2-CCE from [34] and equation (6.12) has two energy parameters: one from the secular hyperfine coupling ($m_S A_n \hat{I}_{zn}$) and the other from the secular dipole–dipole coupling ($b_{mn}\hat{I}_{zm}\hat{I}_{zn}$) via $\Delta A_{mn} := A_n - A_m$, and b_{mn}. These define a modulation frequency:

$$\omega_{mn} := \frac{1}{8\hbar}\sqrt{b_{mn}^2 + \Delta A_{mn}^2}, \tag{6.28}$$

and a modulation depth

$$k_{mn} := \left(\frac{2b_{mn}\Delta A_{mn}}{b_{mn}^2 + \Delta A_{mn}^2}\right)^2. \tag{6.29}$$

The modulation depth goes to one when $|b_{mn}| = |\Delta A_{mn}|$, and the modulation frequency increases with both $|b_{mn}|$ and $|\Delta A_{mn}|$. The five non-exchangeable protons of h_8-glycerol and d_3-glycerol are well positioned to maximize $|b_{mn}|$, which will increase the ω_{mn} for which $|\Delta A_{mn}|$ and $|b_{mn}|$ are on a comparable scale. This is important since if $1/\omega_{mn} \gg T_M$, the electron spin coherence will have faded before the cluster can contribute. The relevant 2-clusters will still likely have $|b_{mn}| < |\Delta A_{mn}|$, and $k_{mn} < 1$, but the five protons on h_8-glycerol and d_3-glycerol still contribute to more significant clusters than a typical OH proton and so systems with CH_5 clusters have shorter T_M than the equivalent system without the CH_5 clusters, explaining the $p < 1$.

4 M Proton Decays vs. Separation
Figure 6.10 shows the simulated echo decays used for figure 6.9C. Note that the color–axis is $r_{\max}$ as the proton concentration is fixed at 4 M.

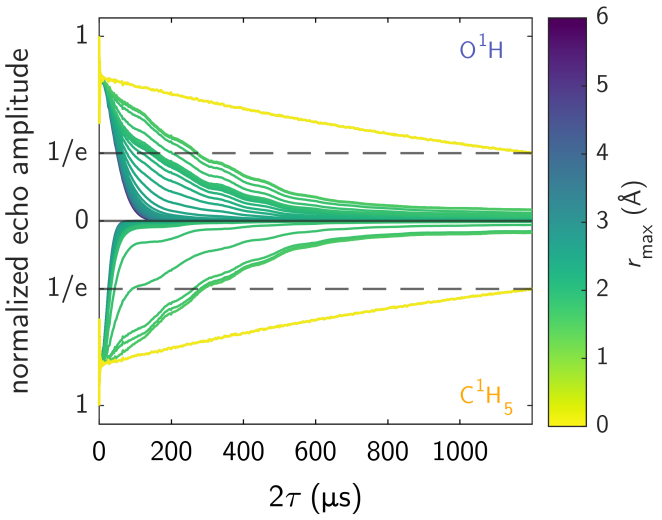

Figure 6.10: Shown here are the simulated Hahn echo decays for the O^1H series (top), and the C^1H_5 series (inverted) at $[^1H] = 4$ M as a function of the maximum included protoni–proton separation (color–axis).

Deuteron Electric Quadrupole Error
Deuterons have an electric quadrupole moment. For the quadrupole coupling the simulations assume that $e^2qQ/h = 213.4$ kHz for O^2H deuterons, which was chosen to match the experimental value in hexagonal ice [174]. To get a sense of the possible error, ices V,VI,VII,IX have $e^2qQ/h \in [220, 236.2]$ kHz [175], or for D_2O in L-serine hydrate, $e^2qQ/h = 240.5$ kHz [176]. As for the C^2H deuterons, a DFT simulation on TEMPO gave $e^2qQ/h = 194.5$ kHz and this value was used for all C^2H deuterons.

To evaluate the impact that an error in the e^2qQ/h could cause, simulations were ran at 1% protiation, varying either O^2H or C^2H e^2qQ/h values. The simulations included instantaneous diffusion and nitrogen ESEEM in the same way as described in equation (6.5). The T_Ms from these simulations are shown in figure 6.11, and together the fitted gradient is

$$\nabla_{e^2qQ/h} T_M = (0.04 \pm 0.05 \frac{\mu s}{kHz})(\widehat{\frac{e^2qQ}{h}})_{OH} + (-0.01 \pm 0.04 \frac{\mu s}{kHz})(\widehat{\frac{e^2qQ}{h}})_{CH}. \quad (6.30)$$

The gradient is in e^2qQ/h-space with $(\widehat{\frac{e^2qQ}{h}})_{OH}$ and $(\widehat{\frac{e^2qQ}{h}})_{CH}$ representing unit vectors along the O^2H or C^2H e^2qQ/h-directions respectively. Starting from $T_M = 91$ μs at a 1% proton fraction and assuming a constant gradient, e^2qQ/h could have a 27 kHz error and T_M would only be expected to change by about 1 μs. This suggests that errors in e^2qQ/h are likely negligible here.

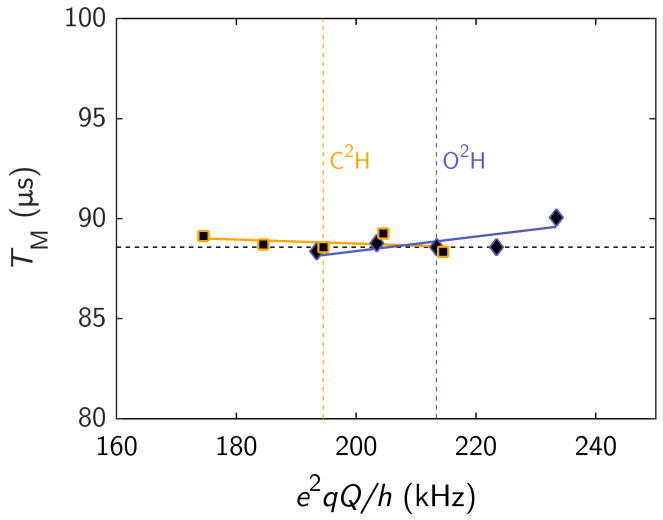

Figure 6.11: Fixing the proton fraction at 0.01, the T_M from simulations where either the O^2H (blue diamonds) or C^2H (yellow squares) e^2qQ/h was varied. The abscissa represents the e^2qQ/h that is varied. The horizontal dashed line is the T_M from using unvaried e^2qQ/h values and the vertical lines indicate those unvaried e^2qQ/h values.

6.5 Conclusion

When present, even at only a small percentage, protons are much better drivers of decoherence compared to deuterons. As a consequence of the $T_M \propto [^1H]^{-0.64}$, the largest absolute increase in coherence times, comes by removing protons from systems with already low proton concentrations ($[^1H] < 10$ M). Even at a constant $[^1H]$, protons that are clustered together are stronger sources of decoherence, so even if removing the protons is not an option, avoiding proton clusters (especially geminal protons) should improve coherence times. These conclusions should generalize to other spin–1/2 nuclei limited coherences, such as in systems limited by ^{13}C or ^{29}Si.

Partially deuterated matrices
can extend the coherence time. Yes please!
Now speaking of T_M, how does it go
with the proton to hydron ratio?
It depends on more than concentrations?
Yes, it depends on correlations.

Chapter 7

Methyl-Driven Decoherence

Acknowledgements
This chapter details work pending publication. The experimental data of TEMPO in n-propanol and glycerol was collected by Rachelle Stowell, University of Washington, Seattle. The TEMPO in water and glycerol data is the same as was discussed in chapter four, originally published in [127]. The principal investigator for this work was Stefan Stoll, University of Washington, Seattle. I set up and ran Molecular Dynamics (MD) and Cluster Correlation Expansion (CCE)[1, 2] simulations. I also did the methyl contribution analysis.

Methyl groups (CH_3) are ubiquitous in organic and biochemical systems. Even at low temperatures, the three hydrogens of the methyl group are usually within tunneling range of each other, and so a correct description of methyl groups must treat methyl groups as a single three-body system rather than three single-body systems[61]. Figure 7.1 shows an overview of the methyl model: figure 7.1(A) shows a Lewis structure of a methyl rotor, along with the pertinent rotational degree of freedom. Figure 7.1(B) illustrates a minimal rotational potential function that captures the relevant physics. Figure 7.1(C) shows a numerical rotational spectrum against the potential barrier height. And figure 7.1(D) shows the tunnel splitting as a function of barrier height.

Methyl groups are known to affect electron spin decoherence [22, 26, 60], and indeed, in chapter 4, we saw in figure 4.4 on page 58 that CCE simulations that neglected methyl tunneling did not reproduce the shape of the experimental Hahn echo decay for h_{18}-TEMPO in water and glycerol, despite getting the correct timescale. In chapter 3, we discussed the theory of methyl groups in more detail, including the necessary modifications to the spin Hamiltonian to incorporate methyl tunneling effects into the Cluster Correlation Expansion (CCE [1, 2]). In summary, for a system with N nuclei,

$$\hat{H}_{\text{methyl}} = \sum_{m=1}^{N-1} \sum_{n=m+1}^{N} J_{mn} \hat{\boldsymbol{I}}_m^{\mathrm{T}} \hat{\boldsymbol{I}}_n \tag{7.1}$$

must be added to the spin Hamiltonian, with

$$J_{mn} := \begin{cases} -\frac{2}{3}\hbar\omega_{\mathrm{t}}, \ m \text{ and } n \text{ on the same methyl, which has tunnel splitting } \hbar\omega_{\mathrm{t}} \\ 0, \ \text{otherwise} \end{cases} , \tag{7.2}$$

as derived by Apaydin-Cloug [108], and applied to CCE in [46]. In this chapter, we will apply the methyl theory to several systems, TEMPO in water and glycerol, as well as in n-propanol and glycerol, and lastly an isolated methyl group.

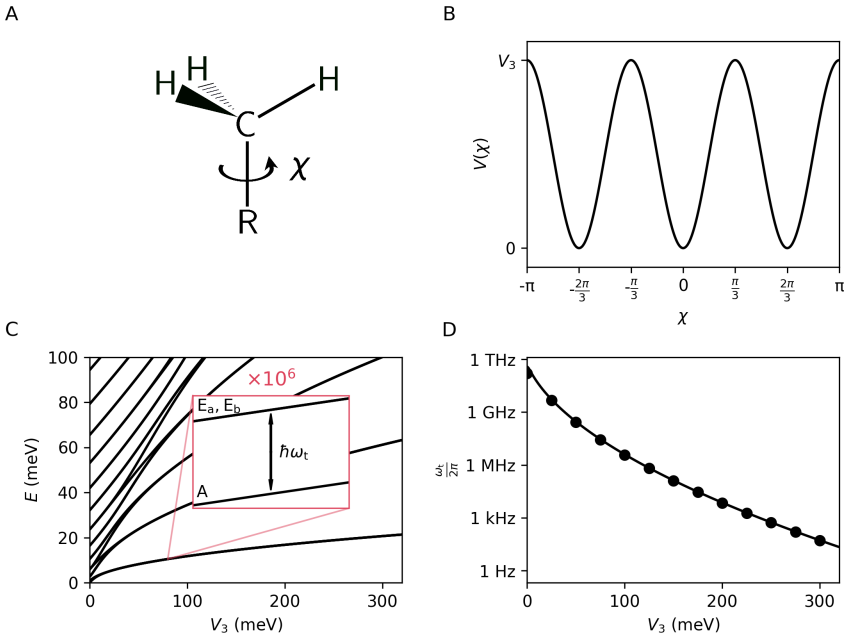

Figure 7.1: **A** shows a Lewis structure of a methyl rotor, with the rotation–axis illustrated by χ. **B** plots the rotational potential $V(\chi) = V_3\frac{\cos(3\chi)+1}{2}$. **C** shows a numeric solution of the Schödinger equation as in [125], by using the 77 lowest free-rotor wavefunctions to diagonalize the hindered rotor Hamiltonian. The inset shows a zoom in by a factor of a million on the $l = 0$ levels around $V_3 = 80$ meV, where the tunnel splitting is indicated as the gap between the A and E states. The tunnel splitting at $V_3 = 80$ meV is $\nu_t = 18$ MHz. **D** plots the tunnel splitting across the numerical [0,300] meV range with dots, as well the analytic approximate tunnel splitting from [123] with the curve.

7.1 Molecular Dynamics

In this chapter we will be looking at TEMPO in two different solvents, 1:1 mass:mass water:glycerol and 1:3 volume:volume *n*-propanol:glycerol. In both cases, there are four methyl groups on TEMPO, but in the water/glycerol solvent there are no other methyl groups, while in *n*-propanol/glycerol solvent, there are also methyl groups on the *n*-propanols. Since methyl groups can cause significant modulations even in small numbers, we were concerned that a single Molecular Dynamics (MD) frame (as we have used before), might not be representative enough of the methyl distribution to give an accurate CCE prediction. To address this concern, the MD methodology was modified from the previously described methods; however, as discussed in the following box, a single frame with sufficient orientation averaging would likely suffice for the systems discussed here.

As before, the molecular dynamics simulations were done in GROMACS, with the CHARMM36 force-field. The steps used for both TEMPO in water/gycerol and TEMPO in *n*-propanol/glycerol were nearly identical. The initial structures were TEMPO with 3026 waters and 600 glycerols randomly placed, and TEMPO surrounded by 251 *n*-propanols and 775 glycerols, randomly placed. These numbers were chosen to reach a final box size of 50 Å per side; however, the initial boxes were intentionally oversized to ensure all the molecules would be easily fit. Prior to a production run, an energy minimization was run, and the systems were time-evolved under NVT and the NPT conditions for 100 ps, each in 2 fs steps at 300 K. Next, using the particle mesh Ewald method for long-range electrostatics, the systems were time-evolved for 85 ns in 1 fs steps at 300 K using the V-rescale modified Berendsen thermostat and at a pressure of 1 bar held by the Parrinello–Rahman barostat. Unlike before, no time–evolution at 100 K was used. The final 60 ns of the MD simulation were kept in 301 frames, separated by 0.2 ns. The final box sizes were 54.9 Å per side for the

TEMPO in water/glycerol system and 50.4 Å per side for the TEMPO in n-propanol/glycerol system.

Orientaion vs. Frame Averaging
To check how important using multiple frames from the MD simulation is, below is the Hahn echo decay for TEMPO in n-propanol/glycerol. There are two different simulations. The green simulation is the one from this text, where 301 MD frames spanning 60 ns were averaged over, each frame rotated randomly. The red dashed simulation uses the single frame from 25 ns into the MD trace, and averages over 302 Lebedev orientations [139]. Otherwise, the simulation procedures are identical to what is described in the main text, with 80 kHz tunnel splitting for the TEMPO methyls and 40 kHz tunnel splitting for the n-propanol methyls. The two simulation are close to each other, and so it appears that at least in this case, it is not necessary to use multiple MD frames. The experimental data is scaled the same as in figure 7.7.

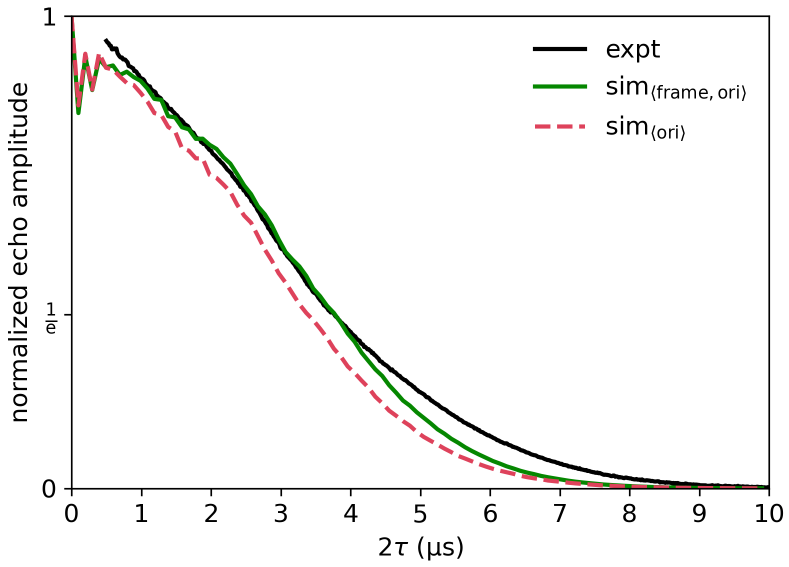

Figure 7.2: The above Hahn echo decay vs. 2τ includes the experimental data in black, the simultaneous frame and orientation averaged simulation in green, and the single frame orientation averaged simulation in red with a dashed line.

7.2 Neighbor Cutoffs

7.2.1 An Improved Neighbor Cutoff

The number of possible clusters for a given size scales combinatorially. Since often most clusters do not contribute much, it is common to apply a neighbor cutoff when forming clusters, and to only evaluate clusters that form either connected graphs or complete graphs, where edges are defined between two vertices (nuclei), if they satisfy the neighbor cutoff. This procedure uses the assumption that n-clusters that contribute significantly contain $(n-1)$-clusters that contribute significantly, which contain significant $(n-2)$-clusters, which eventually contain significant 2-clusters. The idea of the neighbor cutoff is used to select the 2-clusters that are most likely to contribute significantly to the calculation. Importantly, to be useful, the significance estimation must be more efficient than evaluating the cluster signal. Typically 2-clusters are kept if they

are within the system radius and the two nuclei are separated by a distance less than a cutoff distance [34, 36, 127], or the dipole–dipole coupling is above a threshold [46, 64, 146, 164]. Here, we will derive a pair of neighbor cutoffs specialized for the Hahn echo by investigating a simplified spin Hamiltonian.

The Hahn echo for

$$\begin{aligned}\hat{H}(m_{\mathrm{S}}) = & -(-g_{zz}\mu_{\mathrm{B}})B_0 m_{\mathrm{S}} - (g_{\mathrm{p}}\mu_{\mathrm{B}})B_0 \sum_n \hat{I}_{zn} \\ & + m_S \sum_n A_n \hat{I}_{zn} \\ & + \sum_m \sum_{n>m} b_{mn}\Big(\hat{I}_{zm}\hat{I}_{zn} - \frac{1}{4}\left(\hat{I}_{+m}\hat{I}_{-n} + \hat{I}_{-m}\hat{I}_{+n}\right)\Big)\end{aligned} \tag{7.3}$$

is analytically solvable[34]. While this does neglected some terms from the more full Hamiltonian which cause echo modulations, 2-CCE from this simplified Hamiltonian accounts for a signifiant part of the Hahn echo decay. Inspired by [177], we can use the three-spin solution to choose a cluster cutoff. Defining $\Delta A_{mn} := A_n - A_m$, $k_{mn} := \left(\frac{2b_{mn}\Delta A_{mn}}{b_{mn}^2+\Delta A_{mn}^2}\right)^2$, and $\omega_{mn} := \frac{\sqrt{b_{mn}^2+\Delta A_{mn}^2}}{8\hbar}$, the three-spin signal from protons m and n is

$$v_{mn}(2\tau) = \tilde{v}_{mn}(2\tau) = 1 - k_{mn}\sin^4(\omega_{mn}2\tau). \tag{7.4}$$

Since 1-clusters do not contribute under this model, the 2-cluster signal and the 2-cluster auxiliary signal are the same: $v_{mn}(2\tau) = \tilde{v}_{mn}(2\tau)$. For $\omega_{mn}2\tau \gtrapprox 1$, the most this can deviate from unity is the modulation depth k_{mn}. For $\omega_{mn}2\tau \ll 1$, it is helpful to look at the Taylor series.

$$\tilde{v}_{mn}(2\tau) = 1 - k_{mn}\omega_{mn}^4(2\tau)^4 + \mathcal{O}\left((2\tau)^6\right). \tag{7.5}$$

So the deviation from unity for $\omega_{mn}2\tau \ll 1$, is governed by $k_{mn}\omega_{mn}^4$.

Here, based on [177], we set the system radius to 25 Å, so as to be large enough not to limit the simulations. We next chose $k_{mn}\omega_{mn}^4$ and k_{mn} as cutoff parameters. Higher-order Carr–Purcell sequence have analytic three spin solutions as well [177], so similar cutoff parameters could be found.

To explore this cutoff, the full proton-only 2-CCE Hahn echo for TEMPO solvated in water and glycerol (4280 protons) for a single orientation and MD frame, was simulated, using the Hamiltonian of [34], and found that $k_{\mathrm{cutoff}} = (323\ \mu\mathrm{s}^4\mathrm{rad}^{-4})(k\omega^4)_{\mathrm{cutoff}}$ selects for the important 2-clusters reasonably well, and that a $k\omega^4$ cutoff of 10^{-7} $(\mathrm{rad}/\mu\mathrm{s})^4$ and a modulation depth cutoff of 323×10^{-7} works well to balance convergence and computational time. These are the cutoff values we use going forward. Figure 7.3 shows the analysis.

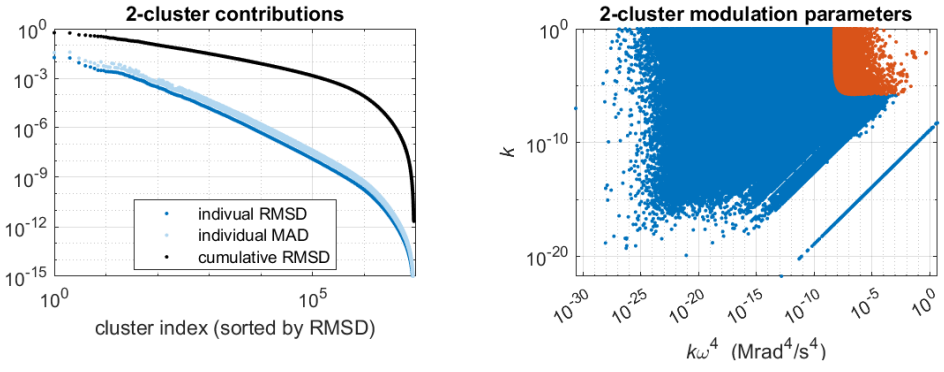

Figure 7.3: In the left plot, the contribution of each 2-cluster is shown sorted by contribution: dark blue shows the RMSD of the Hahn echo decay with and without each cluster; light blue shows the Maximum Absolute Deviation (MAD) of the Hahn echo decay with and without each cluster; black shows the cumulative RMSD for full Hahn echo simulation and the Hahn echo simulated using the n clusters with the highest individual RMSD, where n is given by the cluster index. The right plot shows all 9,157,060 2-clusters placed in ($k_{mn}\omega_{mn}^4$,k_{mn})-space. The 10,000 clusters with the greatest individual RMSD are show in orange, while the remaining are shown in blue.

7.2.2 Incorporating Methyl Exchange Coupling into the Neighbor Cutoff

The exchange coupling acts as another nucleus–nucleus coupling, and so should be accounted for when applying neighbor cutoffs to determine which clusters to include in the CCE calculations. To this end we will return to the three-spin system of an electron and two protons, as it is analytically solvable if the hyperfine coupling is approximated as $\hat{S}_z A_n \hat{I}_{z,n}$, and the dipole–dipole coupling is approximated as $b_{mn}(\hat{I}_{zm}\hat{I}_{zn} - \frac{1}{4}\hat{I}_{+m}\hat{I}_{-n} - \frac{1}{4}\hat{I}_{-m}\hat{I}_{+n})$ [34]. The details are discussed in chapter 2. Adding the methyl tunnel splitting to the spin Hamiltonian that allows for an analytic 2-CCE gives

$$\begin{aligned}\hat{H}(m_{\mathrm{S}}) = & -(-g_{zz}\mu_{\mathrm{B}})B_0 m_{\mathrm{S}} - (g_{\mathrm{p}}\mu_{\mathrm{B}})B_0 \sum_n \hat{I}_{zn} \\ & + m_S \sum_n A_n \hat{I}_{zn} + \sum_m \sum_{n>m} 3J_{mn}\hat{I}_{zm}\hat{I}_{zn} \\ & + \sum_m \sum_{n>m} (b_{mn} - 2J_{mn}) \\ & \quad \times \Big(\hat{I}_{zm}\hat{I}_{zn} - \frac{1}{4}\Big(\hat{I}_{+m}\hat{I}_{-n} + \hat{I}_{-m}\hat{I}_{+n}\Big)\Big).\end{aligned} \tag{7.6}$$

Apart from the $\sum_m \sum_{n>m} 3J_{mn}\hat{I}_{z,m}\hat{I}_{z,n}$, the form of the spin Hamiltonian differs from the one in [34], only by the substitution $b_{mn} \to b'_{mn} := b_{mn} - 2J_{mn}$. Next, we will show that the introduction of $\sum_m \sum_{n>m} 3J_{mn}\hat{I}_{z,m}\hat{I}_{z,n}$ does not affect the solution. The first step is to note that for a three-spin system $\hat{H}(m_S)$ is block diagonal: two one-dimensional blocks of $|\alpha\alpha\rangle$ and $|\beta\beta\rangle$ and a two-dimensional block that mixes $|\alpha\beta\rangle$ and $|\beta\alpha\rangle$. Next, examining

$$3J_{mn}\hat{I}_{z,m}\hat{I}_{z,n} = \frac{3J_{mn}}{4}\begin{bmatrix}1 & 0 & 0 & 0\\ 0 & -1 & 0 & 0\\ 0 & 0 & -1 & 0\\ 0 & 0 & 0 & 1\end{bmatrix}, \tag{7.7}$$

and noting that within each of the Hamiltonian blocks $3J_{mn}\hat{I}_{z,m}\hat{I}_{z,n} \propto \mathbb{1}$, meaning that it will not contribute to the three-spin solution nor to 2-CCE. The 2-CCE Hahn echo under this model is

$$\begin{aligned}v^{(2)}(2\tau) = & \prod_{m<n}\left(1 - \Big(\frac{2b'_{mn}\Delta A_{mn}}{b'^2_{mn} + \Delta A^2_{mn}}\Big)^2 \sin^4\big(\frac{\sqrt{b'^2_{mn} + \Delta A^2_{mn}}}{8\hbar}2\tau\big)\right) \\ =: & \prod_{m<n}\Big(1 - k_{mn}\sin^4(\omega_{mn}2\tau)\Big).\end{aligned} \tag{7.8}$$

This means that when evaluating neighbor cutoffs, the tunnel splitting can be accounted for by using b'_{mn} instead of b_{mn}, when evaluating k_{mn} and $k_{mn}\omega^4_{mn}$.

7.3 TEMPO in a Methyl-Free Solvent

7.3.1 Experiment

The experimental details for the TEMPO in water/glycerol solution are described in chapter 4, and in [127], but are restated here for completeness. The TEMPO in water/glycerol were performed by Elizabeth Canarie. The temperature was set to 20 K. The magnetic field was about 1.2 T, with microwave irradiation at 33.8 GHz (Q-band), from a Bruker Elexsys E580 spectrometer, amplified by a 300 W TWT amplifier (Applied Systems Engineering). Samples were placed in a Bruker D2 dielectric resonator. An echo-detected field sweep was used to determine the magnetic field that would maximize the signal-to-noise ratio, while keeping dispersion low. Spin flip angles were set by varying the pulse lengths, and calibrated by Rabi oscillation experiments: $t_{\pi/2} = 26$ ns, and $t_{\pi} = 52$ ns. The minimum τ used was 200 ns. The T_1 time was estimated to be on the order of a second by varying the shot repetition time until there were no observable changes to the echo amplitude; this occurred roughly in the range of $[0.7, 1]$ s.

7.3.2 Simulation Convergence

When implementing methyl tunneling into CCE, occasionally we would get predicted echo amplitudes significantly greater than the initial amplitude, especially for large tunnel splittings. Upon investigation, clusters that contain partial methyl groups appear to be causing this unphysical behavior. For this reason, we dropped all clusters containing partial methyl groups, from our CCE simulations; this is equivalent to treating methyl groups as pseudo-particles: methyls groups are either included and treated in full or neglected entirely from a given cluster. Using methyl pseudo-particles means that 2-CCE will not include any methyl protons, so at least 3-CCE is needed to model methyl tunneling effects. Additionally, in CCE simulations involving methyl groups, Kveder et al. note, that up to 6-CCE may be necessary [46]. Figure 7.4 shows n-CCE simulation of TEMPO in water/glycerol with an 80 kHz tunnel splitting, for $n \in [2, 6]$ for a single orientation and MD frame, evaluated at the first and last MD frame of the 301 used frames, the frame at 25 ns and the frame at 85 ns. Form figure 7.4, it appears that 4-CCE is sufficiently converged.

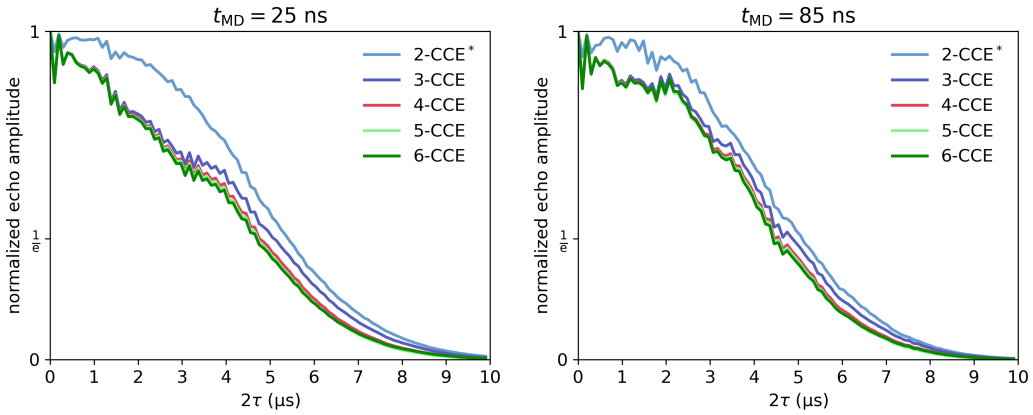

Figure 7.4: The above Hahn echo decay simulations for TEMPO in water/glycerol use a single frame at a fixed orientation and vary the maximum cluster size used for the CCE. The methyl tunnel splitting is set to 80 kHz. Within the last 60 ns of the MD trace used for spin dynamics simulations, the left plot is for the frame at $t_{MD} = 25$ ns, and the right plot is at $t_{MD} = 85$ ns. (*) Note that because methyls are not allowed to be broken apart, 2-CCE does include methyl protons.

To double check that the apparent convergence at 4-CCE is not due to the selected frames/orientations, a 5-CCE 31-frame/orientation average was run, with frames spaced 2 ns apart for $t_{\mathrm{MD}} \in [25, 85]$ ns. Each frame was rotated to a random orientation. This is shown in figure 7.5, along with a 4-CCE simulation that averages over the same 31 frames/orientations. Again, 4-CCE appears to be converged, and so will be used going on.

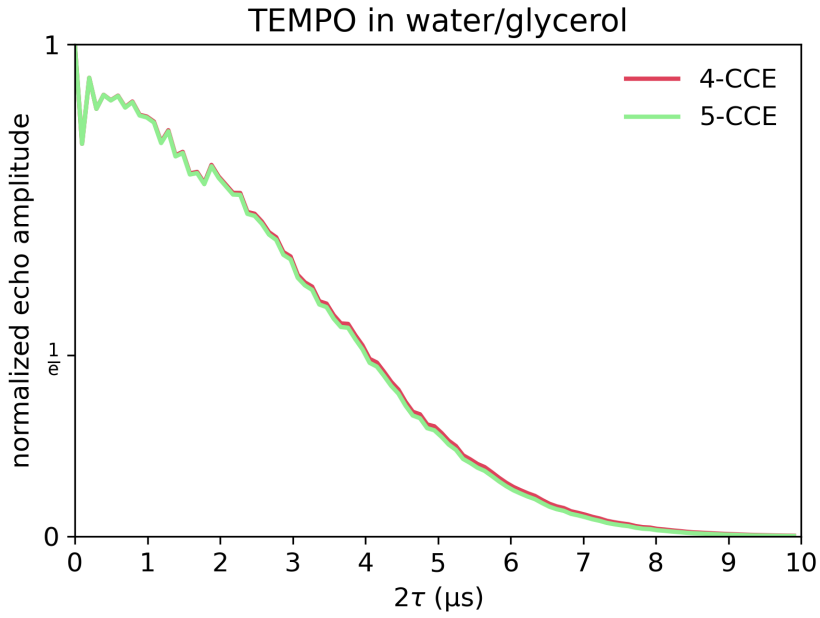

Figure 7.5: The above Hahn echo decay simulations are for TEMPO in water/glycerol. The simulations are done at the 4-CCE level (red) and the 5-CCE level (green). The TEMPO methyl tunnel splitting was set to 80 kHz.

For the main simulations, each of the 301 MD frames spaced 0.2 ns apart was rotated to a random orientation, and the Hahn echo simulated at the 4-CCE level for each frame. To check for convergence, the fully averaged simulation was compared to partially averaged simulations. The fully averaged simulation used 301 frames, 0.2 ns apart. The partially averaged simulation with n_{frames} MD frames used

$$\Delta t_{\mathrm{frame}} = (0.2 \text{ ns}) \left\lfloor \frac{(60 \text{ ns}/0.2 \text{ ns})}{n_{\mathrm{frames}} - 1} \right\rfloor = (0.2 \text{ ns}) \left\lfloor \frac{300}{n_{\mathrm{frames}} - 1} \right\rfloor. \tag{7.9}$$

This cannot show absolute convergence since the RMSD is relative to 301 frames, which forces the RMSD at 301 to be zero, but the convergence behavior leading up to 301 frames can be examined. Figure 7.6 shows the RMSDs of of the paritially averaged simulation for TEMPO in water/glycerol for $\nu_{\mathrm{t}} \in \{(20 \text{ kHz})n; 0 \leq n \leq 15\}$. The RMSD drops to below 1% at least once before 50 frames and fluctuates on the order of a few percent. This suggests that averaging over 301 orientations is reasonable.

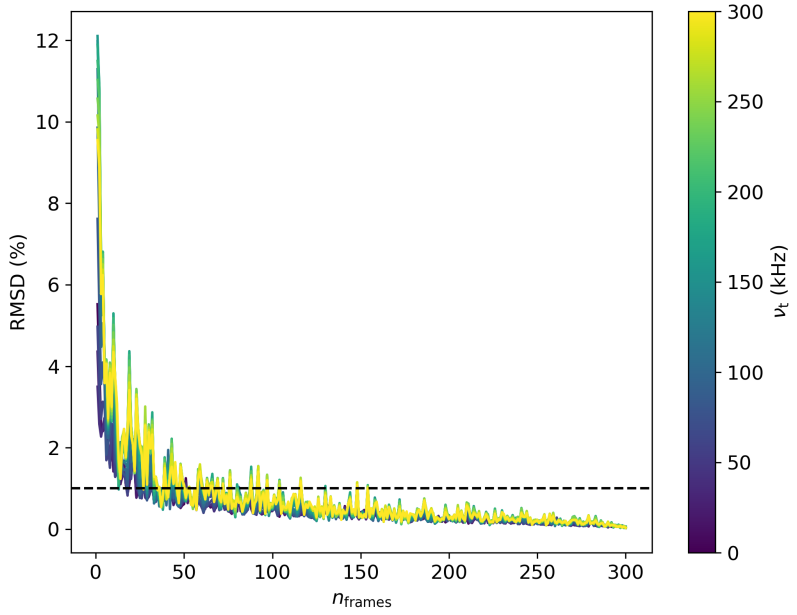

Figure 7.6: The above plots the RMSD with respect to averaging over all 301 frames, from only including n_{frames} MD frames evenly spaced between 25 ns and 85 ns from the MD simulation. Specifically, the frames were spaced with $\Delta t_{\text{frame}} = (0.2\text{ ns})\left\lfloor \frac{(60\text{ ns}/0.2\text{ ns})}{n_{\text{frames}}-1} \right\rfloor$. A dashed line is drawn to indicate the 1% RMSD threshold. The color–axis indicates the TEMPO methyl tunnel splitting.

7.3.3 Results

Figure 7.7 shows the Hahn echo decays for TEMPO in water/glycerol: the experimental data are shown in black, and the simulated data are shown color coded by the TEMPO methyl tunnel splitting used. Because of the experimental dead-time, the absolute scaling of the experimental data is unknown, and so to compare the experiment to the simulations, a scaling procedure must be used. For the comparison, cubic spline interpolation was used to evaluate the simulations at the same 2τ values as the experiment. For a experimental scale factor V_0, the RMSD between the experiment and simulation is

$$\text{RMSD} = \sqrt{\frac{1}{N_{\text{expt}}} \sum_{2\tau \leq 4\ \mu\text{s}} (V_0 v^{\text{expt}}(2\tau) - v^{\text{sim}}(2\tau))^2}, \tag{7.10}$$

where only experimental 2τs are considered in the sum. The choice to restrict the sum to $2\tau \leq 4$ µs is to select a scale from the beginning of the decay to avoid fitting to the tail. Here, N_{expt} is the number of experimental data with $2\tau \leq 4$ µs. The derivative of the RMSD with respect to the experimental scale is

$$\begin{aligned} \frac{\mathrm{d}\,\text{RMSD}}{\mathrm{d}V_0} &= \frac{\frac{1}{N_{\text{expt}}} \sum_{2\tau \leq 4\ \mu\text{s}} v^{\text{expt}}(2\tau)(V_0 v^{\text{expt}}(2\tau) - v^{\text{sim}}(2\tau))}{\sqrt{\frac{1}{N_{\text{expt}}} \sum_{2\tau \leq 4\ \mu\text{s}} (V_0 v^{\text{expt}}(2\tau) - v^{\text{sim}}(2\tau))^2}} \\ &= \frac{1}{\text{RMSD}} \frac{1}{N_{\text{expt}}} \left(\sum_{2\tau \leq 4\ \mu\text{s}} V_0 v^{\text{expt}}(2\tau)^2 - \sum_{2\tau \leq 4\ \mu\text{s}} v^{\text{sim}}(2\tau) v^{\text{expt}}(2\tau) \right). \end{aligned} \tag{7.11}$$

Assuming RMSD, $v^{\text{expt}}(2\tau) > 0$, then $\frac{\mathrm{d}\,\text{RMSD}}{\mathrm{d}V_0} = 0$ at

$$V_0 = \frac{\sum_{2\tau \leq 4\ \mu\text{s}} v^{\text{sim}}(2\tau) v^{\text{expt}}(2\tau)}{\sum_{2\tau \leq 4\ \mu\text{s}} v^{\text{expt}}(2\tau)^2}. \tag{7.12}$$

Or to restate it without explicit reference to V_0, the minimal RMSD occurs when the experimental data is scaled such that

$$\sum_{2\tau \leq 4\ \mu s} v^{\text{sim}}(2\tau) v^{\text{expt}}(2\tau) = \sum_{2\tau \leq 4\ \mu s} v^{\text{expt}}(2\tau)^2. \tag{7.13}$$

To compare the experimental value to a simulation at a particular methyl tunnel splitting, the experiment was scaled according to equation (7.13), and the RMSD calculated. This was repeated for all simulations, and the simulation with the smallest RMSD was the simulation with a 60 kHz TEMPO methyl tunnel splitting. The experimental data in figure 7.7 is scaled to the simulation that uses a 60 kHz methyl tunnel splitting. The experiment and simulation match reasonably well, both in timescale and shape.

Figure 3.2 of chapter 3 shows literature nitroxide tunnel splitting data ranging from 90 kHz to 2 MHz, and corresponding V_3 from 160 meV to 110 meV. The 60 kHz TEMPO methyl tunnel splitting found here is reasonably close to the literature range. The environment of the methyls likely explains some of the variation in V_3: the literature experiments were in a 2,2,4,4-tetramethylcyclobutan-1,3-dione crystal (for $\nu_t = 2$ MHz) [113], frozen toluene solution (for $\nu_t = 0.6$ MHz) [114], or orthoterphenyl (for $\nu_t \in [90, 160]$ kHz) [100].

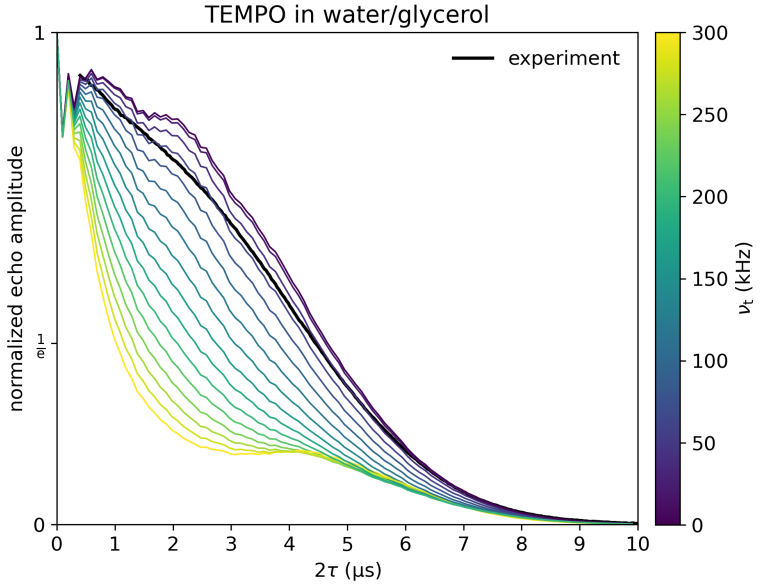

Figure 7.7: The above plots the Hahn echo decays for TEMPO in 1:1 mass:mass water:glycerol. The black decay shows the experiment, and the others are simulated decays with a tunnel splitting given by the color–axis.

7.4 TEMPO in a Methyl-Containing Solvent

Next, we look at TEMPO in a methyl-containing solvent. Methyls are added to the solvent via n-propanol. The rotational potential of n-propanol varies between the trans and gauche rotamers, but V_3 for the trans conformer as been measured, and 118 ± 3 meV found[178]. Experiments by Zecevic et al. with TEMPONE at X-band measured T_M for a 1:1 volume:volume water:glycerol at 40 K to be 4.6 µs, and switching the solvent to a 1:3 volume:volume n-propanol:glycerol reduced T_M to 3.9 µs[22]. This suggests that TEMPO in 1:3 vol:vol n-propanol:glycerol should provide a well understood test system for CCE that contains more methyl groups while staying close to the water/glycerol experimental conditions.

7.4.1 Experiment

The TEMPO in n-propanol/glycerol experiment were performed by Rachelle Stowell. The experimental setup was similar to that of TEMPO in water/glycerol. TEMPO was mixed in a solution of 1:3 volume:volume n-propanol:glycerol to a concentration of 200 µM. The Hahn echo experiments were done in a Bruker D2 dielectric resonator at a temperature of 20 K, with a Bruker Elexsys E580, using an applied magnetic field of 1.20 T, and a microwave frequency of 33.8 GHz, amplified through a 300 W TWT amplifier (Applied Systems Engineering). The Hahn echo used square pulses with lengths decided by Rabi oscillation as $t_{\pi/2} = 6$ ns and $t_\pi = 12$ ns. The shot repetition time was 700 ms.

7.4.2 Simulation Convergence

As before the CCE order needs to be decided. Although the n-propanol/glycerol has about the same proton concentration, the methyl concentration is much greater. Figure 7.8(A,B) shows two single-orientation single-frame n-CCE simulations for $n \in [2, 6]$ using a TEMPO methyl tunnel splitting of 80 kHz, and an n-propanol methyl tunnel splitting of 40 kHz. Again 4-CCE appears to be reasonably well converged.

Again, to check that 4-CCE is converged for multiple frames, figure 7.8(C) shows a 31-frame/orientation average with frames spaced 2 ns apart for both 4-CCE and 5-CCE. Again, 4-CCE appears converged, and again will be used moving forward.

One possibility for why 6-CCE was needed in [46] is that the proton concentration of their system was lower at [^{1}H] = 77 M [CSD: MEMALA01] and 88 M [CSD: ACEMID05]), as compared with the 110 M for water/glycerine [135], and 113 M for n-propanol/glycerol [179] of our systems. Since CCE is a short time approximation, the shorter T_M from our higher proton concentration may be enough for higher-order clusters to not be needed.

With 4-CCE selected, the next step is to check that 301 frame/orientations evenly spaced over 60 ns is enough to reach convergence. Simulations were ran with 60 kHz TEMPO methyl tunnel splitting, as the best fit from the TEMPO in water/glycerol system, and simulation were done for n-propanol methyl tunnel splitting in $\{0, 10, 20, 30, 40, 60, 80\}$ kHz. Figure 7.8(D) compares the 301 frame average to partial averages via RMSD. The RMSDs all have a least one point under 1% RMSD by 50 frames and oscillations on the order of 1% RMSD.

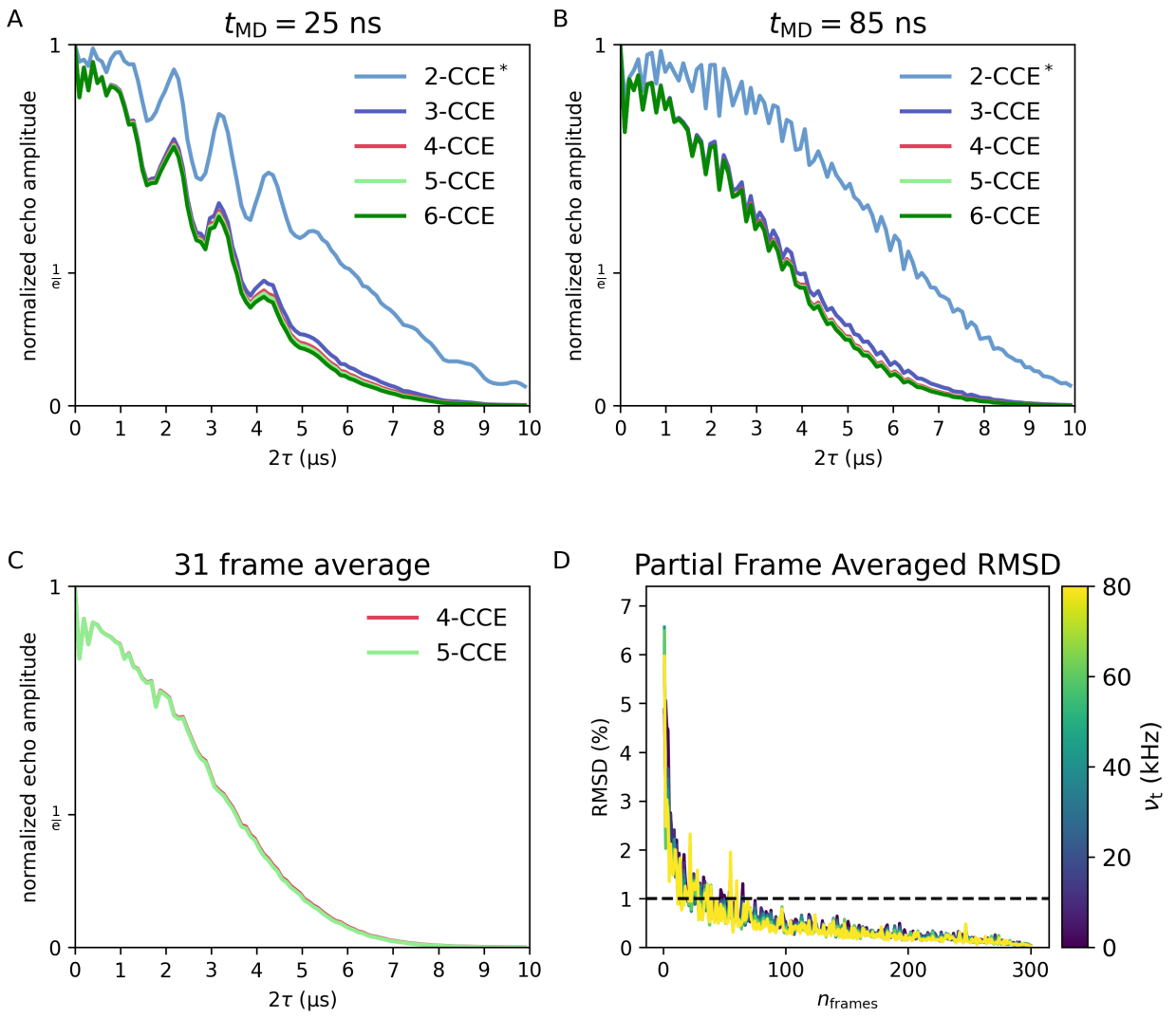

Figure 7.8: **A**,**B**: the above Hahn echo decay simulations for TEMPO in *n*-propanol/glycerol use a single frame at a fixed orientation and vary the maximum cluster size used for the CCE. The TEMPO methyl tunnel splitting is set to 80 kHz. The *n*-propanol methyl tunnel splitting is set to 40 kHz. Note that because methyls are not allowed to be broken apart, 2-CCE cannot include methyl effects. **A** uses the first MD frame of the used MD time range, and the **B** uses the final MD frame. **C**: the above Hahn echo decay simulations are for TEMPO in *n*-propanol/glycerol. The simulations are done at the 4-CCE level (red) and the 5-CCE level (green). The TEMPO methyl tunnel splitting was set to 80 kHz, and the *n*-propanol methyl tunnel splitting is set to 40 kHz. **D**: The above plots the RMSD with respect to averaging over all 301 frames, from only including n_{frames} MD frames evenly spaced between 25 ns and 85 ns from the MD simulation. Specifically, the frames were spaced with $\Delta t_{\text{frame}} = (0.2 \text{ ns}) \left\lfloor \frac{(60 \text{ ns}/0.2 \text{ ns})}{n_{\text{frames}}-1} \right\rfloor$. A dashed line is drawn to indicate the 1% RMSD threshold. These simulations use a 60 kHz tunnel splitting for the TEMPO methyls, and the color–axis indicate the tunnel splitting of the *n*-propanol methyls.

7.4.3 Results

As before, the RMSD between each TEMPO in *n*-propanol/glycerol simulation and the optimally (for that simulation) scaled experimental data was calculated. The smallest RMSD occurred at 40 kHz *n*-propanol methyl tunnel splitting. Figure 7.9 shows all the TEMPO in *n*-propanol/glycerol Hahn echo decays, the experimental data and the simulations. The experimental data shown in figure 7.9 is scaled to the 40 kHz *n*-propanol methyl tunnel splitting The simulations use a TEMPO methyl tunnel splitting of 60 kHz from the best fit in the water/glycerol system, and look at *n*-propanol methyl tunnel splittings in $\{0, 10, 20, 30, 40, 60, 80\}$ kHz. The choice to use a single *n*-propanol methyl tunnel splitting for every *n*-propanol in the system is likely less justified here than for TEMPO, but nonetheless, the match is reasonably good. The tail of the simulated Hahn echo decay fails to follow the experiment; this is possibly due to using only a single *n*-propanol methyl tunnel splitting to represent a distribution of tunnel splittings. While a 40 kHz *n*-propanol methyl tunnel splitiing best reproduces the experiment, this cannot be directly interpreted as mean, median, or mode, of the distribution. This is because the timescales of the Hahn echo, the dead-time and T_M, potentially selects for tunnel splittings that operate on similar timescales. A 40 kHz methyl tunnel splitting corresponds to $V_3 = 170$ meV. In comparison, Dreizier found $V_3 = 118 \pm 3$ meV for the trans confermer of *n*-propanol in *n*-propanol [178]. Our sample is 1:3 volume:volume *n*-propanol:glycerol, so the solvent environment is not identical either. Together, the timescale selectivity and the different solvent environment may partially explain the different V_3s.

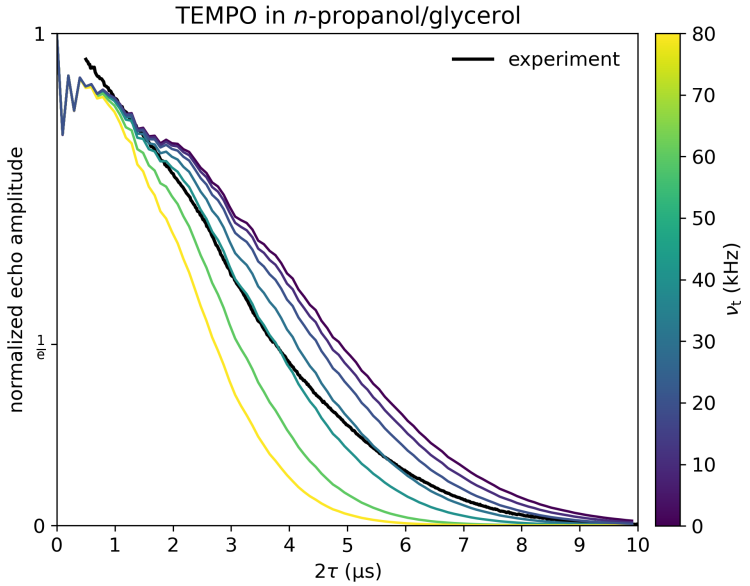

Figure 7.9: The above plots the Hahn echo decays for TEMPO in 1:3 volume:volume *n*-propanol:glycerol. The black decay shows the experiment, and the others are simulated decays with a TEMPO methyl tunnel splitting of 80 kHz, and an *n*-propanol methyl tunnel splitting given by the color–axis.

7.4.4 Methyl Contributions

Since methyl groups are included entirely in any given cluster or not at all, at the 4-CCE level every cluster can have at most a single methyl group in it. Let $\{C_0\}$ be the set of clusters that do not contain any methyl groups, and let $\{C_n\}$ be the set of clusters that contain the nth methyl group, for some arbitrary way of counting the methyl groups. These sets of clusters partition the set of all clusters $\{C\}$: none are empty, $\{C_n\} \neq \emptyset$; they are disjoint: $\{C_m\} \cap \{C_n\} = \emptyset$, for $m \neq n$, and they cover the set: $\bigcup_n \{C_n\} = \{C\}$. Note the distinction between sets of clusters as described above and clusters which are themselves sets of nuclei. Individual spins, specifically non-methyl spins, can and likely do reside in multiple clusters. It is the clusters themselves that are in exactly one of these sets of clusters. The result is that the CCE product can be factored as

$$\begin{aligned} v(2\tau) &= \prod_{C} \tilde{v}_C \\ &= \Big(\prod_{C\in\{C_0\}} \tilde{v}_C\Big)\Big(\prod_{C\in\{C_1\}} \tilde{v}_C\Big)\cdots\Big(\prod_{C\in\{C_{N_{\text{methyl}}}\}} \tilde{v}_C\Big) \\ &= \prod_{n=0}^{N_{\text{methyl}}} \tilde{v}'_n, \end{aligned} \tag{7.14}$$

where $\tilde{v}'_n$, defined as the auxiliary signal from $\{C_n\}$:

$$\tilde{v}'_n := \prod_{C\in\{C_n\}} \tilde{v}_C. \tag{7.15}$$

This is as far as is needed for our case, but to extend this partitioning to 6-CCE above where cluster can have protons from more than one methyl group, new sets need to be introduced. Let $\{C_{m,n}\}$ be the set of clusters that contain spins from both methyl m and methyl n. Similarly, let $\{C_{l,m,n}\}$ be the set of clusters that contain spins from methyl l, methyl m and methyl n. This definition can be extended to an arbitrary number of methyl groups. With these sets, the set of clusters for CCE with any maximum cluster size is partitioned. The auxiliary signal for $\{C_{m,n}\}$ is then

$$\tilde{v}'_{m,n} := \prod_{C\in\{C_{m,n}\}} \tilde{v}_C, \tag{7.16}$$

with analogous expressions for $\{C_{l,m,n}\}$ and up.

From one simulation with the best-fit tunnel splitting and another with all tunnel splittings set to zero using the same set of clusters, additional simulations can be run for any selection of methyl groups set to zero tunnel splitting without needing to diagonalize additional Hamiltonians. This works because at the 4-CCE level each methyl's tunnel splitting only shows up in one of the $\tilde{v}'_n$s. Note, that at 6-CCE and above, more simulations would be needed, since methyl m's tunnel splitting will influence $\tilde{v}'_{m,n}\ \forall\ n \neq m$, and $n \leq N_{\text{methyls}}$, the numbers of methyls in the system.

Being able to toggle individual methyl tunnelings on/off allows the spatial influence of methyl groups to be investigated in silico. Figure 7.10 summarizes the results.

Figure 7.10(A) is the radial correlation function for the detected electron at the origin and the centroid of the three methyl hydrogens at distance r. The correlation function is generated by looking at every electron–methyl distance in each of the 301 used MD frames. There is a large peak at short distances. This is from the TEMPO methyls, which are on the same molecule as the electron and thus highly correlated in position. The other methyls are from n-propanols, which are less highly correlated, although there is still some structure visible. Figure 7.10(A) will help in interpreting figures 7.10(B,C).

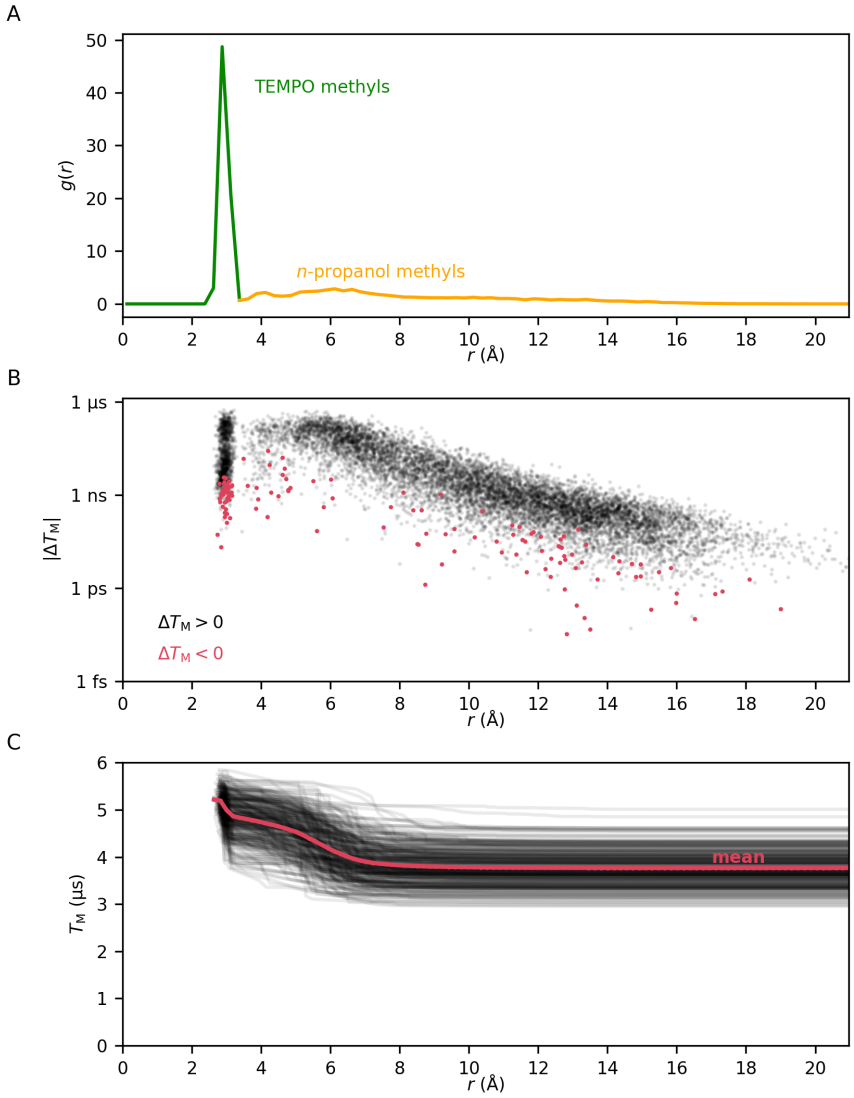

Figure 7.10: **A** shows the radial correlation function for the electron on TEMPO with the centroid of the hydrogens on methyls. The sharp black peak comes from the highly correlated TEMPO methyls, while the broader red peaks come from the *n*-propanol methyls.

Figure 7.10(B) plots $|\Delta T_M|$ for each methyl of each frame. Here ΔT_M for a particular methyl group is defined as the T_M with the tunnel splitting of that methyl group set to zero minus the T_M with the tunnel splitting set to the best fit value, and in both cases all other methyl groups had their best-fit tunnel splittings. This means that if the T_M gets longer when the methyl group's tunnel splitting is toggled off, ΔT_M is positive. This is the case for the majority of cases, and these points are shown in black. The few instances where turning the tunnel splitting off increased the T_M are shown in red. The methyl groups within about 6 Å contribute the most and then the methyl contributions decay with increasing distance from the electron. The simulation used a 2τ resolution of 10 ns. The T_Ms were estimated by first removing the ESEEM modulations: the signals were low-pass filtered with a 3rd-order Butterworth filter with a -3 dB frequency of 500 kHz. The filter was applied twice, once forward and once backward. The T_Ms were found by finding

the first point under 1/e and doing a monotonic cubic interpolation of the four closest points to the 1/e time. The Pearson correlation coefficient between ΔT_{M} and r is -0.5. The correlation coefficients for the two angular coordinates are much smaller, -0.06 for θ and -0.02 for ϕ. These data are shown in figure 7.11, and the definitions for θ and ϕ are the same as in figure 7.12. Note that for an isolated electron–methyl system, all positions are equivalent to one with $\theta \in [0, \pi]$, and $\phi \in [0, \frac{2\pi}{3}]$. In the presence of the environment the equivalency is only approximate, but it is still good and figure 7.11 maps all angles to this range.

Figure 7.10(C) looks at T_{M} vs. r, where only methyl groups with their hydrogen centroid within r are non-zero. Each black curve is $T_{\mathrm{M}}(r)$ for one of the 301 frames/orientations, and the red trace is the average. Note that there is sharp drop in T_{M} corresponding to the distance of the TEMPO methyls, followed by a broader but deeper drop from the nearby (within about 7 Å) n-propanol methyls. After this the T_{M} does not change much with changes in the tunnel splitting for methyls beyond about 7 Å.

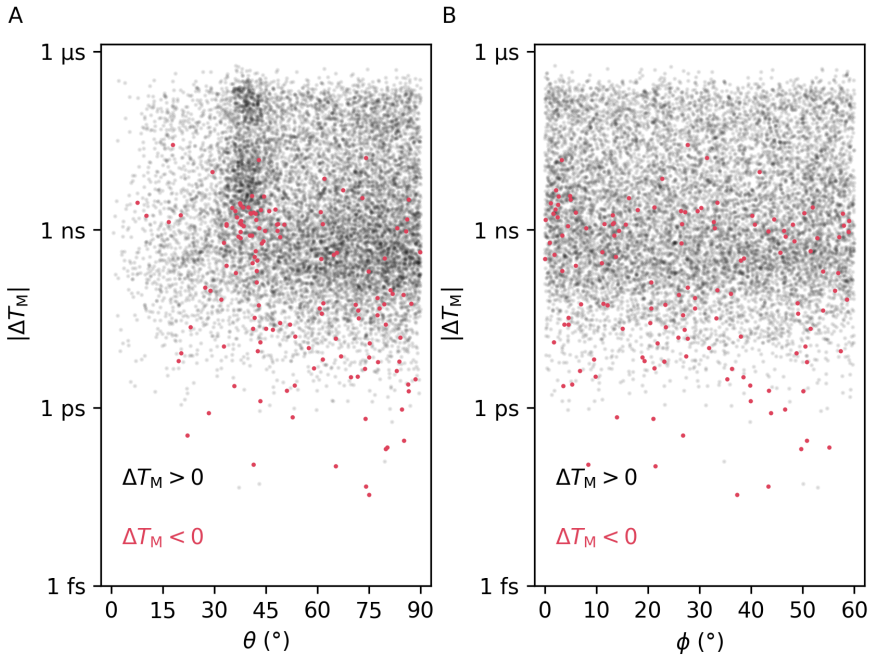

Figure 7.11: **A** shows $\Delta T_{\mathrm{M}}(\theta)$ and **B** shows $\Delta T_{\mathrm{M}}(\phi)$. These are the same data as in figure 7.10, but plotted against different abscissae.

7.5 Lone-Methyl Simulations

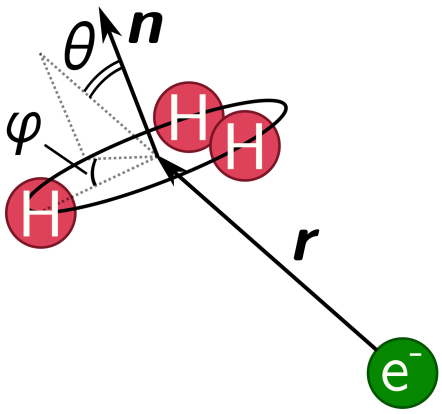

Figure 7.12: The above cartoon illustrate the lone methyl system parameters: r, the distance to the centroid of the methyl hydrogens, θ, the angle between $\boldsymbol{r}$ and the normal vector of the plane defined by the methyl hydrogens, and ϕ, the angle of $\boldsymbol{r}$ projected on the hydrogen plane, where $\phi = 0$ where there is a hydrogen.

Next, we will examine a simple system: an electron and a single methyl. The system is small enough that the full $\hat{H}(m_S)$ is eight-dimensional and easy to numerically diagonalize. We assume the methyl rotor is in an ideal 109.47° tetrahedral geometry with C–H bond lengths of 1.088 Å [126], meaning the H–H distances is 1.78 Å. Once the system is orientation averaged over a 1202 point Lebedev grid [139], there are only a few structural parameters, as illustrated on figure 7.12. The lone methyl system's spatial parameters are the electron-to-methyl-hydrogen centroid distance, $r = |\boldsymbol{r}|$, the angle between $\boldsymbol{r}$ and the unit vector normal to the hydrogen plane (equivalent to the rotor axis in the ideal case), θ, and the angle between $\boldsymbol{r}$ projected onto the hydrogen plane and the separation vector of an arbitrarily selected hydrogen and the hydrogen centroid,. Note, that the symmetry limits the unique systems to those with $\theta \in [0, \pi]$, and $\phi \in [0, \frac{2\pi}{3}]$.

With only three proton, the Hahn echo oscillates and does not acquire the form of a stretched exponential decay, so T_M is not defied. One way to characterize the modulations would be with frequencies and amplitudes, but to better interpret the modulations in the context of the previous systems, we chose to evaluate the Hahn echo modulation at $2\tau = 2$ µs. The logic behind the choice is 2 µs $\lessapprox T_M/2$, which is approximately where the previous systems show methyl contributions the most: the electrons have had time to decohere, yet the signal is still fairly large. Figure 7.13 shows a few of the Hahn echo modulations.

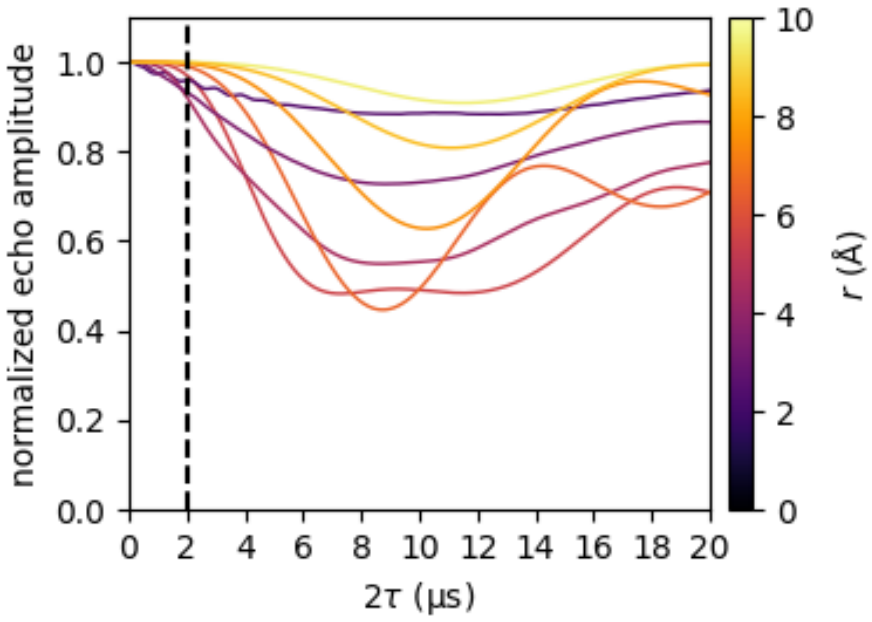

Figure 7.13: The above plot shows the Hahn echo modulations from a lone methyl with $\nu_t = 80$ kHz, $\theta = \phi = 0$, and various rs (coded by the color–axis). A dashed line marks the point where the signal in evaluated: $2\tau = 2$ μs.

For n in the set of non-negative integers, we chose to simulate the systems with $r \in \{(0.5\text{ Å})n;\ 5 \leq n \leq 20\}$; $\theta \in \{10°n;\ n \leq 9\}$, and $\phi \in \{15°n;\ n \leq 4\}$. For each system, multiple tunnel splittings were used: $\nu_t \in \{0, 20, 40, 60, 80, 100, 140, 200, 280, 390, 550, 770, 1100, 1500, 2100, 3000\}$ kHz. Figure 7.14 shows $v(2\tau = 2\text{ μs})$ for each of these systems. The echo amplitude at 2 μs depends strongly on the tunnel splitting and on the distance to the methyl group, but less strongly on θ or ϕ. This is consistent with the TEMPO in n-propanol/glycerol system. While the r-range where $v(2\tau = 2\text{ μs})$ is deepest depends on the tunnel splitting, the range is generally under 7 Å, which again is consistent with the TEMPO in n-propanol/glycerol system. Note that in the 390 kHz tunnel splitting panel, the $v(2\tau = 2\text{ μs}) < 0.3$, and that this from a single methyl group. The amplitude may be surprising, but 390 kHz does make some sense because this is near $(2\text{μs})^{-1} = 500$ kHz, although notably the 500 kHz panel shows shallower modulation.

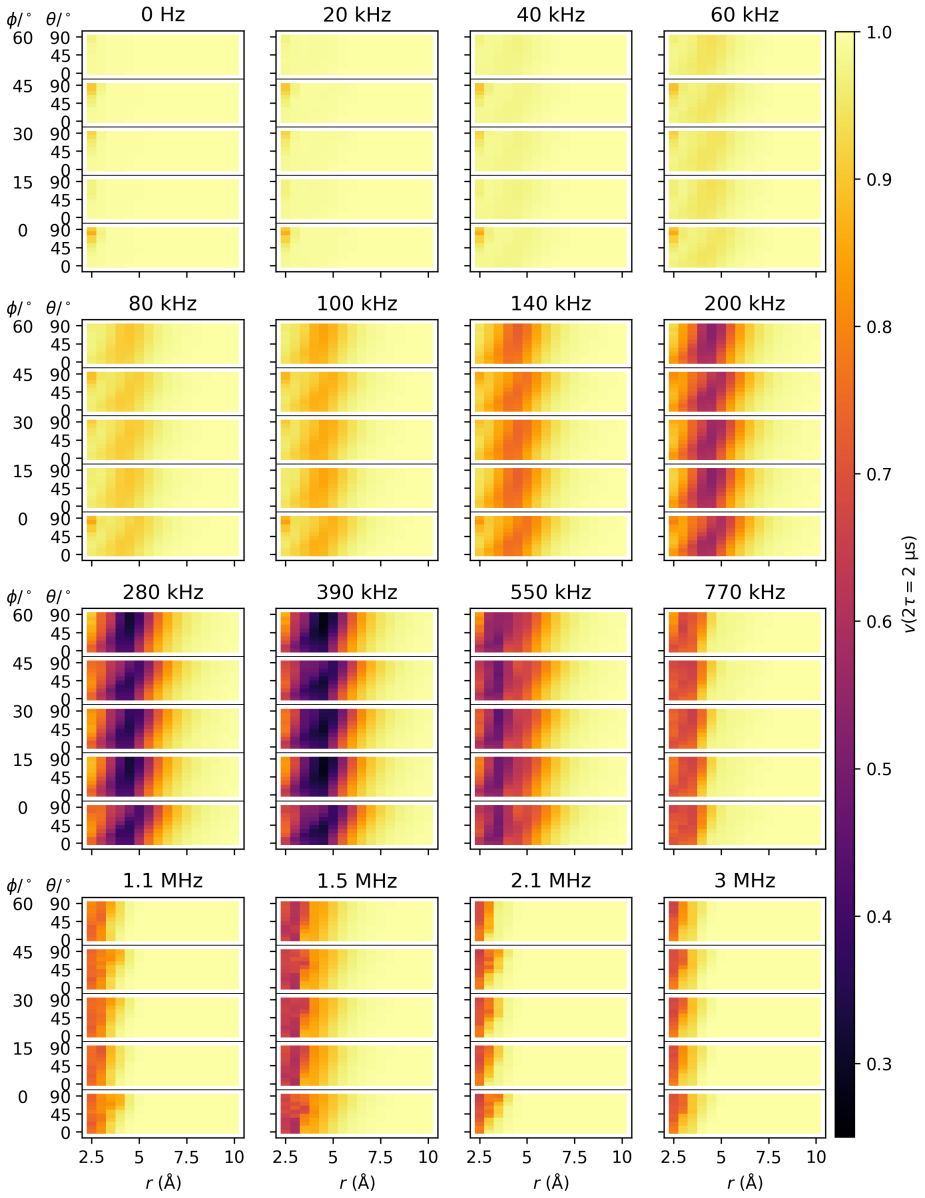

Figure 7.14: Each panel above simulates the Hahn echo for a system with a single methyl, using a different tunnel splitting. Within panel, each sub-panel has a different ϕ, where the vertical axis represents θ, and the horizontal axis represents r. The color–axis indicates the Hahn echo amplitude evaluated a $2\tau = 2$ µs.

7.6 Conclusion

In conclusion, methyl-driven electron spin decoherence can be reasonably well modeled for TEMPO in glassy matrices by 4-CCE, including the effect of methyl tunneling using the Apaydin-Clough effective spin Hamiltonian and assuming uniform tunneling splittings for all solvent methyl and, separately, for all nitroxides methyl. Further improvements could potentially be gained by using a distribution of tunnel splitting. The tunnel splitting is sensitive to the local environment, for example the methyl of n-propanol is reported to have different tunnel splittings for its trans and gauche rotational isomers [178]. Recently, Eggeling at al. used Hahn echo experiments to infer tunnel splitting distributions [100]. Another pathway for improved accuracy, could be including methyl–methyl rotor–rotor couplings [97].

In general, we find that the presence of methyl groups accelerates electron spin decoherence, particularly if the methyl group is between 2.5 to 6 Å from the detected electron. Compared to the electron–methyl distance, the orientation of the methyl group relative to the electron–methyl direction has less impact.

The mechanism of methyl-tunneling-induced decoherence can be pictured as follows: When projected onto spin–space, the methyl rotational Hamiltonian adds an effective nucleus–nucleus coupling. This can increase the effective nucleus–nucleus flip-flop rate and so too increase the magnetic field fluctuations at the position of the detected electron. Since these fluctuations differ between all the sample electrons, they provide a source of spin decoherence.

Methyl groups are ubiquitous in organic chemistry. This applies to proteins as well as potential organic qubit candidates. Being able to effectively model methyl group contributions in disordered environments is an important step to understanding electron spin decoherence for these systems.

Methyls require a tunnel splitting.
The value can be found via fitting.
Within solvents and molecules of host
which methyl rotors contribute the most?
Rotating frame states, methyl groups do mix,
from methyls within Ångströms up to six.

Chapter 8

CluE

The Cluster Correlation Expansion (CCE)[1, 2] simulation done for this work were done in the home-built software CluE (Cluster Evolution). CluE is the software that most of the CCE simulations in this work and in [127, 146, 164] were done with.

The primary purpose of CluE is to take an input structure (a PDB file) and predict the electron spin decoherence behavior. This requires specifying additional details in an options file, notably, the pulse sequence, the location of the detected electron, and the strength of the applied magnetic field, but other options are also available. The are a number of neighbor cutoffs available: nucleus–nucleus separation, nucleus–nucleus dipole–dipole coupling, difference in the nucleus–nucleus hyperfine, as well as cutoffs based on the analytic approximation to the three-spin Hahn echo, the modulation depth and fourth order in 2τ Taylor series coefficient.

CluE defaults to assuming all atoms are their most common isotope, but the isotope ratio can also toggled to used different isotopic ratios. In this mode, CluE will generate a random isotopologue to run CCE on. Averaging over multiple isotopologues is available and recommended. To simulate CCE over larger systems, CluE can apply Periodic Boundary Conditions (PBCs) to the nuclear bath. Note that the detected electron is not copied into the PBCs. For input structure, CluE goes through each nucleus and randomly chooses an isotope, but this can be slow for very large systems, so CluE has an option to speed the process up in the PBCs. Using hydrogens as an example, CluE knows how many hydrogens are in the input structure, and it also knows how many PBCs it created, so it can sample from the binomial distribution with a specified success probability and only initialize that many hydrogens as protons leaving the rest as voids. This is how the very low proton concentration electron spin decoherence systems were simulated in [164] and discussed in chapter 6.

Within CluE is implemented, the ability to model methyl tunelling, as in [46, 108]. CluE can use different tunnel splitting for different types of methyl groups, and has tools to investigate how different methyl groups contribute to the overall signal. These were used in chapter 7.

CluE was originally developed in MATLAB [180], but is rewritten as CluE Oxide in Rust [181], and supports a Python[182] interface. The MATLAB version requires a MATLAB license and some familiarity with MATLAB to use. CluE Oxide runs completely with open source components. CluE Oxide does not require knowledge of Rust to use: it runs through the command line or from Python. Both versions are open source, licensed under GPL-v3. The MATLAB version is available at

https://github.com/StollLab/CluE.

CluE Oxide is available at

https://github.com/jahnsam/clue_oxide.

Both versions take as input an options file and a structure file. The structure file takes the form of a PDB, and specifies where all the atoms are in the system. The options files tells CluE how to run the simulation: how to form clusters, how big the clusters can be, where the detected electron is, what isotopes to use for the atoms, and so on.

Bibliography

(1) Yang, W.; Liu, R.-B. Phys. Rev. B **2008**, *78*, 085315.

(2) Yang, W.; Liu, R.-B. Phys. Rev. B **2009**, *79*, 115320.

(3) Childress, L.; Gurudev Dutt, M. V.; Taylor, J. M.; Zibrov, A. S.; Jelezko, F.; Wrachtrup, J.; Hemmer, P. R.; Lukin, M. D. Science **2006**, *314*, 281–285.

(4) Gaebel, T.; Domhan, M.; Popa, I.; Wittmann, C.; Neumann, P.; Jelezko, F.; Rabeau, J. R.; Stavrias, N.; Greentree, A. D.; Prawer, S.; Meijer, J.; Twamley, J.; Hemmer, P. R.; Wrachtrup, J. Nat. Phys. **2006**, *2*, 408–413.

(5) Balasubramanian, G.; Neumann, P.; Twitchen, D.; Markham, M.; Kolesov, R.; Mizuochi, N.; Isoya, J.; Achard, J.; Beck, J.; Tissler, J.; Jacques, V.; Hemmer, P. R.; Jelezko, F.; Wrachtrup, J. Nat. Mater. **2009**, *8*, 383–387.

(6) Burkard, G.; Loss, D.; DiVincenzo, D. P. Phys. Rev. B **1998**, *59*, 2070–2078.

(7) Bluhm, H.; Foletti, S.; Neder, I.; Rudner, M.; Mahalu, D.; Umansky, V.; Yacoby, A. Nature Phys **2011**, *7*, 109–113.

(8) Zadrozny, J. M.; Niklas, J.; Poluektov, O. G.; Freedman, D. E. ACS Cent. Sci. **2015**, *1*, 488–492.

(9) Jackson, C. E.; Lin, C.-Y.; Johnson, S. H.; van Tol, J.; Zadrozny, J. M. Chem. Sci. **2019**, *10*, 8447–8454.

(10) Atzori, M.; Sessoli, R. J. Am. Chem. Soc. **2019**, *141*, 11339–11352.

(11) Morley, G. W.; Lueders, P.; Hamed Mohammady, M.; Balian, S. J.; Aeppli, G.; Kay, C. W. M.; Witzel, W. M.; Jeschke, G.; Monteiro, T. S. Nat. Mater. **2013**, *12*, 103–107.

(12) Jeschke, G. Annu. Rev. Phys. Chem. **2012**, *63*, 419–446.

(13) Van Doorslaer, S. In eMagRes, Harris, R. K., Wasylishen, R. L., Eds.; John Wiley & Sons, Ltd: Chichester, UK, 2017, pp 51–70.

(14) Harmer, J. R. In eMagRes, Harris, R. K., Wasylishen, R. L., Eds.; John Wiley & Sons, Ltd: Chichester, UK, 2016, pp 1493–1514.

(15) Milov, A. D.; Salikhov, K. M.; Shchirov, M. D. Sov. Phys. Solid State **1981**, *23*, 975–982.

(16) Milov, A. D.; Ponomarev, A. B.; Tsvetkov, Y. D. Chem. Phys. Lett. **1984**, *110*, 67–72.

(17) Larsen, R. G.; Singel, D. J. J. Chem. Phys. **1993**, *98*, 5134–5146.

(18) Jeschke, G.; Polyhach, Y. Phys. Chem. Chem. Phys. **2007**, *9*, 1895.

(19) Eaton, S. S.; Eaton, G. R. In Distance Measurements in Biological Systems by EPR, Berliner, L. J., Eaton, S. S., Eaton, G. R., Eds.; Springer: Boston, USA, 2000; Vol. 19, pp 29–154.

(20) Brown, I. In Time Domain Electron Spin Resonance, Kevan, L., Schwartz, R., Eds.; John Wiley & Sons: New York, 1979, pp 195–229.

(21) Salikhov, K. M.; Tsvetkov, Y. D. In Time Domain Electron Spin Resonance, Kevan, L., Schwartz, R., Eds.; John Wiley & Sons: New York, 1979, pp 279–341.

(22) Zecevic, A.; Eaton, G. R.; Eaton, S. S.; Lindgren, M. Mol. Phys. **1998**, *95*, 1255–1263.

(23) Graham, M. J.; Zadrozny, J. M.; Shiddiq, M.; Anderson, J. S.; Fataftah, M. S.; Hill, S.; Freedman, D. E. J. Am. Chem. Soc. **2014**, *136*, 7623–7626.

(24) Klauder, J. R.; Anderson, P. W. Phys. Rev. **1962**, *125*, 912–932.

(25) Zhidomirov, G. M.; Salikhov, K. M. Sov. Phys. J. Exp. Theor. Phys. **1969**, *29*, 1037–1040.

(26) Milov, A. D.; Salikhov, K. M.; Tsvetkov, Y. D. Sov. Phys. Solid State **1973**, *15*, 802–806.

(27) Hu, P.; Hartmann, S. R. Phys. Rev. B **1974**, *9*, 1–13.

(28) Kuprov, I.; Wagner-Rundell, N.; Hore, P. J. J. Magn. Reson. **2007**, *189*, 241–250.

(29) Butler, M. C.; Dumez, J.-N.; Emsley, L. Chem. Phys. Lett. **0209**, *477*, 377–381.

(30) Dumez, J.-N.; Butler, M. C.; Emsley, L. J. Chem. Phys. **2010**, *133*, 224501.

(31) Hogben, H. J.; Hore, P. J.; Kuprov, I. J. Chem. Phys. **2010**, *132*, 174101.

(32) Dumez, J.-N.; Halse, M. E.; Butler, M. C.; Emsley, L. Phys. Chem. Chem. Phys. **2012**, *14*, 86–89.

(33) Edwards, L. J.; Savostyanov, D. V.; Welderufael, Z. T.; Lee, D.; Kuprov, I. J. Magn. Reson. **2014**, *243*, 107–113.

(34) Witzel, W.; Das Sarma, S. Phys. Rev. B **2006**, *74*, 035322.

(35) Saikin, S. K.; Yao, W.; Sham, L. J. Phys. Rev. B **2007**, *75*, 125314.

(36) Lenz, S.; Bader, K.; Bamberger, H.; Van Slageren, J. Chem. Commun. **2017**, *53*, 4477–4480.

(37) Ma, W.-L.; Wolfowicz, G.; Zhao, N.; Li, S.-S.; Morton, J. J. L.; Liu, R.-B. Nat. Commun. **2014**, *5*, 4822.

(38) Witzel, W. M.; Carroll, M. S.; Cywiński, Ł.; Das Sarma, S. Phys. Rev. B **2012**, *86*, 035452.

(39) Abragam, A., *Principles of Nuclear Magnetism*; Oxford University Press: 1961.

(40) Levitt, M. H., *Spin dynamics: basics of nuclear magnetic resonance*, 2nd ed, OCLC: ocn141380283; John Wiley & Sons: Chichester, England ; Hoboken, NJ, 2008.

(41) Hahn, E. L. Phys. Rev. **1950**, *80*, 580–594.

(42) Lindgren, M.; Eaton, G. R.; Eaton, S. S.; Jonsson, B.-H.; Hammarström, P.; Svensson, M.; Carlsson, U. J. Chem. Soc., Perkin Trans. 2 **1997**, 2549–2554.

(43) Huber, M.; Lindgren, M.; Hammarström, P.; Mårtensson, L.-G.; Carlsson, U.; Eaton, G.; Eaton, S. Biophys. Chem. **2001**, *94*, 245–256.

(44) Soetbeer, J.; Hülsmann, M.; Godt, A.; Polyhach, Y.; Jeschke, G. Phys. Chem. Chem. Phys. **2018**, *20*, 1615–1628.

(45) Soetbeer, J.; Ibáñez, L. F.; Berkson, Z.; Polyhach, Y.; Jeschke, G. Phys. Chem. Chem. Phys. **2021**, *23*, 21664–21676.

(46) Kveder, M.; Rakvin, B.; You, J. J. Chem. Phys. **2019**, *151*, 164124.

(47) Peskin, M. E.; Schroeder, D. V., *An Introduction to Quantum Field Theory*; Addison-Wesley Pub. Co: Reading, Mass, 1995.

(48) Neese, F. In EPR Spectroscopy, Stoll, S., Goldfarb, D., Eds.; eMagRes books; John Wiley & Sons, Incorporated: Newark, 2018.

(49) Brown, J. M. et al. Molecular Physics **2000**, *98*, 1597–1601.

(50) NIST electron g factor `https://www.physics.nist.gov/cgi-bin/cuu/Value?gem` (accessed 06/30/2023).

(51) NIST Bohr magneton `https://www.physics.nist.gov/cgi-bin/cuu/Value?mub` (accessed 06/30/2023).

(52) NIST nuclear magneton `https://www.physics.nist.gov/cgi-bin/cuu/Value?mun` (accessed 06/30/2023).

(53) NIST vacuum magnetic permeability `https://www.physics.nist.gov/cgi-bin/cuu/Value?mu0` (accessed 06/30/2023).

(54) Bennati, M. In EPR Spectroscopy, Stoll, S., Goldfarb, D., Eds.; eMagRes books; John Wiley & Sons, Incorporated: Newark, 2018.

(55) Stoll, S.; Goldfarb, D. In EPR Spectroscopy, Stoll, S., Goldfarb, D., Eds.; eMagRes books; John Wiley & Sons, Incorporated: Newark, 2018.

(56) NIST Planck constant `https://www.physics.nist.gov/cgi-bin/cuu/Value?h` (accessed 06/30/2023).

(57) NIST elementary charge `https://www.physics.nist.gov/cgi-bin/cuu/Value?e` (accessed 06/30/2023).

(58) Schweiger, A.; Jeschke, G., *Principles of Pulse Electron Paramagnetic Resonance*; Oxford University Press: Oxford, UK ; New York, 2001.

(59) Bunker, P. R.; Jensen, P., *Molecular symmetry and spectroscopy*, 2. ed; NRC 46853; NRC Research Press: Ottawa, 2006.

(60) Freed, J. H. J. Chem. Phys. **1965**, *43*, 1710–1720.

(61) Horsewill, A. Prog. Nucl, Magn. Reson. Spectrosc. **1999**, *35*, 359–389.

(62) Hanson, L. G. Concepts Magn. Reson. **2008**, *32A*, 329–340.

(63) NIST reduced Planck constant `https://www.physics.nist.gov/cgi-bin/cuu/Value?hbar` (accessed 07/20/2023).

(64) You, J.; Carić, D.; Rakvin, B.; Štefanić, Z.; Užarević, K.; Kveder, M. J. Chem. Phys. **2019**, *150*, 164124.

(65) Lee, J.; Park, H.; Seo, H. npj 2D Mater Appl **2022**, *6*, 60.

(66) Liu, W. et al. Nat Commun **2022**, *13*, 5713.

(67) Chen, J.-S.; Trerayapiwat, K. J.; Sun, L.; Krzyaniak, M. D.; Wasielewski, M. R.; Rajh, T.; Sharifzadeh, S.; Ma, X. Nat Commun **2023**, *14*, 848.

(68) Le Dantec, M.; Rančić, M.; Lin, S.; Billaud, E.; Ranjan, V.; Flanigan, D.; Bertaina, S.; Chanelière, T.; Goldner, P.; Erb, A.; Liu, R. B.; Estève, D.; Vion, D.; Flurin, E.; Bertet, P. Sci. Adv. **2021**, *7*, eabj9786.

(69) Rančić, M. J.; Dantec, M. L.; Lin, S.; Bertaina, S.; Chanelière, T.; Serrano, D.; Goldner, P.; Liu, R. B.; Flurin, E.; Estève, D.; Vion, D.; Bertet, P. Phys. Rev. B **2022**.

(70) Yang, Z.-S.; Wang, Y.-X.; Tao, M.-J.; Yang, W.; Zhang, M.; Ai, Q.; Deng, F.-G. Ann. Phys. **2020**, *413*, 168063.

(71) Güldeste, E. T.; Bulutay, C. Phys. Rev. B **2021**.

(72) Lee, J.; Tatsuta, M.; Xu, A.-N.; Bauch, E.; Ku, M. J. H.; Walsworth, R. L. In 2022.

(73) Maile, D.; Ankerhold, J. In 2022.

(74) Park, H.; Lee, J.; Han, S.; Oh, S.; Seo, H. npj Quantum Inf **2022**, *8*, 95.

(75) Onizhuk, M.; Galli, G. Decoherence of Nuclear Spins in the Proximity of Nitrogen Vacancy Centers in Diamond, en, arXiv:2302.03257 [quant-ph], 2023.

(76) Ghosh, K.; Ma, H.; Onizhuk, M.; Gavini, V.; Galli, G. npj Comput Mater **2021**, *7*, 123.

(77) Fazio, T.; Fisicaro, G.; Deretzis, I.; Paladino, E.; La Magna, A. MSF **2022**, *1062*, 309–314.

(78) Onizhuk, M.; Galli, G. Appl. Phys. Lett. **2021**, *118*, 154003.

(79) Sajid, A.; Thygesen, K. S. Phys. Rev. B **2022**.

(80) Kanai, S.; Heremans, F. J.; Seo, H.; Wolfowicz, G.; Anderson, C. P.; Sullivan, S. E.; Galli, G.; Awschalom, D. D.; Ohno, H. arXiv **2021**, *2102.02986*.

(81) Zhang, G.-L.; Ma, W.-L.; Liu, R.-B. Phys. Rev. B **2020**, *102*, 245303.

(82) Romanelli, M.; Kevan, L. Concepts Magn Reson **1997**, *9*, 403–430.

(83) Romanelli, M.; Kevan, L. Concepts Magn Reson **1998**, *10*, 1–18.

(84) Mims, W. B. Phys. Rev. **1968**, *168*, 370–389.

(85) Salikhov, K. M.; Dzuba, S. A.; Raitsimring, A. M. J. Magn. Reson. **1981**, *42*, 255–276.

(86) NIST electron gyromagnetic ratio `https://physics.nist.gov/cgi-bin/cuu/Value?gammae` (accessed 07/20/2023).

(87) Sweger, S. R.; Denysenkov, V. P.; Maibaum, L.; Prisner, T. F.; Stoll, S. Magn. Reson. **2022**, *3*, 101–110.

(88) Perras, F. A.; Pruski, M. J. Chem. Phys. **2018**, *149*, 154202.

(89) Clough, S. Solid State Nucl. Magn. Reson. **1999**, *14*, 73–79.

(90) Alefeld, B.; Kollmar, A. Phys. Lett. A **1976**, *57*, 289–290.

(91) Press, W., *Single-particle rotations in molecular crystals*; Springer tracts in modern physics 92; Springer Verlag: Berlin Heidelberg New York, 1981.

(92) Hewson, A. C. J. Phys. C: Solid State Phys. **1982**, *15*, 3841–3853.

(93) Punkkinen, M.; Clough, S. J. Phys. C: Solid State Phys. **1974**, *7*, 3403–3412.

(94) Latanowicz, L. J. Phys. Chem. A **2004**, *108*, 11172–11182.

(95) Freed, J. H. J. Chem. Phys. **1965**, *43*, 2312–2332.

(96) Šimėnas, M.; Klose, D.; Ptak, M.; Aidas, K.; Maczka, M.; Banys, J.; Pöppl, A.; Jeschke, G. Sci. Adv. **2020**, *6*, eaba1517.

(97) Jeschke, G. Appl. Magn. Reson. **2021**, *published online*.

(98) Jeschke, G. Appl Magn Reson **2022**, *53*, 635–651.

(99) Usevičius, G.; Eggeling, A.; Pocius, I.; Kalendra, V.; Klose, D.; Mączka, M.; Pöppl, A.; Banys, J.; Jeschke, G.; Šimėnas, M. Molecules **2023**, *28*, 979.

(100) Eggeling, A.; Soetbeer, J.; Fábregas-Ibáñez, L.; Klose, D.; Jeschke, G. Phys. Chem. Chem. Phys. **2023**, *25*, 11145–11157.

(101) Khazaei, S.; Sebastiani, D. J. Chem. Phys. **2017**, *147*, 194303.

(102) Clough, S.; Poldy, F. The Journal of Chemical Physics **1969**, *51*, 2076–2084.

(103) Chesnut, D. B., *Finite groups and quantum theory*, Reprint 1982 (with corrections); R.E. Krieger Pub. Co: Malabar, Fla, 1982.

(104) Clough, S.; McDonald, P. J. J. Phys. C: Solid State Phys. **1983**, *16*, 5753–5764.

(105) Stevens, K. W. H. J. Phys. C: Solid State Phys. **1983**, *16*, 5765–5772.

(106) Peternelj, J.; Kranjc, T.; Pintar, M. M. Phys. Rev. B **1996**, *54*, 955–961.

(107) Prager, M.; Heidemann, A. Chem. Rev. **1997**, *97*, 2933–2966.

(108) Apaydin, F.; Clough, S. J. Phys. C: Solid State Phys. **1968**, *1*, 932–939.

(109) Nielsen, M. A.; Chuang, I. L., *Quantum computation and quantum information*, 10th anniversary ed; Cambridge University Press: Cambridge ; New York, 2010.

(110) Xue, Y.; Pavlova, M. S.; Ryabov, Y. E.; Reif, B.; Skrynnikov, N. R. J. Am. Chem. Soc. **2007**, *129*, 6827–6838.

(111) Shapiro, Y. E.; Polimeno, A.; Freed, J. H.; Meirovitch, E. J. Phys. Chem. B **2011**, *115*, 354–365.

(112) Vugmeyster, L.; Ostrovsky, D.; Penland, K.; Hoatson, G. L.; Vold, R. L. J. Phys. Chem. B **2013**, *117*, 1051–1061.

(113) Barbon, A.; Brustolon, M.; Maniero, A. L.; Romanelli, M.; Brunel, L.-C. Phys. Chem. Chem. Phys **1999**, *1*, 4015–4023.

(114) Kulik, L. V.; Grigor'ev, I. A.; Salnikov, E. S.; Dzuba, S. A.; Tsvetkov, Y. D. J. Phys. Chem. A **2003**, *107*, 3692–3695.

(115) Hoffmann, F.; Mulder, F. A. A.; Schäfer, L. V. J. Chem. Phys. **2020**, *152*, 084102.

(116) Gradshteyn, I. S.; Ryzhik, I. M.; Jeffrey, A.; Zwillinger, D., *Table of Integrals, Series, and Products, Sixth Edition*, 6th ed.; Academic Press: 2000.

(117) Baker, G. L.; Blackburn, J. A.; Smith, H. J. T. Am. J. Phys. **2002**, *70*, 525–531.

(118) Daniel, D. J. Prog. Theor. Exp. Phys. **2020**, *2020*.

(119) Feynman, R. P. Rev. Mod. Phys. **1948**, *20*, 367–387.

(120) Whittall, M. W. G.; Gehring, G. A. J. Phys. C: Solid State Phys. **1987**, *20*, 1619–1639.

(121) Peternelj, J.; Jencic, I. J. Phys. A: Math. Gen. **1989**, *22*, 1941–1944.

(122) Peternelj, J.; Kranjc, T. Physica B: Condens. Matter **1997**, *240*, 343–352.

(123) Peternelj, J.; Kodeli, I.; Pintar, M. M. Can. J. Phys. **1989**, *67*, 1085–1090.

(124) Coleman, S., *Aspects of symmetry: selected Erice Lectures of Sidney Coleman*, paperback ed., repr., transferred to digital print; Cambridge Univ. Pr: Cambridge, 1999.

(125) Dimeo, R. M. Am. J. Phys. **2003**, *71*, 885–893.

(126) Steiner, T.; Saenger, W. Acta Cryst. **1993**, *A49*, 379–384.

(127) Canarie, E. R.; Jahn, S. M.; Stoll, S. J. Phys. Chem. Lett. **2020**, *11*, 3396–3400.

(128) Dhimitruka, I.; Bobko, A. A.; Eubank, T. D.; Komarov, D. A.; Khramtsov, V. V. J. Am. Chem. Soc. **2013**, *135*, 5904–5910.

(129) Oganesyan, V. S. Phys. Chem. Chem. Phys. **2011**, *13*, 4724.

(130) Hanwell, M. D.; Curtis, D. E.; Lonie, D. C.; Vandermeersch, T.; Zurek, E.; Hutchison, G. R. J Cheminform **2012**, *4*, 17.

(131) Neese, F. Wiley Interdiscip. Rev. Comput. Mol. Sci. **2012**, *2*.

(132) Neese, F. Wiley Interdiscip. Rev. Comput. Mol. Sci. **2018**, *8*.

(133) Jo, S.; Kim, T.; Iyer, V. G.; Im, W. J. Comput. Chem. **2008**, *29*, 1859–1865.

(134) Lindahl; Abraham; Hess; van der Spoel GROMACS 2019.2 Source code, version 2019.2, 2019.

(135) *Physical Properties of Glycerine and Its Solutions*; Glyerine Producers' Association: New York, NY: 1963.

(136) Best, R. B.; Zhu, X.; Shim, J.; Lopes, P. E. M.; Mittal, J.; Feig, M.; Mackerell, A. D. J. Chem. Theory Comput. **2012**, *8*, 3257–3273.

(137) Lerbret, A.; Affouard, F. J. Phys. Chem. B **2017**, *121*, 9437–9451.

(138) De Oliveira, M.; Knitsch, R.; Sajid, M.; Stute, A.; Elmer, L.-M.; Kehr, G.; Erker, G.; Magon, C. J.; Jeschke, G.; Eckert, H. PLoS ONE **2016**, *11*, ed. by Norman, D. G., e0157944.

(139) Lebedev, V.; Laikov, D. Dokl. Math. **1999**, *59*, 477–481.

(140) Rowan, L. G.; Hahn, E. L.; Mims, W. B. Phys. Rev. **1965**, *137*, A61–A71.

(141) Mims, W. B. Phys. Rev. B **1972**, *5*, 2409–2419.

(142) Graham, M. J.; Krzyaniak, M. D.; Wasielewski, M. R.; Freedman, D. E. Inorg. Chem. **2017**, *56*, 8106–8113.

(143) Tan, K. O.; Mardini, M.; Yang, C.; Ardenkjær-Larsen, J. H.; Griffin, R. G. Sci. Adv. **2019**, *5*, eaax2743.

(144) Blumberg, W. E. Phys. Rev. **1960**, *119*, 79–84.

(145) Graham, M. J.; Yu, C.-J.; Krzyaniak, M. D.; Wasielewski, M. R.; Freedman, D. E. J. Am. Chem. Soc. **2017**, *139*, 3196–3201.

(146) Bahrenberg, T.; Jahn, S. M.; Feintuch, A.; Stoll, S.; Goldfarb, D. Magn. Reson. **2021**, *2*, 161–173.

(147) Martin, R. E.; Pannier, M.; Diederich, F.; Gramlich, V.; Hubrich, M.; Spiess, H. W. **1998**, *37*, 2833–2837.

(148) Pannier, M.; Veit, S.; Jeschke, G.; Spiess, H. W. J. Magn. Reson. **2000**, *142*, 331–340.

(149) Borbat, P. P.; Georgieva, E. R.; Freed, J. H. J. Phys. Chem. Lett. **2013**, *4*, 170–175.

(150) Spindler, P. E.; Waclawska, I.; Endeward, B.; Plackmeyer, J.; Ziegler, C.; Prisner, T. F. J. Phys. Chem. Lett. **2015**, *6*, 4331–4335.

(151) Breitgoff, F. D.; Soetbeer, J.; Doll, A.; Jeschke, G.; Polyhach, Y. O. Phys. Chem. Chem. Phys. **2017**, *19*, 15766–15779.

(152) Carr, H. Y.; Purcell, E. M. Phys. Rev. **1954**, *94*, 630–638.

(153) Harbridge, J. R.; Eaton, S. S.; Eaton, G. R. J. Magn Reson. **2003**, *164*, 44–53.

(154) Goldfarb, D.; Lipkin, Y.; Potapov, A.; Gorodetsky, Y.; Epel, B.; Raitsimring, A. M.; Radoul, M.; Kaminker, I. J. Magn. Reson. **2008**, *194*, 8–15.

(155) Mentink-Vigier, F.; Collauto, A.; Feintuch, A.; Kaminker, I.; Tarle, V.; Goldfarb, D. J. Magn. Reson. **2013**, *236*, 117–125.

(156) Stoll, S.; Schweiger, A. Journal of Magnetic Resonance **2006**, *178*, 42–55.

(157) Yang, Z.; Liu, Y.; Borbat, P.; Zweier, J. L.; Freed, J. H.; Hubbell, W. L. J. Am. Chem. Soc. **2012**, *134*, 9950–9952.

(158) Reginsson, G. W.; Kunjir, N. C.; Sigurdsson, S. T.; Schiemann, O. Chem. Eur. J. **2012**, *18*, 13580–13584.

(159) Giannoulis, A.; Yang, Y.; Gong, Y.-J.; Tan, X.; Feintuch, A.; Carmieli, R.; Bahrenberg, T.; Liu, Y.; Su, X.-C.; Goldfarb, D. Phys. Chem. Chem. Phys. **2019**, *21*, 10217–10227.

(160) Feintuch, A.; Otting, G.; Goldfarb, D. In Methods in Enzymology; Elsevier: 2015; Vol. 563, pp 415–457.

(161) Yardeni, E. H.; Bahrenberg, T.; Stein, R. A.; Mishra, S.; Zomot, E.; Graham, B.; Tuck, K. L.; Huber, T.; Bibi, E.; Mchaourab, H. S.; Goldfarb, D. Sci Rep **2019**, *9*, 12528.

(162) Raitsimring, A.; Dalaloyan, A.; Collauto, A.; Feintuch, A.; Meade, T.; Goldfarb, D. J. Magn. Reson. **2014**, *248*, 71–80.

(163) Bahrenberg, T.; Yang, Y.; Goldfarb, D.; Feintuch, A. Magnetochemistry **2019**, *5*, 20.

(164) Jahn, S. M.; Canarie, E. R.; Stoll, S. J. Phys. Chem. Lett. **2022**, *13*, 5474–5479.

(165) El Mkami, H.; Ward, R.; Bowman, A.; Owen-Hughes, T.; Norman, D. G. J. Magn. Reson. **2014**, *248*, 36–41.

(166) Schmidt, T.; Wälti, M. A.; Baber, J. L.; Hustedt, E. J.; Clore, G. M. Angew. Chem. Int. Ed. **2016**, *55*, 15905–15909.

(167) Verheul, M. FEBS Lett. **1998**, 4.

(168) Reslan, M.; Kayser, V. Pharm. Dev. Technol. **2018**, *23*, 1030–1036.

(169) Owenius, R.; Engström, M.; Lindgren, M.; Huber, M. J. Phys. Chem. A **2001**, *105*, 10967–10977.

(170) Brown, I. M. J. Chem. Phys. **1973**, *58*, 4242–4250.

(171) Lunghi, A.; Sanvito, S. J. Magn. Magn. Mater. **2019**, *487*, 165325.

(172) Maze, J. R.; Taylor, J. M.; Lukin, M. D. Phys. Rev. B **2008**, *7*, 094303.

(173) Abe, E.; Isoya, J.; Itoh, K. M. Physica B: Condens. Matter **2006**, *376-377*, 28–31.

(174) Edmonds, D. T.; Mackay, A. L. J. Magn. Reson. **1975**, *20*, 515–519.

(175) Edmonds, D. T.; Goren, S. D.; White, A. A. L.; Sherman, W. F. J. Magn. Reson. **1977**, *27*, 35–44.

(176) Edmonds, D. T.; Hunt, M. J.; Mackay, A. L. J. Magn. Reson. **1975**, *25*, 505–514.

(177) Jeschke, G. J. Magn. Reson. Open **2023**, *14-15*, 100094.

(178) Dreizier, H.; Scappini, F. Z. Naturforsch **1981**, *36*, 1187–1191.

(179) Li, Q.-S.; Su, M.-G.; Wang, S. J. Chem. Eng. Data **2007**, *52*, 1141–1145.

(180) MathWorks MATLAB `https://www.mathworks.com/products/matlab.html` (accessed 09/24/2023).

(181) Foundation, R. Rust A language empowering everyone to build reliable and efficient software. `https://www.rust-lang.org/` (accessed 07/08/2023).

(182) Foundation, P. S. python `https://www.python.org` (accessed 09/24/2023).